INHOMOGENEOUS CHEMICAL EVOLUTION OF THE GALACTIC HALO

INAUGURALDISSERTATION

ZUR
ERLANGUNG DER WÜRDE EINES DOKTORS DER PHILOSOPHIE
VORGELEGT DER
PHILOSOPHISCH - NATURWISSENSCHAFTLICHEN FAKULTÄT
DER UNIVERSITÄT BASEL

VON

DOMINIK ARGAST
AUS BASEL (BS)

BASEL
SEPTEMBER 2002

Genehmigt von der Philosophisch-Naturwissenschaftlichen Fakultät
auf Antrag von
Prof. Dr. F.-K. Thielemann und Dr. S. G. Ryan
(Mitglieder des Dissertationskomitees)

Basel, den 17. September 2002
(Datum der Fakultätssitzung)

Prof. Dr. M. Tanner
Dekan

“We fit everything.”

J. Andersen, UVES Informal Meeting, Garching, 2002

Abstract

I present a stochastic chemical evolution model to investigate the enrichment of the interstellar medium (ISM) during Galaxy formation. Contrary to classical chemical evolution models, it is able to resolve local chemical inhomogeneities in the ISM caused by single core-collapse supernovae. These inhomogeneities lead to different element abundance patterns in very metal-poor stars which can be seen as scatter in the abundances of halo stars with metallicities [Fe/H] < -2.0. The early chemical evolution of the halo proceeds in different enrichment phases: At [Fe/H] < -3.0, the halo ISM is unmixed and dominated by local inhomogeneities caused by individual core-collapse supernova events. For metallicities [Fe/H] > -2.0 the halo ISM is well mixed, showing an element abundance pattern integrated over the initial mass function. In the range $-3.0 <$ [Fe/H] < -2.0 a continuous transition from the unmixed to the well mixed ISM occurs. For some elements (Si, Ca), the scatter in element-to-iron ratios of metal-poor halo stars can be reproduced. Stellar yields of other elements, however, predict a scatter which, compared to observations, is too large (O, Mg) or too small (Ni).

This shows, that inhomogeneous chemical evolution models are heavily dependent on theoretical nucleosynthesis yields of core-collapse supernovae. Hence inhomogeneous chemical evolution models present themselves as a test for stellar nucleosynthesis calculations. One problem revealed by the model is the predicted scatter in [O/Fe] and [Mg/Fe] which is too large compared to the one observed in metal-poor halo stars. This can be either due to the oxygen or magnesium yields or due to the iron yields (or both). However, oxygen and magnesium are α-elements that are produced mainly during hydrostatic burning and thus are not affected by the theoretical uncertainties afflicting the collapse and explosion of a massive star. Stellar iron yields, on the other hand, depend heavily on the choice of the mass-cut between ejecta and proto-neutron star and are therefore very uncertain. In this work, iron yield distributions as function of progenitor mass are derived which are consistent with the abundance distribution of metal-poor halo stars and are in agreement with observed ^{56}Ni yields of core-collapse supernovae with known progenitor masses. The iron yields of lower-mass Type II supernovae (in the range $10 - 20\,\mathrm{M}_{\odot}$) are well constrained by these observations. Present observations, however, do not allow us to determine a unique solution for higher-mass Type II supernovae. Nevertheless, the main dependence of the stellar iron yields as function of progenitor mass can be derived and may be used as a constraint for future core-collapse supernova/hypernova models. A prediction of hypernova models which can be tested by future observations is the existence of ultra α-element enhanced stars at metallicities [Fe/H] ≤ -2.5. The results are of importance for the earliest stages of galaxy formation when the ISM is dominated by local chemical inhomogeneities and the instantaneous mixing approximation is not valid.

The astrophysical nature of r-process sites is a long standing mystery and many probable sources were suggested in the past, among them lower-mass core-collapse supernovae (in the range $8 - 10\,\mathrm{M}_{\odot}$), higher-mass core-collapse supernovae (with masses $\geq 20\,\mathrm{M}_{\odot}$) and neutron star mergers. In this work, I present a detailed inhomogeneous chemical evolution study that considers for the first time neutron star mergers as major r-process sources, and compare this scenario to the ones in which core-collapse supernovae act as dominant r-process sites. Furthermore, the enrichment of the interstellar medium with neutron-capture elements during Galaxy formation by r- and s-process sources is investigated. I conclude that, due to the lack of reliable iron and r-process yields as function of progenitor mass, it is not possible to date to distinguish between the lower-mass and higher-mass supernovae scenario within the framework of inhomogeneous chemical evolution. However, neutron-star mergers seem to be ruled out as *dominant* r-process source, since their low coalescence rates are not consistent with observations of r-process elements at very low metallicities. Furthermore, the considerable injection of r-process material by a single neutron-star merger leads to a scatter in r-process abundances at later times which is much too large compared to observations. Finally, a low star-formation efficiency is required during halo formation to be consistent with the appearance of s-process elements at very low metallicities.

Contents

Abstract **v**

List of Figures **ix**

List of Tables **xi**

List of Chapter Images **xiii**

1 Introduction **1**

- 1.1 In the beginning. . . 3
- 1.2 Nucleosynthesis in stars during hydrostatic burning phases 5
  - 1.2.1 H burning 5
  - 1.2.2 He burning 7
  - 1.2.3 C, Ne, O and Si burning 7
- 1.3 Nucleosynthesis in core-collapse supernovae 8
  - 1.3.1 The core-collapse supernova mechanism 8
  - 1.3.2 Explosive burning phases in SNe II 9
  - 1.3.3 Yields from core-collapse SNe 11
- 1.4 Formation of neutron capture elements 11
  - 1.4.1 The s-process 11
  - 1.4.2 The r-process 13
- 1.5 Classic chemical evolution models 14
- 1.6 ICE – Inhomogeneous chemical evolution 16
  - 1.6.1 Mass infall 17
  - 1.6.2 Star formation law 17
  - 1.6.3 Stellar lifetimes 18
  - 1.6.4 Stars of low and intermediate mass ($< 10\,\mathrm{M}_{\odot}$) 18
  - 1.6.5 Core-collapse SNe ($10 - 50\,\mathrm{M}_{\odot}$) 18
  - 1.6.6 Type Ia SNe 19
  - 1.6.7 Sources of neutron capture elements 19
  - 1.6.8 Chemical inhomogeneities in the early ISM 19

2 Metal-poor halo stars as tracers of ISM mixing processes during halo formation **23**

- 2.1 Introduction 25
- 2.2 The Model 25
- 2.3 SN II yields and their uncertainties 27
- 2.4 Observational Data 30
- 2.5 Results 30
  - 2.5.1 Chemical Mixing of the Halo ISM 30

2.5.2 Comparison with Observations 35
2.5.3 Individual Elements and Nucleosynthesis 37
2.5.4 Age–Metallicity Relation 39
2.5.5 Ultra Metal-poor Stars 39
2.6 Conclusions & Discussion 40

3 Implications of O and Mg abundances in metal-poor halo stars for stellar iron yields 43
3.1 Introduction 45
3.2 The chemical evolution model 46
3.3 Observations and basic model results 47
3.4 Global constraints on stellar Fe yields 48
3.4.1 Uncertainties in O, Mg and Fe yields 48
3.4.2 The influence of Z and SNe from Population III stars 51
3.4.3 Putting constraints on Fe yields with the help of observations 52
3.5 Implications for stellar Fe yields 56
3.6 Conclusions 65

4 Neutron star mergers, core-collapse supernovae and neutron capture elements in the early Galaxy 67
4.1 Introduction 69
4.2 The chemical evolution model 70
4.2.1 Basic ingredients 70
4.2.2 Treatment of r- and s-process sources in the model 72
4.3 Basic model results in comparison to observations 75
4.4 Enrichment of the ISM with neutron capture elements 78
4.4.1 A robust r-process beyond barium? 78
4.4.2 Disentangling the r- and s-process contributions to neutron capture elements 79
4.4.3 Constraints on the SFR in the early Galaxy 82
4.5 Results 85
4.5.1 A low SF efficiency model 85
4.5.2 SN II as dominating r-process sites 89
4.5.3 NSM as dominating r-process sites 92
4.6 Conclusions 98

5 Conclusions 101

References 107

Acknowledgements 113

Declaration 115

Curriculum Vitae 117

List of Figures

1.1 Enrichment of the interstellar medium with oxygen and iron . . . 20
2.1 Cut through the computed volume . . . 31
2.2 Element-to-iron ratios [el/Fe] of O, Mg, Si, Ca, Cr, Mn, Ni and Eu . . . 33
2.3 Normalized nickel-to-iron ratio [Ni/Fe] . . . 35
2.4 Relative frequency of stars in [Si/Fe] bins . . . 36
2.5 Scatter in [Si/Fe] of the model and observed stars . . . 37
2.6 Metallicity [Fe/H] vs. age of single model stars . . . 39
2.7 Metallicity distribution of model stars . . . 40
3.1 [O/Fe] and [Mg/Fe] ratios vs. metallicity [Fe/H] of metal-poor halo stars and model stars . . . 47
3.2 [O/Mg] vs. [Mg/H] ratios of metal-poor halo stars . . . 48
3.3 O and Mg yields from different authors as function of progenitor mass . . . 50
3.4 Fe yields from different authors as function of progenitor mass . . . 50
3.5 $Y_{\mathrm{Fe}}\,(m)$ as function of progenitor mass . . . 54
3.6 Continuously increasing iron yields $Y_{\mathrm{Fe}}\,(m)$ . . . 56
3.7 Distribution of [O/Fe] ratios resulting from continuously increasing iron yields . . . 56
3.8 Increasing then decreasing iron yields $Y_{\mathrm{Fe}}\,(m)$ . . . 57
3.9 Distribution of [O/Fe] ratios resulting from increasing then decreasing iron yields . . . 57
3.10 Iron yields of model S1 . . . 58
3.11 Iron yields of model H1 . . . 58
3.12 Iron yields of model H2 . . . 58
3.13 Iron yields of model S2 . . . 58
3.14 [el/Fe] distribution of model S1 . . . 60
3.15 [el/Fe] distribution of model H1 . . . 61
3.16 [el/Fe] distribution of model H2 . . . 62
3.17 [el/Fe] distribution of model S2 . . . 63
4.1 Overview of basic model results . . . 76
4.2 G-dwarf distribution . . . 77
4.3 Neutron capture element abundances in BD +17°3248 . . . 78
4.4 [Ba^s/Eu] and [Ba/Eu] vs. [Fe/H] in stars compared to results of the standard model . . . 83
4.5 Overview of the low SF efficiency model . . . 86
4.6 Age-metallicity relations of the standard model and the low SF efficiency model . . . 87
4.7 [Ba^s/Eu] and [Ba/Eu] vs. [Fe/H] in stars compared to results of the low SF efficiency model . 88
4.8 Eu and Ba abundances vs. metallicity [Fe/H]. SN II in the range $8-10\,\mathrm{M}_\odot$ are assumed to be the dominating r-process sites . . . 90
4.9 Eu and Ba abundances vs. metallicity [Fe/H]. SN II in the range $20-25\,\mathrm{M}_\odot$ are assumed to be the dominating r-process sites . . . 91
4.10 Eu and Ba abundances vs. metallicity [Fe/H]. NSM occurring at a global rate of $2\cdot 10^{-4}\mathrm{yr}^{-1}$ are assumed to be the dominating r-process sites . . . 93

4.11 [Ba^r/Fe] and [Ba^s/Eu] vs. [Fe/H] for different NSM rates ($t_c = 10^6$ yr) 95
4.12 [Ba^r/Fe] and [Ba^s/Eu] vs. [Fe/H] for different NSM rates ($t_c = 10^7$ yr) 96
4.13 [Ba^r/Fe] and [Ba^s/Eu] vs. [Fe/H] for different NSM rates ($t_c = 10^8$ yr) 97

List of Tables

1.1 Schematic internal structure of a highly evolved massive star 6
2.1 Reference list of the observational data 29
2.2 Pollution factor and SN Type II frequency 34
2.3 Expected frequency of metal-poor halo stars 40
2.4 Frequency of model stars 40
3.1 Best fit O and Mg yields 51
3.2 Proposed iron yields $Y_{\mathrm{Fe}}\,(m)$ 64
4.1 Parameter values of the standard model 72
4.2 Parameter values adopted for NSM events 74
4.3 Comparison of r- and s-process contributions to Ba in ultra metal-poor halo stars (solar r-process fraction of Ba set to 0.15) 81
4.4 Comparison of r- and s-process contributions to Ba in ultra metal-poor halo stars (solar r-process fraction of Ba set to 0.20) 81

List of Chapter Images

1 Protostar HH–34 in Orion (ESO PR Photo 40b/99) 1
2 Giant Nebula NGC 3603 and Starburst Cluster (STScI PR 99-20) 23
3 SN 1987A in the Large Magellanic Cloud (STScI PR 98-08) 43
4 Artist's Impression of a Millisecond Pulsar (ESA/NASA 2002) 67
5 Crab Nebula in Taurus (ESO PR Photo 40f/99) 101

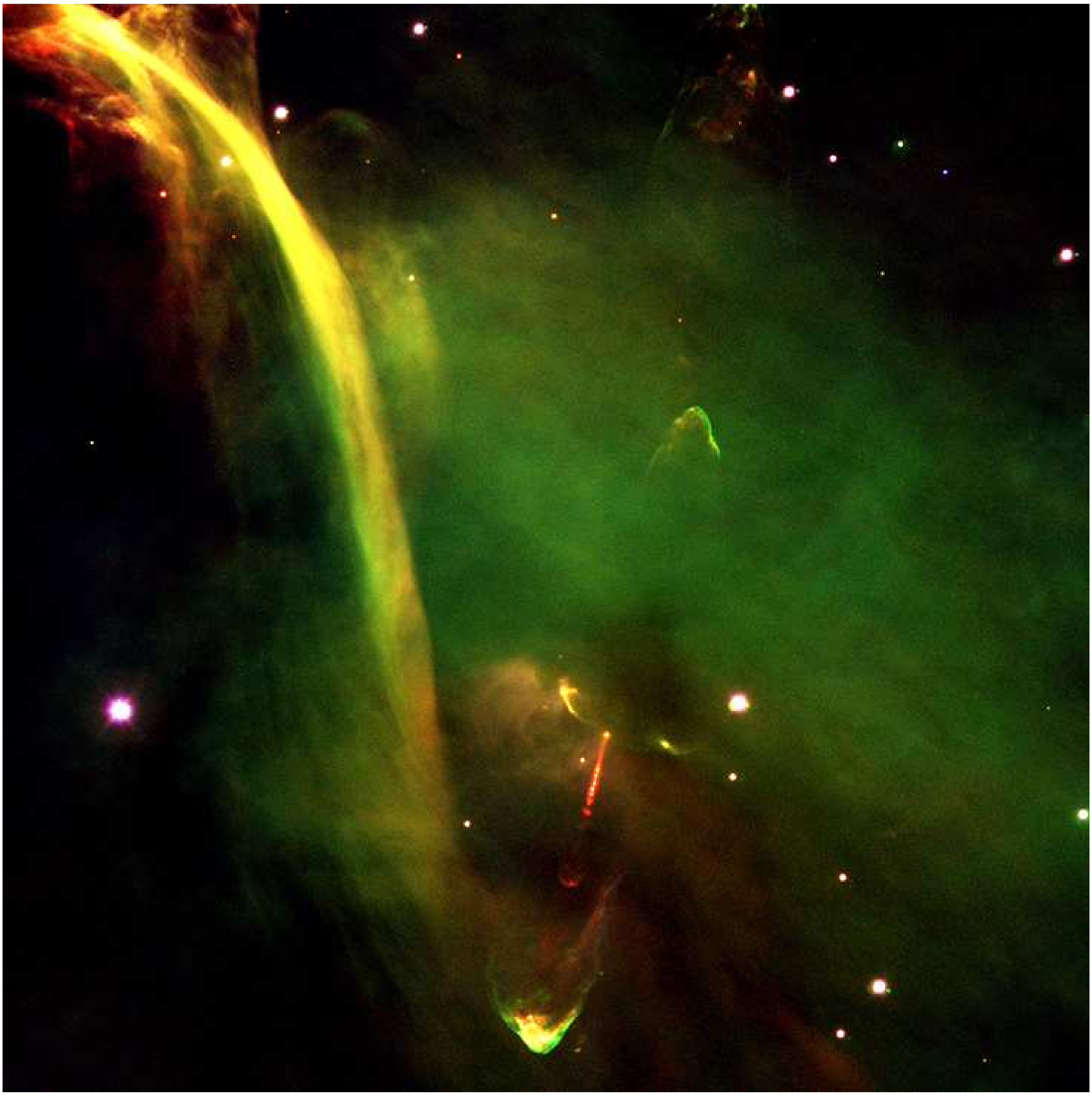

1

Introduction

1.1. In the beginning…

In the beginning, there was nothing, which exploded.

The universe came into being. Any cosmologist will tell you that all the interesting stuff happened in the first couple of minutes, when nothingness bunched together to form space and time and lots of really tiny black holes appeared and so on. After that, they say, it became just a matter of, well, matter. It was basically all over bar the microwave radiation. Seen from close by, though, it had certainly a gaudy attraction.

The little man sniffed.

"Too showy," he said. "You don't need all that noise. It could easily have been a Big Hiss, or a bit of music."

"Could it?" said Rincewind.

"Yeah, and it looked pretty iffy around the two picosecond mark. Definitely a bit of ropy filling-in. But that's how it goes these days. No craftsmanship. When I was a lad, it took days *to make a universe. You could take a bit of pride in it. Now they all throw it together and it's back on the lorry and away."*

Rincewind stared at him.

"Who are *you?"*

The man took the pencil from behind his ear and looked reflectively at the space around Rincewind. "I make things," he said.

"You're the Creator*?"*

The little man looked very embarrassed. "Not the. Not the. *Just* a. *I don't contract for the big stuff, the stars, the gas giants, the pulsars and so on." He gave him a look of defiant pride. "I do all my own trees, you know," he confided. "Craftsmanship. Takes years to learn how to make a tree. Even the conifers."*

"Oh," said Rincewind.

*"*Some *people think it's enough to install a few basic physical formulas and then take the money and run. A billion years later you got leaks all over the sky, black holes the size of your head, and when you pray up to complain there's just a girl at the counter who says she don't know where the boss is. Well, nice to have met you. If you need any extra work, you know, an extra moon or something—"*

"Hey!"

The creator reappeared, his eyebrows raised in polite surprise.

"What happens now?" said Rincewind.

(Pratchett 1990)

Much has happened since Rincewind witnessed the creation of the universe and, since its bewildering complexity suggests that it was indeed created by uncaring people who just installed some physical laws and ran, it is up to us to figure out exactly *what* had happened. It turns out that this is not an easy task, as can be seen by the age old struggle to explain the mysteries surrounding us. Yet, during the last few hundred years understanding dawned at last, and we started to tell ourselves more or less convincing stories about the nature of the universe.

One of the most convincing stories to date is the beginning of the universe with the "Big Bang", parodied above by Terry Pratchett (1990). As a consequence of this story, the baryonic matter in the universe shortly after the Big Bang is thought to consist only of light elements, primarily H and ^{4}He (making up roughly 75% and 25% by mass, respectively) and traces of deuterium (D or ^{2}H), tritium (T or ^{3}H), ^{3}He, and ^{7}Li. Thus, the question arises where all the heavier elements, such as carbon, oxygen, iron, silver or gold, originate. The answer to this question began to emerge during the first decades of the 20th century, and is inextricably linked to the question why stars shine.

At the beginning of the last century, it was clear that neither gravitational contraction nor chemical reactions could be the source of the enormous amounts of energy emitted by the Sun during its long life. Soon after the discovery of the equivalence of mass and energy by Albert Einstein in 1905 it was obvious that nuclear reactions in stellar cores, converting hydrogen into helium by the *pp* chain or the CNO cycle, are the main energy source in ordinary stars (Atkinson 1931a, 1931b, 1936; von Weizsäcker 1937, 1938; Bethe 1939). Yet nucleosynthesis of heavier elements in stars seemed improbable at that time, so that the mystery of the origin of heavy nuclei remained. The riddle was solved by Öpik (1951) and Salpeter (1952) who realized that a star undergoes gravitational contraction after hydrogen exhaustion. Consequently, the temperature and density in its core increase and a new nuclear reaction, the triple α process, occurs, transforming three ^{4}He nuclei into one ^{12}C nucleus. This fundamental discovery opened the road to the modern understanding of nucleosynthesis of heavy elements, and by 1957 most of the relevant processes were known (Burbidge, Burbidge, Fowler & Hoyle 1957, hereafter B^2FH).

But not only the question of the origin of heavy elements needs answering. Of equal interest is in which way heavy elements are distributed in the Galaxy and how their enrichment proceeds with time. From this, insights into the processes at work during Galaxy formation can be gained. First attempts to understand the enrichment history of heavy elements during the evolution of the Galaxy were made around the same time as the most important nucleosynthesis channels were identified.

Schwarzschild & Spitzer (1953) proposed that for stars of Population II "*the metal abundance [. . .] is likely to be as low as one-tenth of that of Population I. [. . .] Since these stars of extreme Population II were presumably formed in the very earliest stages of our Galaxy, it is tempting to assume that their chemical composition represents the original chemical composition of our Galaxy. [. . .] If indeed it should be true that [. . .] the bulk of the heavy elements now in Population I stars originated after the formation of the earliest stars of Population II, one might assume [. . .] that the death of heavy, fast living stars is the cause of [this enrichment].*" Thus, the first observational evidence that the abundances of heavy elements changed during galactic evolution was assembled and it became clear that old, metal-poor stars can be used to trace the chemical composition of the Galaxy at early times. In addition, Schwarzschild & Spitzer (1953) correctly identified one of the main sources responsible for heavy element enrichment: Fast evolving, massive stars that end their life as core-collapse supernovae.

However, it took about twenty years until the study of galactic chemical evolution could start in earnest. The ultimate goal of chemical evolution studies is to unravel the processes that were at work during Galaxy formation and to understand the observed enrichment of heavy elements. Thus, possible sources of heavy elements have to be identified and their element yields (i.e. the amount of a given element produced by a source) have to be estimated first. In addition, an inventory of heavy element abundances in as many stars as possible is needed to provide a basis of comparison. Unfortunately, it is almost impossible to determine the age of single stars accurately to date, so that a direct comparison of element abundances as function of age is not feasible. Instead, the abundance of iron with respect to hydrogen ([Fe/H][1]) is mostly used as an age indicator. Thus, after the first nucleosynthesis calculations in explosive environments (or, in other words, core-collapse supernovae) became available (e.g. Arnett 1969; Truran & Arnett 1970 and others), the fundamental ingredients needed for successful models of galactic chemical evolution were in place (e.g. Cameron & Truran 1971; Talbot & Arnett 1973; Tinsley 1974 and others). Since then, chemical evolution models became more and more sophisticated, as did nucleosynthesis calculations in core-collapse supernovae and other sources of heavy elements. Additionally, with the advent of the new telescopes of the 8 m and 10 m class and space-based observational facilities, the resolution and signal-to-noise ratio of stellar spectra increased considerably. Thus, it is possible today to determine element abundances in stars of very low metallicity (down to approximately 1/10'000 of the iron content of the Sun, or equivalently [Fe/H] ≈ -4) with unprecedented accuracy, so that even local chemical inhomogeneities in the interstellar medium (ISM) during the earliest stages of Galaxy formation can be detected.

The occurrence of such inhomogeneities in the early ISM and the evolution from the unmixed, metal-poor ISM to the well mixed, metal-rich ISM is addressed in this work. An extensive part of this chapter discusses the major nucleosynthesis processes relevant for this work. Hydrostatic burning in stars is treated in Sect. 1.2, followed by a brief overview of the core-collapse supernova (SN II) mechanism and explosive burning phases in Sect. 1.3. Formation of neutron capture elements is discussed in Sect. 1.4. In Sect. 1.5 a short introduction to classic chemical evolution models is given and my stochastic chemical evolution model, which is able to resolve local chemical inhomogeneities in the ISM, is presented in Sect. 1.6. The model is used to investigate the influence of chemical inhomogeneities on the enrichment of heavy elements in the early halo ISM (Chapter 2). In Chapter 3, an attempt to determine the progenitor mass dependence of iron yields from core-collapse supernovae is made, and Chapter 4 deals with the enrichment of neutron capture elements during Galaxy formation. Finally, concluding remarks are given in Chapter 5.

---

[1] In this work, the standard notation [X/Y] = $\log(X/Y)_\star - \log(X/Y)_\odot$ is used for any chemical species. In addition, the term *element abundance* means [el/Fe] for a given element *el* and *metallicity* is used as synonym for [Fe/H], unless otherwise noted.

Note that the results of the model were published/are to be published in various issues of Astronomy & Astrophysics and are included in this work "as is", i.e. no changes to the published texts were made. Thus, the reader may skip the redundant sections describing the chemical evolution model in Chapters 2, 3 and 4. The references to the published articles are:

Chapter 2: Argast, D., Samland, M., Gerhard, O. E., & Thielemann, F.-K. 2000, A&A, 356, 873
Chapter 3: Argast, D., Samland, M., Thielemann, F.-K., & Gerhard, O. E. 2002, A&A, 388, 842
Chapter 4: Argast, D., Samland, M., Thielemann, F.-K., & Qian, Y.-Z. 2003, astro-ph/0309237

1.2. Nucleosynthesis in stars during hydrostatic burning phases

The complex evolution of a star from the pre-main-sequence stage to the end of its life as a white dwarf, neutron star or black hole depends on many parameters, e.g. initial composition, main-sequence mass, convection, rotation, mass loss episodes, etc. Since this work mainly deals with the origin of elements in stellar sources and the chemical evolution of the Galaxy, the following section only lists the main nuclear burning phases and does not address complex changes in the stellar structure during stellar evolution, such as core and shell burning episodes, thermal pulses, convection or rotationally induced mixing.

The nuclear evolution of a star can be represented in a very schematic way by a cycle of

… → nuclear burning → fuel exhaustion → core contraction & heating → nuclear burning → …

In each cycle the ashes of the preceding burning phase are reused as fuel for the next nuclear burning episode. This is possible since core temperatures increase as the core contracts[2]. As soon as temperatures are high enough to activate the next nucleosynthesis channel, the internal energy production can stop the contraction. Then, as the fuel gets exhausted, the stellar core contracts again, etc.

Finally, the internal structure of a highly evolved, massive star can be approximated in a simplified but intuitive way to consist of "onion-skins", in which each skin is made up of only a few predominant nuclear species. The composition of the layers, the burning phase responsible for the layer below, the mass fraction of a layer in comparison to the stellar mass and approximate temperatures and densities at the base of a layer are listed in Table 1.1. After Si exhaustion, no further nuclear fuel is available. The star collapses and ends its life as a core-collapse supernova.

The nuclear reactions presented here cover the basic processes relevant to this work and list only the major nucleosynthesis channels of a given burning phase. For a detailed review on nucleosynthesis in stars refer to Wallerstein et al. (1997), which is the source of most of the information below (unless otherwise noted).

In the following, a compact notation for nuclear reactions is used most of the time, e.g. the reaction

$$^{1}\mathrm{H} + {}^{1}\mathrm{H} \rightarrow \mathrm{D} + e^{+} + \nu_e$$

is written in a compact form as

$$\mathrm{H}(\mathrm{H}, e^{+}\,\nu_e)\mathrm{D}.$$

1.2.1. H burning

Hydrogen burning is the main energy source during the main-sequence stage of a star and sets in as core temperatures reach $T \approx 8 \cdot 10^{6}$ K. The burning may proceed either via the *pp* chain or the CNO cycle. The net result of both nucleosynthesis channels is the fusion of four ^{1}H nuclei (also simply denoted as H or p) into one ^{4}He nucleus (or α particle). The energy release by the *pp* chain dominates the energy production in main-sequence stars with masses below $\approx 1.5\,\mathrm{M}_{\odot}$. Stars with larger masses have core temperatures in excess of $T \approx 2 \cdot 10^{7}$ K. In these cases, the CNO cycle acts as main energy source.

a. The pp chain

The first reaction in the *pp* chain is the fusion of two hydrogen nuclei into deuterium. Since one of the pro-

---

[2] This is only true for non-degenerate cores. In some stars, the core becomes degenerate during contraction and the thermal evolution decouples from the mechanical evolution, i.e. contraction does not lead to increasing temperatures anymore. The cycle of nuclear burnings is interrupted and can only be reactivated by secondary effects. A possibility to remove the degeneracy is by burning nuclear fuel in one or more shell(s) surrounding the stellar core.

Table 1.1. Schematic internal structure of a highly evolved massive star ("onion-skin structure"). The first column gives the approximate mass fraction of a layer. In the second column, dominant nuclear species in the layer are listed. The third column denotes the nuclear burning phases responsible for the layer below and the fourth column lists the nuclei involved in the respective burning phase and its main products. The next to last and last columns indicate approximate temperatures and densities at the bottom of each layer, respectively. (Adapted from Kippenhahn & Weigert 1990.)

$\Delta m/M$	Composition	Burning	Major products	$\log T$	$\log \rho$
0.60	^{1}H, ^{4}He	H burning	H → He	7.0	−2
0.10	^{4}He	He burning	He → C, O	8.3	3.0
0.05	^{12}C, ^{16}O	C burning	C → O, Ne, Mg	8.7	3.8
0.15	^{16}O, ^{20}Ne, ^{24}Mg	Ne burning	Ne → O, Mg, Si	8.9	4.5
0.02	^{16}O, ^{24}Mg, ^{28}Si	O burning	O → Si, S	9.5	6.3
0.08	^{28}Si, ^{32}S	Si burning	Si → Fe, Ni	9.9	9.6

tons has to undergo a β^+ decay[3] at the moment of fusion, this reaction is highly unlikely. Its cross section is so small that it cannot be measured directly under laboratory conditions. It does, however, depend only on well known properties of the weak interaction and is therefore well determined. At the central temperature and density of the Sun, the expected time for two protons to collide and to form a deuterium nucleus is of the order of 10^{10} years. Deuterium then immediately reacts with another proton to form ^{3}He, i.e.

$$\mathrm{H}(\mathrm{H}, e^+ \nu_e)\mathrm{D}$$
$$\mathrm{D}(\mathrm{H}, \gamma)^3\mathrm{He}.$$

The completion of the *pp* chain can proceed by three different channels, of which

$$^3\mathrm{He}(^3\mathrm{He}, 2\mathrm{H})^4\mathrm{He} \tag{pp1}$$

is the most important at temperatures $T \lesssim 10^7$ (Kippenhahn & Weigert 1990). As temperatures rise over this threshold, the reactions

$$\begin{aligned} &^3\mathrm{He}(^4\mathrm{He}, \gamma)^7\mathrm{Be} \\ &^7\mathrm{Be}(e^-, \nu_e)^7\mathrm{Li} \\ &^7\mathrm{Li}(\mathrm{H}, ^4\mathrm{He})^4\mathrm{He} \end{aligned} \tag{pp2}$$

and

$$\begin{aligned} &^3\mathrm{He}(^4\mathrm{He}, \gamma)^7\mathrm{Be} \\ &^7\mathrm{Be}(\mathrm{H}, \gamma)^8\mathrm{B} \\ &^8\mathrm{B} \to {}^8\mathrm{Be} + e^+ + \nu_e \\ &^8\mathrm{Be} \to {}^4\mathrm{He} + {}^4\mathrm{He} \end{aligned} \tag{pp3}$$

begin to dominate the energy production in a star.

b. The CNO cycle

In the CNO cycle, carbon, nitrogen and oxygen act as catalysts to bypass the "bottleneck" (i.e. the first reaction) in the *pp* chain. The CNO cycle requires that these catalysts are present in a star. Thus it can not be the (initial) energy source of metal-free (Population III) stars. However, there exists the possibility that the CNO cycle is activated in Population III stars as soon as traces of ^{12}C are formed *in situ* by the triple α process (e.g. Baraffe et al. 2001).

The energy generation by the CNO cycle is much more temperature dependent than in the case of the *pp* chain. Although the *pp* chain is still active, the energy production is dominated by the CNO cycle in stars more massive than $\approx 1.5\,\mathrm{M}_\odot$.

The main CNO cycle is a sequence of the following reactions and is completed after the initial ^{12}C nucleus is restored:

$$\begin{aligned} &^{12}\mathrm{C}(\mathrm{H}, \gamma)^{13}\mathrm{N} \\ &^{13}\mathrm{N} \to {}^{13}\mathrm{C} + e^+ + \nu_e \\ &^{13}\mathrm{C}(\mathrm{H}, \gamma)^{14}\mathrm{N} \\ &^{14}\mathrm{N}(\mathrm{H}, \gamma)^{15}\mathrm{O} \\ &^{15}\mathrm{O} \to {}^{15}\mathrm{N} + e^+ + \nu_e \\ &^{15}\mathrm{N}(\mathrm{H}, ^4\mathrm{He})^{12}\mathrm{C} \end{aligned}$$

One possible branching occurs at the last reaction via $^{15}\mathrm{N}(\mathrm{H}, \gamma)^{16}\mathrm{O}$, but it is about 10^4 times less probable than the main cycle (Kippenhahn & Weigert 1990). The main effect of this branching is the transformation of the initially present ^{16}O into ^{17}O and finally into ^{14}N by subsequent reactions with protons.

The bottleneck in the CNO cycle is the reaction $^{14}\mathrm{N}(\mathrm{H}, \gamma)^{15}\mathrm{O}$. Nearly all initially present C, N, and

---

[3] $(Z, A) \to (Z-1, A) + e^+ + \nu_e$, where Z is the number of protons of a nuclear species and A the atomic mass number.

O nuclei will be transformed into ^{14}N, waiting to react with another proton to ^{15}O. Thus, the rate of this reaction plays an important role in determining evolution timescales of massive stars and globular cluster ages.

1.2.2. He burning

After the hydrogen supply in the core of a star is exhausted (when roughly 10% of its total hydrogen content are consumed), the star opens up a new energy source by contraction of its core. The star leaves the main-sequence and evolves to the red giant stage. At this stage, the core consists mainly of ^{4}He. As a consequence of the contraction temperature and density in the core increase until the triple α reaction sets in at $T \gtrsim 10^8$ K. The key reaction is the formation of ^{12}C from three ^{4}He nuclei. The probability of a triple collision of α particles is vanishingly small, so that the reaction occurs in two steps:

$$
\begin{aligned}
&^{4}\mathrm{He} + {}^{4}\mathrm{He} \rightleftharpoons {}^{8}\mathrm{Be} \\
&^{8}\mathrm{Be} + {}^{4}\mathrm{He} \rightarrow {}^{12}\mathrm{C}
\end{aligned}
$$

The nucleus ^{8}Be is highly unstable and decays back into two ^{4}He nuclei after a few times 10^{-16} s. However, the lifetime of ^{8}Be is sufficiently long to guarantee the formation of some ^{12}C by another collision with ^{4}He under the physical conditions occurring in the centre of the stellar core.

Once a sufficient amount of ^{12}C has been built up, further α captures on ^{12}C occur, leading to the formation of ^{16}O by

$$^{12}\mathrm{C}(\alpha,\gamma)^{16}\mathrm{O}.$$

Subsequent α captures on ^{16}O would lead to ^{20}Ne, ^{24}Mg, ..., but reactions going beyond ^{16}O under typical He burning conditions in stellar environments are rare.

Unfortunately the important $^{12}\mathrm{C}(\alpha,\gamma)^{16}\mathrm{O}$ reaction rate is very uncertain, which leads to some uncomfortable consequences: This rate determines how much of the ^{12}C is converted into ^{16}O, and thus directly affects the amount of carbon and oxygen ejected in core-collapse SNe and the C/O ratio in the interiors of white dwarfs. In addition, the C/O ratio in the core of a massive star sets the initial conditions of subsequent burning stages that lead to the formation of heavy elements such as iron-peak nuclei[4]. Thus the further evolution of massive stars depends critically on this rate, which leads in turn to large uncertainties in the yields of SNe II.

1.2.3. C, Ne, O and Si burning

After He exhaustion, the core of a star consists of a mixture of carbon and oxygen. Massive stars subsequently burn C, Ne, O and Si. An important difference to H and He burning is that the total luminosity of a star is dominated by neutrino emission rather than the usual emission of radiation at the stellar surface. Since neutrinos can leave the stellar core freely, a large energy loss occurs and the further evolution of massive stars occurs on progressively shorter time-scales (Kippenhahn & Weigert 1990).

a. C burning

Carbon burning sets in at temperatures in the range $(5-10)\cdot 10^8$ K. Two ^{12}C nuclei form an excited ^{24}Mg nucleus, which decays preferably through one of the following channels:

$$
\begin{aligned}
^{12}\mathrm{C} + {}^{12}\mathrm{C} &\rightarrow {}^{20}\mathrm{Ne} + {}^{4}\mathrm{He} \\
&\rightarrow {}^{23}\mathrm{Na} + p \\
&\rightarrow {}^{23}\mathrm{Mg} + n
\end{aligned}
$$

The ^{4}He nuclei produced by the first reaction can subsequently act on other nuclei present, resulting in a wealth of different nuclear species ranging from Ne to P, but the main products of C burning are ^{20}Ne (also from $^{23}\mathrm{Na}(p,\alpha)^{20}\mathrm{Ne}$), ^{24}Mg (by the reactions $^{20}\mathrm{Ne}(^{4}\mathrm{He},\gamma)^{24}\mathrm{Mg}$ and $^{23}\mathrm{Na}(p,\gamma)^{24}\mathrm{Mg}$) and ^{16}O (by α capture on ^{12}C).

b. Ne burning

Following carbon burning, temperatures are high enough ($T \approx 1.2 \cdot 10^9$ K) that photodisintegration of

---

[4] Nuclei in the mass range $40 < A < 65$ are referred to as iron-peak nuclei. This mass range corresponds to the elements Sc, Ti, V, Cr, Mn, Fe, Co, Ni and Cu.

^{20}Ne occurs. The freed α particles subsequently react with other ^{20}Ne nuclei to ^{24}Mg. The two reactions

$$^{20}\mathrm{Ne}(\gamma,{}^{4}\mathrm{He})^{16}\mathrm{O}$$
$$^{20}\mathrm{Ne}({}^{4}\mathrm{He},\gamma)^{24}\mathrm{Mg}$$

can be summarized as

$$^{20}\mathrm{Ne} + {}^{20}\mathrm{Ne} \rightarrow {}^{16}\mathrm{O} + {}^{24}\mathrm{Mg}.$$

Furthermore, ^{28}Si can be formed by α capture on ^{24}Mg. Thus, at the end of Ne burning, the stellar core consists mainly of ^{16}O, ^{24}Mg and some ^{28}Si.

c. O burning

After most of the ^{20}Ne has been destroyed in the core, temperatures rise (again due to contraction) to $T \approx 2 \cdot 10^9$ and oxygen burning sets in. Two ^{16}O nuclei react to form mainly one of the following products

$$\begin{aligned} ^{16}\mathrm{O} + {}^{16}\mathrm{O} &\rightarrow {}^{28}\mathrm{Si} + {}^{4}\mathrm{He} \\ &\rightarrow {}^{31}\mathrm{P} + p \\ &\rightarrow {}^{31}\mathrm{S} + n \\ &\rightarrow {}^{30}\mathrm{Si} + 2p \\ &\rightarrow {}^{30}\mathrm{P} + \mathrm{D} \end{aligned}$$

The released p, n and α react with other nuclei present to form a wide range of nuclei from Si to Cr. Main products of O burning are ^{28}Si and ^{32}S (e.g. by the reaction $^{28}\mathrm{Si}(\alpha,\gamma)^{32}\mathrm{S}$).

d. Si burning

As temperatures rise to $T \approx 2.7 \cdot 10^9$ K core silicon burning starts, which is characterized by a wealth of different nucleosynthesis channels active at the same time. In a simplified picture, part of the present ^{28}Si is broken down by photodisintegration, i.e. by the processes (γ,α), (γ,p) and (γ,n). The released particles are consecutively added to heavier nuclei present in the core (e.g. to ^{28}Si) by (α,γ), (p,γ) and (n,γ) reactions until iron-peak nuclei are formed. At the end of Si burning, the most abundant nuclear species in the core are ^{54}Fe, ^{56}Fe and ^{58}Ni. The internal structure of a massive star at this evolutionary stage sets the initial conditions for subsequent explosive burning in core-collapse SN events and is schematically summarized in Table 1.1.

After Si exhaustion, energy production ceases, the core collapses and the massive star ends its live as a core-collapse SN. The synthesized iron-peak nuclei belonging to the innermost core of the massive star are not ejected into space, but are locked up in the stellar remnant.

1.3. Nucleosynthesis in core-collapse supernovae

This section is based in large parts on the book *Nuclear evolution of the universe* by Cowan, Thielemann & Truran (in preparation).

1.3.1. The core-collapse supernova mechanism

Stars may end their evolution in various forms[5]. Low-mass and intermediate mass stars ($M \lesssim 8\,\mathrm{M}_\odot$) end their life as white dwarfs with stable CO cores from He burning. Some white dwarfs may be the progenitors of Type Ia supernovae (SNe Ia), e.g. if mass accretion from an evolved companion or merging with another white dwarf increases the stellar mass over the Chandrasekar limit and carbon is ignited in the core. Stars in the mass range $8\,\mathrm{M}_\odot \lesssim M \lesssim 10\,\mathrm{M}_\odot$ form a degenerate O-Ne-Mg core from carbon burning with a mass close to the Chandrasekar mass. Subsequent carbon shell burning may lead to an increase in the mass of the core and electron capture on ^{20}Ne and ^{24}Mg sets in. This reduces the Chandrasekar mass, the core contracts and oxygen and silicon ignite during the contraction until a collapsing Fe core is formed. Close binary evolution with mass transfer episodes onto the companion may prevent this fate. Stars with larger masses undergo all hydrostatic burning phases described in Sect. 1.2 until the core only consists of Fe and Ni nuclei. Since these nuclei have the highest binding energy per nucleon, no further nuclear burning episodes are possible. The core collapses and the star ends its life in a Type II or Ib/c SN event. The stellar remnant is either a neutron star or a black hole. The dividing line between these two cases is not clear cut, but may be around $20 - 25\,\mathrm{M}_\odot$ (e.g. Maeder 1992; Fryer 1999).

---

[5] When energy production due to nuclear burning ceases, stellar cores can only be stable, if they do not exceed a limiting mass. In the case of white dwarfs, this is the famous Chandrasekar mass ($\approx 1.4\,\mathrm{M}_\odot$). The exact value of the Chandrasekar mass depends (among others) on the electron abundance $Y_e = n_e/\rho N_A$, where n_e is the electron number density, ρ the gas density and N_A the number of particles per mole. For neutron stars, the mass limit is somewhat higher ($\approx 1.5 - 2\,\mathrm{M}_\odot$). The exact value of this so-called Oppenheimer-Volkov mass depends on the adopted equation of state. For cores more massive than this value, the collapse can not be stopped and the end product is a black hole.

At the end of stellar evolution the iron core contracts, as soon as the Chandrasekar mass limit is exceeded. Typical values for the central density and temperature at this point are $\rho_c = (4 - 10) \cdot 10^{10}$ g cm^{-3} and $T_c = (8 - 10) \cdot 10^9$ K. Due to electron capture on long timescales during O and Si burning, the electron abundance Y_e is reduced from 0.5 at the beginning of stellar evolution to $0.41 - 0.42$ at the onset of core-collapse. During contraction electron capture increases, further reducing the electron pressure and thus the Chandrasekar mass. The Chandrasekar mass becomes smaller than the total core mass, dividing the iron core into an inner and outer region. The contraction of the inner core turns into a homologous collapse, i.e. $v(r) \propto r$, with subsonic velocities. At the edge of the inner core, infall velocities reach supersonic values up to a significant amount of the free-fall velocity.

During the whole course of stellar evolution, neutrinos can escape freely from the core due to their small cross sections. This behaviour changes as densities reach $\rho \approx (3 - 10) \cdot 10^{11}$ g cm^{-3}: neutrinos get trapped inside the so-called "neutrino sphere" due to processes including neutrino-electron scattering and scattering on nucleons. For $\rho = 10^{12}$ g cm^{-3}, the radius of this sphere is approximately 78 km. Beyond this radius, neutrinos can still escape freely. Below the neutrino sphere, electron captures and neutrino captures reach an equilibrium, $e^- + p \leftrightharpoons n + \nu$. Consequently, Y_e stops to decrease and the Chandrasekar mass stays constant.

As the collapsing inner core approaches nuclear densities (of the order of $3 \cdot 10^{14}$ g cm^{-3}), nuclei dissolve into free nucleons and short range nuclear forces suddenly increase the stiffness of the equation of state. Approximately $30 - 50$ ms after the onset of collapse the core collapse halts, the core rebounds and a pressure wave emerges from the centre, which steepens into a shock wave that moves outwards at supersonic speed. Typical values for the kinetic energy of the shock wave after bounce are of the order of $(4 - 8) \cdot 10^{51}$ erg. The mass of the inner core typically is $\approx 0.8\,\mathrm{M}_\odot$, much smaller than the mass of the initial iron core. At first glance, the kinetic energy of the shock seems to be sufficient to explain the typical kinetic energies observed in SN II events ($\approx 10^{51}$ erg). But as the shock wave ploughes through the infalling matter of the outer iron core, much of its kinetic energy is used up to dissociate the heavy nuclei as they pass through the shock front. For stars in the mass range $8 - 10\,\mathrm{M}_\odot$, the shock might still be energetic enough to reach the surface, so that a *prompt* SN explosion occurs, whereas for higher mass progenitors the shock wave is unable to reach the surface. It stalls and turns into an accretion shock.

During the collapse, the inner core liberated a few times 10^{53} erg of gravitational binding energy which is radiated away by neutrinos of all flavours. Since the neutrinos are liberated inside the neutrino sphere, they leak out of the accreting proto-neutron star on diffusion timescales of the order of 0.5 s to a few seconds (depending on their energies). As they reach the neutrino sphere they can leave the collapsing star freely and their energy is lost. But if less than 1% of the total energy available in neutrinos can be transformed into kinetic energy behind the shock (due to neutrino capture on neutrons, antineutrino capture on protons, neutrino-electron scattering and neutrino-antineutrino induced electron-positron pair creation), the shock might be revived and a *delayed* explosion occurs.

Although this is the accepted core-collapse SN mechanism, no successful (realistic) models of SN II explosions exist to date (see Liebendörfer et al. 2001 for a detailed description of a failed spherical symmetric SN II simulation with accurate input physics and including general relativistic effects). Yet it is possible that instabilities in the shock front observed in multidimensional calculations allow a more efficient energy deposition behind the shock (due to increased densities in the instabilities) and thus result in a successful explosion.

1.3.2. Explosive burning phases in SNe II

After the accretion shock is revived by neutrinos leaking out of the proto-neutron star, it ploughes through the outer shells of a massive star. The detailed structure of these shells is set by the preceding stellar evolution and is illustrated in Table 1.1. The passage of the shock front leads to explosive burning of the nuclei in the shells and the burning products are finally ejected into space. The mass-cut, defined as the dividing line between accreting proto-neutron star and the ejecta, is generally located somewhere in the Si shell and determines the amount of iron-peak nuclei that can be liberated in a SN II event.

Many of the nucleosynthesis processes discussed in Sect. 1.2 also occur in explosive environments, characterized by much higher temperatures and shorter burning timescales. Since many β decay[6] life times of unstable products are longer than the timescales on which explosive burning occurs (on the order of seconds), nuclear cross sections for unstable nuclei are needed for accurate calculations. The dominating fuels in explosive burning are α-particle nuclei such as ^{12}C, ^{16}O, ^{20}Ne, ^{24}Mg and ^{28}Si. Due to the short timescales, only few β decays are possible, resulting in heavier nuclei also with $N \approx Z$. Depending on the temperatures occurring during burning, intermediate to heavy nuclei may be formed. In some explosive environments, the formation of r-process and rp-process nuclei, i.e. nuclei close to the neutron- and proton-drip line, may also be possible.

Zones experiencing peak temperatures in excess of $(4-5) \cdot 10^9$ K undergo explosive Si burning. Such temperatures may lead to complete silicon exhaustion and iron-peak nuclei are produced. The doubly magic nucleus ^{56}Ni, with the largest binding energy per nucleon for $N = Z$, is the most abundant nuclear species resulting from this burning. Since the matter of the original iron core of a massive star is locked up in the stellar remnant, the part of ^{56}Ni that gets ejected during the SN II event is the source of a large fraction of the iron observed in the universe[7]. Depending on the peak temperatures during the passage of a shock front, explosive Si burning can be divided into three different groups: complete Si burning with normal or α-rich freeze-out and incomplete Si burning.

Complete Si burning requires temperatures in excess of $5 \cdot 10^9$ K. At such high temperatures Coulomb barriers can be overcome and nuclear statistical equilibrium is established. Some ^{28}Si is broken down due to (γ, α) and other photodisintegration reactions. The freed α particles subsequently are added to other ^{28}Si nuclei, and $(\gamma, \alpha) \leftrightharpoons (\alpha, \gamma)$ reactions come into a steady-state balance between $A = 28$ and $A = 56$. In this equilibrium, iron-peak nuclei are formed with ^{56}Ni as most abundant nucleus if $Y_e > 0.49$. (Note, that the electron fraction Y_e strongly influences the final composition after the passage of the shock.)

An α-rich freeze out occurs generally at low densities, when the triple α reaction is not fast enough to keep the α abundance in equilibrium during the fast expansion and cooling in explosive events. In an α-rich freeze out, final α capture transforms some of the ^{56,57,58}Ni into ^{60,61,62}Zn and leaves traces of α-capture nuclei such as ^{32}S, ^{36}Ar, ^{40}Ca, ^{44}Ti, ^{48}Cr which could not make their way up to ^{56}Ni, as well as some ^{52}Fe, ^{54}Fe and ^{55}Co. As the remaining α fraction increases, the dominant isotopes ^{56,57,58}Ni get depleted, while abundances of the other nuclei mentioned above increase.

Incomplete Si burning occurs at temperatures in the range of $(4-5) \cdot 10^9$ K. Temperatures are not high enough to efficiently burn Si, so that ^{28}Si and ^{32}S still dominate the abundances after the passage of the shock front. In addition, ^{36}Ar and ^{40}Ca are synthesized in appreciable amounts, while ^{56}Ni and ^{54}Fe dominate the abundances of iron-peak nuclei.

At peak temperatures in excess of $3.3 \cdot 10^9$ K, explosive oxygen burning occurs with the main burning products being ^{28}Si, ^{32}S, ^{36}Ar, ^{40}Ca, ^{38}Ar and ^{34}S. Zones in which the peak temperatures reach $4 \cdot 10^9$ K also show traces of iron-peak nuclei.

Explosive neon burning takes place at temperatures of $2.1 \cdot 10^9$ K. The main burning products are similar to the hydrostatic case: ^{16}O is formed by $^{20}\mathrm{Ne}(\gamma,\alpha)^{16}\mathrm{O}$ and ^{24}Mg and ^{28}Si are formed by $^{20}\mathrm{Ne}(\alpha,\gamma)^{24}\mathrm{Mg}(\alpha,\gamma)^{28}\mathrm{Si}$. In addition, substantial amounts of ^{27}Al, ^{29}Si, ^{32}S, ^{30}Si, ^{31}P are synthesized.

At peak temperatures in excess of $1.9 \cdot 10^9$ K, explosive carbon burning occurs. It is important for Type Ia SNe which occur due to ignition of a CO core, but mostly is of no significance for SN II originating from massive stars. The most abundant nuclei formed in

---

[6] $(Z, A) \rightarrow (Z+1, A) + e^- + \overline{\nu}_e$, where Z is the number of protons of a nuclear species and A the atomic mass number.

[7] ^{56}Ni is unstable and decays via ^{56}Co to ^{56}Fe. This decay can be directly observed, since it powers to a great extent the light curves of supernovae. Another major source of iron-peak nuclei are Type Ia SNe.

SN Ia by this explosive burning are ^{20}Ne, ^{23}Na and ^{24,25,26}Mg.

Explosive He and H burning are not encountered in core-collapse SNe but are important for classical novae, X-ray bursts and supermassive Population III stars.

1.3.3. Yields from core-collapse SNe

For an accurate determination of core-collapse SN yields, self-consistent models of the SN event, following the collapse of the iron core, the bounce at nuclear densities and the propagation of the shock wave until it stalls and is revived by neutrinos diffusing out of the proto-neutron star, are needed. Unfortunately, such models do not exist to date and the yields from core-collapse SNe, which are of paramount importance to chemical evolution studies, are affected by various sources of uncertainties.

A first group is founded in uncertainties in the stellar evolution, since the exact core structure at the onset of core-collapse defines the initial conditions for the subsequent explosive burning phases. Most important for the core structure is the badly known $^{12}\mathrm{C}(\alpha,\gamma)^{16}\mathrm{O}$ reaction rate. Further uncertainties are introduced by the treatment of convection, semiconvection and overshooting, rotationally induced mixing and mass loss episodes.

A second group of uncertainties is a consequence of the unknown explosion mechanism. Artificially induced explosions (piston, kinetic bomb or thermal bomb) have to be used to follow the explosive burning phases and determine the ejecta in a SN II event. Different methods to ensure an explosion lead to differences in element yields of up to 30%. In addition, the dependence of explosion energies on progenitor mass and the detailed structure of the outgoing shock wave are not known. Another important and badly defined parameter, which influences the composition of the ejecta, is the time delay between core bounce and the explosion via neutrino heating behind the accretion shock. The largest uncertainty which directly affects the yields of iron-peak nuclei, results from the arbitrary placement of the mass cut, i.e. the dividing line between ejecta and nascent neutron star.

In some cases, observations of light curves of SN II yield constraints on the ejected ^{56}Ni mass (and thus the mass cut) and observations of Type Ib/c SNe, which lack the large H envelope, give an estimate of He-core masses. For most progenitor masses, however, such constraints are not available. It is possible to identify the dominant source of some major elements, which probe different aspects of the SN mechanism. Yields of C, O, Ne and Mg are essentially determined by hydrostatic He and C burning, with some contribution from explosive Ne/C burning, and vary strongly over progenitor mass. Thus, they can be used to test the progenitor models. S, Ar and Ca are mainly produced by explosive O and Si burning and are not expected to vary much with progenitor mass. Si shows some contribution of hydrostatic burning and seems to vary with progenitor mass by a factor of 2-3. Thus, S, Ar, Ca and Si probe the explosion energy and the structure of the shock wave. The amount of ejected iron-peak nuclei directly depends on the explosion mechanism and thus the placement of the mass-cut, since they origin from explosive Si burning with alpha rich freeze out.

The *average* yields of the core-collapse SN models available to date are mostly consistent with element abundances observed in metal-poor halo stars, but some element yields are uncertain by a factor of two (e.g. iron, one of the most important elements for chemical evolution studies). This is demonstrated by classic chemical evolution models, which reproduce the average element abundances observed in metal-poor stars. Yields as function of progenitor mass, however, are uncertain, as will be discussed in Chapters 2 and 3.

1.4. Formation of neutron capture elements

This section is based in large parts on the review by Wallerstein et al. (1997) and the book *Nuclear evolution of the universe* by Cowan, Thielemann & Truran (in preparation).

1.4.1. The s-process

An important source of neutron capture elements beyond the iron peak is the s-process. This nucleosynthesis channel is characterized by the slow capture of neutrons on seed nuclei (such as iron). Subsequent β decay of unstable nuclei along the neutron capture chain occurs on timescales faster than the corresponding neutron capture timescales. Thus, the s-process path remains close to the valley of β stability and most of the neutron rich isotopes are formed by the r-process (see below). The s-process path terminates at mass $A = 209$ (i.e. Pb and Bi), since all nuclei more massive are unstable and approach the valley of β stability by rapid α or β decay. Pronounced abundance peaks at strontium ($A = 88$), barium ($A = 138$) and lead ($A = 208$) result from the small neutron capture cross sections of nuclei with closed neutron shells at "magic neutron numbers" $N = 50, 82$ and 126. An additional feature of s-process nucleosynthesis is a pronounced odd-even abundance variation. Nuclei formed in the s-process with even mass numbers are more abundant than their immediate neighbours with odd mass numbers. Since nuclei participating in the s-process are stable or have β decay lifetimes of the order of 10 - 100 years, the s-process is associated with the hydrostatic burning phases occurring in stars. Possible neutron sources either are the $^{13}\mathrm{C}(\alpha, n)^{16}\mathrm{O}$ or the $^{22}\mathrm{Ne}(\alpha, n)^{25}\mathrm{Mg}$ reaction. These two neutron sources exhibit very different characteristics, which opens up the possibility to deduce the dominating neutron source from observations of s-process enriched stars.

There is a great number of different stellar classes which show s-process enrichment, such as Ba and CH giants, subgiants and main-sequence stars, carbon dwarf stars, N-type carbon stars, MS and S stars. It has been shown, however, that only the s-process enrichment in asymptotic giant branch (AGB) stars (such as N-type carbon stars, S and MS stars) is due to the mixing of fresh s-process matter to the surface. This was demonstrated by the detection of technetium in red giant stars of spectral class S (Merrill 1952). Since all isotopes of Tc are short-lived (with half-life periods of $10^5 - 10^6$ years), the observed Tc must have been formed recently and was mixed to the surface. Other stars showing s-process enrichment belong to binary systems with white dwarf companions. Thus, the s-process excess in those stars has its origin in mass transfer episodes during the AGB phase of the initially more massive companion.

The (main) s-process in AGB stars is associated with He burning, occurring at temperatures $T \approx 10^8$ K in the case of the $^{13}\mathrm{C}$ source, while the $^{22}\mathrm{Ne}$ source operates at higher temperatures $T \approx (2 - 3) \cdot 10^8$ K. The different temperatures required for the activation of these neutron sources are achieved in AGB stars of different masses (with the transition occurring roughly at $4\,\mathrm{M}_{\odot}$).

$^{22}\mathrm{Ne}$ is produced by α captures on $^{14}\mathrm{N}$ in the He burning shell of AGB stars, with the initial $^{14}\mathrm{N}$ coming from H burning in the CNO cycle[8]. Thus, the $^{22}\mathrm{Ne}$ number density ($N_{^{22}\mathrm{Ne}}$) depends on metallicity and is roughly proportional to the iron number density (N_{Fe}). On the other hand, the production of $^{13}\mathrm{C}$ requires extra mixing of protons into the He burning shell to produce $^{13}\mathrm{C}$ via $^{12}\mathrm{C}(p, \gamma)^{13}\mathrm{N}(\beta^+, \nu_e)^{13}\mathrm{C}$. Note that the physical nature of this extra mixing is not known. Since $^{12}\mathrm{C}$ is formed *in situ* by He burning, the number density $N_{^{13}\mathrm{C}}$ of the $^{13}\mathrm{C}$ neutron source does not depend on metallicity (assuming that the He shell structure in AGB stars and the extra mixing is also independent of metallicity).

The s-process also requires the presence of seed nuclei, which act as targets for the free neutrons. Under the assumption of local equilibrium between production and destruction of neutrons, the neutron density N_n in the He burning shell is given by

$$N_n = \frac{\sum N_i N_j \langle\sigma\rangle_{i,j}}{\sum N_k \langle\sigma\rangle_{k,n}}.$$

Here, $\sum N_i N_j \langle\sigma\rangle_{i,j}$ is summed over all neutron producing reactions between nuclear species i, j with cross-section $\langle\sigma\rangle_{i,j}$, while the denominator $\sum N_k \langle\sigma\rangle_{i,j}$ is summed over all neutron absorbing nuclei with cross-section $\langle\sigma\rangle_{k,n}$. Under the simplifying assumption that neutron producing reactions come from α captures and that Fe is the dominant neutron absorber, this equation can be approximated by

$$N_n \propto \frac{N_{\mathrm{He}} N_j}{N_{\mathrm{Fe}}},$$

where N_j is equal to $N_{^{13}\mathrm{C}}$ or $N_{^{22}\mathrm{Ne}}$ for the $^{13}\mathrm{C}$ or $^{22}\mathrm{Ne}$ source, respectively. As discussed above, $N_{^{22}\mathrm{Ne}} \propto N_{\mathrm{Fe}}$, so that in the case of the $^{22}\mathrm{Ne}$ source N_n is expected to be roughly independent of metallicity. On the other hand, the abundance of the $^{13}\mathrm{C}$ source is not expected to change with metallicity, so that in this case we find $N_n \propto N_{\mathrm{Fe}}^{-1}$. This different behaviour of the neutron density as function of metallicity has observable consequences:

---

[8] Since the bottleneck in the CNO cycle is the $^{14}\mathrm{N}(\mathrm{H}, \gamma)^{15}\mathrm{O}$ reaction, the largest part of the initially present C, N and O nuclei are transformed into $^{14}\mathrm{N}$.

A dependence of the neutron density on metallicity directly translates into a metallicity dependence of [hs/ls] abundances, where hs and ls denote heavy s-process nuclei (Ba, La, Ce) and light s-process nuclei (Y and Zr), respectively. In addition, due to a branching in the s-process at $^{85}\mathrm{Kr}$, [Rb/Zr] abundances depend on the neutron exposure[9] and thus on the neutron density during s-process nucleosynthesis. These dependencies on metallicity are indeed observed, and are in good agreement with the predictions of the simple argument presented above for the case of the $^{13}\mathrm{C}$ neutron source. (For a detailed discussion of this effect see Wallerstein et al. 1997 and references therein.)

Thus, $^{22}\mathrm{Ne}$ seems to be ruled out as dominant neutron source and recent s-process models focus on lower-mass AGB stars in the range $1 - 4\,\mathrm{M}_\odot$ which provide the required low temperatures. The formation of $^{13}\mathrm{C}$ requires some sort of extra mixing (e.g. due to semiconvection) at the H-He interface in models of thermally pulsing asymptotic giant branch (TP-AGB) stars. As a consequence of this mixing, pockets of $^{13}\mathrm{C}$ are formed during interpulse phases at the H-He interface. Thermal pulses liberate a double burst of neutrons: The first burst from $^{13}\mathrm{C}(\alpha,\gamma)^{16}\mathrm{O}$ dominates s-process nucleosynthesis. In a later stage of the pulse, as temperatures reach the required values, a weak burst from $^{22}\mathrm{Ne}(\alpha,\gamma)^{25}\mathrm{Mg}$ occurs. Neutron densities reached in such pulses are of the order of $10^7\ \mathrm{cm}^{-3}$, consistent with the required neutron densities deduced from observations of [Rb/Zr] abundances. Note that in stars more massive than $4\,\mathrm{M}_\odot$ the $^{22}\mathrm{Ne}$ neutron source would dominate s-process nucleosynthesis, providing neutron densities of the order of $10^8 - 10^9\ \mathrm{cm}^{-3}$. Such neutron densities are much too high to be consistent with observations of [Rb/Zr]. After a thermal pulse, s-process matter is dredged-up to the stellar surface, giving rise to the observed overabundances of s-process elements.

The description above applies only to the *main* s-process component, responsible for elements in the mass range $90 < A < 204$. The s-process isotopes in the mass range $60 < A < 90$ are attributed to the *weak* s-process component, which possibly occurs in the cores of massive stars. Finally, there might also exist a *strong* s-process component which is responsible for the heavy isotopes of Pb and Bi. Its astrophysical nature, however, is unknown.

1.4.2. The r-process

The second source of neutron capture elements is the r-process. In contrast to the s-process, where neutron capture on seed nuclei occurs on long timescales in red giant stars, neutron capture timescales in the r-process are (much) shorter than β decay life times. This requires a large neutron density of the order of $\gtrsim 10^{20}\ \mathrm{cm}^{-3}$ and temperatures $\gtrsim 10^9$ K. These may be reached in explosive environments, such as core-collapse SNe or neutron star mergers. If the conditions required for r-process nucleosynthesis are met, highly unstable, neutron-rich nuclei can be produced within $\approx 10^{-4}$ s. The large neutron densities carry the nuclei into the neutron-rich region towards the neutron-drip line, so that the most neutron-rich isotopes far from the valley of β stability can be formed. Such nuclei have short β decay timescales of the order of $10^{-2} - 10^{-3}$ seconds, which are nevertheless larger than neutron capture timescales.

Assuming high temperatures and abundant reaction partners, a simplified picture of r-process nucleosynthesis can be drawn. Since nuclei far from β stability are susceptible to photodisintegration, the physical conditions will lead to equilibrium between neutron capture and photodisintegration $(n,\gamma) \leftrightharpoons (\gamma,n)$. Since β decay life times during r-process nucleosynthesis are longer than neutron capture and photodisintegration timescales, each isotopic chain (Z = constant) will be populated according to these equilibrium reactions and the nucleus with maximum abundance must wait for the longer β decay life times (waiting point approximation). Further flow from one isotopic chain to the next then is governed by beta decay. In this picture, the abundance maxima in each isotopic chain are determined only by neutron density and temperature. As the neutron flux ceases, the nuclei formed in the r-process rapidly approach the valley of β stability by β decay, until a stable isotope is reached.

In realistic calculations the flow of nuclei along an isotopic chain is steadily depleted by β decay. Fur-

---

[9] The neutron exposure τ is defined as

$$\tau = \int_0^{t'} N_n(t)V(t)dt,$$

where $N_n(t)$ is the neutron density, $V(t)$ the thermal velocity of neutrons and the integral is taken over the duration of the s-process episode.

thermore, beta-delayed neutron emission, fission cycling, time-dependent neutron densities and temperatures, etc. have to be incorporated. Note that, while the s-process is controlled by neutron capture timescales, the r-process is controlled by β decay timescales. Thus, r-process calculations need accurate predictions of β decay life times to yield correct r-process abundance distributions. Unfortunately, it is not possible to measure these directly for nuclei far from stability, so β decay life times have to be extrapolated from laboratory experiments close to β stability.

Some neutron rich, stable isotopes close to the valley of β stability can only be formed by the r-process. Since further β decay is inhibited, these nuclei "shield" other neutron capture isotopes from the formation via r-process nucleosynthesis. An example of this shielding mechanism is the stable r-only isotope ^{186}W ($Z = 74$): It generates an impenetrable barrier for the r-process, so that ^{186}Os ($Z = 76$) can only be formed by s-process nucleosynthesis.

The large neutron densities in the r-process lead to abundance peaks at somewhat lower mass numbers ($A = 80, 130$ and 190) than in the case of the s-process, since the closed neutron shells at the magic neutron numbers $N = 50, 82$ and 126 are encountered on the neutron rich side of the valley of β stability at lower proton numbers. Furthermore, the pronounced odd-even effect seen in s-process nucleosynthesis is much reduced or even absent in r-process nucleosynthesis.

Due to the required large neutron densities and the short dynamical timescales involved in r-process nucleosynthesis, explosive environments are good candidates for astrophysical r-process sites. Proposed environments can be classified as *primary* and *secondary* production sites. In primary scenarios, seed nuclei are produced *in situ*, whereas in secondary scenarios the seed nuclei come from a previous generation of stars. Inhomogeneous primordial nucleosynthesis, core-collapse SNe, jets and bubbles inside rotating stellar cores and coalescing neutron star binaries have been suggested as primary sites. Candidates of secondary sites include explosive helium or carbon burning in massive stars, helium core flashes in low mass stars, accretion disks around neutron stars and classical novae. Despite (or rather because of) the many suggested scenarios, the astrophysical nature of the r-process is still unknown. Observations of r-process elements at very low metallicities strongly suggest a primary production site at least for the heavier r-process elements beyond barium ($Z \geq 56$). The situation for lighter r-process elements is not clear and a second source may be required to reproduce the observed solar system r-process abundance curve.

1.5. Classic chemical evolution models

The evolution of a galaxy can be roughly divided into three categories: dynamical evolution, chemical evolution and evolution of photometric properties. A realistic model of a galaxy has to address all three categories since they are all interconnected. This was not feasible for a long time due to the missing computational power and still can only be done by applying many simplifications. But models of Galaxy formation and evolution are restricted not only due to the lack of computational power but also due to the lack of a deeper understanding of the physical processes at work. As an example, the physics of star formation, arguably one of the most important processes during galaxy formation and evolution, is not well understood. Thus it is sensible to investigate the three categories separately and, for the beginning, keep the models as simple as possible.

Classic chemical evolution models neglect the distribution of stars and gas in space and only look at integral properties of a system. There are four fundamental quantities which determine the chemical evolution of a stellar system:

1. The total mass of the system, $M_{tot}\left(t\right)$
2. The mass existing in the form of stars and stellar remnants, $M_{star}\left(t\right)$
3. The mass of the interstellar medium (gas and dust), $M_{gas}\left(t\right)$
4. The abundance of the elements of interest, $Z\left(t\right)$. The abundance is usually given as a mass fraction, i.e. $0.0 \leq Z\left(t\right) \leq 1.0$, and has values close to zero for elements other than H and He.

In principle these quantities are related to each other in a straightforward way, but many badly determined or even unknown terms play a crucial role in their interplay.

The star formation rate $\psi\left(t\right)$ (SFR) and the initial mass function $\phi\left(m\right)$ (IMF) are two of the key quantities entering the calculation. Some constraints on the SFR can be gained from observations, but the SFR in the past of the Galaxy is not well known. Most of the time simple laws relating the SFR to the ISM density are adopted (e.g. Schmidt 1959).

The IMF determines the relative number of stars in a given mass interval, i.e. $dN/dm = \phi(m)$, and can be fixed by observations. The most widely used IMFs are simple power laws (e.g. Salpeter 1952; Scalo 1986) and are usually assumed to be constant in time. In addition, lower (m_{lo}) and upper (m_{up}) mass limits of the IMF have to be specified.

The total system mass may change with time and is determined by inflow and outflow of material, the gas mass and the mass locked in stars and stellar remnants. The gas mass and the mass contained in stars is related to the total mass by

$$M_{tot}(t) = M_{gas}(t) + M_{star}(t), \tag{1.1}$$

whereas the change of the total mass is governed by inflow $\zeta(t)$ of material from outside the system and outflow $\omega(t)$ of material in a galactic wind:

$$\frac{d}{dt} M_{tot}(t) = \zeta(t) - \omega(t). \tag{1.2}$$

The functional forms of $\zeta(t)$ and $\omega(t)$ are not known *a priori* and appropriate assumptions have to be made, e.g. exponential infall and no outflow.

The mass in stars is determined by

$$\frac{d}{dt} M_{star}(t) = \psi(t) - \xi(t), \tag{1.3}$$

where $\psi(t)$ is the star formation rate and $\xi(t)$ is the return rate of matter from stars. The mass return rate can be calculated if the lifetime of a star, $\tau(m)$, of mass m and the mass of its stellar remnant, m_{rem}, are known. These can be constrained by stellar evolution calculations and by observations. Recall that a star of mass m was formed at time $(t - \tau(m))$ if it dies at time t. Thus, the mass return rate at time t is given by

$$\xi(t) = \int_{m_t}^{m_{up}} (m - m_{rem})\, \psi(t - \tau(m))\, \phi(m)\, dm. \tag{1.4}$$

The integral has to be taken over the range of masses which end their life before time t, i.e. m_t is the mass with $\tau(m) = t$. This equation assumes a sudden mass loss as a star ends its life. This is reasonable since mass loss episodes occur mostly in a final small fraction of the stellar evolution.

The gas mass is determined by the star formation rate, the mass return rate and inflows/outflows:

$$\frac{d}{dt} M_{gas}(t) = -\psi(t) + \xi(t) + \zeta(t) - \omega(t). \tag{1.5}$$

In the following, it is assumed that the ISM is well mixed and chemically homogeneous at all times ("instantaneous mixing approximation"). Note that this assumption is dropped in the case of inhomogeneous chemical evolution models. The enrichment of the ISM with stable, primary elements[10] is governed by star formation, inflows/outflows and the production of fresh material in stars.

The mass of elements in the gas is $(M_{gas}Z)$ and its change is given by

$$\frac{d}{dt}(M_{gas}Z) = -Z\psi + \xi_Z + Z_\zeta \zeta - Z_\omega \omega, \tag{1.6}$$

Note that all quantities in Eq. 1.6 depend on t. $Z_\zeta(t)$ is the element abundance in the infalling gas and $Z_\omega(t)$ the element abundance of gas in the galactic wind. As an example, $Z_\zeta(t) = 0$ for elements heavier than lithium for the infall of primordial gas and the quantity $Z_\omega(t)$ may be determined by the fraction of elements locked in a hot gas phase heated by massive stars or supernova events. $\xi_Z(t)$ includes elements which are both newly synthesized and were present in the star at birth but are re-ejected at the end of its life. The abundance of an element in a star is the same as the abundance in the gas at the time of its birth if the ISM is chemically homogeneous.

The amount of freshly synthesized material is calculated similar to the mass return rate (Eq. 1.4):

$$\int_{m_t}^{m_{up}} Y_Z(m)\, \psi(t - \tau(m))\, \phi(m)\, dm. \tag{1.7}$$

The quantity $Y_Z(m)$ will be called *stellar yield* in this work and equals to the synthesized mass of a given element by a star of mass m. It can be deduced from stellar evolution models or nucleosynthesis calculations in supernova events. The amount of unprocessed material in a star of metallicity $Z(t - \tau(m))$ is given by $(m - m_{rem} - Y_Z)$ and has to be added to Eq. 1.7 to get $\xi_Z(t)$, i.e.

---

[10] The production of primary elements does not depend on the metallicity of a star, e.g. ^{12}C and ^{16}O. Secondary elements are synthesized from seed nuclei heavier than He which were already present at birth, e.g. ^{13}C and ^{14}N.

$$\xi_Z(t) = \int_{m_t}^{m_{up}} \left[(m - m_{rem} - Y_Z)\, Z\,(t - \tau\,(m)) + Y_Z\,(m)\right] \psi\,(t - \tau\,(m))\, \phi\,(m)\, dm. \tag{1.8}$$

These equations completely determine the chemical evolution of the system and can easily be solved numerically. The real effort in chemical evolution models has to be put into the determination of the astrophysical quantities. Thus, chemical evolution models can be used to test stellar evolution models or nucleosynthesis calculations.

The equations become especially simple and can be solved analytically if stellar lifetimes are neglected (instantaneous recycling). This approximation is very crude and has been dropped in the sophisticated models in use today. The simple (1-zone) model of galactic chemical evolution still in use makes the following assumptions:

1. The system is isolated with a constant total mass.
2. The system is well mixed at all times.
3. The system starts at primordial abundances.
4. The IMF and nucleosynthesis yields of stars do not change in time.

Today much more sophisticated models of chemical evolution are available, taking into account several zones (e.g. halo, thick disk, thin disk and bulge), time delays in the nucleosynthesis of elements (e.g. by core-collapse SNe of different masses, Type Ia SNe and AGB stars), metallicity dependent yields and IMFs or two separate (hot and cold) gas phases and their interaction (condensation and evaporation). Recently, the chemical evolution of the Galaxy was also coupled to its dynamical evolution (e.g. Samland 1998) and even to the evolution of its photometric properties (Westera et al. 2002; Samland & Gerhard 2003).

In contrast to classic models, inhomogeneous chemical evolution models allow for local chemical inhomogeneities in the ISM. This can be done in various ways. The model presented in Sect. 1.6 actually resolves the positions, masses and chemical properties of single stars and the density distribution of the ISM in three dimensions. The positions and masses of the stars in the volume are determined stochastically, whereas their chemical properties are determined by the chemistry of the local ISM. The equations presented above are implicit in the model but are not solved explicitly.

1.6. ICE – Inhomogeneous chemical evolution

Observations of very metal-poor halo stars with metallicities [Fe/H] $\lesssim -2.5$ reveal a scatter in abundances of some elements of order 1 dex. The scatter gradually decreases at higher metallicities until a mean element abundance is reached at [Fe/H] $\gtrsim -1.5$. This average abundance corresponds to [el/Fe] ratios of stellar yields from core-collapse SNe, integrated over the initial mass function (IMF). The scatter in element abundances is generally attributed to local chemical inhomogeneities of the interstellar medium (ISM) during the earliest stages of Galaxy formation and enrichment (e.g. McWilliam et al. 1995a, 1995b; Ryan et al. 1996; Burris et al. 2000; Mishenina & Kovtyukh 2001) since it is significantly larger than observational errors (of order 0.1 dex).

The aim of the stochastic chemical evolution model presented here is to understand the scatter seen in observations and to investigate how the metal-poor ISM evolves chemically. Note that, since the SN remnant formation is the only dynamical process taken into account, this model shows the least possible mixing efficiency of the ISM. This is just the opposite to classic chemical evolution models which assume that the ISM is well mixed at all times (“instantaneous mixing approximation”). Thus, these models are not able to explain the scatter in element abundances observed at low metallicities.

Several other authors also developed inhomogeneous chemical evolution models (Ishimaru & Wanajo 1999; Raiteri et al. 1999; Tsujimoto, Shigeyama & Yoshii 1999, 2000; Argast et al. 2000; Travaglio et al. 2001). Although the methods employed by these authors differ significantly, the model results are in qualitative agreement. The notion of inhomogeneous chemical evolution therefore seems to be well established.

The model described in this section corresponds to the latest version used to investigate the enrichment of the ISM with neutron capture elements (Chapter 4). It features an infall of primordial matter into the modelled volume, a star formation rate (SFR) which is coupled to the local ISM density and includes Type Ia supernova events (SN Ia) and neutron capture element sources. These features were not included in the versions used in Chapters 2 and 3. Instead, a constant SFR and initially homogeneously distributed ISM have been assumed and SN Ia events have been neglected. However, this does not invalidate the results given in Chapters 2 and 3, since in these cases the enrichment of the ISM as function of metallicity [Fe/H] was investigated and no absolute timescales (e.g. infall timescale vs. SN Ia timescale) were involved. In addition, the enrichment of the ISM was only followed up to an average metallicity [Fe/H] $= -1.0$, since at this stage SN Ia events start to influence the enrichment significantly.

1.6.1. Mass infall

The chemical enrichment of the halo ISM is modelled within a cube of(2.0 kpc)^3, down to a resolution of 50 pc. Thus, contrary to classic chemical evolution models, local chemical inhomogeneities in the ISM can be resolved and every cell of the grid contains detailed information about the enclosed ISM and the mass distribution of stars. In this work, the enrichment of the ISM with α-elements (O, Mg, Si and Ca), iron-peak elements (Cr, Mn, Fe and Ni) and neutron capture elements (Ba and Eu) is investigated.

Primordial matter is assumed to be falling into this volume, following an infall law of the form

$$\dot{M}(t) = a \cdot t^b \cdot \exp(-t/\tau). \tag{1.9}$$

Instead of specifying parameters a and b directly, the fact that with this description the time of maximal infall, t_{max}, is given by

$$t_{max} = b \cdot \tau, \tag{1.10}$$

is used, and that the total mass, M_{tot}, falling into the volume is

$$M_{tot} = \int_0^{t_{end}} a \cdot t^b \cdot \exp(-t/\tau)\, dt, \tag{1.11}$$

where t_{end} is the age of the system. The infall law is therefore fully described by the parameter set $\{M_{tot}, \tau, t_{max}, t_{end}\}$.

1.6.2. Star formation law

A crucial ingredient of chemical evolution models is the treatment of star formation (SF). Unfortunately, it is also one of the least understood. In this work a simple SF description based on Schmidt's law (Schmidt 1959) is adopted. The number $n(t)$ of stars that are formed per time-step (of duration 10^6 yr) is determined by the product

$$n(t) = \frac{\nu}{N_{tot}} \cdot \sum_{i=1}^{N_{tot}} \rho_i^{\alpha}(t), \tag{1.12}$$

where $\rho_i(t)$ is the local ISM density at time t in a cell of volume (50 pc)^3 and the sum goes over all cells in the volume (N_{tot}). The parameter ν determines the star formation efficiency, whereas possible values for α range from 1 (SF proportional to gas density) to 2 (SF triggered by cloud-cloud collisions, Larson 1991). The factor N_{tot}^{-1} was introduced to keep the number of newly formed stars independent of the model resolution, so that Eq. 4.4 evaluates to $n(t) = \nu \langle \rho(t) \rangle^{\alpha}$ if the ISM is homogeneously distributed ($\rho_i(t) = \langle \rho(t) \rangle$ for all i).

The masses of newly formed stars are chosen randomly, with the condition that the mass distribution of all stars follows a Salpeter initial mass function ($dN/dm \propto m^{-2.35}$) with lower and upper mass limits of $m_{lo} = 0.1\,\mathrm{M}_{\odot}$ and $m_{up} = 50\,\mathrm{M}_{\odot}$, respectively. Thus, the average mass $\langle m \rangle$ of a star, integrated over the initial mass function (IMF), is given by

$$\langle m \rangle = \frac{\int_{m_{lo}}^{m_{up}} m \cdot dN}{\int_{m_{lo}}^{m_{up}} dN}. \tag{1.13}$$

The number $n(t)$ of star formation events translates into an average star formation rate (SFR) at each time-step by multiplication with the average stellar mass $\langle m \rangle$, i.e.

$$\begin{aligned} \langle SFR(t) \rangle &= n(t) \cdot \langle m \rangle \\ &= \frac{\nu}{N_{tot}} \cdot \sum_{i=1}^{N_{tot}} \rho_i^{\alpha}(t) \cdot \frac{\int_{m_{lo}}^{m_{up}} m \cdot dN}{\int_{m_{lo}}^{m_{up}} dN}. \end{aligned} \tag{1.14}$$

Due to the stochastic nature of our SF law, small deviations from the average SFR have to be expected at each time-step.

The cells that undergo star formation are also chosen randomly, though the probability for a cell to get selected scales with its density. In this description, patches of denser material, e.g. in the neighbourhood of supernova remnants, are predominantly chosen for star formation events. Note that a cell is only allowed to form stars, if it contains at least $50\,\mathrm{M}_\odot$ of gas. This restriction has to be imposed, so that the IMF is not biased towards low mass stars, i.e. if a cell forms a star, then it can be of any mass in the range $0.1 - 50\,\mathrm{M}_\odot$. Consequently no SF will occur until enough material has fallen into the volume to exceed this limit. Newly formed stars inherit the abundance pattern of the ISM out of which they formed, carrying therefore information about the chemical composition of the ISM at the place and time of their birth.

1.6.3. Stellar lifetimes

To determine the lifetime of a star an approximation to the metallicity dependent mass-lifetime relation of the *Geneva Stellar Evolution and Nucleosynthesis Group* (cf. Schaller et al. 1992; Schaerer et al. 1993a; Schaerer et al. 1993b; Charbonnel et al. 1993) is used, given by

$$\begin{aligned}\log(T) = \; & (3.79 + 0.24 \cdot Z) \\ & - (3.10 + 0.35 \cdot Z) \cdot \log(M) \\ & + (0.74 + 0.11 \cdot Z) \cdot \log^2(M)\,,\end{aligned} \tag{1.15}$$

where T is the lifetime in units of 10^6 yr, Z the metallicity in units of solar metallicity $Z_\odot$ and M the mass in units of solar masses $\mathrm{M}_\odot$.

1.6.4. Stars of low and intermediate mass $(< 10\,\mathrm{M}_\odot)$

Low mass stars ($\lesssim 1\,\mathrm{M}_\odot$) do not evolve significantly during the considered time but serve to lock up part of the total gas mass, affecting therefore the abundances of elements with respect to hydrogen. Stars of intermediate mass ($\sim 1-10\,\mathrm{M}_\odot$) return most of their mass after their stellar lifetime, leaving a white dwarf as stellar remnant. Additionally, they may act as progenitors of SN Ia and/or as sources of s-process elements.

1.6.5. Core-collapse SNe $(10 - 50\,\mathrm{M}_\odot)$

Stars in a range of $10-50\,\mathrm{M}_\odot$ are assumed to explode as SNe II (or hypernovae, the term SNe II is assumed to include hypernovae unless otherwise noted) resulting in an enrichment of the neighbouring ISM. Stellar yields of α- and iron-peak elements are taken from Thielemann et al. (1996) and Nomoto et al. (1997) and are scaled according to Samland (1998) to account for the global chemical enrichment of the Galaxy. Additionally, since there are no nucleosynthesis calculations for $10\,\mathrm{M}_\odot$ progenitors, their yields were set to $1/10$ of the yields of the $13\,\mathrm{M}_\odot$ model. Then, the stellar yields were linearly interpolated, since the mass distribution of stars in the simulation is continuous (following a Salpeter IMF). The interpolation gives IMF averaged values of [el/Fe] ratios which are in good agreement (within 0.1 dex) with observed mean values of metal-poor stars.

Since the explosion energy of SNe II is believed to depend only slightly on the mass of its progenitor (Woosley & Weaver 1995, hereafter WW95; Thielemann et al. 1996), we assume that each SN II sweeps up about $5 \times 10^4\,\mathrm{M}_\odot$ of gas (Ryan et al. 1996; Shigeyama & Tsujimoto 1998). The swept up, enriched material is condensed in a spherical, chemically well mixed shell. Its radius depends on the local ISM density ($R \sim \langle\rho\rangle^{-1/3}$, where $\langle\rho\rangle$ is the average density of the ambient ISM) and lies typically between 100 pc and 200 pc. The material in the shell subsequently mixes with the ISM of the cells where the expansion of the remnant stopped. The interior of the remnant is assumed to be filled with about $5\,\mathrm{M}_\odot$ of dilute enriched gas from the SN event. This gas is unable to form stars until it is swept up by another SN event and mixed with the surrounding ISM. Thus it contributes to the enrichment only after some delay.

Stars which form out of material enriched by a single SN II inherit its abundance ratios and therefore show an element abundance pattern which is characteristic for this particular progenitor mass. This gives rise to a large scatter in [el/Fe] ratios, as long as local inhomogeneities caused by SN II events dominate the halo ISM. As time progresses, supernova remnants overlap and the abundance pattern in each cell approaches the IMF average, leading to a decrease in the [el/Fe] scatter at later times.

1.6.6. Type Ia SNe

To determine which intermediate mass stars form Type Ia SN events, the following simple procedure is adopted: With probability P_{SNIa} a newly formed intermediate mass star has a companion in the same mass range and one of these two stars will end its life as SN Ia. The mass of its companion (again in the range $1-10\,\mathrm{M}_{\odot}$ and following a Salpeter IMF) is determined randomly and the SN Ia event occurs after the less massive of the two stars enters the red giant stage. Although this procedure admittedly is rather simple, it has the advantage that the SN Ia frequency is determined by only one free parameter, namely the probability P_{SNIa}. This parameter is chosen in such a way that the slope observed in [α/Fe] abundances at [Fe/H] $\gtrsim -1$ is reproduced. To be consistent with the lower mass limit of SN II progenitors, the upper mass limit for SN Ia progenitors is set to $10\,\mathrm{M}_{\odot}$. Since such a simplified description to determine the occurrence of SN Ia is used, the upper mass limit of SN Ia progenitors is not very relevant: Assuming a Salpeter IMF, more than 99% of the binary systems will consist of stars with masses $\leq 8\,\mathrm{M}_{\odot}$ each. Finally, the yields of Type Ia SNe are taken from Iwamoto et al. (1999, Model CDD2).

1.6.7. Sources of neutron capture elements

Neutron capture elements may be formed by slow (s-process) or rapid (r-process) capture of neutrons on seed nuclei. In Chapter 4, contributions to neutron capture elements from the main s-process (occurring during the thermally pulsing asymptotic giant branch phase of intermediate mass stars) and the r-process are considered. Since the astrophysical nature of r-process sites is unknown to date, three possible major r-process sources are considered, namely lower-mass SNe II ($8-10\,\mathrm{M}_{\odot}$), higher-mass SNe II ($\geq 20\,\mathrm{M}_{\odot}$) or coalescing neutron star binaries. Since the enrichment of the ISM with neutron capture elements is treated not until Chapter 4, we refer the reader to Sect. 4.2.2 for a detailed discussion of the implementation of r- and s-process sources in the model.

1.6.8. Chemical inhomogeneities in the early ISM

Fig. 1.1 illustrates the evolution of the early ISM from the metal-poor stage ([Fe/H] ≤ -3), dominated by local chemical inhomogeneities, to the more metal-rich, chemically well mixed stage ([Fe/H] ≥ -1). The four panels in Fig. 1.1 show the oxygen abundance [O/Fe] in the ISM in a cut through the computed volume. (See also Fig. 2.1 which shows the ISM density distribution in a cut through the volume. Note however, that Figs. 1.1 and 2.1 are results of model runs with different parameter sets, so that they may not be compared directly. However, the general features of the different enrichment stages can be easily recognized.)

The panel to the upper left shows the state of the ISM at metallicity [Fe/H] $= -4$. Regions with primordial abundances are shown as black, SN II remnants show up as yellowish structures. (The red boundaries surrounding the SN II remnants are an artifact of the plot routine.) Shades of yellow/orange in the panel indicate different [O/Fe] abundances that originated from core-collapse SNe of different progenitor masses. Note especially the oval structure with two different shadings, slightly to the upper right in this panel. In this case, two SN II events occurred close to each other, so that parts of their remnants overlapped. Stars forming in this region show an element abundance pattern which is determined by a mixture of the ejecta of both SNe II. On the other hand, stars forming in the neighbourhood of isolated remnants inherit the abundance pattern characteristic of the respective progenitor mass. Note that all remnants in this panel originated from fast-evolving SNe II with progenitors more massive than $\approx 20\,\mathrm{M}_{\odot}$ and therefore all show [O/Fe] $\gtrsim 0.4$.

At [Fe/H] $= -3$ (panel to the upper right), the halo ISM is still dominated by local chemical inhomogeneities. Also, some patches of primordial material are still visible. At this stage most of the remnants already overlap, indicating the start of the mixing in the metal-poor ISM. The panel to the lower left ([Fe/H] $= -2$) shows the ISM in a stage of advanced mixing. The dark patches visible in this panel are due to lower-mass SNe ($\lesssim 18\,\mathrm{M}_{\odot}$) with somewhat longer evolution timescales than higher mass SNe II which generate regions of low oxygen abundance ([O/Fe] ≤ 0.0).

In the panel to the lower right ([Fe/H] $= -1$), the ISM can be considered chemically homogeneous. The yellow or dark red patches still visible correspond to the interior of SNe II remnants which will not form stars (due to their low ISM density). Thus star formation only occurs in the regions of IMF average [O/Fe] ratios, shown as dull orange. Note especially that the

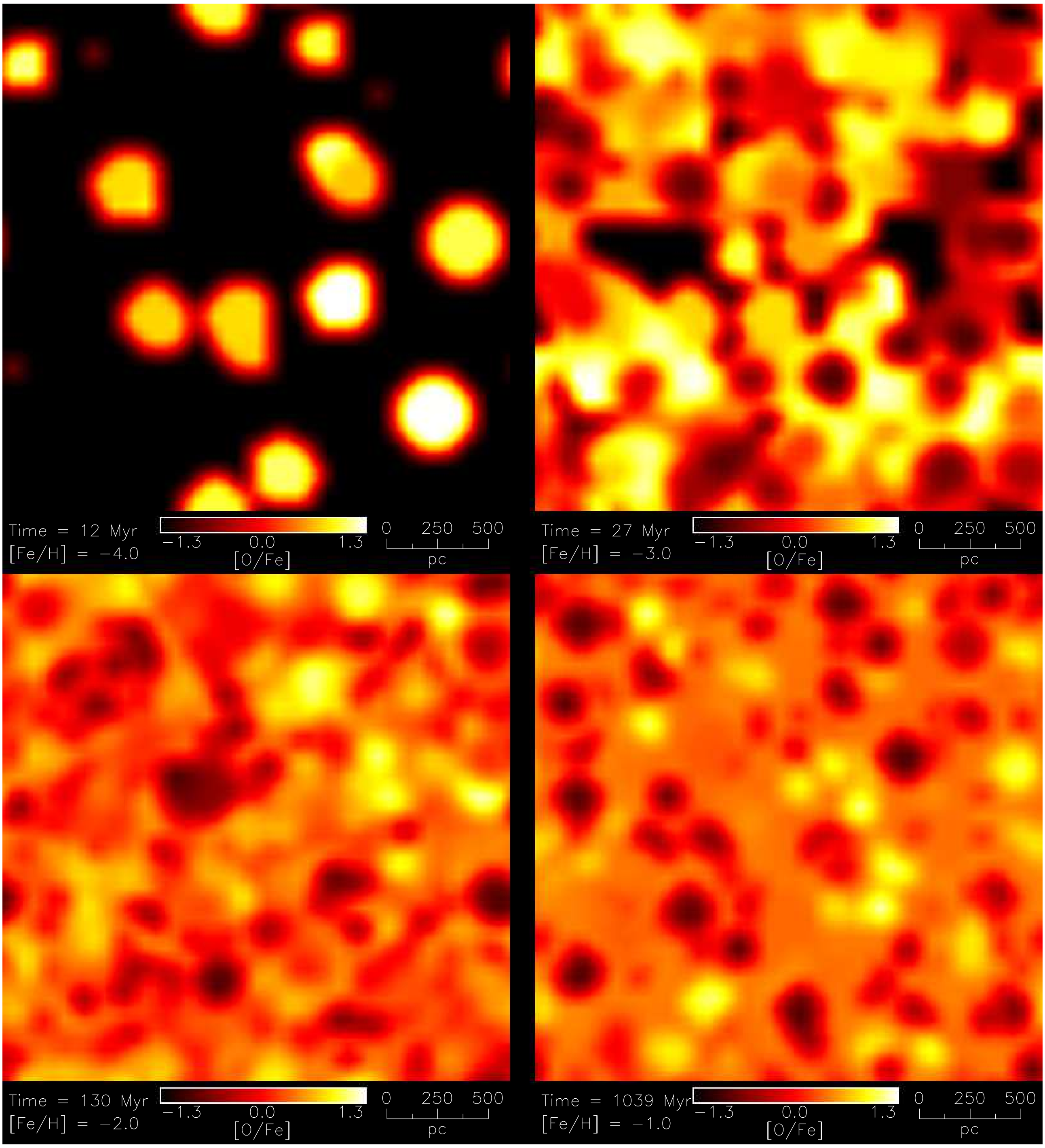

Fig. 1.1. Enrichment of the interstellar medium with oxygen and iron.

average colour in this sequence of figures evolves from yellow/bright orange (i.e. high [O/Fe] ratios) in the panel to the upper left to the dull orange (corresponding to [O/Fe] ≈ 0.4) in the panel to the lower right.

Finally, I emphasize one important result: Starting with a primordial ISM and taking into account local inhomogeneities caused by SNe II, the *initial* scatter in [el/Fe] ratios is determined solely by the adopted nucleosynthesis yields. The details of the chemical evolution model only determine how fast a chemically homogeneous ISM is reached, i.e. how the scatter evolves with time or (equivalently) iron abundance [Fe/H]. Thus, the range of [el/Fe] ratios of the most metal-poor stars does not depend on specific model parameters but is already fixed by the stellar yields.

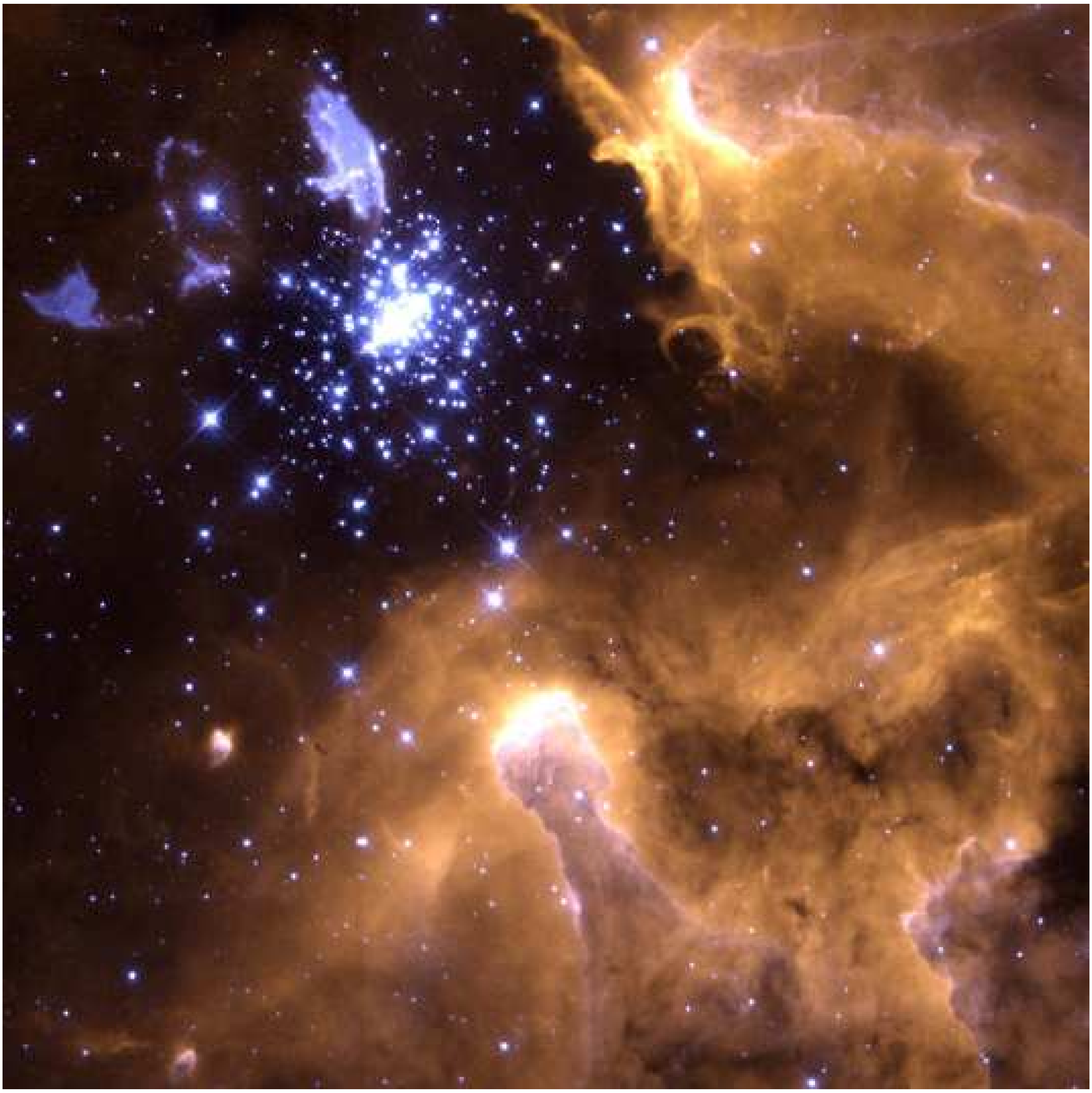

2

Metal-poor halo stars as tracers of ISM mixing processes during halo formation

Abstract. We introduce a stochastic halo formation model to compute the early chemical enrichment of the interstellar medium (ISM) of the halo. Contrary to 1-zone chemical evolution models, we are able to resolve local inhomogeneities in the ISM caused by single core-collapse supernovae. These inhomogeneities lead to different element abundance patterns in very metal-poor stars, which can be seen as scatter in the abundances of halo stars with metallicities [Fe/H] <-2.0.

The early chemical evolution of the halo proceeds in different enrichment phases: At [Fe/H] <-3.0, the halo ISM is unmixed and dominated by local inhomogeneities caused by individual core-collapse supernova (SN) events. For metallicities [Fe/H] >-2.0 the halo ISM is well mixed, showing an element abundance pattern integrated over the initial mass function. In the range $-3.0<$ [Fe/H] <-2.0 a continuous transition from the unmixed to the well mixed ISM occurs.

For some elements (Si, Ca, Eu), the scatter in the element-to-iron ratio [el/Fe] of metal-poor halo stars can be reproduced. Stellar yields of other elements predict a scatter which, compared to the observations, is too large (O, Mg) or too small (Ni). Cr and Mn show a decreasing trend for lower metallicities, which can not be explained by metallicity independent yields, provided that the mixing of the ejecta with the interstellar medium does not depend on progenitor mass. This demonstrates the need for revised, self-consistent SN yields.

Finally, we discuss the metallicity distribution in the model. Compared to the 28 very metal-poor stars observed with metallicities in the range $-4.0<$ [Fe/H] <-3.0, no star is known with confirmed metallicity [Fe/H] <-4.0, while our model predicts 5 ± 2 stars with [Fe/H] <-4.0. These should be present if the halo ISM started at primordial metallicities and no pre-enrichment by population III stars occurred.

2.1. Introduction

The low metal abundances and high peculiar velocities of halo stars indicate that the halo is an old, if not the oldest component of the Milky Way. Age determinations of globular clusters and halo field stars point to an age of 14-15 billion years with no detectable age gradient with galactocentric distance (Harris et al. 1997). The halo has therefore special significance for the formation of the Milky Way. There are two quantities which play important rôles in the investigation of the formation of the halo: the orbits of halo stars and their chemical composition. Since halo stars form a collisionless system, their orbits contain information about the dynamics at the time of star formation and thus the formation of the halo (e.g. Carney et al. 1996; Chiba & Yoshii 1998). Information about the chemical composition of the interstellar medium (ISM) of the halo is more direct. The element abundances observed in low mass halo stars directly reflect the chemical abundances and the chemical inhomogeneity of the ISM during halo formation (McWilliam 1997).

Examinations of element abundance ratios as function of metallicity [Fe/H] show that star-to-star differences rise with decreasing metallicity (Ryan et al. 1996). Most of the chemical elements are ejected during supernovae Type II (SNe II) explosions. The enrichment of the halo depends on how many SNe II explode and how effectively the ejected gas is mixed with the surrounding ISM. If the ejected metals are distributed over a large volume, a spatially homogeneous enrichment takes place. If the mixing volume is small, the ISM in the vicinity of a core-collapse supernova (SN II) is highly enriched, while large parts of the halo gas remain metal-poor. In this case the ISM is chemically highly inhomogeneous and newly formed stars are of different chemical composition, depending on where they form. In this scenario one should moreover expect that the metal-poorest stars have chemical compositions corresponding to the stellar yields of single SNe II (Ryan et al. 1996).

In this paper we present a stochastic chemical evolution model and investigate the inhomogeneous enrichment of the halo ISM. The description of the model is given in Sect. 2.2, followed by an overview of theoretical SN II yields and their uncertainties in Sect. 2.3. The employed observational data is presented in Sect. 2.4. The results of our model and the conclusions are given in Sect. 2.5 and 2.6, respectively.

2.2. The Model

Very metal-poor halo stars show a great diversity in their element abundances and therefore a scatter in their element-to-iron ratios [el/Fe] of order 1 dex. This scatter gradually decreases at higher metallicities until a mean element abundance is reached which corresponds to the [el/Fe] ratio of the stellar yields integrated over the initial mass function (IMF). The aim of our stochastic halo formation model is to understand the trends seen in the observations and to investigate how the metal-poor interstellar medium (ISM) in the halo evolves chemically.

Our fully 3D-code, contrary to 1-zone chemical evolution models, enables us to resolve local inhomogeneities in the ISM with a spatial resolution of 50 pc. All in all, we model a volume of (2.5 kpc)^3, divided into 50^3 cells. Every cell of our grid contains detailed information about the enclosed ISM and the mass distribution of stars. We consider simultaneously the evolution of nine elements, the α-elements O, Mg, Si and Ca, the iron-peak elements Cr, Mn, Fe and Ni and the r-process element Eu.

Our initial conditions assume a halo ISM consisting of a homogeneously distributed single gas phase with primordial abundances and a density of 0.25 particles per cm^3, which gives a total mass of about 10^8 M$_\odot$ in a volume of (2.5 kpc)^3. We adopt a constant time-step of 10^6 years since it has to be longer than the dynamical evolution of a supernova (SN) remnant and shorter than the lifetime of the most massive stars. At each time-step 20 000 cells are chosen randomly and independently of each other and of the state of the enclosed ISM. Each selected cell may create a star with a probability proportional to the square of the local ISM density (Larson 1988). The number of stars formed per time-step is the product of the number of cells tested with the probability of star formation in each cell. Various combinations of these parameters are possible to achieve a given SFR; the choice of 20 000 cells proved computationally convenient. The absolute value of the SFR influences the *time-scale* of the enrichment process (cf. Sect. 2.5.1), but *not* the evolution of [el/Fe]-ratios as function of [Fe/H]. Therefore, the main results of this paper are insensitive to the values of these parameters.

The mass of a newly formed star is chosen randomly from a Salpeter IMF. The lower and upper mass limits of the IMF are taken to be 0.1 M$_\odot$ and 50 M$_\odot$, respectively. About 5000 stars are formed on average during each step. Newly born stars inherit the abundance pattern of the ISM out of which they form, carrying therefore information about the state of the ISM at the place and time of their birth. To determine the lifetime of a star an approximation to the metallicity dependent mass-lifetime relation of the *Geneva Stellar Evolution and Nucleosynthesis Group* (cf. Schaller et al. 1992; Schaerer et al. 1993a; Schaerer et al. 1993b; Charbonnel et al. 1993) is used, given by

$$\begin{aligned}\log(T) = \;& (3.79 + 0.24 \cdot Z) \\ & - (3.10 + 0.35 \cdot Z) \cdot \log(M) \\ & + (0.74 + 0.11 \cdot Z) \cdot \log^2(M)\,,\end{aligned} \tag{2.1}$$

where T is the lifetime in units of 10^6 yr, Z the metallicity in units of solar metallicity $Z_\odot$ and M the mass in units of solar masses M$_\odot$.

Stars in a range of $10 - 50\,\mathrm{M}_\odot$ will explode as core-collapse supernovae (SNe II), resulting in an enrichment of the neighbouring ISM. Stellar yields are taken from Thielemann et al. (1996) and Nomoto et al. (1997) for all elements except Eu. Since there are no theoretical predictions of stellar Eu yields, we use the indirectly deduced yields of Tsujimoto & Shigeyama (1998) which assume that r-process elements originate from SNe II (see the discussion of stellar yields in Sect. 2.3). We linearly interpolate the stellar yields given in these papers, since we use a finer mass-grid in our simulation. For SNe with masses below 13 M$_\odot$ stellar yields are not available. Since the nucleosynthesis models show declining yields towards low progenitor masses, we have for the interpolation arbitrarily set the yields of a 10 M$_\odot$ SN to one thousandth of those of a 13 M$_\odot$ SN. The interpolation gives IMF averaged values of the [el/Fe] ratios, which are in good agreement with the observed mean values of metal-poor stars in all elements except Ca, which shows a [Ca/Fe] ratio that is about 0.3 dex lower than the observed mean. We do not include supernovae (SNe) of Type Ia, since we are only interested in the very early enrichment of the halo ISM, which is dominated by SNe of Type II.

Intermediate mass stars will evolve to planetary nebulae, returning only slightly enriched material in the course of their evolution. This locally influences the enrichment pattern of the gas, since metal-poor material is returned into the evolved and enriched ISM. It will not change the element abundances [el/H] significantly, but can affect the local element-to-iron ratios [el/Fe] considerably. Low mass stars do not evolve significantly during the considered time. In our model, they serve to lock up part of the gas mass, affecting therefore the local element abundances [el/H] in the ISM.

Since the explosion energy of a core-collapse supernova (SN II) depends only slightly on the mass of its progenitor (Woosley & Weaver 1995; Thielemann et al. 1996), every SN II sweeps up a constant mass of about 5×10^4 $M_\odot$ of gas (Ryan et al. 1996; Shigeyama & Tsujimoto 1998). In our model the radius of the SN remnant then is computed from the local density of the ISM and lies typically between 100 pc and 200 pc. The ejecta of the SN II and all the swept up, enriched material are condensed in a spherical shell which is assumed to be chemically well mixed. The material in the shell subsequently mixes with the ISM of the cells where the expansion of the remnant stopped. The interior of the remnant, where all the material was swept up, is assumed to be filled with about 5 $M_\odot$ of dilute gas from the SN event with the corresponding metal abundances. This gas is unable to form stars until it is swept up by another SN event and mixed with the surrounding ISM. Thus this material contributes to the enrichment only after some delay.

The star formation rate of cells influenced by the remnant will rise, since their density is higher than the average density of a cell and the probability to form a star is assumed to be proportional to the square of the local density. It is still possible to form stars in the field, but cells that are influenced by a SN remnant are favoured. Stars which form out of material enriched by a single SN inherit its abundances and therefore show an abundance pattern which is characteristic for this particular progenitor mass. The most metal-poor stars that form out of material which was enriched by only one SN would therefore allow to reconstruct the stellar yields of single core-collapse SN, if the average swept up mass and the absolute yield of one element were known (Shigeyama & Tsujimoto 1998).

The SN remnant expansion is the only dynamical process taken into account in our model. Therefore, this model has the least possible mixing of the ISM. This is the opposite limit as in the case of closed box models, which assume a complete mixing of the ISM at all times and are therefore not able to explain the scatter seen at low metallicities. We continue our calculation up to an averaged iron abundance of [Fe/H] $= -1.0$. At this metallicity SN events of Type Ia, which we have not included in our model, would start to influence the ISM.

2.3. SN II yields and their uncertainties

In the present investigation we make use of the nucleosynthesis results by Thielemann et al. (1996) and Nomoto et al. (1997). Here we want to give a short summary of the key features together with an assessment of the uncertainties by comparing with available independent calculations. The synthesized elements form three different classes which are sensitive to different aspects of the stellar models and supernovae explosion mechanism: (1) stellar evolution, (2) stellar evolution plus the explosion energy, and (3) details of the explosion mechanism which includes aspects of stellar evolution determining the size of the collapsing Fe-core. Due to reaction equilibria obtained in explosive burning, the results do not show a strong sensitivity to the applied reaction rate library (Hoffman et al. 1999).

1: The abundances of C, O, Ne, and Mg originate from the unaltered (essentially only hydrostatically processed) C-core and from explosive Ne/C-burning. They are mainly dependent on the structure and zone sizes of the pre-explosion models resulting from stellar evolution. These zones and therefore the amount of ejected mass varies strongly over the progenitor mass range. O, Ne, and Mg vary by a factor of 10-20 between a 13 $M_\odot$ and a 25 $M_\odot$ progenitor star. This behaviour can vary with the treatment of stellar evolution and is strongly related to the amount and method of mixing in unstable layers. Woosley & Weaver (1995) employ the Ledoux criterion with semiconvection for Schwarzschild-unstable but Ledoux-stable layers. Nomoto & Hashimoto (1988) make use of the Schwarzschild criterion for convection (neglecting composition gradients) which ensures mixing over more extended regions than the Ledoux criterion. The Schwarzschild criterion causes larger convective cores (see also Chieffi et al. 1998) which leads to larger ^{16}O, ^{20}Ne, and ^{24}Mg yields, the latter being also dependent on the $^{12}\mathrm{C}(\alpha,\gamma)$ rate (Langer & Henkel 1995). In addition, it is important to know the mixing velocity in unstable regions. Recent calculations by Umeda et al. (1999), within the diffusion approximation for mixing (Spruit 1992; Saio & Nomoto 1998) but with a remaining free parameter - permitted to vary between 0 and 1 - show that the Woosley & Weaver (1995) results can be reproduced with a small choice of this parameter of 0.05. A further effect is due to rotation. When also treating rotation correctly (Langer et al. 1997; Talon et al. 1997; Meynet & Maeder 1997; Heger et al. 2000), rotational instabilities lead to additional mixing which can bring the models making use of the Ledoux criterion closer to those evolved with the Schwarzschild criterion and the compositions closer to those obtained with instantaneous mixing (high mixing velocities). Thus, the amount of mixing (being influenced by the mixing criterion utilized, the mixing velocity, and rotation) determines in stellar evolution the size of the C/O core. While the yield of O can be fixed with a combination of the still uncertain $^{12}\mathrm{C}(\alpha,\gamma)$ rate (Buchmann 1996, 1997) and a mixing description, the yields of Ne and Mg depend on the extent of mixing. Recent galactic chemical (but not dynamic) evolution calculations (Thomas et al. 1998; Matteucci et al. 1999; Chiappini et al. 1999) prefer apparently a larger extent of mixing (caused by either of the effects mentioned above) in order to reproduce the observed Mg in low metallicity stars.

2: The amount of mass for the elements Si, S, Ar and Ca, originating from explosive O- and Si-burning, is almost the same for all massive stars in the Thielemann et al. (1996) models. They do not show the strong progenitor mass dependence of C, O, Ne, and Mg. Si has some contribution from hydrostatic burning and varies by a factor of 2-3. Thus, the first set of elements (C, O, Ne, Mg) tests the stellar progenitor models, while the second set (Si, S, Ar, Ca) tests the progenitor models and the explosion energy, because the amount of explosive burning depends on the structure of the model plus the energy of the shock wave which passes through it. Present models make use of an artificially induced shock wave via thermal energy deposition (Thielemann et al. 1996) or a piston (Woosley & Weaver 1995) with shock energies which lead, after the reduction of the gravitational binding of ejected matter, to a given kinetic energy. In our models this is an average energy of 10^{51} erg, known from remnant observations, which does not reflect possible explosion energy variations as a function of progenitor mass. The apparent underproduction of Ca seen in some chemical evolution calculations (e.g. Thomas et al. 1998; Matteucci et al. 1999; Chiappini et al. 1999) could apparently be solved by a progenitor mass dependent explosion mechanism and energy.

3: The amount of Fe-group nuclei ejected (which includes also one of the so-called alpha elements, i.e. Ti) and their relative composition depends directly on the explosion mechanism, connected also to the size of the collapsing Fe-core. Observational checks of individual supernovae are presently still required to test the detailed working of a supernova. The present situation is still uncertain and depends on Fe-cores from stellar evolution, the supranuclear equation of state and maximum neutron star mass, related to the total amount of gravitational binding energy release of the collapsed protoneutron star, the resulting total amount of neutrinos, and the time release (luminosity), dependent on neutrino transport via numerical treatment, convective transport, and opacities (Burrows 1990; Herant et al. 1994; Janka & Müller 1995, 1996; Keil & Janka 1995; Burrows et al. 1995; Burrows 1996; Reddy & Prakash 1997; Burrows & Sawyer 1998; Mezzacappa et al. 1998; Messer et al. 1998; Yamada et al. 1999; Pons et al. 1999). Three types of uncertainties are inherent in the Fe-group ejecta, related to (i) the total amount of Fe (-group) nuclei ejected and the mass cut between neutron star and ejecta, mostly measured by ^{56}Ni decaying to ^{56}Fe, (ii) the total explosion energy which influences the entropy of the ejecta and with it the degree of alpha-rich freeze-out from explosive Si-burning and the abundances of radioactive ^{44}Ti as well as ^{48}Cr, the latter decaying later to ^{48}Ti and being responsible for elemental Ti, and (iii) finally the neutron richness or Y_{e}=$< Z/A >$ of the ejecta, dependent on stellar structure and the delay time between collapse and explosion. Y_{e} influences strongly the ratios of isotopes 57/56 in Ni (Co, Fe) and the overall elemental Ni/Fe ratio. The latter being dominated by ^{58}Ni and ^{56}Fe. The position of the mass cut has also a side effect (besides determining the total amount of ^{56}Ni/Fe), it influences the ratio of abundances from alpha-rich freeze-out and incomplete Si-burning, affecting in this way the abundances of the elements Mn (^{55}Co decay), Cr (^{52}Fe decay) and Co (^{59}Cu decay) as discussed in Nakamura et al. (1999).

There is limited direct observational information from individual supernovae with known progenitors (SN 1987A, SN 1993J, 1997D?, 1996N?, 1994I) and possible hypernovae (SN1997ef, 1998bw), leading to direct O, Ti or Fe (Ni) observations (e.g. Shigeyama & Nomoto 1990; Iwamoto et al. 1994, 1998; Iwamoto 1999a, 1999b; Turatto et al. 1998; Sollerman et al. 1998; Kozma & Fransson 1998; Bouchet et al. 1991a; Suntzeff et al. 1992). As explosive nucleosynthesis calculations cannot presently rely on self-consistent explosion models, the position of the mass cut is in all cases an assumption and has mostly been normal-

Table 2.1. Reference list of the observational data. Elements marked with “c” were adjusted to the same solar abundance scale by S. G. Ryan (Ryan et al. 1996 and private communication), unaltered observations are marked with “x”. Unmarked entries were not observed in the corresponding study. Newer publications (after 1995) are listed separately.

Author	O	Mg	Si	Ca	Cr	Mn	Fe	Ni	Eu
Gratton (1989)						c	c		
Magain (1989)		c		c	c		c		x
Molaro & Bonifacio (1990)		c		c	c		c		
Molaro & Castelli (1990)		c	c	c	c	c	c	c	
Peterson et al. (1990)	x	c	c	c	c	c	c	c	
Zhao & Magain (1990)				c	c		c	c	
Bessell et al. (1991)	x						x		
Gratton & Sneden (1991a)			c	c	c		c	c	
Gratton & Sneden (1991b)							x		x
Ryan et al. (1991)	x	c	c	c	c	c	c	c	x
Spiesman & Wallerstein (1991)	x						x		
Spite & Spite (1991)	x						x		
Francois et al. (1993)							x		x
Norris et al. (1993)		c		c	c	c	c	c	
Beveridge & Sneden (1994)	x	x	x	x	x	x	x	x	x
King (1994)	x						x		
Nissen et al. (1994)	x	x		x	x		x		
Primas et al. (1994)		c	c	c	c	c	c		
Sneden et al. (1994)		x	x	x	x	x	x		x
Fuhrmann et al. (1995)	x						x		
McWilliam et al. (1995a)		c	c	c	c	c	c	c	x
Balachandran & Carney (1996)	x						x		
Ryan et al. (1996)		c	c	c	c	c	c	c	c
Israelian et al. (1998)	x						x		
Jehin et al. (1999)		x		x	x		x	x	x

ized to observations of SN 1987A. Whether there is a decline in Fe-ejecta as a function of progenitor mass (as assumed in Thielemann et al. 1996) or actually an increase (Woosley & Weaver 1995) or a more complex rise, maximum and decline (Nakamura et al. 1999) is not really understood. Thus, the results by Thielemann et al. (1996) utilized here are showing the correct IMF integrated behaviour of e.g. Si/Fe, but one has to keep in mind that e.g. O/Fe, Mg/Fe, Si/Fe, Ca/Fe yields of individual supernovae could be quite uncertain and even show an incorrect progenitor mass dependence or a larger scatter than (yet unknown) realistic models. Ratios within the Fe-group (like e.g. Ni/Fe) have been obtained by mass cut positions which reproduce the solar ratios. Thus, the theoretical yields might show already the average values and a much smaller scatter than some observations (see e.g. Henry 1984). Later work attempted to choose mass cuts in order to represent some specific element trends like e.g. in Cr/Fe, Co/Fe or Mn/Fe (Nakamura et al. 1999).

In general we should keep in mind that as long as the explosion mechanism is not completely and quantitatively understood yet, one has to assume a position of the mass cut. Dependent on that position, which is a function of explosion energy and the delay time between collapse and final explosion, the total amount of Fe-group matter can vary strongly, Ti-yields can vary strongly due to the attained explosion energy and entropy, and the ejected mass zones will have a variation in neutron excess which automatically changes relative abundances within the Fe-group, especially the Ni/Fe element ratio.

4: r-Process Yields. SNe II have long been expected to be the source of r-process elements. Some recent calculations seemed to be able to reproduce the solar r-process abundances well in the high entropy neutrino wind, emitted from the hot protoneutron star after the SN II explosion (Takahashi et al. 1994; Woosley et al. 1994). If the r-process originates from supernovae, a specific progenitor mass dependence has to be assumed in order to reproduce the r-process abundances in low metallicity stars as a function of [Fe/H] (Mathews et al. 1992; Wheeler et al. 1998). Such a "hypothetical" r-process yield curve has been constructed by Tsujimoto & Shigeyama (1998), in agreement with ideas of Ishimaru & Wanajo (1999) and Travaglio et al. (1999), and is used in the present galactic evolution calculation. However, we should keep in mind that present-day supernova models have difficulties to reproduce the entropies required for such abundance calculations. In addition, they could exhibit the incorrect abundance features of lighter r-process nuclei (Freiburghaus et al. 1999a), we know by now that at least two r-process sources have to contribute to the solar r-process abundances (Wasserburg et al. 1996; Cowan et al. 1999), and that possible other sources exist (Freiburghaus et al. 1999b). A larger scatter in the r/Fe ratio in low metallicity stars than predicted by the constructed supernova yields would also indicate the need of such another r-process source.

2.4. Observational Data

As shown in Table 2.1, the observational data were selected from various high-resolution studies. Elements marked with "c" were adjusted to the same solar abundance scale by S. G. Ryan (Ryan et al. 1996 and private communication), entries marked with "x" remained unaltered. Unmarked entries were not observed in the corresponding study. All observations of very metal-poor stars published after 1989 were taken into account. In the case where multiple observations of stars exist, we used the most recent data. If they were published in the same year or *after* 1995, the values were averaged.

Typical abundance errors given for these observations are about 0.1 dex (see Ryan et al. 1996). These may not fully account for systematic errors, which could, e.g., be caused by the choice of the employed stellar atmosphere models and parameters, or by the employed solar abundance values. If there are systematic offsets between different subsamples, this could enhance the scatter in the combined sample.

Special attention has to be paid to Cr, Mn and O. In the case of Cr and Mn, data published after 1995 show a decrease in the [Cr/Fe] and [Mn/Fe] ratios for lower metallicities. Such trends are not present in older observations. Regardless of this, it is not possible to reproduce metallicity-dependent trends with our model, since we only use the stellar yields of Thielemann et al. (1996), which assume constant solar progenitor star metallicity. A possible explanation of the [Cr/Fe] and [Mn/Fe] trends is the dependency of stellar yields on the metallicity of the progenitor star of a SN Type II (Samland 1998) or a progenitor mass dependent mixing of SN II yields with the ISM (Nakamura et al. 1999).

In the data set of Israelian et al. (1998), the [O/Fe] ratio increases at lower metallicities. This behaviour is apparently different from previous determinations and is not yet understood, but almost identical results were published by a different group of observers (Boesgaard et al. 1999). The α-elements oxygen and magnesium are produced mainly during the hydrostatic burning phase of a high mass star and are only slightly affected by the actual explosion. Furthermore, their yields depend in almost the same way on the mass of the progenitor star (Thielemann et al. 1996; Woosley & Weaver 1995). Thus observations of Mg for the objects discussed in the O abundance determinations by Israelian et al. (1998) and Boesgaard et al. (1999) would be very interesting.

2.5. Results

2.5.1. Chemical Mixing of the Halo ISM

Starting with an ISM of primordial abundances, a first generation of ultra metal-poor stars is formed in the model. After the first high-mass stars exploded as SNe of Type II, the halo ISM is dominated by local inhomogeneities, since the SN events are spatially well separated and no mixing has yet occurred. In a very metal-poor medium, a single SN event heavily influences its surroundings, so that its remnant shows the element abundance pattern produced by that particular core-collapse SN. Stars born out of this enriched material therefore inherit the same abundances. Since SNe of different progenitor masses have different stellar yields, stars formed out of an incompletely mixed ISM show a great diversity in their element abundances.

Fig. 2.1 shows a cut through the computed volume, giving the density distribution of the halo ISM at four different times, ranging from the unmixed to the well mixed stage. Each panel shows a different mean metallicity and has a lateral length of 2.5 kpc. The density of

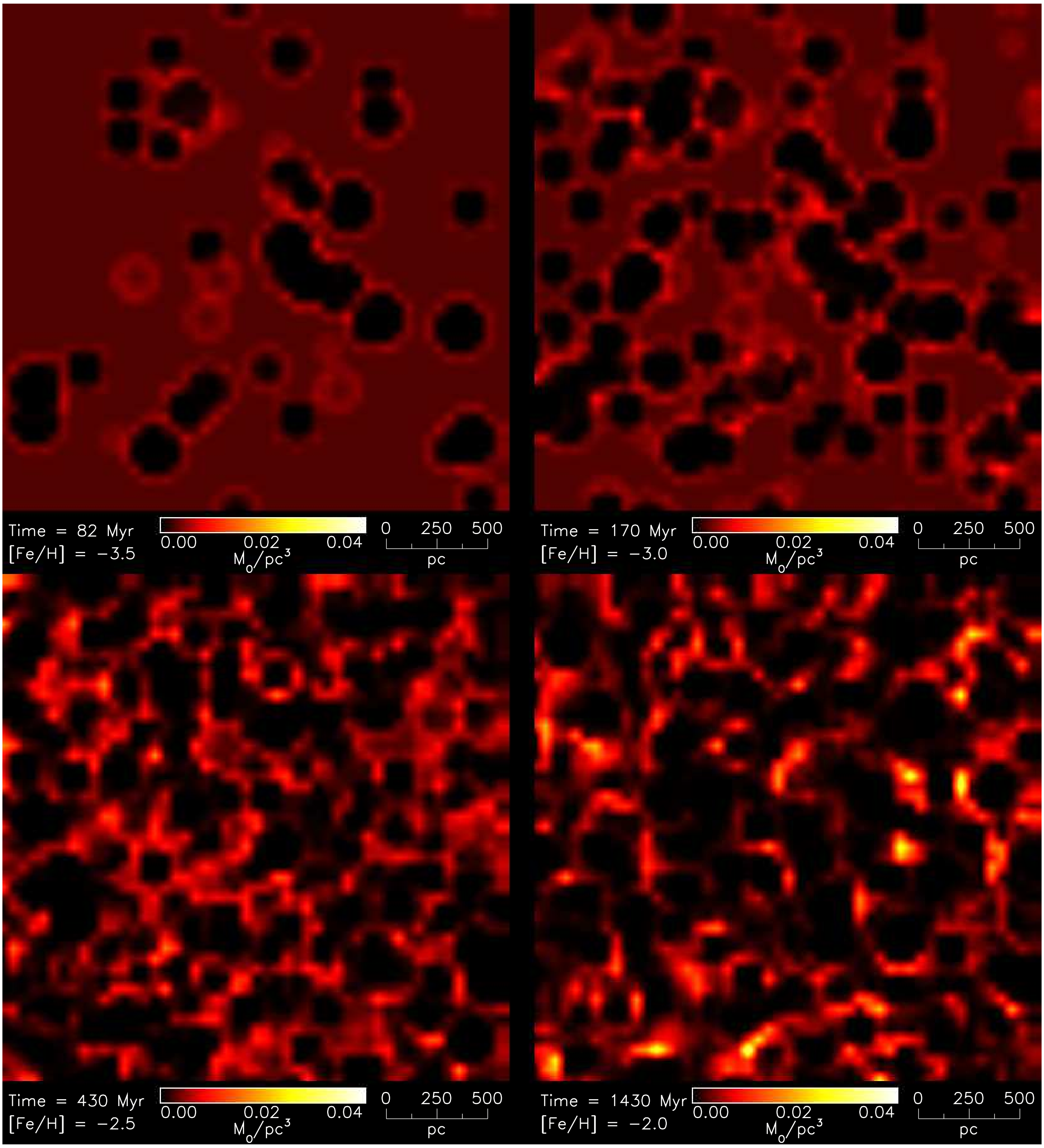

Fig. 2.1. Cut through the computed volume, showing the density distribution of the halo ISM during the transition from the unmixed to the well mixed stage (see text for details).

the ISM ranges from $6 \cdot 10^{-7}$ $M_\odot/pc^3$ in the inner part of a remnant to $0.04\,M_\odot/pc^3$ in the densest clouds, which is about the gas density of the solar neighbourhood (Binney & Tremaine 1987).

Upper left: After 82 Myr (see below for the scaling of the time units with the assumed SFR), the mean metallicity of the halo ISM is [Fe/H] $= -3.5$. Most of the volume was not yet affected by SN events, which can be seen as bright patches in the otherwise homogeneously distributed ISM. In the inner part of the remnants most of the gas has been swept up and condensed in thin shells, which show up as dark, ring-like structures. The regions influenced are well separated and no or only slight mixing on a local scale has taken place. The halo ISM has to be considered unmixed and is dominated by local inhomogeneities. Stars forming in the neighbourhood of such inhomogeneities show an abundance pattern which is determined by the ejecta of a single SN or a mixture of at most two to three SN events.

Upper right: Beginning of the transition from the unmixed to the well mixed halo ISM, after 170 Myr at a mean metallicity of [Fe/H] $= -3.0$. The separation of single SN remnants has become smaller and a higher number of remnants may overlap. The abundance pattern in overlapping shells still shows a great diversity but is closer to the IMF averaged element abundance than at the completely unmixed stage.

Lower left: After 430 Myr, at a mean metallicity of [Fe/H] $= -2.5$, enough SN events have occurred to pollute the mass of the whole ISM twice. Nevertheless there are still cells which were not influenced by a SN, showing therefore primordial abundances.

Lower right: After 1430 Myr, a mean metallicity of [Fe/H] $= -2.0$ is reached. At this time, no patches with primordial abundances exist and the ISM starts to be chemically well mixed. The once homogeneous, primordial medium has now a lumpy structure with large density fluctuations and shows mainly an IMF averaged abundance pattern.

Our calculations confirm that the incomplete mixing of the ISM during the halo formation plays a significant rôle in the early enrichment of the metal-poor gas. This can be seen in the [el/Fe] ratios of the considered elements, shown in Fig. 2.2. The small, filled squares show the [el/Fe] ratio of single model-stars. For comparison, observed metal-poor stars are represented by open squares. In the case of O, Cr and Mn, observations taken before 1995 were marked with open triangles. This was done to highlight possible trends in the [el/Fe] ratio of these elements. If multiple observations of a metal-poor star occurred and the abundances had to be averaged, open diamonds were used (see Sect. 2.4 for details).

The numbered circles show the [el/Fe] and [Fe/H] ratios of a single SN II with the indicated mass. The [Fe/H] ratio in the shell of the SN remnants are determined by the mass of the exploding star and the $5 \times 10^4\,M_\odot$ of gas that are swept up by the shock front. This ratio represents the maximal abundance a *single* SN II can produce and determines the position of the open circles on the [Fe/H] axis in Fig. 2.2. If the swept up material subsequently mixes with the surrounding medium, this abundance decreases and stars with lower [Fe/H] abundance can be formed. On the other hand, the [el/Fe] ratio is determined solely by the stellar yields of a SN II and is independent of the mixing mass. For the uncertainties of Fe-ejecta and [el/Fe] ratios in individual SNe II see the discussion in Sect. 2.3.

We divide the chemical enrichment process in the early evolution of the halo ISM into different enrichment stages: at metallicities [Fe/H] < -3.0, the ISM is completely unmixed and dominated by local inhomogeneities, originating from SN II events. At about [Fe/H] > -2.0 the halo ISM shows an IMF averaged abundance pattern and has to be considered chemically well mixed. The continuous transition between these two phases is marked by incomplete mixing which gradually becomes better, as more and more high-mass stars explode as SN II.

The different phases in the enrichment of the halo ISM seen in Fig. 2.2 can be distinguished in all [el/Fe] – [Fe/H] plots. At very low metallicities ([Fe/H] $<$ -3.0), only a few stars exist, showing a considerable spread in their [el/Fe] ratios, ranging from 0.5 dex in the case of Ni to more than 2 dex in the cases of O, Mg and Eu. At this stage, the scatter of the model stars is given by the spread in metallicities of the SN models. At the end of this early phase, less than 0.5% of the total halo ISM mass has been transformed into stars.

At a metallicity of $-3.0 <$ [Fe/H] < -2.0, the SN remnants start to overlap and a first, incomplete mixing occurs. New stars form out of material which was influenced by several SNe of different masses. Therefore, they do not show the typical abundance pattern

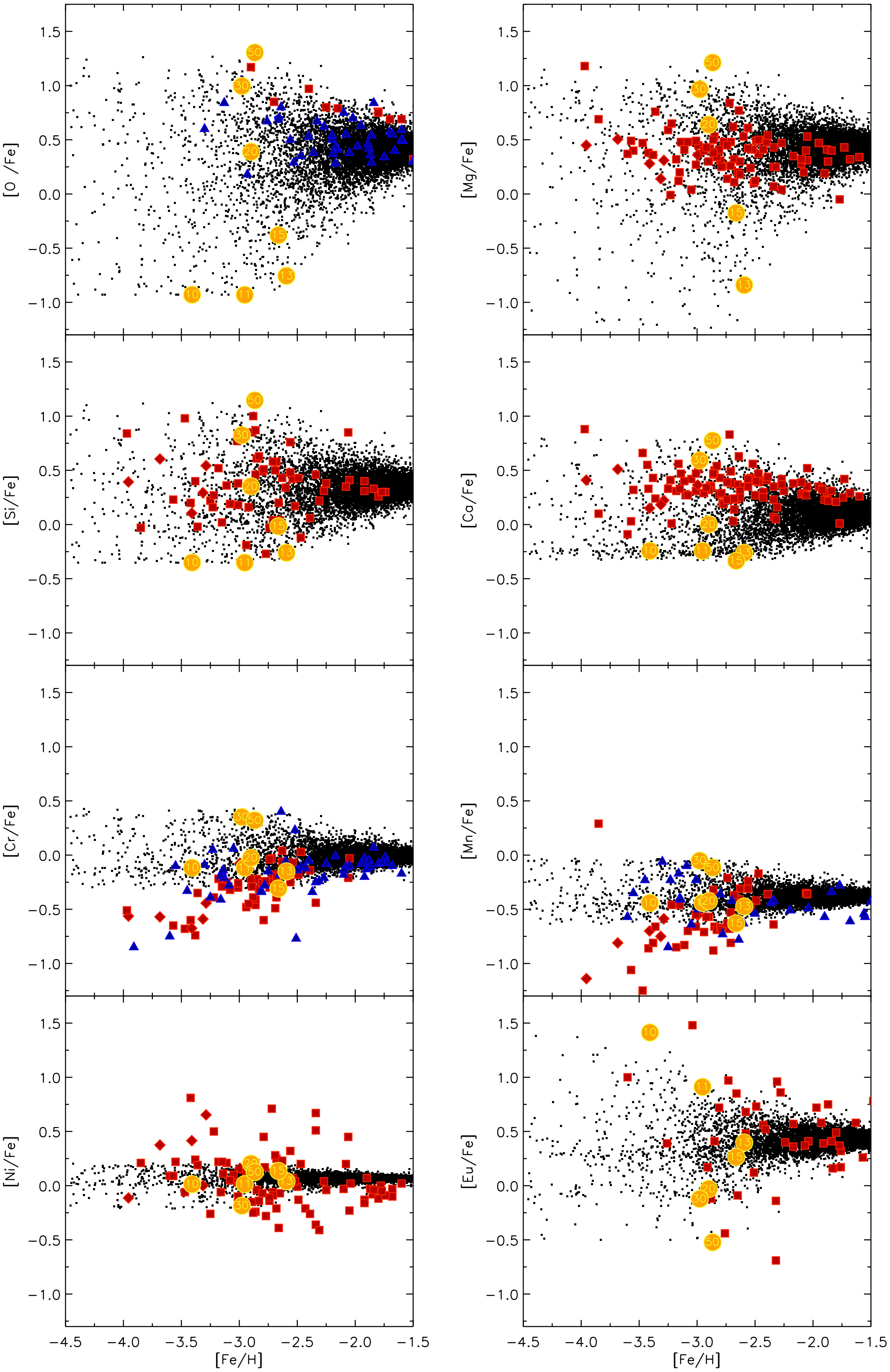

Fig. 2.2. Element-to-iron ratios [el/Fe] of O, Mg, Si, Ca, Cr, Mn, Ni and Eu. Open circles depict [el/Fe] ratios of SN II models of the given progenitor mass. Small filled squares represent model stars, open symbols show observed stars.

of a single SN, but show an average of the SNe which contributed to the enrichment of the local ISM. The spread in the metallicities gradually decreases from [Fe/H] $= -3.0$ to -2.0, reflecting the ongoing mixing process as more and more SNe pollute the ISM. At the beginning of the well-mixed phase, star-formation has consumed about 2.5% of the total halo ISM mass.

This late phase is characterized by a well mixed ISM and begins at [Fe/H] > -2.0, where the abundance scatter in the model is reduced to a third of its initial value. At this stage, the whole volume considered was influenced several times by SN events. This leads to an IMF averaged [el/Fe] ratio in the ISM which is the same as predicted by simple 1-zone models and which is observed in stars with metallicity [Fe/H] > -2.0. Even in an enriched medium, however, a SN event will still have an influence on its neighbourhood, although the change in the abundance pattern will not be as prominent as in a very metal-poor medium. This explains the fact, that even in the well-mixed case, the [el/Fe] ratios show a certain dispersion. At [Fe/H] $= -1.0$, about 8% of the total halo ISM mass has been used to form stars.

The onset of SNe of Type Ia marks the beginning of a third phase in the chemical enrichment history of the galaxy, but we will not consider this phase any further. Note, that the mean [el/Fe] ratios at [Fe/H] $= -1.0$ in our model do not have to be equal to zero (by definition the solar metallicity), since we have neglected the influence of SN Ia events.

To quantify the enrichment of the ISM we introduce the concept of the polluted mass $M_{\rm poll}$ in a unit volume at time τ. It is defined as the total mass which gets polluted by $N_{\rm SN}$ *isolated* SNe, where $N_{\rm SN}$ is the number of SNe in the unit volume that occurred during the elapsed time τ. For a constant mixing-mass $M_{\rm sw}$ swept up by a SN event, $M_{\rm poll} = N_{\rm SN} \cdot M_{\rm sw}$. Since the polluted mass is directly proportional to the number of SNe, it can become larger than the total ISM mass in the unit volume, $M_{\rm tot}$. Furthermore, the pollution factor $f_{\rm poll}$ is defined as the ratio $M_{\rm poll}/M_{\rm tot}$ and only depends on $N_{\rm SN}$, for fixed $M_{\rm sw}$ and $M_{\rm tot}$. When $f_{\rm poll} = 1$, enough SNe have contributed to the chemical enrichment to theoretically pollute the entire ISM in the unit volume, even though there still may be patches of material which were not yet affected by any SN. A higher pollution factor results in a better mixing of the halo ISM, decreasing the local abundance differences and the amount of material with primordial abundances. Therefore, the ratio $M_{\rm sw}/M_{\rm tot}$ determines the mixing efficiency in our model, i.e. how many SNe in the unit volume are needed to reach a certain value of $f_{\rm poll}$. Given $f_{\rm poll}$, $M_{\rm sw}$ and the mean, IMF integrated iron yield $\langle M_{\rm Fe}\rangle$ of a typical SN II, the mean metallicity of the ISM then is determined by

Table 2.2. Pollution factor and SN Type II frequency.

[Fe/H]	$f_{\rm poll}$	$N_{\rm SN}$ [kpc^{-3}]	τ [Myr]
-3.5	0.2	27	82
-3.0	0.7	83	170
-2.5	2.1	260	430
-2.0	6.5	810	1430

$$\begin{aligned}[\mathrm{Fe/H}] &= \log \frac{N_{\rm SN}\cdot\langle M_{\rm Fe}\rangle}{M_{\rm tot}} - C \\ &= \log \frac{f_{\rm poll}\cdot\langle M_{\rm Fe}\rangle}{M_{\rm sw}} - C,\end{aligned} \qquad (2.2)$$

where C is the solar iron abundance.

The local inhomogeneities of the ISM begin to disappear when most of the gaseous SN remnants start to overlap. This is the case when more or less every cloud in the halo was influenced at least once by a SN event, i.e. the pollution factor is about equal to one. With the adopted mixing mass of $M_{\rm sw} = 5\times10^4\ \mathrm{M}_\odot$ this is the case at [Fe/H] ≈ -2.8. This metallicity gives an upper limit for the end of the early phase and the beginning of the transition to the second, well-mixed enrichment phase.

Table 2.2 shows the pollution factor needed to reach the mean metallicities shown in the panels of Fig. 2.1. Also shown are the corresponding SN frequency $N_{\rm SN}$ and elapsed time τ, which depend on our model parameters. Here, the SN frequency is defined as the number of SNe per kpc^3 and depends on the total ISM mass in the unit volume, whereas the elapsed time scales with the average SFR as

$$\tau' = \tau \cdot \left(\frac{\langle \mathrm{SFR}\rangle}{1.06\cdot10^{-4}}\right)^{-1}, \qquad (2.3)$$

where $1.06\cdot10^{-4}\ \mathrm{M}_\odot\,\mathrm{yr}^{-1}\,\mathrm{kpc}^{-3}$ is the mean SFR in the unit volume in our model. Note that the evolution of the abundance ratios as a function of [Fe/H] is independent of the star formation timescale and the SFR specified in the model.

2.5.2. Comparison with Observations

The scatter in the [el/Fe] ratios of the model stars as a function of [Fe/H] shows the same general trend for every element considered, independent of the individual stellar yields. The inhomogeneous mixing of the very metal-poor halo ISM at [Fe/H] < -3.0 leads to a scatter in the [el/Fe] ratios of up to 1 dex. This scatter continuously decreases for higher metallicities, reflecting the ongoing mixing of the ISM. At [Fe/H] > -2.0 the model stars show an IMF averaged abundance pattern with an intrinsic scatter of about 0.1 to 0.2 dex. This behaviour matches the general trend of the observations well, as can be seen in Fig. 2.2. The observations also show a large scatter at low metallicities which again decreases for higher [Fe/H], with some exceptions, however: the iron-group elements Cr and Mn show a strong decrease in the [Cr/Fe] and [Mn/Fe] ratio for lower metallicities. This behaviour can not be reproduced with our adopted metallicity-independent stellar yields and the progenitor-independent mixing mass.

Compared to the observations, the distribution of [Ni/Fe] ratios of the model stars in Fig. 2.2 shows a scatter that is much too small. This is most likely due to the choice of mass cuts in the SNe II models, which have been set with the aim to reproduce the average solar [Ni/Fe] ratio. Thielemann et al. (1996) discuss in detail that large variations can easily occur. See also the discussion in Sect. 2.3. We therefore now want to investigate whether the sequence of enrichment stages seen in our model is similar to the observed evolution of abundance ratios even in cases when the employed yields may be incorrect.

To this end we have normalized the scatter in [Ni/Fe] of the model-stars at low [Fe/H] to unity, and have similarly renormalized the range of values for the observed stellar [Ni/Fe] ratios to one. The mean values of both distributions were left unchanged. The resulting renormalized distributions are shown in Fig. 2.3. The remarkably good agreement of both distributions after this procedure indicates that the enrichment history of the halo ISM implied by the model is consistent with the data, even though the employed Ni yields are not. Based on similar comparisons, we conclude that the abundance ratio data of most elements except Mn and Cr are consistent with the predicted enrichment history, and the scatter plots in Fig. 2.2 can thus be used to compare the range of the theoretically predicted nucleosynthesis yields with observations.

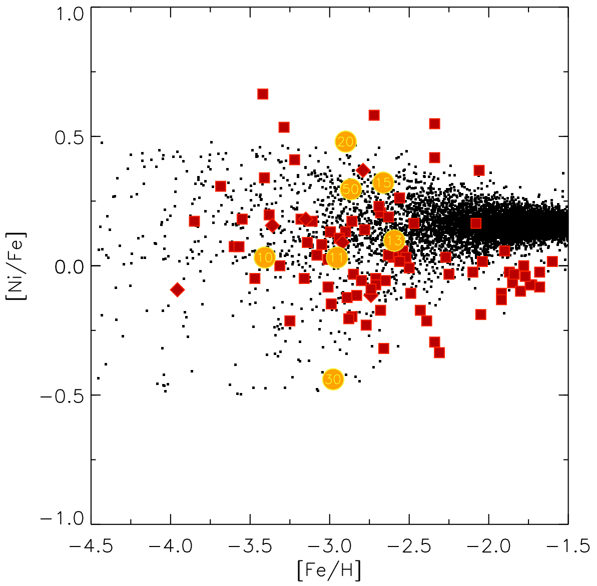

Fig. 2.3. Normalized nickel-to-iron ratio [Ni/Fe] as function of metallicity [Fe/H]. Symbols are the same as in Fig. 2.2. The scatter of the model-stars and the halo stars was normalized to unity to highlight the enrichment phases of the halo ISM.

To describe the transition from the metal-poor, unmixed to the enriched, well mixed ISM more quantitatively, the relative frequency of stars at a given [el/Fe] ratio has been analysed for the different enrichment phases. In the case of silicon, this detailed enrichment history is shown in Fig. 2.4. The different enrichment phases from [Fe/H] < -3.0, $-3.0 <$ [Fe/H] < -2.0 and [Fe/H] > -2.0 are given in the panels from top to bottom. The solid line shows the relative frequency of observed halo stars per [Si/Fe] bin for each enrichment phase and the dashed line the relative frequency of computed model stars per bin.

To account for the effect of observational errors on our data, we added a random, normally distributed error with standard deviation 0.1 dex in the [el/Fe] and [Fe/H] ratios to the model stars. The bin size in the [Si/Fe] ratio is 0.1 dex for observed and computed stars, while the position of the histogram for the model stars is shifted by 0.01 dex to the left for better visibility. The total number of stars included in the plot is given in the upper left corner of each panel, where N_{obs} and N_{mod} are the number of observed stars and of model stars, respectively.

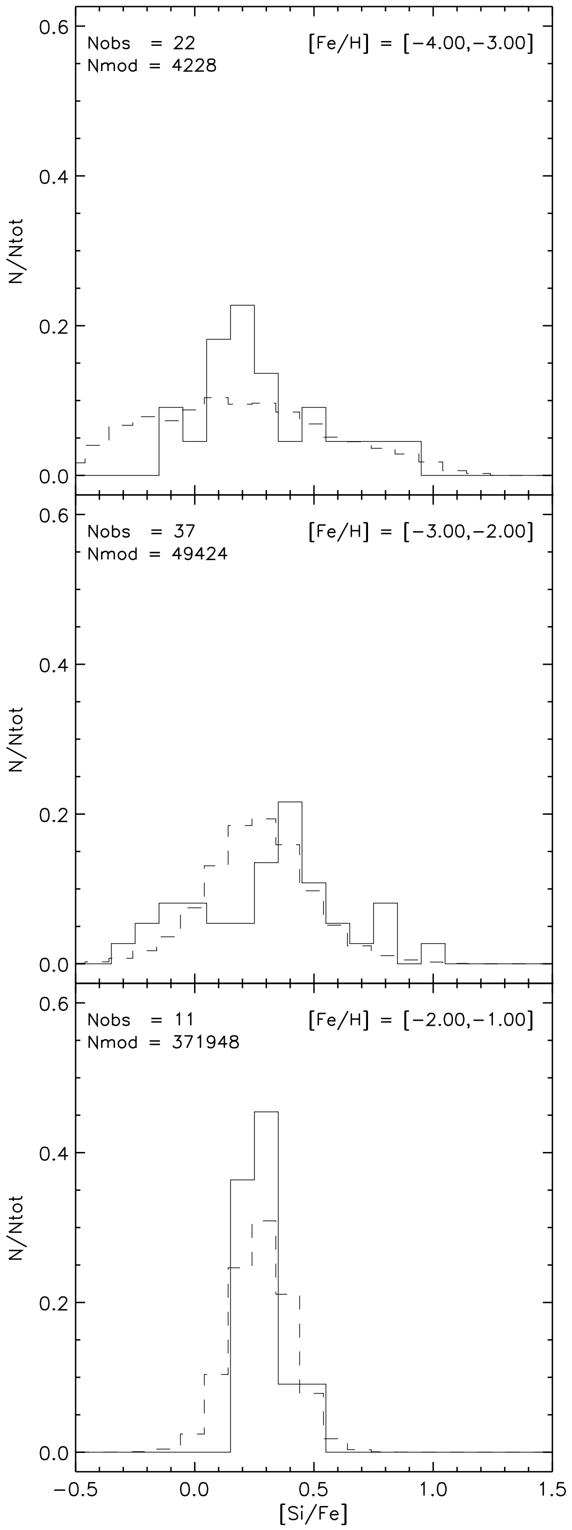

Fig. 2.4. Relative frequency of stars normalized to unity in [Si/Fe] bins for three different metallicity ranges (see text). The solid line shows observational data, the dashed line the model stars. The number of included stars is given in the upper left corner.

In the upper panel, the distributions of both the 22 observed and the 4226 model stars show a spread in the [Si/Fe] ratio of more than one dex. The distribution of the model stars shows two wide, protruding wings and a faint peak at [Si/Fe] $\approx$ 0.2. The "right" wing shows a shallow rise from [Si/Fe] $\approx$ 1.1 to the peak. The "left" wing is not as extended and shows a rather steep cutoff at [Si/Fe] ≈ -0.3. This asymmetry is due to the nucleosynthesis models of core-collapse SNe, which show a more or less constant value of [Si/Fe] ≈ -0.3 for progenitor masses in the range of 10 − 13 $M_{\odot}$, as can be seen in Fig. 2.2. The distribution of the halo stars peaks at the same location as the model stars but extends only down to [Si/Fe] ≈ -0.1. We attribute this to the poor statistic of the data set, since this gap is filled in the middle panel.

The middle panel of Fig. 2.4 shows the same distribution for the intermediate mixing stage of the ISM. The distribution of the model stars now has smaller wings, and peaks at [Si/Fe] $\approx$ 0.3. It is still broader than 1 dex, but the majority of the stars fall near the IMF averaged [Si/Fe] ratio. The prominent peak is caused by the already well-mixed regions, whereas the broad distribution shows that the halo ISM is still chemically inhomogeneous. The peak of the observational sample has shifted by about 0.2 dex to the right and lies now at [Si/Fe] $\approx$ 0.4. Compared to the prediction of the model, the relative frequency of the halo stars is too high in the wings of the distribution and too low to the left of the peak.

The lower panel shows the late stage, where the halo ISM is well mixed. The broad wings have completely disappeared and only the very prominent peak at the IMF averaged value remains. The distributions of the 11 observed stars and the 370 000 model stars are in good agreement. At this metallicity no SN of Type Ia should have polluted the by now well mixed ISM and the metal abundance is high enough to restrict the impact of single SN II events on the ISM.

The most prominent feature which characterizes the different enrichment phases, is the intrinsic scatter in the abundances of metal-poor stars. This can be seen in Fig. 2.5, which shows the standard deviation of [Si/Fe] as a function of metallicity [Fe/H] for the model and the halo stars. The bin size used to compute the standard deviation was 0.1 dex in metallicity. The solid line shows the scatter of the unmodified model stars. The influence of observational errors on our data was simulated by adding a random, normally distributed

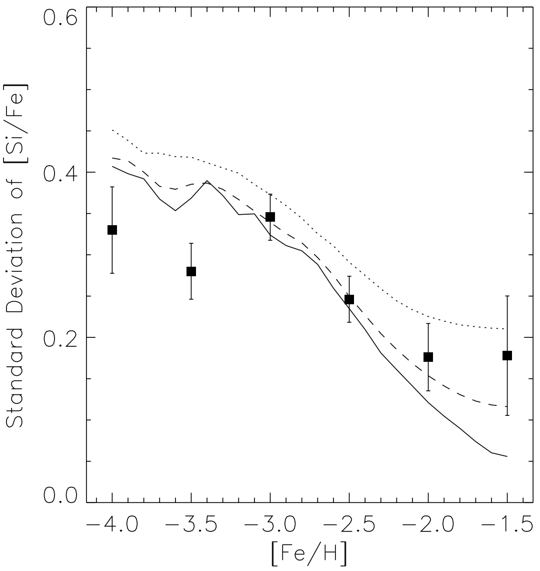

Fig. 2.5. Scatter in [Si/Fe] of the model and observed stars. The solid line gives the scatter of the model stars, the dashed and dotted lines show the scatter of the model stars, folded with an error of 0.1 and 0.2 dex. Filled squares give the standard deviation of the observed stars (see text).

error with standard deviation 0.1 and 0.2 dex in both [Si/Fe] and [Fe/H]. The resulting scatter in dependence of metallicity is given by the dashed and dotted lines. In the range of $-4.0 <$ [Fe/H] < -3.0 the scatter has a more or less constant value of approximately 0.4 dex. It declines rather steeply in the range $-3.0 <$ [Fe/H] < -2.0 and levels off again at metallicities higher than -2.0, depending on the assumed observational errors of 0.0, 0.1 or 0.2 dex. These curves show that for errors in this range the scatter at low metallicities is dominated by the intrinsic differences in the element abundances of single stars.

For comparison, the scatter in the [Si/Fe] ratio of observed halo stars is represented by filled squares. The observations were binned with a bin size of 0.5 dex to compute the standard deviations. To estimate the reliability of their scatter in [Si/Fe], we built several new data sets by adding a normally distributed random error with standard deviation 0.1 dex to the [Si/Fe] ratio and the metallicity of the stars. For each new data set, the standard deviation in the different bins was computed. The standard deviation for the results from these artificial data sets is given in the plot as 1-σ error-bars. The scatter of the observed abundance ratios shows nicely the features already seen in the curves for the model stars. At the first stage of the enrichment, it is approximately constant, followed by a steady decline in the intermediate mixing phase. At higher metallicities, the scatter levels off again.

Since the scatter in [Si/Fe] at [Fe/H] $= -4.0$ is about 0.4 dex the observational errors have little influence on the analysis at these low metallicities, unless unknown systematic or confusion errors were large enough to inflate the scatter at [Fe/H] $= -4.0$ to also about 0.4 dex. On the other hand, observational errors do dominate the scatter at metallicities [Fe/H] > -2.0, when the halo ISM is well mixed and the intrinsic scatter of the stars is negligible compared to the observational errors.

2.5.3. Individual Elements and Nucleosynthesis

Oxygen & Magnesium: As expected, the IMF averaged [el/Fe] ratios for O and Mg reproduce the mean abundance of the observed metal-poor stars nicely. The [O/Fe] ratio seems to be slightly too low, whereas [Mg/Fe] is slightly too high, but both deviations are smaller than 0.1 dex. No trend in the observational data of Mg can be seen and a trend in O only becomes visible if the observations of Israelian et al. (1998) are considered.

An important fact is that the scatter in the data, although increasing at lower metallicities, does not match the large scatter of more than two dex predicted by the stellar yields. Since no other mixing effects than the overlapping of SN remnants are included in our model, the expected scatter is determined by the nucleosynthesis yields. If gas flows and the random motion of stars in the halo accelerated the chemical mixing, a smaller scatter in the model data would be expected. Even then, the fact that the observed stars only show [O/Fe] or [Mg/Fe] ratios corresponding to the stellar yields produced by $18 - 50\,\mathrm{M}_\odot$ SNe would remain unexplained.

If we assume a top-heavy IMF which favoured high-mass SNe, this problem could be solved. However, the abundance pattern of the other elements should then also reflect this, which is not the case. This leaves us with two explanations: Either the stellar yields of O *and* Mg or of Fe are incorrect (or both).

Since the exact location of the mass cut is not known, the actual Fe yields are not very well determined (Woosley & Weaver 1995; Thielemann et al. 1996) and direct observational information which links a progenitor to an ejected Fe mass is very limited, maybe with the exception of SN 1987A and 1993J. Otherwise only the IMF integrated Fe-yields are constrained, but not necessarily their progenitor mass dependence (declining, rising, or with a maximum, see Nakamura et al. 1999 and Sect. 2.3). In order to attain a fit to the observational data within our evolution model we would need to decrease the Fe yields of the 13 or 15 $M_{\odot}$ stars by a factor of six. Without adjusting Fe-yields of the more massive stars, and assuming a standard Salpeter IMF, this would increase the IMF averaged [O/Fe] and [Mg/Fe] ratio by about 0.3 dex (a factor of two) and would therefore result in a much too high IMF averaged value. Equally, every other abundance ratio would be affected by this change.

On the other hand, the stellar yields of the α-elements O and Mg could be too low for the 13 and 15 $M_{\odot}$ progenitors. The abundances of O and Mg are mainly determined in the hydrostatic burning phases and do not depend heavily on the explosion mechanism. Changing the stellar yields of O and Mg for the 13 and 15 $M_{\odot}$ progenitor stars would therefore require to adjust the existing stellar models, which suffer from uncertainties in the theory of convection and the treatment of rotation.

Silicon: The IMF averaged [Si/Fe] ratio and the scatter predicted by the stellar yields fit the observations perfectly. The decrease in the scatter for higher metallicities and therefore the different enrichment phases of the halo ISM are clearly visible. At [Fe/H] < -3.0, the scatter in the model points reflects the scatter predicted by the stellar yields. During the transition from the unmixed to the well mixed ISM, in the range $-3.0 <$ [Fe/H] < -2.0, the scatter decreases steadily and leads to the IMF averaged [Si/Fe] ratio, which is reached at [Fe/H] > -2.0.

Calcium: The IMF averaged [Ca/Fe] ratio is about 0.2 dex lower than the observed mean for metal-poor stars. If the model data is shifted by this value to reproduce the mean of the observational data, the scatter for very metal-poor stars and the transition to the less metal-poor stars fits the data well. Note that, contrary to the other α-elements, the stellar yields of Ca are no longer approximately proportional to the mass of the progenitor. This behaviour becomes more pronounced in the cases of Cr, Mn and Ni.

Chromium & Manganese: The iron-peak elements Cr and Mn are both produced mainly during explosive silicon burning and show an almost identical, complicated dependence on the mass of the progenitor. The IMF averaged [el/Fe] ratio reproduces the observations of the less metal-poor stars well. The scatter predicted by the stellar yields is only about 0.8 dex and is not as large as for the α-elements.

A notable feature of the observations is the decrease of the [Cr/Fe] and [Mn/Fe] ratios for lower metallicities, seen in the newer data. If these trends are real, they can not be reproduced by metallicity-independent yields unless one assumes a progenitor mass dependent amount of mixing with the interstellar medium (Nakamura et al. 1999).

The upper limits of the [el/Fe] ratios of Cr and Mn are given by the stellar yields of a 30 $M_{\odot}$ SN and correspond to the highest [Cr/Fe] and [Mn/Fe] ratios seen in metal-poor stars, with the exception of the binary CS 22876-032 which shows an unusual high [Mn/Fe] ratio of 0.29 dex. Recent high-signal-to-noise, high-resolution data result in a lower [Mn/Fe] value for this star, placing it near the IMF averaged value (S. G. Ryan, private communication). On the other hand, the lower limits of the observed [Cr/Fe] and [Mn/Fe] ratios do not correspond at all with those given by the stellar yields, which show a ratio which is too high by up to 0.5 dex in the Thielemann et al. (1996) yields. Only a different choice of mass cuts as a function of progenitor mass (Nakamura et al. 1999) or as a function of metallicity would be able to rectify this.

Nickel: The stellar yields of the most important iron-peak element besides Fe completely fail to reproduce the observations. The scatter of the stellar yields is only about 0.5 dex compared to about 1.2 dex seen in the observational data. Compared to the mean of the observations, the IMF averaged abundance of the model-stars is about 0.1 dex to high. The small scatter in the [Ni/Fe] ratio originates from an almost constant ratio of Ni and Fe yields, which means that in the models Ni is produced more or less proportional to iron. To reproduce the scatter seen in the observations, Ni would have to depend on the progenitor mass differently from Fe. This is a shortfall of the employed yields, adjusted to reproduce the average solar [Ni/Fe] ratio with the choice of their mass cuts. Varying neutron excess in the yields, however, can change the [Ni/Fe] ratio drastically (Thielemann et al. 1996 and Sect. 2.3).

Europium: The r-process element Eu reproduces the scatter and the mean of the observational data quite well. But compared to the α-elements O, Mg, Si and Ca its behaviour is very different. The highest [Eu/Fe] ratio is produced by low mass SN and the lowest ratio by high mass SN, as required when one constructs yields under the assumption that the r-process originated from SNe II (see Sect. 2.3). This is exactly the opposite to what is found for the α-elements. Therefore, a top-heavy IMF would lead to a steadily increasing [Eu/Fe] ratio, since the most massive SNe will explode first (cf. *Oxygen & Magnesium*).

2.5.4. Age–Metallicity Relation

Common 1-zone chemical evolution models are based on the assumption that the system is well mixed at all times. An important consequence of this assumption is a monotonically increasing metallicity, which leads to a well defined age–metallicity relation. Therefore, it is in principle possible to deduce the age of a star if its metallicity is known. This basic assumption of 1-zone chemical evolution models was dropped in our stochastic approach. Therefore, it is not surprising that the well defined age–metallicity relation has to be replaced by a statistical relation. In Fig. 2.6, the metallicity [Fe/H] of model stars is plotted against the time of their formation. Model stars are represented by small filled squares. For comparison the white line visible in the middle of the black strip shows the mean age–metallicity relation, corresponding to the relation given by a 1-zone model. As can be seen, there is no clear age–metallicity relation at any time. Stars which were formed in the first 500 million years show a metallicity ranging from [Fe/H] < -4.0 up to [Fe/H] > -2.0 and in one extreme case up to [Fe/H] ≈ -1.5. On the other hand, stars with metallicity [Fe/H] $= -2.0$ could have formed at any time in the first 3×10^9 years. Taking these huge uncertainties into account, it is no longer possible to speak of a well-defined age–metallicity relation.

While the mean [Fe/H] abundance increases about linearly with time, the scatter in Fig. 2.6 again reflects the different enrichment phases of the ISM. The steep rise at early times marks the metal-poor and chemically inhomogeneous stage of the halo ISM. Contrary to this first phase, where SN events dominated the metal-poor ISM locally and the enrichment of isolated clouds could be very efficient, the late stage is characterized by a well mixed ISM and therefore an inefficient enrichment, which is reflected by the slow increase of the age–metallicity "relation" at later times.

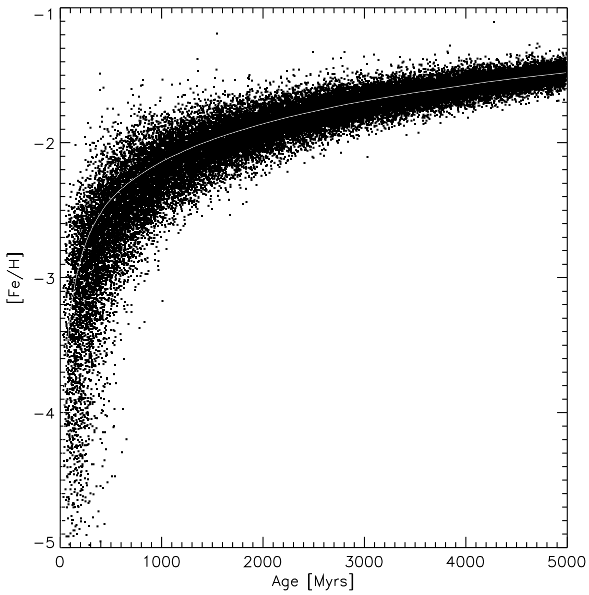

Fig. 2.6. Metallicity [Fe/H] vs. age of single model stars.

2.5.5. Ultra Metal-poor Stars

From our calculations, we can deduce the number of metal-poor stars which we expect to observe in different metallicity bins. The normalized distribution is shown in Fig. 2.7 for bin sizes of 0.2 dex and 1.0 dex. The number distribution is approximately a power law with slope 0.7 for [Fe/H] < -3.5 and slope 0.9 for [Fe/H] > -3.0. Also plotted are the observed data from a homogeneous intermediate resolution sample of Ryan & Norris (1991) and the combined high resolution data from Table 2.1, both rebinned to the large bin size (see Tables 2.3 and 2.4 for the numerical values). It is possible that the high resolution sample is incomplete in the range $[-3.0, -2.0]$, whereas the intermediate resolution sample might have a shortage of stars with [Fe/H] < -3.0. Table 2.3 also lists the number of model stars expected in the three 1.0 dex bins, normalized such that the number of model stars in the range $-4.0 <$ [Fe/H] < -3.0 is equal to the number of observed halo stars in the high-resolution sample in this metallicity range. As can be seen, in this case we expect 5 ± 2 model stars with $-5.0 <$ [Fe/H] < -4.0

Table 2.3. Top: Relative frequency of stars in the homogeneous intermediate resolution survey of Ryan & Norris (1991), denoted as RN, the combined high resolution data from Table 2.1 and our model, binned with binsize 1 dex. Bottom: Absolute numbers. The last row gives the number of stars per bin which we expect to be present, if our model gives a fair representation of the halo metallicity distribution. The number of model-stars is normalized to the number of stars in the range $-4.0 < \text{[Fe/H]} < -3.0$ in the high resolution sample. No star was detected with confirmed $\text{[Fe/H]} < -4.0$, in contrast to the 5 ± 2 stars predicted by the model.

[Fe/H]	$[-3.0, -2.0]$	$[-4.0, -3.0]$	$[-5.0, -4.0]$
RN	0.943	0.057	0.000
High Res	0.654	0.346	0.000
Model	0.865	0.115	0.020
RN	99	6	0
High Res	53	28	0
Expected	211 ± 15	28 ± 5	5 ± 2

Table 2.4. Relative frequency of model stars, binned with binsize 0.2 dex.

[Fe/H]	N/N_{tot}	$\log(N/N_{tot})$
$[-5.0, -4.8]$	$1.92 \cdot 10^{-3}$	-2.72
$[-4.8, -4.6]$	$2.37 \cdot 10^{-3}$	-2.63
$[-4.6, -4.4]$	$3.43 \cdot 10^{-3}$	-2.46
$[-4.4, -4.2]$	$5.10 \cdot 10^{-3}$	-2.29
$[-4.2, -4.0]$	$7.51 \cdot 10^{-3}$	-2.12
$[-4.0, -3.8]$	$1.00 \cdot 10^{-2}$	-2.00
$[-3.8, -3.6]$	$1.31 \cdot 10^{-2}$	-1.88
$[-3.6, -3.4]$	$1.93 \cdot 10^{-2}$	-1.71
$[-3.4, -3.2]$	$2.82 \cdot 10^{-2}$	-1.55
$[-3.2, -3.0]$	$4.41 \cdot 10^{-2}$	-1.36
$[-3.0, -2.8]$	$6.71 \cdot 10^{-2}$	-1.17
$[-2.8, -2.6]$	$1.02 \cdot 10^{-1}$	-0.99
$[-2.6, -2.4]$	$1.47 \cdot 10^{-1}$	-0.83
$[-2.4, -2.2]$	$2.11 \cdot 10^{-1}$	-0.68
$[-2.2, -2.0]$	$3.38 \cdot 10^{-1}$	-0.47

while the high resolution sample contains none. If the ratio of stars in these two metallicity bins for this admittedly inhomogeneous sample is representative for the Galactic halo stars, this would suggest a genuine shortage of the most metal-poor stars. In this case a possible solution could be the pre-enrichment of the halo ISM by population III stars. It is conceivable that these already produced an iron abundance of $\text{[Fe/H]} \approx -4.0$ before they disappeared, leaving only a pre-enriched ISM.

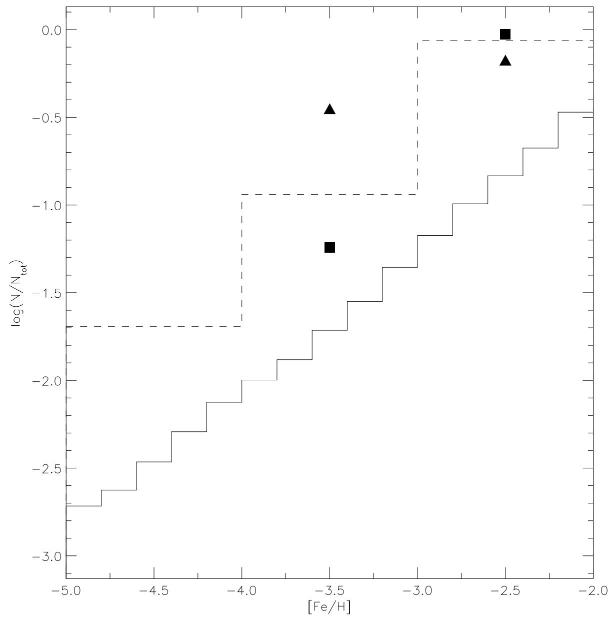

Fig. 2.7. Metallicity distribution of model stars at the end of the calculation ($\text{[Fe/H]} = -1$). The number of stars with metallicity [Fe/H] is shown (a) in bins of 0.2 dex (b) in bins of 1.0 dex. In both cases the total number of stars is normalized to one. The solid squares show the intermediate resolution data of Ryan & Norris (1991), the solid triangles the combined high resolution data from Table 2.1, both binned with bin size 1.0 dex and similarly normalized. There are no observed stars with $\text{[Fe/H]} < -4.0$. See Tables 2.3, 2.4 and text.

2.6. Conclusions & Discussion

We have developed a stochastic model of the early chemical enrichment of the halo ISM. The aim of the model is to understand the scatter in the [el/Fe] ratios of observed stars at very low metallicities and the transition to the smaller scatter seen at higher metallicities. We computed the evolution of the abundances of the α-elements O, Mg, Si and Ca, the iron-peak elements Cr, Mn, Fe and Ni and the r-process element Eu and investigated the mixing of the halo ISM.

We divide the enrichment history of the halo ISM into different phases. At metallicities $\text{[Fe/H]} < -3.0$, the ISM is not mixed and is dominated by local abundance inhomogeneities, which are caused by individual Type II SNe of different progenitor masses. The second phase at $\text{[Fe/H]} > -2.0$ is defined by a well mixed ISM which shows IMF averaged abundances and is too metal-rich to be dominated by single SN events. A continuous transition from the first to the second phase occurs between $-3.0 < \text{[Fe/H]} < -2.0$.

The onset of SN Ia events marks the beginning of a third phase in the enrichment of the ISM.

The different enrichment phases of the halo ISM can be distinguished in every considered element, after normalising to the stellar yields. On the other hand, Fig. 2.2 shows that some stellar yields reproduce the IMF averaged element-to-iron ratio [el/Fe] well, but fail to reproduce the abundance scatter observed in metal-poor halo stars. Especially the stellar yields of the α-elements O and Mg predict stars with a low element-to-iron ratio ([O/Fe] or [Mg/Fe] < 0.0), which are not observed. Typically, metal-poor halo stars show an overabundance of α-elements of about [α/Fe] ≈ 0.3 to 0.4, as can be seen in Fig. 2.2. This is especially troublesome, since an attempt to solve this problem would either require a change in the iron yields of the 13 and 15 $\mathrm{M}_\odot$ models of up to a factor six, which would raise every other mean element abundance by about 0.3 dex (a factor of two), or a change in the stellar yields of oxygen and magnesium, which are produced mainly during the hydrostatic burning phases.

Recent observations of metal-poor stars show a decrease of the [Cr/Fe] and [Mn/Fe] ratios for lower metallicities. It is not possible to explain these trends with the metallicity independent stellar yields we have used. Also, the stellar yields of the iron-peak element Ni predict a scatter in [Ni/Fe] which is much too small compared to the observational data. These problems argue strongly for a revision of the theoretical nucleosynthesis models and their extension to lower metallicities.

The unfortunate situation is, however, that there exists no theoretical foundation to do so for Fe-group yields as long as the supernova explosion mechanism is not understood. Thielemann et al. (1996) discussed in detail uncertainties of Fe-group yields due to the choice of mass cut, explosion energy and entropy, as well as the delay time between collapse and explosion, affecting also the neutron-richness of matter. Multidimensional aspects might add further degrees of freedom (Nagataki et al. 1997, 1998). Thus, there is an understanding of dependences, coincidences of abundance features etc., but at present only observational information combined with galactic evolution modelling like in the present paper or, e.g., Tsujimoto & Shigeyama (1998) and Nakamura et al. (1999) can try to provide sufficient constraints for a further understanding of supernova nucleosynthesis.

The advancing enrichment process of the halo ISM can be characterized by the pollution factor $f_{\rm poll}$, defined as the ratio of the mass $M_{\rm poll} = N_{\rm SN} \cdot M_{\rm sw}$ polluted by $N_{\rm SN}$ preceding SNe and the ISM mass $M_{\rm tot}$, all in a unit volume. The enrichment history of the halo ISM now is mainly determined by the mixing efficiency which in turn is fixed by the ratio of the mass $M_{\rm sw}$ of swept-up material in a SN event and $M_{\rm tot}$. The more mass a SN sweeps up, the less SN events are needed to reach a certain value of $f_{\rm poll}$, making the mixing more efficient. $M_{\rm sw}$ also determines the average metallicity [Fe/H] of the halo ISM for a given pollution factor. A larger swept-up mass leads to a lower mean ISM metallicity and vice versa. Therefore, the metallicity where the transition from one enrichment stage to the next occurs, depends only on the mixing efficiency $M_{\rm sw}/M_{\rm tot}$ and not on the SFR. The SFR is only important if one is interested in the *elapsed time* that is needed to reach a certain mean metallicity of the halo ISM.

Figures 2.4 and 2.5 support our adopted value of 5×10^4 $\mathrm{M}_\odot$ of swept up material. If the swept up mass is higher, the mixing would be more efficient, resulting in an IMF averaged chemical abundance pattern at lower metallicities. This would produce a narrower peak in Fig. 2.4 and a steeper slope in Fig. 2.5. Moreover, the whole curve in Fig. 2.5 would be shifted towards lower metallicities. On the other hand, a smaller mixing mass would reduce the efficiency of the enrichment of the ISM, which could be seen in a broader distribution at higher metallicities in Fig. 2.4 and a shallower slope in Fig. 2.5.

Standard 1-zone chemical evolution models predict a well defined age–metallicity relation, based on the assumption that the ISM is well mixed at all times. In our stochastic model the chemical inhomogeneity of the halo ISM and therefore the scatter in metallicity at any time is much too high to reasonably establish such a relation. Nevertheless, the steep rise with large scatter seen in Fig. 2.6 at very early times marks the chemically inhomogeneous enrichment phase, while the slow increase later-on reflects the well mixed, metal-rich ISM.

The results of our model also quantify the problem of the missing ultra metal-poor stars. From it we have deduced the expected number of ultra metal-poor stars (with [Fe/H] < -4.0) which should have been observed, normalized to the number of halo stars in the combined high-resolution sample with metallicities in the range $-4.0 < [\mathrm{Fe/H}] < -3.0$. We expect about 5 ± 2 ultra metal-poor stars whereas none was found to date. It is possible that Population III stars have caused a pre-enrichment of the ISM to $[\mathrm{Fe/H}] \approx -4.0$ and already have disappeared before the onset of the formation of the Galaxy.

Acknowledgements. We would like to thank the referee S. G. Ryan for helpful and motivating discussions and for providing us with some of the observational data. This work was supported by the Swiss Nationalfonds.

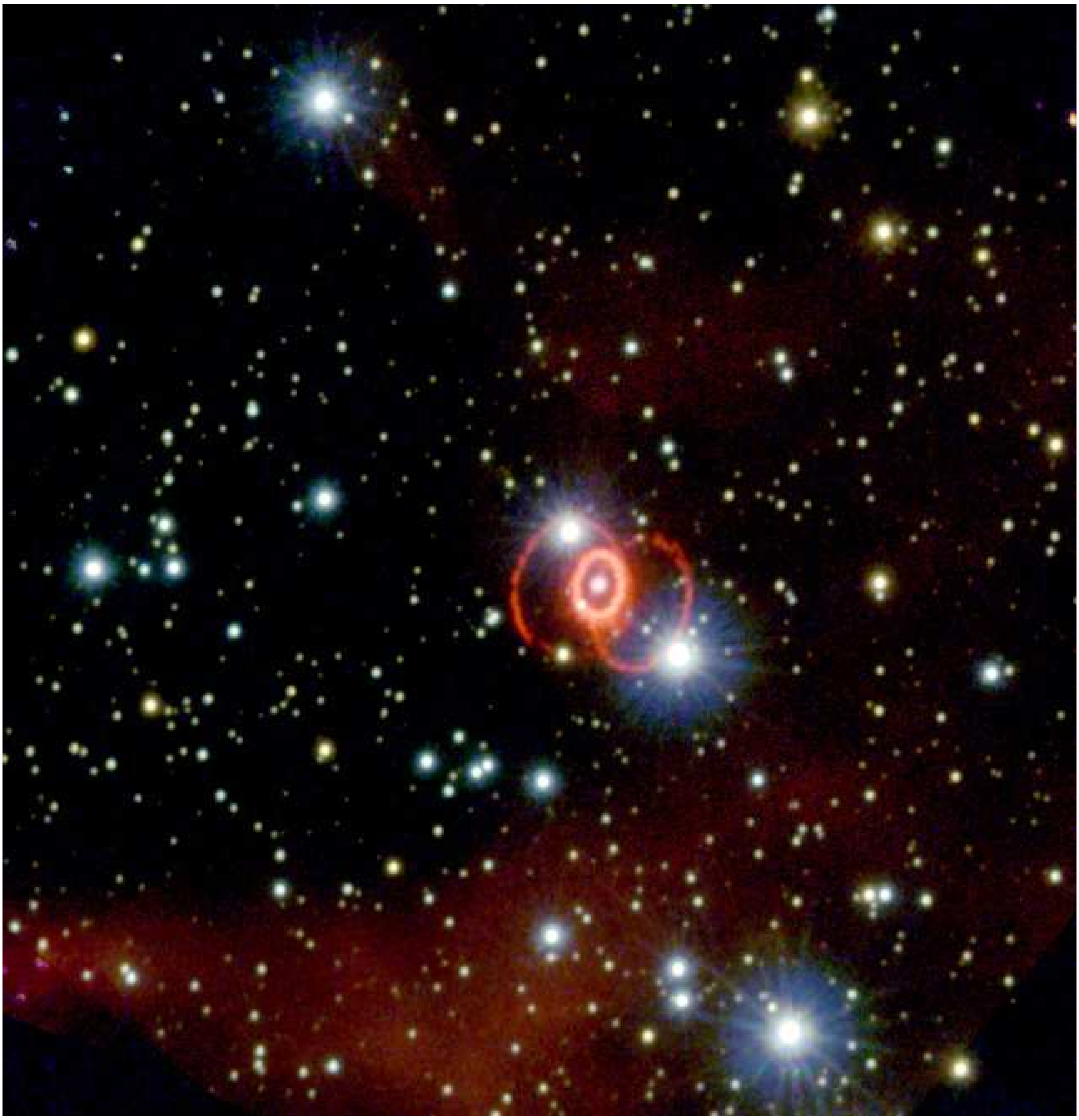

3

Implications of O and Mg abundances in metal-poor halo stars for stellar iron yields

Abstract. Inhomogeneous chemical evolution models of galaxies which try to reproduce the scatter seen in element-to-iron ratios of metal-poor halo stars are heavily dependent on theoretical nucleosynthesis yields of core-collapse supernovae (SNe II). Hence inhomogeneous chemical evolution models present themselves as a test for stellar nucleosynthesis calculations. Applying such a model to our Galaxy reveals a number of shortcomings of existing nucleosynthesis yields. One problem is the predicted scatter in [O/Fe] and [Mg/Fe] which is too large compared to the one observed in metal-poor halo stars. This can be either due to the oxygen or magnesium yields or due to the iron yields (or both). However, oxygen and magnesium are α-elements that are produced mainly during hydrostatic burning and thus are not affected by the theoretical uncertainties afflicting the collapse and explosion of a massive star. Stellar iron yields, on the other hand, depend heavily on the choice of the mass-cut between ejecta and proto-neutron star and are therefore very uncertain. We present iron yield distributions as function of progenitor mass that are consistent with the abundance distribution of metal-poor halo stars and are in agreement with observed ^{56}Ni yields of core-collapse supernovae with known progenitor masses. The iron yields of lower-mass SNe II (in the range $10 - 20\,\mathrm{M}_{\odot}$) are well constrained by these observations. Present observations, however, do not allow us to determine a unique solution for higher-mass SNe. Nevertheless, the main dependence of the stellar iron yields as function of progenitor mass can be derived and may be used as a constraint for future core-collapse supernova/hypernova models. A prediction of hypernova models is the existence of ultra α-element enhanced stars at metallicities [Fe/H] ≤ -2.5, which can be tested by future observations. The results are of importance for the earliest stages of galaxy formation when the ISM is dominated by local chemical inhomogeneities and the instantaneous mixing approximation is not valid.

3.1. Introduction

The key to the formation and evolution of the Galaxy lies buried in the kinematic properties and the chemical composition of its stars. Especially old, metal-poor halo stars and globular clusters are ideal tracers of the formation process. Although many of the properties of the halo component and its substructures have been unveiled, it is still not possible to decide whether the Galaxy formed by a fast monolithic collapse (Eggen, Lynden-Bell & Sandage, 1962), by the slower merging and accretion of subgalactic fragments (Searle & Zinn 1978) or within the context of a hybrid picture, combining aspects of both scenarios. Recently, Chiba & Beers (2000) made an extensive investigation to address this question, concluding that a hybrid scenario, where the inner part of the halo formed by a fast, dissipative collapse and the outer halo is made up of the remnants of accreted subgalactic fragments, best explains the observational data. It also seems to be consistent with the theory of galaxy formation based on cold dark matter scenarios (see e.g. Steinmetz & Müller 1995; Gnedin 1996; Klypin et al. 1999; Moore et al. 1999; Pearce et al. 1999; Bekki & Chiba 2000; Navarro & Steinmetz 2000).

However, the kinematic structure of the halo alone is not sufficient to draw a conclusive picture of the formation of the Galaxy. Old, unevolved metal-poor halo stars allow us to probe the chemical composition and (in)homogeneity of the early interstellar medium (ISM) and its evolution with time, since element abundances in the stellar atmospheres of those stars directly reflect the chemical composition of the material out of which they formed. It is almost impossible to determine the age of single stars (except in a few cases where radioactive thorium or uranium was detected, see e.g. Cayrel et al. 2001). Therefore, the metallicity Z or iron abundance [Fe/H] of a star is taken as an age estimate, knowing that an *age–metallicity relation* can only be used in a statistical sense for the bulk of stars (see e.g. Argast et al. 2000, hereafter Paper I).

Common chemical evolution models mostly assume that the metal-rich ejecta of supernovae (SNe) are mixed instantaneously and homogeneously into the ISM. Models using this approximation, together with theoretical nucleosynthesis yields of type Ia and type II SNe, can explain the behaviour of element-to-iron ratios ([el/Fe]) of stars as function of metallicity [Fe/H] for many elements and for [Fe/H] ≥ -2. This shows that the instantaneous mixing approximation is valid at this stage and – since at these metallicities even some of the lowest mass core-collapse supernovae (SNe II) have exploded – that the stellar yields *averaged over the initial mass function (IMF)* are for most elements accurate within a factor of two (see e.g. Samland 1998).

However, observations of very metal-poor stars show significant scatter in [el/Fe] ratios at $[\mathrm{Fe/H}] < -2$, implying that the ISM was not well mixed at this stage (Paper I). These local chemical inhomogeneities were probably mainly caused by SNe II, since progenitors of SN Ia have much longer lifetimes and are unimportant for the chemical enrichment of the ISM until approximately $[\mathrm{Fe/H}] \geq -1$. At these early stages of galaxy formation, the instantaneous mixing approximation is not valid and yields depending on the mass of individual SNe II become important. Therefore, accurate nucleosynthesis yields as a function of progenitor mass are crucial for the understanding of the earliest stages of galaxy formation.

In Paper I, a stochastic chemical evolution model was presented which accounts for local chemical inhomogeneities caused by SNe II with different progenitor masses. The model successfully reproduces the scatter in [el/Fe] ratios as function of [Fe/H] for some elements like Si or Ca, but fails quantitatively in the case of the two most abundant α-elements, O and Mg. The scatter in [O/Fe] and [Mg/Fe] is much larger than observed and predicts stars with [O/Fe] and $[\mathrm{Mg/Fe}] \leq -1.0$. This result depends mainly on the employed stellar yields, demonstrating that either the oxygen/magnesium or the iron yields (or both) as a function of progenitor mass are not well determined by existing nucleosynthesis models.

The solution to this problem is important for the understanding of the chemical evolution of our Galaxy. In this work, we try to reconcile element abundance observations of metal-poor halo stars with the predictions of our inhomogeneous chemical evolution model by changing the progenitor mass dependence of stellar yields. The formation of oxygen and magnesium in hydrostatic burning and ejection during a SN event is much better understood than the formation and ejection of ^{56}Ni (which decays to ^{56}Fe and forms the bulk of the ejected iron), since the amount of ejected ^{56}Ni is directly linked to the still not fully understood explosion mechanism (c.f. Liebendörfer et al. 2001; Mezzacappa et al. 2001; Rampp & Janka 2000). Any attempt to alter stellar yields should therefore start with iron and iron-group elements. We present a method to derive stellar iron yields as function of progenitor mass from the observations of metal-poor halo stars, assuming given yields of oxygen and magnesium.

In Sect. 3.2 we give a short description of the stochastic chemical evolution model, followed by a summary of observations and basic model results in Sect. 3.3. The discussion of uncertainties in stellar yields and how global constraints on stellar iron yields can be gained from observations is given in Sect. 3.4. Implications for stellar iron yields and conclusions are given in Sect. 3.5 and Sect. 3.6, respectively.

3.2. The chemical evolution model

Observations of very metal-poor halo stars show a scatter in [el/Fe] ratios of order 1 dex. This scatter gradually decreases at higher metallicities until a mean element abundance is reached which corresponds to the [el/Fe] ratio of the stellar yields integrated over the initial mass function. Our stochastic chemical evolution model of Paper I follows the enrichment history of the halo ISM in a cube with a volume of $(2.5\ \mathrm{kpc})^3$, down to a resolution of $(50\ \mathrm{pc})^3$. Every cell of the grid contains detailed information about the enclosed ISM and the mass distribution of stars. For the purpose of this paper, the enrichment of the ISM with O, Mg, Si, Ca and Fe is computed.

At every time-step, randomly chosen cells may create stars. The likelihood for a cell to form a star is proportional to the square of the local ISM density. The mass of a newly formed star is chosen randomly, with the condition that the mass distribution of all stars follows a Salpeter IMF. The lower and upper mass limits for stars are taken to be $0.1\,\mathrm{M}_\odot$ and $50\,\mathrm{M}_\odot$, respectively. Newly born stars inherit the abundance pattern of the ISM out of which they formed, carrying therefore information about the chemical composition of the ISM at the place and time of their birth.

Stars in a range of $10 - 50\,\mathrm{M}_\odot$ are assumed to explode as SNe II (or hypernovae, we will use the term SNe II to include hypernovae unless otherwise noted) resulting in an enrichment of the neighbouring ISM. Intermediate mass stars form planetary nebulae, which return only slightly enriched material. Low mass stars do not evolve significantly during the considered time but serve to lock up part of the mass, affecting therefore the abundances of elements with respect to hydrogen. Stellar yields are taken from Thielemann et al. (1996, hereafter TH96) and Nomoto et al. (1997). Additionally, since there are no nucleosynthesis calculations for $10\,\mathrm{M}_\odot$ progenitors, their yields were set to

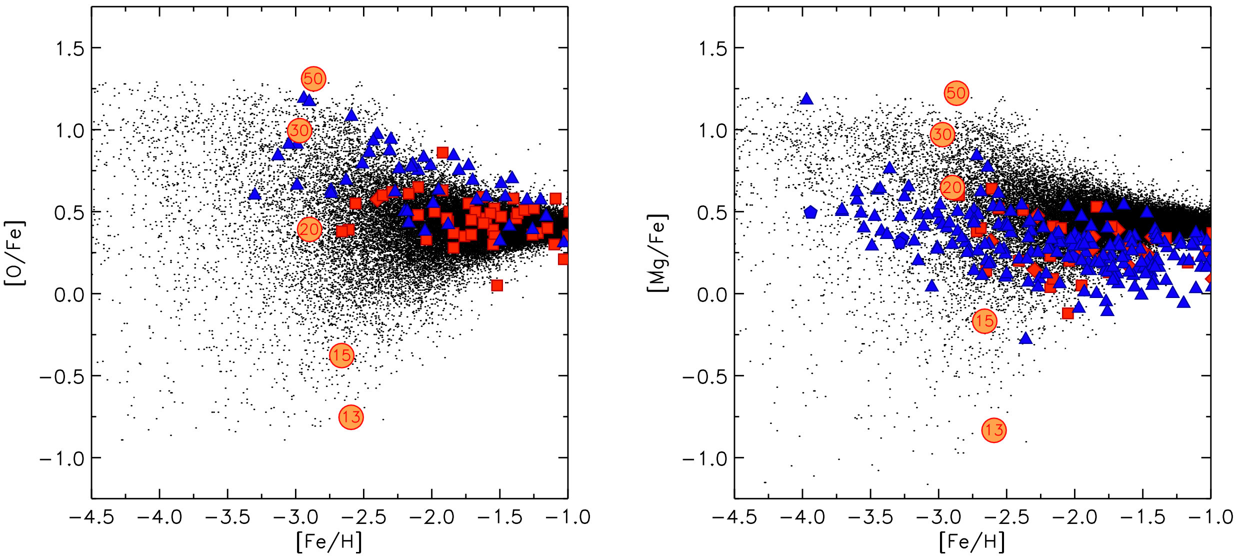

Fig. 3.1. [O/Fe] and [Mg/Fe] ratios vs. metallicity [Fe/H] of metal-poor halo stars (squares and triangles) and model stars (dots). Circles depict [O/Fe] and [Mg/Fe] ratios of SN II models of the given progenitor mass. (See text for details.) In contrast to observations, model stars with subsolar [O/Fe] and [Mg/Fe] ratios are predicted by the applied stellar yields, as visible by the location of the 13 and 15 $M_\odot$ SNe.

1/10 of the yields of the 13 $M_\odot$ model. We then linearly interpolated the stellar yields given in these papers, since we use a finer mass-grid in our simulation. The interpolation gives IMF averaged values of [el/Fe] ratios which are in good agreement (within 0.1 dex) with the observed mean values of metal-poor stars.

The SN remnant sweeps up the enriched material in a spherical, chemically well mixed shell. Since the explosion energy of SNe II is believed to depend only slightly on the mass of its progenitor (Woosley & Weaver 1995, hereafter WW95; Thielemann et al. 1996), we assume that each SN II sweeps up about 5×10^4 $M_\odot$ of gas (Ryan et al. 1996; Shigeyama & Tsujimoto 1998). Stars which form out of material enriched by a single SN inherit its abundance ratios and therefore show an element abundance pattern which is characteristic for this particular progenitor mass. This will lead to a large scatter in the [el/Fe] ratios, as long as local inhomogeneities caused by SN events dominate the halo ISM. As time progresses, supernova remnants overlap and the abundance pattern in each cell approaches the IMF average, leading to a decrease in the [el/Fe] scatter at later times. Since the SN remnant formation is the only dynamical process taken into account, this model shows the least possible mixing efficiency for the halo ISM. This is just the opposite to chemical evolution models which use the instantaneous mixing approximation. We continue our calculation up to an average iron abundance of [Fe/H] $= -1.0$. At this metallicity, SN Ia events which are not included in our model start to influence the ISM significantly. A more detailed description of the model can be found in Paper I.

We emphasize one important result: Starting with a primordial ISM and taking into account local inhomogeneities caused by SNe II, the *initial* scatter in [el/Fe] ratios is determined solely by the adopted nucleosynthesis yields. The details of the chemical evolution model only determine how fast a chemically homogeneous ISM is reached, i.e. how the scatter evolves with time or (equivalently) iron abundance [Fe/H]. Therefore, the range of [el/Fe] ratios of the most metal-poor stars does not depend on specific model parameters but is already fixed by the stellar yields.

3.3. Observations and basic model results

As mentioned in the introduction, existing nucleosynthesis models, combined with a chemical evolution model taking local inhomogeneities into account, predict [O/Fe] and [Mg/Fe] ratios less than solar for some metal-poor stars. This is in contrast to observations of metal-poor halo stars, as can be seen in Fig. 3.1. The left hand panel shows the [O/Fe] ratio of observed and model stars as function of iron abundance [Fe/H] and the right hand panel the same for [Mg/Fe], where the model stars are plotted as small dots. The observational data were collected from Magain (1989), Molaro & Bonifacio (1990), Molaro & Castelli (1990), Peterson et al. (1990), Bessell et al. (1991), Ryan et al. (1991), Spiesman & Wallerstein (1991), Spite & Spite (1991), Norris et al. (1993), Beveridge & Sneden (1994), King (1994), Nissen et al. (1994), Primas et al. (1994), Sneden et al. (1994), Fuhrmann et al. (1995), McWilliam et al. (1995a), Balachandran & Carney (1996), Ryan et al. (1996), Israelian et al. (1998), Jehin et al. (1999), Boesgaard et al. (1999), Idiart & Thévenin (2000), Carretta et al. (2000) and Israelian et al. (2001).

Combining data from various sources is dangerous at best, since different investigators use different methods to derive element abundances with possibly different and unknown systematic errors. This influences the scatter in [el/Fe] ratios, which plays a crucial rôle in determining the chemical (in)homogeneity of the ISM as function of [Fe/H]. Unfortunately, there is no investigation with a sample of oxygen/magnesium abundances of metal-poor halo stars that is large enough for our purpose. Therefore, we are forced to combine different data sets, keeping in mind that unknown systematic errors can enlarge the intrinsic scatter in element abundances of metal-poor stars. Recently, Idiart & Thévenin (2000) and Carretta et al. (2000) reanalyzed data previously gathered by other authors and applied NLTE corrections to O, Mg and Ca abundances, which is a first step in reducing the scatter introduced by systematic errors.

Therefore, we divided the collected data into two groups, namely the data of Idiart & Thévenin (2000) and Carretta et al. (2000), which is represented in Fig. 3.1 by triangles, and the data of all other investigators, represented by squares. If multiple observations of a single star exist, abundances are averaged and pentagons and diamonds are used for the first and second group, respectively. (Averaging of data points was only necessary in a few cases for Mg, Si and Ca abundances.) Note, that the average *random* error in element abundances is of the order 0.1 dex.

Also plotted in Fig. 3.1 as circles are [el/Fe] ratios predicted by nucleosynthesis calculations of TH96. The numbers in the circles give the mass of the progenitor star in solar masses. In the picture of inhomogeneous chemical evolution, a single SN event enriches the primordial ISM locally (in our model by mixing with $5 \times 10^4\,M_\odot$ of ISM) with its nucleosynthesis products. Depending on the mass of the progenitor star, the resulting [O/Fe] and [Mg/Fe] ratios in these isolated patches of ISM cover a range of over two dex and as long as the ISM is dominated by these local inhomogeneities, newly formed stars will show the same range in their [el/Fe] ratios. In particular, this means that stars with [O/Fe] and [Mg/Fe] as small as -1.0 are inevitably produced by our model. This is in contrast to the bulk of observed metal-poor halo stars, which show [O/Fe] and [Mg/Fe] ratios in the range between 0.0 and 1.2, and is a strong indication that existing nucleosynthesis models may correctly account for IMF averaged abundances but fail to reproduce stellar yields as function of progenitor mass.

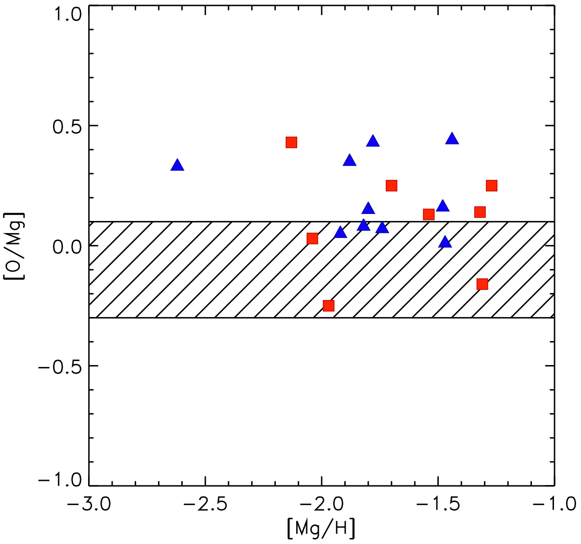

Fig. 3.2. [O/Mg] vs. [Mg/H] ratios of metal-poor halo stars. Nucleosynthesis models predict a narrow region of possible [O/Mg] ratios (hatched) which is not consistent with the scatter of observations. Symbols are as in Fig. 3.1.

3.4. Global constraints on stellar Fe yields

3.4.1. Uncertainties in O, Mg and Fe yields

Apart from the shortcomings of nucleosynthesis yields discussed in Sect. 3.3, there seems to be an additional uncertainty concerning either the stellar yields of O and Mg or the derivation of their abundances in metal-poor halo stars, as shown in Fig. 3.2:

The theoretical nucleosynthesis yields of oxygen ($Y_{\rm O}\,(m)$) and magnesium ($Y_{\rm Mg}\,(m)$) show a very similar dependence on progenitor mass m, i.e. in first order we can write $Y_{\rm Mg}\,(m) \approx 6.7 \cdot 10^{-2} \cdot Y_{\rm O}\,(m)$. Thus, for model stars [O/Mg] ≈ 0.0 on average, and due to chemical inhomogeneities in the early ISM, model stars scatter in the range $-0.3 \leq$ [O/Mg] ≤ 0.1 (hatched region in Fig. 3.2). In contrast to theoretical predictions, observations of metal-poor halo stars scatter in the range $-0.3 \leq$ [O/Mg] ≤ 0.5, with a mean of [O/Mg] ≈ 0.15. This result is very important, since it means that either even our understanding of nucleosynthesis processes during hydrostatic burning is incomplete or that oxygen abundances at very low metallicities tend to be overestimated (or magnesium abundances underestimated).

The problem hinted at in Fig. 3.2 is also connected to the recent finding that the mean [O/Fe] ratio of metal-poor halo stars seems to increase with decreasing metallicity [Fe/H], whereas the mean [Mg/Fe] ratio seems to stay constant (see e.g. Israelian et al. 1998, 2001; Boesgaard et al. 1999; King 2000; but see also Rebolo et al. 2002). This result can not be explained by changes in the surface abundances due to rotation, since rotation tends to *decrease* the oxygen abundance in the stellar atmosphere, whereas magnesium abundances remain unaffected (Heger & Langer 2000; Meynet & Maeder 2000). However, the problem described with Fig. 3.2 would disappear, if the increase in [O/Fe] with decreasing metallicity is not real but due to some hidden systematic error. Then oxygen abundances would have to be reduced, resulting in a smaller scatter and lower mean in [O/Mg].

Regarding nucleosynthesis products, a crude argument shows that (at least in the non-rotating case) we should not expect a drastic change in the progenitor mass dependence of O and Mg yields: Oxygen and magnesium are produced mainly during hydrostatic burning in the SN progenitor and only a small fraction of the ejecta stems from explosive neon- and carbon-burning (see e.g. Thielemann et al. 1990, 1996). Magnesium is to first order a product of hydrostatic carbon- and ensuing neon-burning in massive stars. The amount of freshly synthesized magnesium depends on the available fuel, i.e. the size of the C-O core after hydrostatic He burning, which also determines the amount of oxygen that gets expelled in the SN event. Thus, O and Mg yields as function of progenitor mass should be roughly proportional to each other. A very large mass loss during hydrostatic carbon burning could reduce the size of the C-O core and thus decrease the amount of synthesized magnesium for a given progenitor mass. This would result in a larger scatter of [O/Mg] ratios than indicated by the hatched region in Fig. 3.2. But the evolutionary timescale of carbon burning is very short indeed ($\approx\ 5.8 \cdot 10^3$ yr for a $25\,{\rm M}_\odot$ star, e.g. Imbriani et al. 2001), making a significant change in the structure of the C-O core unlikely.

Although the hydrostatic burning phases are thought to be well understood, one has to keep in mind that the important (effective) $^{12}{\rm C}(\alpha,\,\gamma)^{16}{\rm O}$ reaction rate is still uncertain and that the treatment of rotation and convection may also influence the amount of oxygen and magnesium produced during hydrostatic burning. Recently, Heger et al. (2000) showed that even in the case of slow rotation important changes in the internal structure of a massive star occur.

Rotationally induced mixing is important prior to central He ignition. After central He ignition, the timescales for rotationally induced mixing become too large compared to the evolutionary timescales, and the further evolution of the star is similar to the non-rotating case. Nevertheless, He cores of rotating stars are more massive, corresponding to He cores of non-rotating stars with about 25% larger initial mass. Furthermore, for a given mass of the He core, the C-O cores of rotating stars are larger than in the non-rotating case. At the end of central He burning, fresh He is mixed into the convective core, converting carbon into oxygen. Therefore, the carbon abundance in the core is decreased, whereas the oxygen abundance is increased. Unfortunately, no detailed nucleosynthesis yields including rotation have been published yet, but since the size of the He core is increased in rotating stars, at least changes in the yields of α-elements have to be expected. (For a review of the changes in the stellar parameters induced by rotation see Maeder & Meynet 2000.)

Contrary to oxygen and magnesium which originate from hydrostatic burning, iron-peak nuclei are a product of explosive silicon-burning. Unfortunately, no self-consistent models following the main-sequence evolution, collapse and explosion of a massive star exist to date which would allow to determine reliably

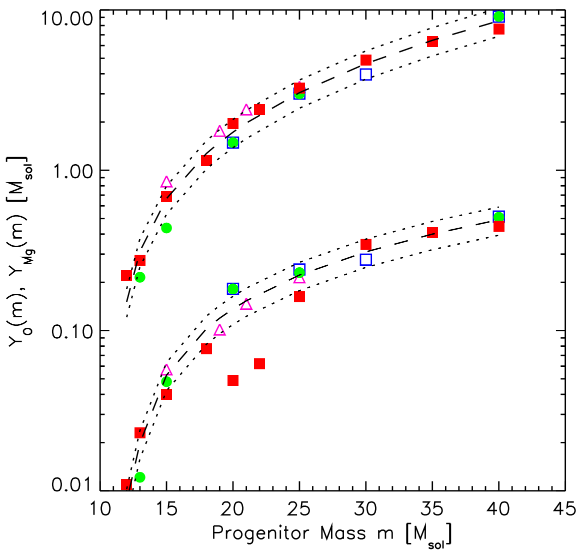

Fig. 3.3. O and Mg yields from different authors as function of progenitor mass. Models are from: WW95, filled squares; TH96, filled circles; Nakamura et al. (2001), open squares; Rauscher et al. (2002), open triangles. Upper points correspond to O yields, lower points to Mg yields. Dashed and dotted lines represent best fit curves to the different nucleosynthesis models (see text for details).

the explosion energy and the location of the mass-cut between the forming neutron star and the ejecta (Liebendörfer et al. 2001; Mezzacappa et al. 2001; Rampp & Janka 2000). Therefore, nucleosynthesis models treat the mass cut usually as one of several free parameters and the choice of its value can heavily influence the abundance of ejected iron-group nuclei. For this reason, we feel that oxygen and magnesium yields of nucleosynthesis models are more reliable than iron yields, in spite of the uncertainties discussed above.

To illustrate this point we show a comparison of O and Mg yields ($Y_{\rm O}\,(m)$, $Y_{\rm Mg}\,(m)$, Fig. 3.3) and of Fe yields ($Y_{\rm Fe}\,(m)$, Fig. 3.4) of nucleosynthesis calculations (neglecting rotation) from different authors. The models of WW95 (solar composition "C" models) are marked by filled squares, TH96 by filled circles, Nakamura et al. (2001, 10^{51} erg models) by open squares and Rauscher et al. (2002, "S" models) by open triangles. Upper points in Fig. 3.3 correspond to O yields, lower points to Mg yields. Apart from the dip visible in $Y_{\rm Mg}\,(m)$ of the WW95 models, the O and Mg yields of the different authors agree remarkably well. Chemical evolution calculations by Thomas et al. (1998) show that WW95 underestimate the average Mg yield due to this dip. The minor differences between the models can mostly be attributed to different progenitor models prior to core-collapse, the employed ^{12}C(α, γ)^{16}O reaction rate, the applied convection criterion (e.g. Schwarzschild vs. Ledoux) and artificial explosion methods after core-collapse (e.g. piston vs. artificially induced shock wave). On the other hand, as visible in Fig. 3.4, $Y_{\rm Fe}\,(m)$ of the different authors differs by more than an order of magnitude for certain progenitor masses, which is mostly due to the arbitrary placement of the "mass-cut" between proto-neutron star and ejecta. In order to reconcile the results of the inhomogeneous chemical evolution model with observed [O/Fe] and [Mg/Fe] abundance ratios, it is therefore clearly preferable to artificially adjust $Y_{\rm Fe}\,(m)$ rather than $Y_{\rm O}\,(m)$ and $Y_{\rm Mg}\,(m)$.

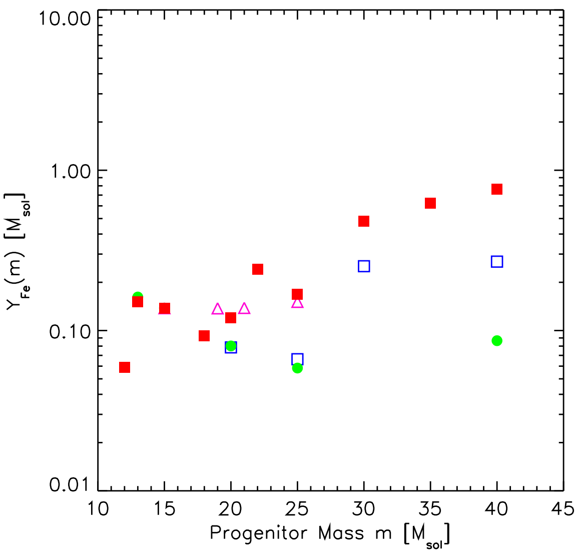

Fig. 3.4. Fe yields from different authors as function of progenitor mass. Symbols are the same as in Fig. 3.3. Contrary to O and Mg yields, different authors obtain very different Fe yields for a given progenitor mass. This is mostly due to the arbitrary placement of the mass cut.

For the following discussion, reliable O and Mg yields as function of progenitor mass with an estimate of their error range are needed. To this end, we calculated best fit curves to the $Y_{\rm O}\,(m)$ and $Y_{\rm Mg}\,(m)$ yields of the different authors, visible as dashed lines in Fig. 3.3. The low Mg yields of the 20 and 22 $M_\odot$ WW95 models were neglected for this purpose. The deviations $\Delta\epsilon\,(m)$ of the original O and Mg yields

$Y_{\mathrm{el}}\,(m)$ from our best fit yields $\overline{Y}_{\mathrm{el}}\,(m)$ is defined as

$$\Delta\epsilon\,(m) = \frac{Y_{\mathrm{el}}\,(m) - \overline{Y}_{\mathrm{el}}\,(m)}{\overline{Y}_{\mathrm{el}}\,(m)}. \tag{3.1}$$

The error $\Delta\epsilon\,(m)$ depends on progenitor mass, but is generally small. To account for the uncertainty in $Y_{\mathrm{el}}\,(m)$ introduced by the different nucleosynthesis models, we replace in the following the original $Y_{\mathrm{el}}\,(m)$ by $(1 \pm \Delta\epsilon) \cdot \overline{Y}_{\mathrm{el}}\,(m)$, where we dropped the dependence of $\Delta\epsilon\,(m)$ on m in the notation. For most progenitor masses, $\Delta\epsilon \leq 0.2$ for both O and Mg and the maximal deviation is in both cases smaller than 0.5. The dotted lines in Fig. 3.3 show the curves $(1 \pm \Delta\epsilon) \cdot \overline{Y}_{\mathrm{el}}\,(m)$ with $\Delta\epsilon = 0.2$. Since $\Delta\epsilon$ is small, the impact of the uncertainties in the stellar O and Mg yields is almost negligible for the derivation of constraints on $Y_{\mathrm{Fe}}\,(m)$. On the other hand, these small uncertainties may (almost) be able to explain the discrepancy in the scatter of [O/Mg] ratios between observations and model stars visible in Fig. 3.2. Allowing for a mean deviation of $\Delta\epsilon = 0.2$, the maximal scatter in [O/Mg] over all progenitor masses may extend to $-0.25 \leq$ [O/Mg] ≤ 0.3, which is very close to the one observed. Future nucleosynthesis calculations have to show whether this interpretation is correct or not.

For the remaining discussion, we adopt the term $(1 \pm \Delta\epsilon) \cdot \overline{Y}_{\mathrm{el}}\,(m)$ with $\Delta\epsilon = 0.2$ for the stellar oxygen and magnesium yields as a function of progenitor mass, assuming that they reproduce the true production in massive stars well enough. The values adopted for the best fit yields $\overline{Y}_{\mathrm{el}}\,(m)$ are given in Table 3.1.

Table 3.1. Best fit O and Mg yields $\overline{Y}_{\mathrm{el}}\,(m)$ proposed in Sect. 3.4.1. The first column gives the progenitor mass m and the following columns the oxygen and magnesium yields (all values in solar masses).

m	$\overline{Y}_{\mathrm{O}}\,(m)$	$\overline{Y}_{\mathrm{Mg}}\,(m)$	m	$\overline{Y}_{\mathrm{O}}\,(m)$	$\overline{Y}_{\mathrm{Mg}}\,(m)$
10	2.2e-02	1.2e-03	31	5.0e+00	3.3e-01
11	8.6e-02	4.9e-03	32	5.4e+00	3.5e-01
12	1.5e-01	8.5e-03	33	5.7e+00	3.6e-01
13	3.1e-01	2.0e-02	34	6.1e+00	3.8e-01
14	4.9e-01	3.6e-02	35	6.5e+00	4.0e-01
15	6.7e-01	5.3e-02	36	6.9e+00	4.2e-01
16	8.7e-01	6.9e-02	37	7.3e+00	4.4e-01
17	1.1e+00	8.6e-02	38	7.7e+00	4.5e-01
18	1.3e+00	1.0e-01	39	8.1e+00	4.7e-01
19	1.5e+00	1.2e-01	40	8.6e+00	4.9e-01
20	1.7e+00	1.4e-01	41	9.0e+00	5.2e-01
21	2.0e+00	1.5e-01	42	9.5e+00	5.4e-01
22	2.2e+00	1.7e-01	43	1.0e+01	5.6e-01
23	2.5e+00	1.9e-01	44	1.0e+01	5.9e-01
24	2.8e+00	2.0e-01	45	1.1e+01	6.1e-01
25	3.0e+00	2.2e-01	46	1.1e+01	6.4e-01
26	3.4e+00	2.4e-01	47	1.2e+01	6.6e-01
27	3.7e+00	2.6e-01	48	1.2e+01	6.8e-01
28	4.0e+00	2.7e-01	49	1.3e+01	7.1e-01
29	4.3e+00	2.9e-01	50	1.3e+01	7.3e-01
30	4.6e+00	3.1e-01			

3.4.2. The influence of Z and SNe from Population III stars

Apart from the uncertainties in the O and Mg yields discussed in Sect. 3.4.1, nucleosynthesis yields may also depend on the metallicity of the progenitor. Unfortunately, the question how important metallicity effects are is far from solved. Nucleosynthesis calculations in general neglect effects of mass loss due to stellar winds. WW95 present nucleosynthesis results for a grid of metallicities from metal-free to solar and predict a decrease in the ejected O and Mg mass with decreasing metallicity. However, the O yields presented lie all in the range covered by the best fit yields $(1 \pm \Delta\epsilon) \cdot \overline{Y}_{\mathrm{el}}\,(m)$ with $\Delta\epsilon = 0.2$ adopted for this paper. This is not true in the case of Mg. But since the "dip" in $Y_{\mathrm{Mg}}\,(m)$ visible in Fig. 3.3 gets more and more pronounced with lower Z and since it is known (Thomas et al., 1998), that WW95 underestimate the average production of Mg, we feel that the metallicity dependence of Mg yields is not established well enough to include this feature into our analysis.

Contrary to the results obtained by WW95, Maeder (1992) showed that stellar O yields decrease with increasing metallicity due to strong mass loss in stellar winds. (No detailed results were given in the case of magnesium.) Stars more massive than $25\mathrm{M}_{\odot}$ with solar metallicity (Z=0.02), eject large amounts of He and C in stellar winds (prior to the conversion into oxygen) which results in dramatically reduced O yields. Metal-poor stars (Z$\leq$0.001) do not undergo an extended mass-loss phase and their O yields are comparable to the ones given by WW95 and TH96. Since Z$\leq$0.001 roughly corresponds to [Fe/H] ≤ -1.5 and we are mainly concerned with metal-poor halo stars in this metallicity range, we can neglect changes in O yields due to metallicity.

Recently, Heger & Woosley (2000) published nucleosynthesis calculations of pair-instability SNe from very massive, metal-free (Population III) stars in the mass range from $140\mathrm{M}_\odot$ to $260\mathrm{M}_\odot$. For Population III stars in the mass range $25 - 140\mathrm{M}_\odot$ and stars more massive than $260\mathrm{M}_\odot$, black hole formation without ejection of nucleosynthesis yields seems likely (Heger & Woosley 2000). In order to investigate the influence of those massive metal-free stars on the enrichment of the ISM and especially their impact on the distribution of model stars in [O/Mg] vs. [Mg/H] plots (c.f. Sect. 3.4.1), we carried out several inhomogeneous chemical evolution calculations with varying SF efficiencies and IMF shapes for the Population III stars. The detailed results will not be shown here, but some basic conclusions are discussed in the following:

The theoretical scatter in [O/Mg] predicted by the massive Population III stars lies in the range $-0.3 \leq$ [O/Mg] ≤ 0.3. This could help to explain the scatter in [O/Mg] observed in metal-poor stars, if we take observational errors of the order of 0.1 dex into account. Models with a high SF efficiency for Population III stars indeed show some stars with high [O/Mg] ratios. However, 61% of the metal-poor stars ([Fe/H] ≤ -1.0) with observed O and Mg abundances show [O/Mg] ≥ 0.1 (see Fig. 3.2), whereas less than 1% of the model stars have [O/Mg] ratios in this range (the exact number depends on the shape of the IMF). Clearly, the observations of metal-poor stars can not be explained as a consequence of such massive, metal-free SNe. Furthermore, the distribution of model-stars in [O/Fe] and [Mg/Fe] can not be reconciled with observations of metal-poor stars. If the SF efficiency of Population III stars is small, these discrepancies in [O/Fe] and [Mg/Fe] disappear, but the number of model stars with [O/Mg] ≥ 0.1 decreases even further. We therefore conclude that – at least for the purpose of this paper – the (possible) influence of SNe from very massive Population III stars can safely be neglected.

3.4.3. Putting constraints on Fe yields with the help of observations

In order to reproduce the scatter of observed [O/Fe] and [Mg/Fe] ratios of metal-poor halo stars while keeping the oxygen and magnesium yields fixed, we have to adjust the stellar iron yields $Y_{\mathrm{Fe}}(m)$ as function of progenitor mass m. Since it is not known from theory what functional form $Y_{\mathrm{Fe}}(m)$ follows (increasing with m, declining or a more complex behaviour), we have the freedom to make some *ad hoc* assumptions. Nevertheless, some important constraints on $Y_{\mathrm{Fe}}(m)$ can be drawn from the scatter, range and mean of observed [O/Fe] and [Mg/Fe] abundances, as visible from Fig. 3.1:

1. IMF averaged stellar yields (integrated over a complete generation of stars) should reproduce the mean oxygen and magnesium abundances of metal-poor halo stars, i.e. [O/Fe] $\approx$ 0.4 and [Mg/Fe] ≈ 0.4.
2. Stellar yields have to reproduce the range and scatter of observed [el/Fe] ratios. Using oxygen and magnesium as reference this requires:

$$0.0 \leq [\mathrm{O/Fe}] \leq 1.2, \tag{3.2}$$
$$-0.1 \leq [\mathrm{Mg/Fe}] \leq 1.2. \tag{3.3}$$

   (Note, that the error in abundance determinations is of order 0.1 dex.)
3. There exist a few Type II and Type Ib/c SN observations (1987A, 1993J, 1994I, 1997D, 1997ef and 1998bw) where the ejected ^{56}Ni mass and the mass of the progenitor was derived by analyzing and modelling the light-curve (e.g. Suntzeff & Bouchet 1990; Shigeyama & Nomoto 1990; Shigeyama et al. 1994; Iwamoto et al. 1994, 1998, 2000; Kozma & Fransson 1998; Turatto et al. 1998; Chugai & Utrobin 2000; Sollerman et al. 2000). These observations give important constraints on $Y_{\mathrm{Fe}}(m)$ since they constrain the stellar yields for some progenitor masses, although they are not unambiguous, c.f. (c).
4. Since observations of metal-poor halo stars show no clear trends in [Mg/Fe] with decreasing [Fe/H] we require that modified iron yields likewise do not introduce any skewness in the distribution of model stars. In the case of oxygen, it is not clear yet whether the apparent slope in [O/Fe] in recent abundance studies is real or due to some systematic errors (see Fig. 3.1 and Sect. 3.4.1).

It is clear that it is not possible to predict $Y_{\mathrm{Fe}}(m)$ unambiguously, since the information drawn from observations is afflicted by errors. We therefore do not attempt to find a solution which reproduces the observations perfectly, but try to extract the *global properties* of $Y_{\mathrm{Fe}}(m)$ needed to explain the behaviour of observed [el/Fe] ratios in metal-poor halo stars.

a. IMF averaged iron yields

Since the yields of TH96 were calibrated so that the first constraint is fulfilled, we require that the average iron yield of SNe II stays constant when we change the progenitor mass dependence of $Y_{\rm Fe}\,(m)$. Assuming a Salpeter IMF ranging from $0.1\,{\rm M}_\odot$ to $50\,{\rm M}_\odot$ and assuming that all stars more massive than $10\,{\rm M}_\odot$ turn into core-collapse SNe (or hypernovae, see e.g. Nakamura et al. 2001), a SN II produces on average $\langle\overline{Y}_{\rm O}\rangle \approx 1.9\,{\rm M}_\odot$ of oxygen, $\langle\overline{Y}_{\rm Mg}\rangle \approx 0.12\,{\rm M}_\odot$ of magnesium and $\langle Y_{\rm Fe}\rangle \approx 0.095\,{\rm M}_\odot$ of iron. Leaving the average oxygen and magnesium yields unchanged and modifying the stellar iron yields, we therefore always have to require that on average $\approx 0.095\,{\rm M}_\odot$ of iron are ejected per SN. Thus, $Y_{\rm Fe}\,(m)$ has to satisfy the following condition:

$$\begin{aligned}\langle Y_{\rm Fe}\rangle &= \frac{\int_{10}^{50} Y_{\rm Fe}\,(m)\, m^{-2.35} dm}{\int_{10}^{50} m^{-2.35} dm} \\ &\approx 0.095\,{\rm M}_\odot\,.\end{aligned} \tag{3.4}$$

Note that the average [el/Fe] ratio of the model stars depends on the lower and upper mass limits of stars that turn into SNe II and their yields. If we raise the lower mass limit, the average oxygen yield of a SN will increase since many stars with a low oxygen yield no longer contribute to the enrichment of the ISM. The same is true for magnesium and iron and the combination of the new averaged yields may lead to slightly changed average [el/Fe] ratios. Since there are only a few SNe with large progenitor masses, changing the upper mass limit will have a very small influence on the average [el/Fe] ratios. For the remaining discussion, we will keep the lower and upper mass limits of SNe II fixed at $10\,{\rm M}_\odot$ and $50\,{\rm M}_\odot$, respectively.

b. Range and scatter of observations

The second constraint can be used to calculate the range that $Y_{\rm Fe}\,(m)$ has to cover. In our picture of inhomogeneous chemical evolution, we assume that the first SNe locally enrich the primordial ISM. Stars forming out of this enriched material therefore inherit the [el/Fe] ratios produced by these SNe which is determined in turn by the stellar yields $\overline{Y}_{\rm el}\,(m)$. (For the time being, we neglect the additional uncertainty hidden in the factor $(1 \pm \Delta\epsilon)$.)

Thus, for the first few generations of stars formed at the time the ISM is dominated by local chemical inhomogeneities, the following identity holds (with the exception of H and He where also the abundances in the primordial ISM have to be taken into account):

$$\begin{aligned}[{\rm el/Fe}] &= \log\frac{N_{{\rm el},\star}/N_{{\rm Fe},\star}}{N_{{\rm el},\odot}/N_{{\rm Fe},\odot}} \\ &= \log\frac{M_{{\rm el},\star}/M_{{\rm Fe},\star}}{M_{{\rm el},\odot}/M_{{\rm Fe},\odot}} \\ &= \log\frac{\overline{Y}_{\rm el}\,(m)\,/Y_{\rm Fe}\,(m)}{M_{{\rm el},\odot}/M_{{\rm Fe},\odot}},\end{aligned} \tag{3.5}$$

where $N_{{\rm el},\odot}$ $(N_{{\rm el},\star})$ is the number density of a given element *el* in the solar (stellar) atmosphere and $M_{{\rm el},\odot}$ $(M_{{\rm el},\star})$ the corresponding mass fraction. (Solar abundances were taken from Anders & Grevesse 1989). Now, let $\overline{Y}_{\rm el}\,(m)$ be either the stellar yields of oxygen or of magnesium and α, β the minimal and maximal [el/Fe] ratios derived from observations. Then the constraint gives:

$$\alpha \le [{\rm el/Fe}] \le \beta \qquad \Longleftrightarrow \tag{3.6}$$

$$\alpha \le \log\frac{\overline{Y}_{\rm el}\,(m)\,/Y_{\rm Fe}\,(m)}{M_{{\rm el},\odot}/M_{{\rm Fe},\odot}} \le \beta \qquad \Longleftrightarrow \tag{3.7}$$

$$\begin{aligned}\overline{Y}_{\rm el}\,(m)\cdot 10^{-\beta}\cdot\frac{M_{{\rm Fe},\odot}}{M_{{\rm el},\odot}} &\le Y_{\rm Fe}\,(m) \\ &\le \overline{Y}_{\rm el}\,(m)\cdot 10^{-\alpha}\cdot\frac{M_{{\rm Fe},\odot}}{M_{{\rm el},\odot}}.\end{aligned} \tag{3.8}$$

Since the yields of oxygen and magnesium as function of progenitor mass are assumed to be known, we now have two sets of inequalities for the stellar iron yields. The first is derived from the minimal and maximal [O/Fe] ratios (Eq. 3.2):

$$\begin{aligned}8.37\cdot 10^{-3}\cdot\overline{Y}_{\rm O}\,(m) &\le Y_{\rm Fe}\,(m) \\ &\le 1.33\cdot 10^{-1}\cdot\overline{Y}_{\rm O}\,(m)\,,\end{aligned} \tag{3.9}$$

and the second from the minimal and maximal [Mg/Fe] ratios (Eq. 3.3):

$$\begin{aligned}1.23\cdot 10^{-1}\cdot\overline{Y}_{\rm Mg}\,(m) &\le Y_{\rm Fe}\,(m) \\ &\le 2.46\cdot\overline{Y}_{\rm Mg}\,(m)\,,\end{aligned} \tag{3.10}$$

where the uncertainty in the O and Mg yields given by the factor $(1 \pm \Delta\epsilon)$ was neglected. Thus, for any given progenitor mass, $Y_{\rm Fe}\,(m)$ is only determined within a

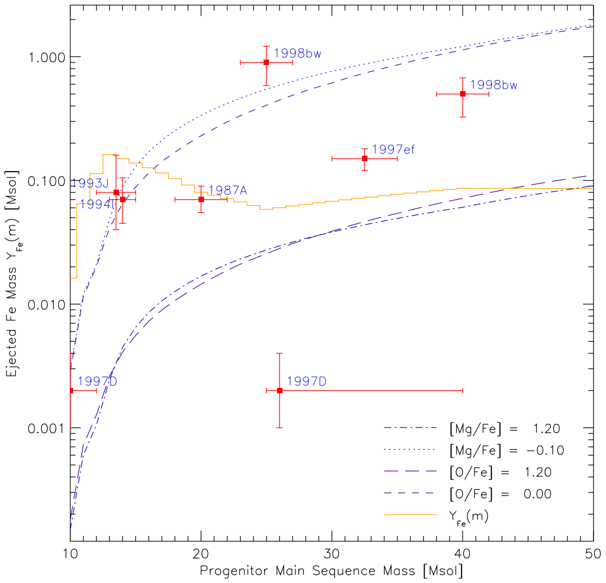

Fig. 3.5. $Y_{\mathrm{Fe}}\,(m)$ as function of progenitor mass and boundaries constraining the range stellar iron yields have to satisfy to reproduce the scatter in [O/Fe] and [Mg/Fe] of metal-poor halo stars. According to nucleosynthesis models of Thielemann et al. (1996) and Nomoto et al. (1997), SNe in the range $10 - 15\,\mathrm{M}_{\odot}$ clearly eject too much iron to be consistent with observations. Also shown are observations of core-collapse SNe with known progenitor mass and ejected ^{56}Ni mass.

factor of 20 – 25 and further constraints are needed to derive a reliable iron yield.

Fig. 3.5 shows the stellar iron yields $Y_{\mathrm{Fe}}\,(m)$ (solid line) from Thielemann et al. (1996) and Nomoto et al. (1997), binned with a bin size of 1 $\mathrm{M}_{\odot}$. To reproduce the range and scatter of [O/Fe] and [Mg/Fe] ratios observed in metal-poor halo stars, $Y_{\mathrm{Fe}}\,(m)$ should remain in the region enclosed by the boundaries given by Eqs. (3.9) and (3.10), which are shown as dashed (representing [O/Fe] $=$ 0.0), long dashed (representing [O/Fe] $= 1.2$), dotted (representing [Mg/Fe] $= -0.1$) and dash-dotted (representing [Mg/Fe] $=$ 1.2) lines. Note that the lower lines in Fig. 3.5 represent the *upper* boundaries derived from metal-poor halo stars and vice versa. Evidently, the iron yields of SNe with progenitor masses in the range $10 - 15\,\mathrm{M}_{\odot}$ are outside the boundaries given by metal-poor halo stars, leading to the stars in our model with much too low [O/Fe] and [Mg/Fe] abundances (Paper I, c.f. also Fig. 3.1). Therefore, we can already conclude that the iron yields of these SNe have to be reduced to be consistent with observations. Consequently, the iron yields of some higher-mass SNe have to be increased to keep the IMF averaged [el/Fe] ratios constant (Eq. (3.4)). This can easily be achieved by assuming a higher explosion energy than the "canonical" 10^{51} erg of standard SN models for the more massive stars ($\mathrm{M} \geq 30\,\mathrm{M}_{\odot}$), as was shown recently by Nakamura et al. (2001). The reader should note that Thielemann et al. (1996) and Nomoto et al. (1997) calculated models only for the 13, 15, 18, 20, 25, 40 and 70 $\mathrm{M}_{\odot}$ progenitors. For the 10 $\mathrm{M}_{\odot}$ progenitor we assumed an *ad hoc* iron yield of one tenth of the yield of a 13 $\mathrm{M}_{\odot}$ star and interpolated the intermediate data points. The details of the interpolation and especially the extrapolation down to the 10 $\mathrm{M}_{\odot}$ star influence the mean [el/Fe] ratio of the ISM at late stages, when it can be considered chemically homogeneous. However, this does not change the conclusion that the 13 and 15 $\mathrm{M}_{\odot}$ models of TH96 produce too much iron (if we assume the oxygen and magnesium yields to be correct), as is evident from Figs. 3.1 and 3.5.

c. ^{56}Ni *yields from observed core-collapse SNe*

There are six core-collapse SNe with known progenitor mass and ejected ^{56}Ni mass (which is the main source of ^{56}Fe in SNe II explosions, by the decay $^{56}\mathrm{Ni} \rightarrow {}^{56}\mathrm{Co} \rightarrow {}^{56}\mathrm{Fe}$), namely 1987A, 1993J, 1994I, 1997D, 1997ef and 1998bw, that are shown in Fig. 3.5. Of these, SN 1987A is the most extensively studied (see e.g. Suntzeff & Bouchet 1990; Shigeyama & Nomoto 1990; Bouchet et al. 1991a, 1991b; Suntzeff et al. 1992; Bouchet & Danziger 1993; Kozma & Fransson 1998; Fryer et al. 1999a) and the results agree remarkably well. The progenitor mass was estimated to be $20 \pm 2\,\mathrm{M}_{\odot}$, while $0.070^{+0.020}_{-0.015}\,\mathrm{M}_{\odot}$ of ^{56}Ni were ejected during the SN event.

SN 1993J had a progenitor in the mass range between 12 to 15 $\mathrm{M}_{\odot}$ and ejected approximately 0.08 $\mathrm{M}_{\odot}$ of ^{56}Ni (Shigeyama et al. 1994; Houck & Fransson 1996), which is very similar to SN 1994I with a 13 to 15 $\mathrm{M}_{\odot}$ progenitor and 0.075 $\mathrm{M}_{\odot}$ of ejected ^{56}Ni (Iwamoto et al. 1994). Although the amount of ^{56}Ni ejected by those SNe lies at the upper limit allowed under our assumptions, Fig. 3.5 shows that these values are still consistent with the constraints given by Eqs. 3.9 and 3.10.

Also consistent with our constraints is SN 1997ef with a progenitor mass of $30-35\,\mathrm{M}_{\odot}$ and a ^{56}Ni mass of $0.15 \pm 0.03\,\mathrm{M}_\odot$ (Iwamoto et al. 2000). The corresponding iron yield of SN 1997ef is higher than predicted by the nucleosynthesis models of TH96. This is exactly the behaviour needed to adjust $Y_{\mathrm{Fe}}\,(m)$ according to our constraints. SN 1997ef does not seem to be an ordinary core-collapse supernova. The model with the best fit to the lightcurve has an explosion energy which is about eight times higher than the typical 10^{51} erg of standard SN models. Such hyperenergetic Type Ib/c SNe are also termed *hypernovae* and probably indicate a change in the explosion mechanism around $25 - 30\,\mathrm{M}_\odot$ which could result in a discontinuity in the iron yields in this mass range.

In the case of SN 1997D, the situation is not clear. Turatto et al. (1998) propose two possible mass ranges for its progenitor: They favour a $26\,\mathrm{M}_\odot$ star (although the progenitor mass can vary from $25 - 40\,\mathrm{M}_\odot$) over a possible $8 - 10\,\mathrm{M}_\odot$ progenitor. A recent investigation by Chugai & Utrobin (2000) implies a progenitor mass in the range $8 - 12\,\mathrm{M}_\odot$. Both groups deduce an extremely small amount of newly synthesized ^{56}Ni of only $\approx\ 0.002\,\mathrm{M}_\odot$ and an unusual low explosion energy of only a few times 10^{50} erg. Since the situation about the progenitor mass remains unclear, both possible mass ranges are shown in Fig. 3.5. On the basis of the small amount of synthesized oxygen of only $0.02{-}0.07\,\mathrm{M}_\odot$ (Chugai & Utrobin 2000), we strongly favour the low-mass progenitor hypothesis, since according to nucleosynthesis calculations by TH96 and WW95 a high-mass progenitor would produce a large amount of oxygen ($\approx 3\,\mathrm{M}_\odot$ for a $25\,\mathrm{M}_\odot$ progenitor). Moreover, in the latter case the observed ^{56}Ni abundance lies completely outside the boundaries derived in (b), as can be seen in Fig. 3.5.

SN 1998bw seems to be another hypernova with a kinetic energy of $(2 - 5) \times 10^{52}$ erg and may be physically connected to the underluminous γ-ray burst GRB980425 (Galama et al. 1998; Iwamoto et al. 1998; Iwamoto 1999a, 1999b). The hypernova model assumes a progenitor mass of about $40\,\mathrm{M}_\odot$, ejecting $\approx 0.7\,\mathrm{M}_\odot$ of ^{56}Ni. Recently, Sollerman et al. (2000) observed SN 1998bw at late phases and made detailed models of its light curve and spectra. They propose two possible scenarios for this hypernova: one with a progenitor mass of $40\,\mathrm{M}_\odot$ and ejected nickel mass of $0.5\,\mathrm{M}_\odot$ and the other with a $25\,\mathrm{M}_\odot$ progenitor and $0.9\,\mathrm{M}_\odot$ of nickel. Note that the amount of nickel presumably synthesized by this $25\,\mathrm{M}_\odot$ SN is about 10 times larger than predicted by SN models that use the "canonical" kinetic explosion energy of 10^{51} erg. Nevertheless, it is still consistent with the constraints derived in (b) and with recent calculations of explosive nucleosynthesis in hypernovae by Nakamura et al. (2001).

d. Slopes in [el/Fe] vs. [Fe/H] distributions

Using only the constraints discussed in (a) and (b) still allows for a wide variety of possible iron yields $Y_{\mathrm{Fe}}\,(m)$. This is demonstrated by Figs. 3.6 and 3.8, where two simple *ad hoc* iron yield functions are shown. The distributions of model stars resulting from these iron yields are plotted in Figs. 3.7 and 3.9.

In Fig. 3.6 the iron yield $Y_{\mathrm{Fe}}\,(m)$ starts at the [O/Fe] $=$ 1.2 boundary, increases continuously with increasing progenitor mass and ends at the [O/Fe] $=$ 0.0 boundary. Consequently, low-mass SNe create a high [O/Fe] ratio in their surrounding primordial ISM, whereas it is close to solar in the neighbourhood of high-mass SNe. The resulting [O/Fe] distribution of model stars can be seen in Fig. 3.7. The distribution shows a clear trend from high to low [O/Fe] ratios with increasing [Fe/H]. A simple least-square fit to our data yields [O/Fe] $= -0.21 \times$ [Fe/H] $+ 0.01$. This is in surprisingly good agreement with the result of King (2000), who finds the relation [O/Fe] $= -0.18 \times [\mathrm{Fe/H}] + 0.02$ after considering the effects of NLTE corrections to oxygen abundance determinations from UV OH-lines.

The reason for the slope in our model is given by the distribution of [O/Fe] and [Fe/H] ratios induced in the metal-poor ISM by core-collapse SNe with different progenitor masses, as indicated by the position of the circles in Fig. 3.7. All the low mass SNe with progenitors up to $15\,\mathrm{M}_\odot$ induce high [O/Fe] and low [Fe/H] ratios in the neighbouring *primordial* ISM, whereas high-mass SNe produce low [O/Fe] and high [Fe/H] ratios (recall that a constant mixing mass of $5 \times 10^4\,\mathrm{M}_\odot$ per SN event is assumed, c.f. Sect. 3.2). SNe with intermediate masses induce [O/Fe] ratios that lie approximately on a straight line connecting the two extrema. The distribution of model stars of the first few stellar generations follows this line closely. As the mixing and chemical enrichment of the halo ISM proceeds, the distribution then converges to the IMF averaged [O/Fe] ratio. Although the inhomogeneous enrichment is responsible for the slope which

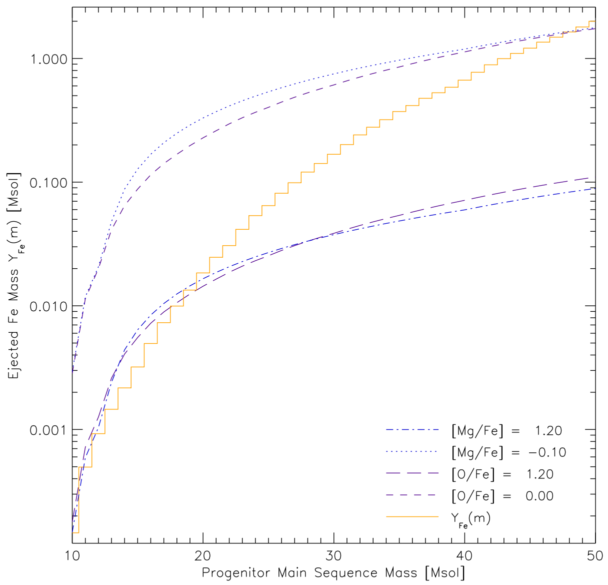

Fig. 3.6. Iron yields $Y_{\mathrm{Fe}}\,(m)$ respecting the constraints given by observations of metal-poor halo stars. $Y_{\mathrm{Fe}}\,(m)$ starts at a very low value and increases continuously. A linear increase is not possible since the mean [el/Fe] ratios have to be conserved.

is in good agreement with observations by e.g. Israelian et al. (1998), Boesgaard et al. (1999), and King (2000), it fails to reproduce the scatter seen in observed oxygen abundances. Model stars with [O/Fe] $\approx$ 1.2 exist only at [Fe/H] ≤ -3.5 and not at [Fe/H] $\approx\ -2.5$, where several are observed. Furthermore, a similar slope is introduced in the [Mg/Fe] distribution ([Mg/Fe] $= -0.26 \times$ [Fe/H] $- 0.07$), where none is seen in observations and several model stars show [Mg/Fe] ratios as large as ≈ 1.5. Therefore, this $Y_{\mathrm{Fe}}\,(m)$ has to be rejected (see however Rebolo et al. 2002 concerning [Mg/Fe]).

The situation displayed in Figs. 3.8 and 3.9 is even worse. Here, the iron yield starts at the [O/Fe] $= 0.0$ boundary, increases with progenitor mass, reaches its maximum around $30\,\mathrm{M}_{\odot}$, decreases again and ends at the [O/Fe] $= 1.2$ boundary. The resulting distribution in [O/Fe] shows a *rising* slope, which is clearly in contradiction with observations. The slope is a consequence of the fact that the iron yields $Y_{\mathrm{Fe}}\,(m)$ of SNe in the range $10 - 15\,\mathrm{M}_{\odot}$ stay very close to the boundary that represents the ratio [O/Fe] $= 0.0$. SNe in this mass range form the bulk of SN II events and it is therefore not surprising that their large number introduces such a slope in the distribution of model stars. Thus, this $Y_{\mathrm{Fe}}\,(m)$ also has to be discarded.

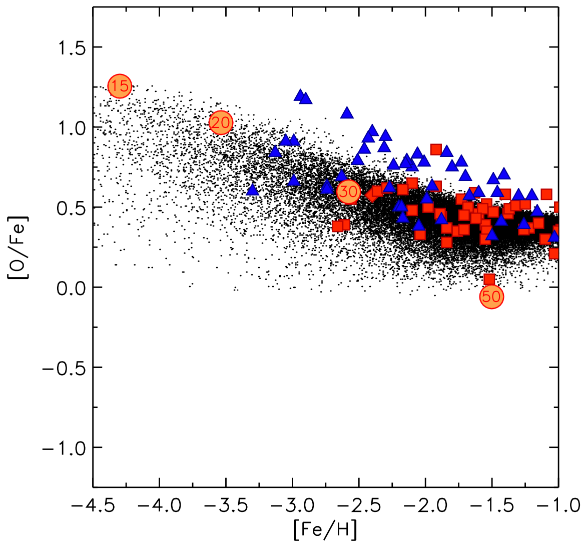

Fig. 3.7. Distribution of [O/Fe] ratios vs. metallicity [Fe/H] of model stars resulting from the iron yields shown in Fig. 3.6. The slope in the distribution of the model stars is consistent with observations of oxygen abundances. A similar slope is introduced in the [Mg/Fe] distribution which can not be reconciled with observed magnesium abundances (See text for details, symbols are as in Fig. 3.1).

These simple examples show that $Y_{\mathrm{Fe}}\,(m)$ should not run parallel to the boundaries over a large progenitor mass interval, otherwise an unrealistic slope is introduced in the [el/Fe] distribution of model stars. They demonstrate further, that the information drawn from metal-poor halo stars alone is not sufficient to derive reliable iron yields, and that information from SN II events and the shape of the [el/Fe] distribution as function of [Fe/H] (i.e. how fast the scatter decreases and whether slopes are present or not) has to be included in our analysis.

3.5. Implications for stellar Fe yields

In (d) we have shown that the iron yields of lower-mass SNe (in the range $10 - 20\,\mathrm{M}_{\odot}$) are crucial to the distribution of model stars in [el/Fe] vs. [Fe/H] plots, since progenitors in this mass range compose the bulk (approximately 69%) of SN II events. Thus, the iron yields of lower-mass SNe should not introduce a slope in the [el/Fe] distribution but should cover

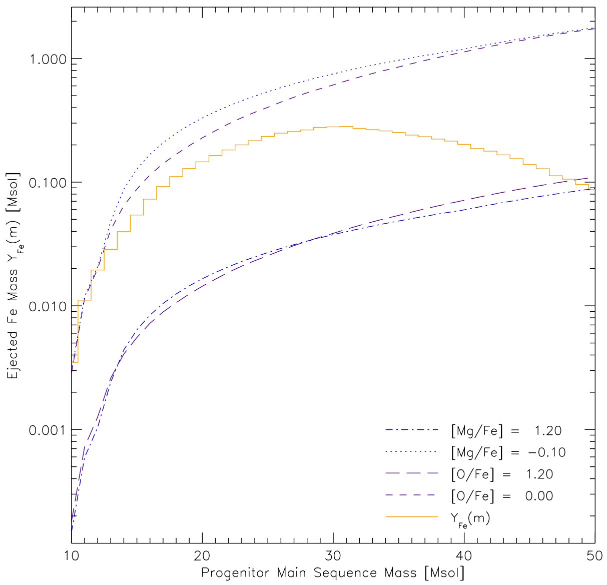

Fig. 3.8. Iron yields $Y_{\mathrm{Fe}}(m)$ respecting the constraints given by observations of metal-poor halo stars. $Y_{\mathrm{Fe}}(m)$ starts at a somewhat higher value than in Fig. 3.6, reaches a maximum at about $30\,\mathrm{M}_{\odot}$ and decreases again.

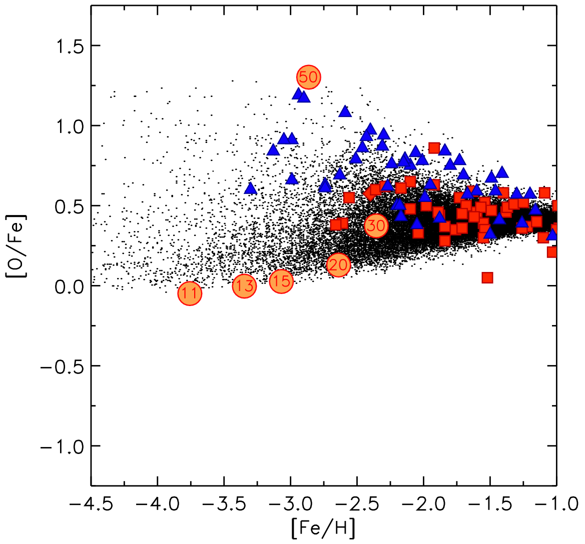

Fig. 3.9. Distribution of [O/Fe] ratios vs. metallicity [Fe/H] of model stars resulting from the iron yields shown in Fig. 3.8. Clearly, the rising slope in the distribution of model stars is not consistent with observations of metal-poor halo stars. Symbols are as in Fig. 3.1.

the entire range of observed [O/Fe] and [Mg/Fe] ratios in order to reproduce the observations. To accomplish this, $Y_{\mathrm{Fe}}(m)$ should not lie too close to the boundaries given in Eqs. (3.9) and (3.10) in this mass range but should start at the lower boundary ([O/Fe] = 1.2) and reach the upper boundary ([O/Fe] = 0.0) for some progenitor in the mass range $10 - 20\,\mathrm{M}_{\odot}$. If the observed ^{56}Ni production of SN 1993J, 1994I and 1987A are also taken into account, the observational constraints are stringent enough to fix the iron yields of the low mass SNe apart from small variations: $Y_{\mathrm{Fe}}(m)$ starts at the lower boundary, increases steeply in the range $10 - 15\,\mathrm{M}_{\odot}$ to the values given by SN 1993J and 1994I and remains almost constant in the range $15 - 20\,\mathrm{M}_{\odot}$ (to account for SN 1987A). For the remaining discussion we therefore assume the Fe yields in this range to be $\approx 1.5 \cdot 10^{-4}\,\mathrm{M}_{\odot}$ for a $10\,\mathrm{M}_{\odot}$ progenitor, $\approx 5.5 \cdot 10^{-2}\,\mathrm{M}_{\odot}$ for a $15\,\mathrm{M}_{\odot}$ progenitor and $\approx 7.0 \cdot 10^{-2}\,\mathrm{M}_{\odot}$ for a $20\,\mathrm{M}_{\odot}$ progenitor. (The detailed yields resulting from our analysis are listed in Table 3.2). We now take a look at possible iron yields of higher mass SNe corresponding to the different models of the progenitor masses of SN 1997D and 1998bw. There are four possible combinations of the progenitor masses of those two SNe.

S1: The first case (model S1, shown in Fig. 3.10) gives the best fit to abundance observations of metal-poor halo stars. Here, we preferred the lower mass progenitor models of SN1997D and SN 1998bw over the higher mass models. The curve is characterized by a peak of $0.59\,\mathrm{M}_{\odot}$ of iron at $25\,\mathrm{M}_{\odot}$ and a slow decline of the yields down to $9.5 \cdot 10^{-2}\,\mathrm{M}_{\odot}$ for the $50\,\mathrm{M}_{\odot}$ progenitor. The yields have to decline again to meet the mean abundances observed in metal-poor halo stars. Obviously, $Y_{\mathrm{Fe}}(m)$ fulfils the constraints discussed in (a), (b) and (c). Since no slope is visible in the resulting distribution of [O/Fe], [Mg/Fe], [Si/Fe] and [Ca/Fe] ratios (shown in Fig. 3.14), the constraint described in (d) is also respected. The distribution of model stars in [O/Fe], [Mg/Fe] and [Si/Fe] is in good agreement with the distribution of observed stars, whereas a few stars with too low [Ca/Fe] ratios are predicted. However, this may be due to the fact that Ca stems from explosive O and Si burning and therefore depends on the structure of the progenitor model and the (assumed) explosion energy (Paper I). Note, that the mean [Mg/Fe] and [Ca/Fe] ratios in the [el/Fe] plots are slightly shifted compared to the mean of observations. This problem also occurs when the original yields of TH96 are used (Paper I) and will persist for every $Y_{\mathrm{Fe}}(m)$ we present, since we did not change

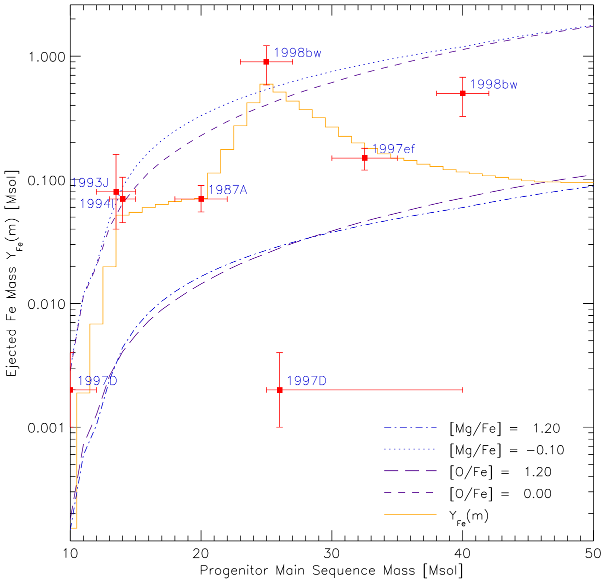

Fig. 3.10. Model S1: Iron yields $Y_{\mathrm{Fe}}\,(m)$ respecting the constraints deduced from metal-poor halo stars and SN observations. The $10\,\mathrm{M}_\odot$ model of SN 1997D and $25\,\mathrm{M}_\odot$ model of SN 1998bw are assumed to be correct.

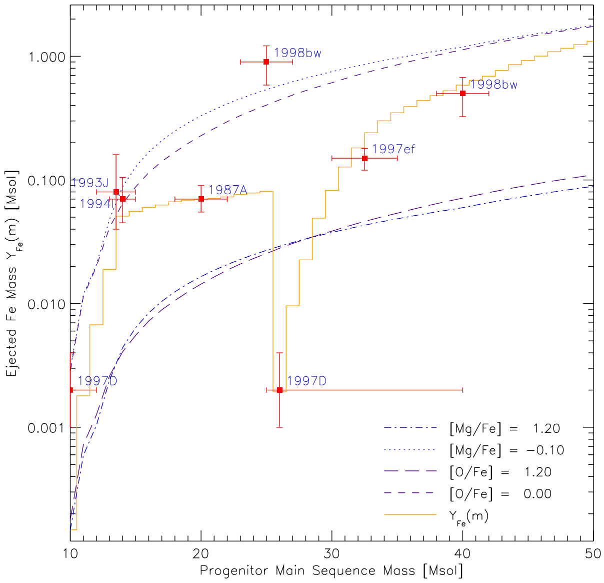

Fig. 3.11. Model H1: Iron yields $Y_{\mathrm{Fe}}\,(m)$ respecting the constraints deduced from metal-poor halo stars and SN observations. The $26\,\mathrm{M}_\odot$ model of SN 1997D and $40\,\mathrm{M}_\odot$ model of SN 1998bw are assumed to be correct.

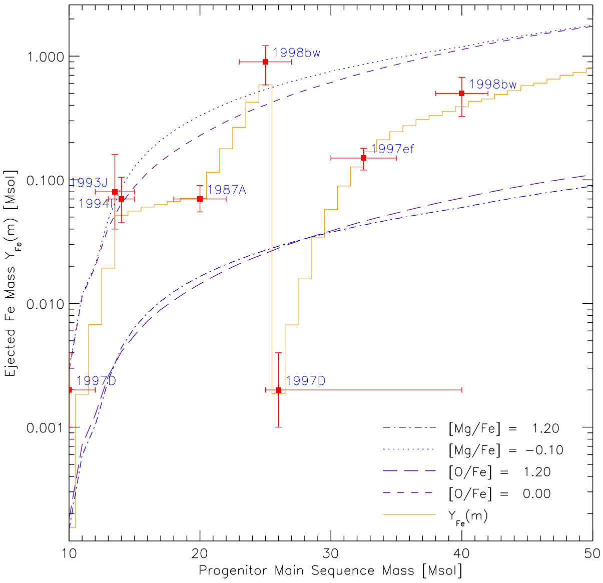

Fig. 3.12. Model H2: Iron yields $Y_{\mathrm{Fe}}\,(m)$ respecting the constraints deduced from metal-poor halo stars and SN observations. The $26\,\mathrm{M}_\odot$ model of SN 1997D and $25\,\mathrm{M}_\odot$ model of SN 1998bw are assumed to be correct.

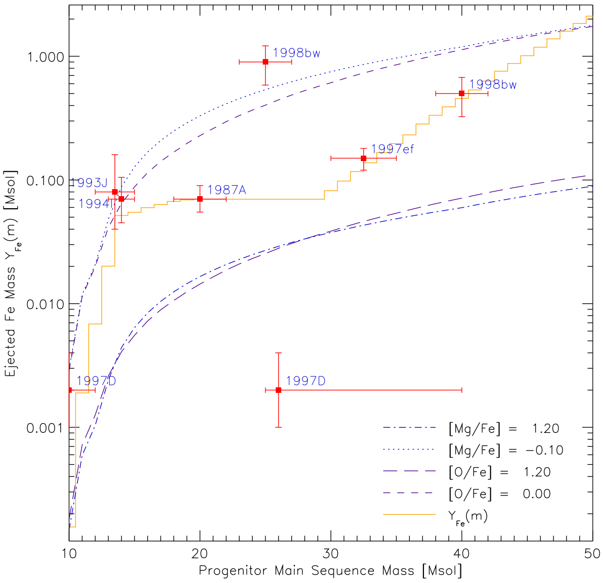

Fig. 3.13. Model S2: Iron yields $Y_{\mathrm{Fe}}\,(m)$ respecting the constraints deduced from metal-poor halo stars and SN observations. The $10\,\mathrm{M}_\odot$ model of SN 1997D and $40\,\mathrm{M}_\odot$ model of SN 1998bw are assumed to be correct.

the mean iron yield of $0.095\,\mathrm{M}_\odot$ (Eq. (3.4)). Especially noteworthy is the good agreement in [Si/Fe], since we did not include Si in the derivation of the constraints discussed above. Moreover, the hypothetical iron yields in the other models below all result in [Si/Fe] distributions that do not fit the observations as well as model S1. Therefore, we feel that model S1 gives the best fit to element abundances in metal-poor halo stars.

H1: Fig. 3.11 shows the iron yields under the assumption that the higher mass models of SN 1997D and SN 1998bw are correct (model H1). Here $Y_{\mathrm{Fe}}\,(m)$ stays almost constant up to $25\,\mathrm{M}_\odot$, followed by a sudden plunge of the yields down to $1.9 \cdot 10^{-3}\,\mathrm{M}_\odot$ to account for SN 1997D and then a continuous rise to $0.79\,\mathrm{M}_\odot$ of synthesized iron for the $50\,\mathrm{M}_\odot$ progenitor that is necessary to account for the IMF averaged yield. This sudden decrease of the iron yields could indicate a change in the explosion mechanism from supernovae with "canonical" kinetic explosion energies of 10^{51} erg to hypernovae with $10 - 100$ times higher explosion energies. However, as visible in Fig. 3.11, the very low iron yield of the $26\,\mathrm{M}_\odot$ progenitor violates the [O/Fe] $= 1.2$ and [Mg/Fe] $= 1.2$ boundaries derived from observations, so we would expect model stars with much too high [O/Fe] and [Mg/Fe] ratios. This is indeed the case, as can be seen in the corresponding [el/Fe] distribution (Fig. 3.15). A closer examination of the [el/Fe] distributions, on the other hand, reveals that these model stars are mainly present at very low metallicities ([Fe/H] ≤ -2.5). This makes it difficult to decide, whether model H1 with its dip in $Y_{\mathrm{Fe}}\,(m)$ has to be discarded or not. The situation for oxygen remains unclear since no oxygen abundances were measured at metallicities where the effect is most pronounced ([Fe/H] ≤ -3.0). However, in the range $-3.0 \leq$ [Fe/H] ≤ -1.5 there are many observations with [O/Fe] ≥ 0.6 whereas the bulk of model stars in this range shows [O/Fe] ≈ 0.4. Furthermore, many observations of Mg abundances in halo stars with [Fe/H] ≤ -3.0 exist, but only one shows a ratio of [Mg/Fe] ≥ 1.0. The remaining stars all have [Mg/Fe] ≤ 0.8, which is in contrast to the predictions of the model. Contrary to O and Mg, there are indeed several observations of metal-poor halo stars with very high [Si/Fe] and [Ca/Fe] ratios at [Fe/H] ≤ -2.5 and the fit in [Si/Fe] and [Ca/Fe] is not too bad. However, there are some observed stars with [Si/Fe] ≤ 0.0 that are not reproduced by the inhomogeneous chemical evolution model. All told, model H1 clearly does not fit the observations as well as model S1.

H2: The iron yields shown in Fig. 3.12 (model H2) are a result of the assumption that the $26\,\mathrm{M}_\odot$ model of SN 1997D together with the $25\,\mathrm{M}_\odot$ model of SN 1998bw are correct. Coincidentally, $Y_{\mathrm{Fe}}\,(m)$ is also compatible with the $10\,\mathrm{M}_\odot$ and $40\,\mathrm{M}_\odot$ models of SN 1997D and SN 1998bw due to the requirement to keep the average iron yield constant. Fig. 3.16 shows the resulting [el/Fe] distributions. Due to the low amount of ^{56}Ni ejected by the $26\,\mathrm{M}_\odot$ progenitor that is the same for models H1 and H2 (c.f. Figs. 3.11, 3.12 and Table 3.2), the problems in [O/Fe] and [Mg/Fe] described in the discussion of model H1 still persist. Compared to model H1, the fit in [Si/Fe] is now significantly improved, whereas model stars with [Ca/Fe] abundances that are too low are again generated by the inhomogeneous chemical evolution code (compare with model S1). However, although models H1 and H2 predict metal-poor halo stars with [O/Fe] and [Mg/Fe] ratios as high as ≈ 1.5, they can not be clearly discarded and the discovery of stars with metallicities [Fe/H] ≤ -2.5 and $0.8 \leq$ [Mg/Fe] ≤ 1.5 would be a strong argument for the validity of the sudden decrease in the iron yields proposed by the models H1 and H2.

S2: Finally, in Fig. 3.13 we show possible iron yields assuming that the $10\,\mathrm{M}_\odot$ model of SN 1997D and $40\,\mathrm{M}_\odot$ model of SN 1998bw are correct (model S2). Here, $Y_{\mathrm{Fe}}\,(m)$ shows a plateau in the progenitor mass range from $15\,\mathrm{M}_\odot$ to $30\,\mathrm{M}_\odot$, followed by an increasing yield with increasing progenitor mass. The resulting [el/Fe] distributions are shown in Fig. 3.17. A shallow slope in the [el/Fe] ratios is visible in every element, violating the constraint discussed in (d). Furthermore, the scatter in [O/Fe] and [Si/Fe] clearly is not fitted by the model stars. This is especially conspicuous in the case of Si: According to the model we would expect the bulk of [Si/Fe] abundances to lie in the range $0.4 \leq$ [Si/Fe] ≤ 0.8. To the contrary, most of the observed stars have [Si/Fe] ≤ 0.4. Model S2 therefore gives the worst fit to element abundance determinations in metal-poor halo stars.

A physical explanation for a sudden drop of the iron yields of SNe with progenitor masses around $25\,\mathrm{M}_\odot$ was suggested by Iwamoto et al. (2000): Observational and theoretical evidence indicate that stars with main-sequence masses $\mathrm{M}_{\mathrm{ms}} \leq 25\,\mathrm{M}_\odot$ form neutron stars with a typical iron yield of $\approx 0.07\,\mathrm{M}_\odot$, while

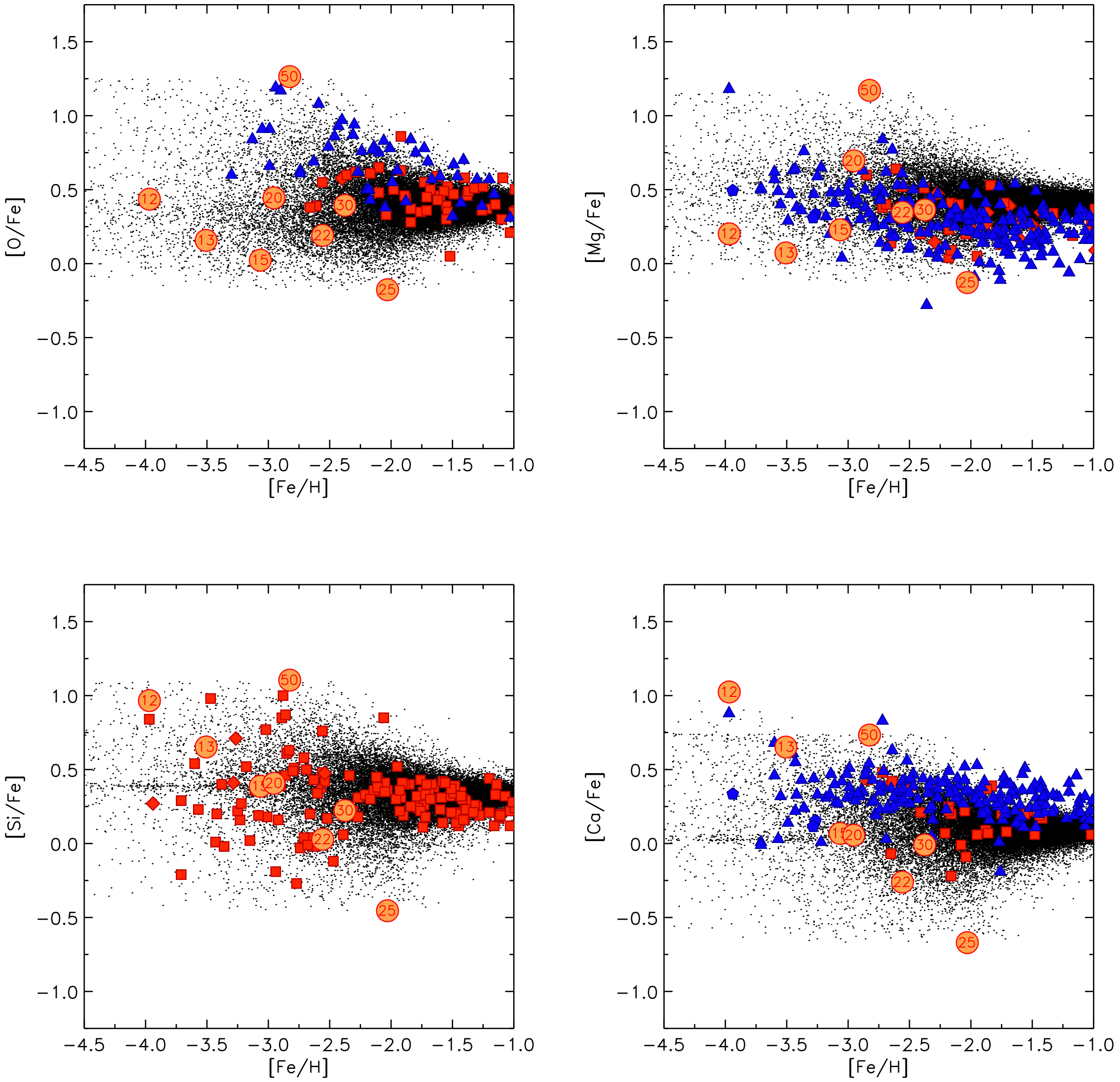

Fig. 3.14. [el/Fe] distribution of model stars for O, Mg, Si and Ca resulting from the iron yields shown in Fig. 3.10 (model S1).

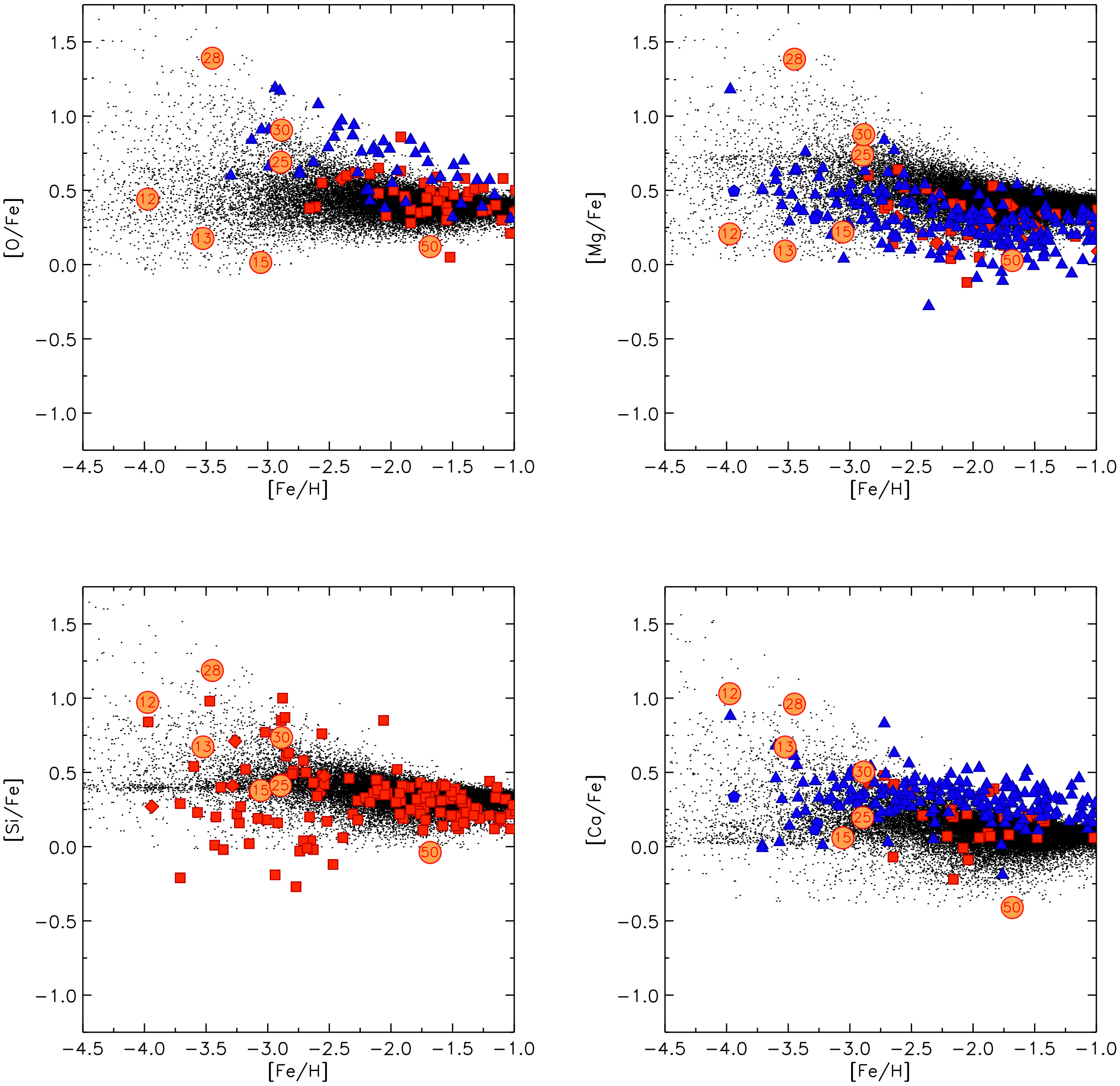

Fig. 3.15. [el/Fe] distribution of model stars for O, Mg, Si and Ca resulting from the iron yields shown in Fig. 3.11 (model H1).

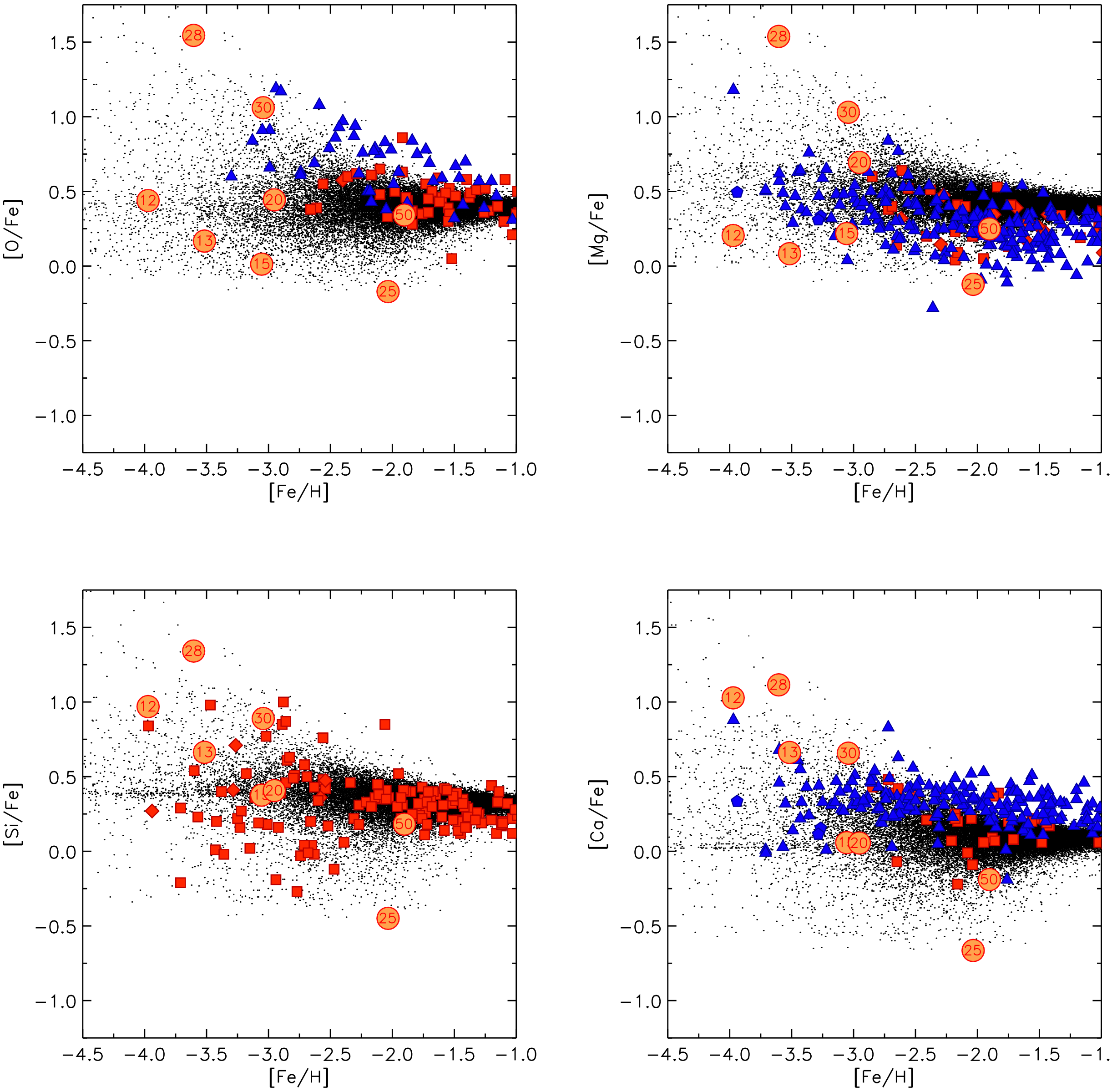

Fig. 3.16. [el/Fe] distribution of model stars for O, Mg, Si and Ca resulting from the iron yields shown in Fig. 3.12 (model H2).

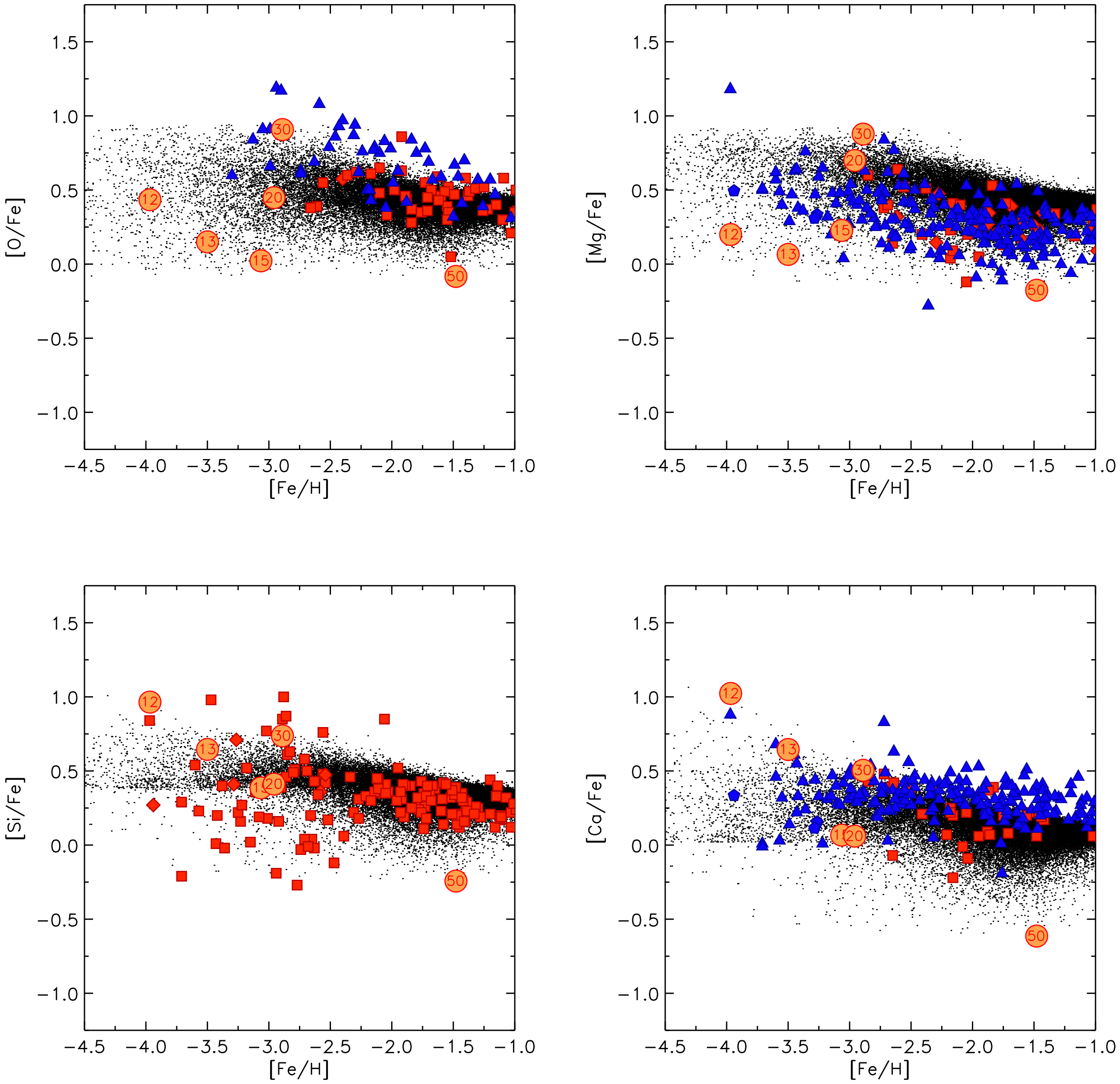

Fig. 3.17. [el/Fe] distribution of model stars for O, Mg, Si and Ca resulting from the iron yields shown in Fig. 3.13 (model S2).

progenitors more massive than this limit might form black holes and, due to the deep gravitational potential, have a very low (or no) iron yield. This might have been the case for SN 1997D. One of the two possible models reconstructing its light-curve assumes a $26\,\mathrm{M}_\odot$ progenitor and a very low kinetic energy of only a few times 10^{50} erg and an equally low ^{56}Ni yield of $\approx 0.002\,\mathrm{M}_\odot$. On the other hand, hypernovae such as 1997ef or 1998bw with progenitor masses around $30\,\mathrm{M}_\odot$ and $40\,\mathrm{M}_\odot$ and explosion energies as high as $10-100 \times 10^{51}$ erg might be energetic enough to allow for high iron yields even when a black hole forms during the SN event (see e.g. MacFadyen et al. 2001). However, one of the models of SN 1998bw proposes a $25\,\mathrm{M}_\odot$ progenitor with a kinetic energy typical for hypernovae (i.e. much larger than the explosion energy of SN 1997D). This is in some sense a contradiction to the case of SN 1997D if we assume that a black hole formed in both cases: If the explosion mechanism is the same for SN 1998bw and SN 1997D it is natural to assume that the explosion energy scales with the mass of the progenitor and it is hard to imagine a mechanism that would account for a hypernova from a $25\,\mathrm{M}_\odot$ progenitor with an explosion energy that is ≈ 100 times larger than the explosion energy from a $26\,\mathrm{M}_\odot$ progenitor.

Therefore, model H1 would fit nicely into the (qualitative) hypernova scenario proposed by Iwamoto et al. (2000), whereas models S1, S2 and H2 (yet) lack a physical explanation. On the other hand, model S1 gives a much better fit to the observations than H1, H2 and S2. Models H1 and H2 could be tested, since they predict a number of stars with very high [O/Fe], [Mg/Fe], [Si/Fe] and [Ca/Fe] ratios (up to 1.5 dex) at metallicities $[\mathrm{Fe/H}] < -2.5$. The discovery of such ultra α-element enhanced stars would be a strong argument in favour of the hypernova scenario proposed by Iwamoto et al. (2000) and the existence of a sudden drop in the iron yields of supernovae/hypernovae with progenitors around $25\,\mathrm{M}_\odot$.

Table 3.2 lists the numerical values of $Y_{\mathrm{Fe}}\,(m)$ as function of progenitor mass m for the models discussed above. Model S1 gives the best fit to the distribution of α-element abundances in metal-poor halo stars while S2 gives the worst. Although the models H1 and H2 violate the constraints discussed in (b) and thus do not give a fit as good as the one of S1, they cannot be ruled out on the basis of the observational data available to date.

Table 3.2. Iron yields $Y_{\mathrm{Fe}}\,(m)$ proposed in Sect. 3.5. The first column gives the progenitor mass m in solar masses. The following columns give the iron mass (in solar masses) synthesized in the corresponding SN event according to nucleosynthesis calculations of Thielemann et al. (1996) and Nomoto et al. (1997) – denoted by TN – and the models S1, S2, H1 and H2.

m	TN	S1	S2	H1	H2
10	1.6e-02	1.5e-04	1.6e-04	1.5e-04	1.5e-04
11	8.0e-02	1.9e-03	1.9e-03	1.8e-03	1.8e-03
12	1.3e-01	6.8e-03	6.8e-03	6.7e-03	6.8e-03
13	1.6e-01	2.0e-02	2.0e-02	1.9e-02	1.9e-02
14	1.6e-01	5.2e-02	5.2e-02	5.1e-02	5.1e-02
15	1.4e-01	5.5e-02	5.5e-02	5.6e-02	5.6e-02
16	1.2e-01	6.0e-02	6.0e-02	6.0e-02	6.0e-02
17	1.1e-01	6.3e-02	6.3e-02	6.3e-02	6.3e-02
18	1.0e-01	6.7e-02	6.7e-02	6.7e-02	6.7e-02
19	9.0e-02	7.0e-02	6.9e-02	6.9e-02	7.1e-02
20	8.0e-02	7.1e-02	7.0e-02	6.9e-02	7.1e-02
21	7.4e-02	1.1e-01	7.0e-02	7.1e-02	1.1e-01
22	7.0e-02	1.8e-01	7.0e-02	7.3e-02	1.8e-01
23	6.5e-02	2.7e-01	7.0e-02	7.6e-02	2.7e-01
24	6.1e-02	4.2e-01	7.0e-02	7.8e-02	4.2e-01
25	5.8e-02	5.9e-01	7.0e-02	8.1e-02	5.9e-01
26	5.9e-02	5.1e-01	7.0e-02	1.9e-03	1.9e-03
27	6.1e-02	4.3e-01	7.0e-02	9.6e-03	6.7e-03
28	6.3e-02	3.7e-01	7.0e-02	2.3e-02	1.6e-02
29	6.5e-02	3.2e-01	7.0e-02	4.9e-02	3.4e-02
30	6.7e-02	2.7e-01	8.2e-02	8.2e-02	5.8e-02
31	6.9e-02	2.2e-01	9.8e-02	1.3e-01	8.9e-02
32	7.1e-02	2.0e-01	1.2e-01	1.8e-01	1.3e-01
33	7.3e-02	1.8e-01	1.4e-01	2.4e-01	1.7e-01
34	7.5e-02	1.6e-01	1.7e-01	3.0e-01	2.1e-01
35	7.7e-02	1.5e-01	2.0e-01	3.5e-01	2.4e-01
36	7.9e-02	1.4e-01	2.3e-01	3.9e-01	2.7e-01
37	8.1e-02	1.3e-01	2.8e-01	4.4e-01	3.1e-01
38	8.3e-02	1.3e-01	3.3e-01	4.8e-01	3.3e-01
39	8.5e-02	1.2e-01	3.9e-01	5.3e-01	3.6e-01
40	8.6e-02	1.2e-01	4.6e-01	5.8e-01	3.9e-01
41	8.7e-02	1.1e-01	5.3e-01	6.4e-01	4.3e-01
42	8.7e-02	1.1e-01	6.3e-01	6.9e-01	4.5e-01
43	8.7e-02	1.0e-01	7.6e-01	7.7e-01	4.9e-01
44	8.7e-02	1.0e-01	8.8e-01	8.6e-01	5.3e-01
45	8.7e-02	9.8e-02	1.0e-00	9.3e-01	5.8e-01
46	8.7e-02	9.6e-02	1.2e-00	1.0e-00	6.1e-01
47	8.7e-02	9.6e-02	1.4e-00	1.1e-00	6.5e-01
48	8.7e-02	9.5e-02	1.6e-00	1.2e-00	7.0e-01
49	8.6e-02	9.5e-02	1.8e-00	1.2e-00	7.4e-01
50	8.6e-02	9.5e-02	2.1e-00	1.3e-00	7.9e-01

3.6. Conclusions

Inhomogeneous chemical evolution models in conjunction with a current set of theoretical nucleosynthesis yields predict the existence of very metal poor stars with subsolar [O/Fe] and [Mg/Fe] ratios (Argast et al. 2000). This result is a direct consequence of the progenitor mass dependence of stellar yields, since core-collapse SNe of different masses imprint their unique element abundance patterns on the surrounding ISM. No observational evidence of the existence of such stars is found, and recent investigations on the contrary indicate an increasing [O/Fe] ratio with decreasing metallicity [Fe/H]. This result of the inhomogeneous chemical evolution calculations is primarily due to the input stellar yields and not due to the details of the model itself. This is a strong indication that the progenitor mass dependence of existing nucleosynthesis models is not fully understood. This in itself is not surprising, since no self-consistent models of the core-collapse and the ensuing explosion exist to date (c.f. Liebendörfer et al. 2001; Mezzacappa et al. 2001; Rampp & Janka 2000). A crucial parameter of explosive nucleosynthesis models is the mass-cut, i.e. the dividing line between proto-neutron star and ejecta. This gives rise to a large uncertainty in the amount of iron that is expelled in the explosion of a massive star. On the other hand, oxygen and magnesium are mainly produced during hydrostatic burning and are therefore not strongly affected by the details of the explosion mechanism. However, the distribution of [O/Mg] ratios of metal-poor halo stars suggests that either uncertainties exist even for O and Mg yields, or that observations overestimate oxygen or underestimate magnesium abundances in such metal-poor stars.

The predictions of our inhomogeneous chemical evolution model can be rectified under the assumption that the stellar yields of oxygen and magnesium reflect the true production in massive stars well enough, and by replacing the stellar iron yields of Thielemann et al. (1996) and Nomoto et al. (1997) by *ad hoc* iron yields $Y_{\rm Fe}\,(m)$ as function of progenitor mass m. These are derived in this paper from observations of metal-poor halo stars and core-collapse SNe with known progenitor and ejected ^{56}Ni mass (the main source of ^{56}Fe by the decay $^{56}\mathrm{Ni} \to {}^{56}\mathrm{Co} \to {}^{56}\mathrm{Fe}$). Such *ad hoc* iron yields have to satisfy the following constraints: First, the IMF averaged stellar yields should reproduce the mean [O/Fe] and [Mg/Fe] abundances of metal-poor halo stars. Second, the range and scatter observed in [O/Fe] and [Mg/Fe] ratios of metal-poor halo stars must be reproduced. This, in conjunction with stellar oxygen and magnesium yields, leads in turn to upper and lower boundaries for $Y_{\rm Fe}\,(m)$. Third, no slope should be introduced by $Y_{\rm Fe}\,(m)$ in the [el/Fe] distribution of model stars that is not compatible with observations. And finally, the progenitor mass dependence of the iron yields should be consistent with the ejected ^{56}Ni mass of observed core-collapse SNe with known main-sequence mass. Here, the situation is complicated by SN 1997D and SN 1998bw. The models recovering their light-curves give in each case two significantly different progenitor masses. These constraints severely curtail the possible iron yield distributions but are not stringent enough to determine $Y_{\rm Fe}\,(m)$ unambiguously.

The main results of this paper are summarized in the following points:

1. Observations of O and Mg abundances in metal-poor halo stars and of the ejected ^{56}Ni mass in core-collapse SNe, in conjunction with oxygen and magnesium yields from nucleosynthesis calculations and inhomogeneous chemical evolution models, provide a valuable tool to constrain the amount of iron ejected in a SN event as function of the main-sequence mass of its progenitor.
2. The [el/Fe] distribution of model stars as function of metallicity [Fe/H] is sensitive to the iron yields of SNe with progenitors in the mass range $10 - 20\,\mathrm{M}_\odot$. A steep increase of $Y_{\rm Fe}\,(m)$ from $\approx 1.5 \cdot 10^{-4}\,\mathrm{M}_\odot$ for a $10\,\mathrm{M}_\odot$ progenitor to $\approx 5.5 \cdot 10^{-2}\,\mathrm{M}_\odot$ for a $15\,\mathrm{M}_\odot$ progenitor followed by a slow increase to $\approx 7.0 \cdot 10^{-2}\,\mathrm{M}_\odot$ for a $20\,\mathrm{M}_\odot$ progenitor is required to give an acceptable fit to the observations of metal-poor halo stars.
3. The further trend of $Y_{\rm Fe}\,(m)$ in the mass range $20 - 50\,\mathrm{M}_\odot$ cannot be unambiguously determined by the available data. For this mass range we have deduced four possible iron yield distributions (models S1, S2, H1 and H2) that explore the available freedom. These correspond to the four different combinations of probable progenitor masses of SN 1997D and SN 1998bw. Iron yield distributions that differ significantly form the presented models can be excluded.
4. Model S1 gives the best fit to observations while models H1 and H2 can not be ruled out. Model S2 gives the worst fit to observed [el/Fe] ratios in

metal-poor halo stars. A change in the explosion mechanism of SNe II around $25\,\mathrm{M}_\odot$ is expected in the case of the "H" models. A test to distinguish between models S1 and H1/H2 would be the discovery of very metal-poor stars ([Fe/H] ≤ -2.5) that are highly enriched in α-elements.

5. Iron yield distributions derived from observations through inhomogeneous chemical evolution models yield constraints on the mass-cut in a SN II event if the detailed structure of the progenitor model is known (i.e. the size of the iron core and the zone that undergoes explosive Si burning). Thus, they can be used as benchmarks for future core-collapse supernova/hypernova models.

In the future, a large and above all homogeneously analyzed sample of O, Mg and Fe abundances in very metal-poor stars is needed to derive more stringent constraints on $Y_{\mathrm{Fe}}\,(m)$. Not only would this allow us to determine the exact extent of the scatter in [O/Fe] and [Mg/Fe] ratios, but would also answer the important question whether the scatter in [O/Mg] is real or due to some (yet) unknown systematic errors in O and Mg abundance determinations. If the scatter in [O/Mg] turns out to be real, updated nucleosynthesis calculations including rotation and mass loss due to stellar winds are needed to understand O and Mg abundances in metal-poor halo stars.

Also very valuable would be the observation and analysis of further core-collapse supernovae or hypernovae. Only six core-collapse SNe with known progenitor and ejected $^{56}\mathrm{Ni}$ mass are known to date, and for two of them their progenitor masses are not clearly determined. Especially the discovery of a SN II with a progenitor in the critical mass range from $20-30\,\mathrm{M}_\odot$ could provide us with the information needed to discern between the four models presented above, or at least whether the "S" or "H" models have to be preferred. This would also be a step towards answering the question whether a change in the explosion mechanism of core-collapse SNe occurs, i.e. the formation of a black hole and significant increase of the explosion energy for $m \geq 25\,\mathrm{M}_\odot$.

Acknowledgements. We thank the referee R. Henry for his valuable suggestions that helped to improve this paper significantly. D. Argast also thanks A. Immeli for frequent and interesting discussions. This work was supported by the Swiss Nationalfonds.

4

Neutron star mergers, core-collapse supernovae and neutron capture elements in the early Galaxy

Abstract. The astrophysical nature of r-process sites is a long standing mystery and many probable sources were suggested in the past, among them lower-mass core-collapse supernovae (in the range $8 - 10\,\mathrm{M}_{\odot}$), higher-mass core-collapse supernovae (with masses $\geq 20\,\mathrm{M}_{\odot}$) and neutron star mergers. In this work, we present a detailed inhomogeneous chemical evolution study that considers for the first time neutron star mergers as major r-process sources, and compare this scenario to the ones in which core-collapse supernovae act as dominant r-process sites. Furthermore, the enrichment of the interstellar medium with neutron-capture elements during Galaxy formation by r- and s-process sources is investigated.

We conclude that, due to the lack of reliable iron and r-process yields as function of progenitor mass, it is not possible to date to distinguish between the lower-mass and higher-mass supernovae scenario within the framework of inhomogeneous chemical evolution. However, neutron-star mergers seem to be ruled out as *dominant* r-process source, since their low coalescence rates are not consistent with observations of r-process elements at very low metallicities. Additionally, the considerable injection of r-process material by a single neutron-star merger leads to a scatter in [r-process/Fe] ratios at later times which is much too large compared to observations. Finally, a low star-formation efficiency is required during halo formation to be consistent with the appearance of s-process elements at very low metallicities.

4.1. Introduction

Since the ground-breaking article by Burbidge, Burbidge, Fowler & Hoyle ($\mathrm{B}^2\mathrm{FH}$, 1957), the production mechanism of heavy elements beyond the iron-peak by slow (s-process) and rapid (r-process) neutron capture on seed nuclei is well known. The basic ideas presented in $\mathrm{B}^2\mathrm{FH}$ are still valid, though some details have changed in the light of new observations and improved measurements. However, although the physical requirements for the occurrence of s- and r-process nucleosynthesis are well understood, the astrophysical nature of r-process sites is still unknown.

A wealth of possible r-process sites was put forth in the past, many of them linked to the violent death of massive stars in supernova events. Hillebrandt et al. (1984) and Wheeler et al. (1998) argue that, during the prompt explosion of a massive star in the range $8-10\,\mathrm{M}_{\odot}$, physical conditions in the innermost mass layers are sufficiently extreme for the r-process to work and that the amount of r-process matter ejected is consistent with observed Galactic r-process abundances. This has been recently confirmed by detailed r-process calculations in the prompt explosions of a $11\,\mathrm{M}_{\odot}$ progenitor (Sumiyoshi et al. 2001). Although it has not yet been established that *prompt* explosions of massive stars may occur in reality, low-mass progenitors are the only ones that show any hope to do so (Wheeler et al. 1998; Sumiyoshi et al. 2001; but see also Liebendörfer et al. 2001).

On the other hand, neutrino-driven winds from nascent neutron-stars present also a promising site for r-process nucleosynthesis (e.g. Woosley & Hoffman 1992; Woosley et al. 1994; Qian & Woosley 1996; Thompson et al. 2001; Wanajo et al. 2001). Following the *delayed* explosion of a massive star ($\gtrsim 20\,\mathrm{M}_{\odot}$), neutrinos diffusing out of the contracting proto-neutron star heat and ablate material from its surface and a neutrino-driven wind develops. Such winds exhibit sufficiently high entropies and/or sufficiently short dynamical timescales, leading to a neutron-to-seed ratio that favour r-process nucleosynthesis. The r-process yields obtained in this scenario also seem to be consistent with observed r-process abundances in stars.

It should be noted, however, that both scenarios are affected by considerable theoretical uncertainties since the physics of core-collapse SNe is not really understood (e.g. Liebendörfer et al. 2001). Furthermore, it seems questionable whether the high entropies required to reproduce the solar system r-process signature can be provided by Type II supernovae (Meyer & Brown 1997; Freiburghaus et al. 1999a).

Recently, Freiburghaus et al. (1999b) presented for the first time r-process nucleosynthesis yields in neutron star mergers (NSM). Coalescing neutron stars provide in a natural way the large neutron fluxes required for the build-up of heavy elements due to rapid neutron capture. This scenario was subsequently explored and refined by Rosswog et al. (1999; 2000). Their calculations show that a few times 10^{-3} – $10^{-2}\,\mathrm{M}_{\odot}$ of r-process matter are ejected in a merger event. This number is significantly higher than the typical $10^{-5}\,\mathrm{M}_{\odot}$ of r-process material thought to be ejected in core-collapse SN events (Woosley et al. 1994; Wanajo et al. 2001). On the other hand, the NSM rate in the Galaxy is significantly lower than the occurrence of Type II SNe (Tamman et al. 1994; Belczynski et al. 2002), so that each of the sources discussed above is able to account for the total amount of r-process matter in the Galaxy (Qian & Woosley 1996; Rosswog et al. 1999).

However, Qian (2000) argues that NSM fail to be a major r-process source, since the low coalescence rate of binary compact objects would prevent any correlation between abundances of r-process elements and iron, which is clearly in disagreement with observed r-process abundances in stars more metal-rich than [Fe/H] $\gtrsim -2.5$. This argument deserves closer examination, especially since no detailed chemical evolution calculations exist to date that assume NSM to be the major r-process source. Chemical evolution studies, that treat SN with either low-mass ($8 - 10\,\mathrm{M}_\odot$) or high-mass ($\geq 20\,\mathrm{M}_\odot$) progenitors as major r-process source, were carried out by Ishimaru & Wanajo (1999), Travaglio et al. (1999) and Tsujimoto et al. (2000). Unfortunately, the authors do not agree on the astrophysical nature of the r-process site: They conclude that either lower-mass SNe (Travaglio et al. 1999), higher-mass SNe (Tsujimoto et al. 2000), or both (Ishimaru & Wanajo 1999) are acceptable from the viewpoint of chemical evolution.

Another major contribution to the enrichment of the interstellar medium (ISM) with neutron capture elements comes from s-process nucleosynthesis. The main s-process occurs during the thermally pulsing asymptotic giant branch (TP-AGB) phase of lower mass stars in the range $1 - 4\,\mathrm{M}_\odot$ (Lambert et al. 1995; Gallino et al. 1998; Busso et al. 1999; Arlandini et al. 1999). By comparing abundances of neutron capture elements produced primarily by the main s-process (such as Ba) to elements synthesized by the r-process (such as Eu), the star formation history during halo formation can be constrained, since these elements sample processes occurring on very different timescales.

The purpose of this work is threefold: First, neutron star mergers as major r-process site are included for the first time in detailed chemical evolution calculations. Second, we compare the enrichment of the ISM with r-process elements under the assumption that neutron star mergers, lower-mass SNe II or higher-mass SNe II are the dominant r-process sites. Third, constraints on the star-formation history during halo formation are gained with the help of r- and s-process abundances in metal-poor stars.

This work is organized as follows: In Sects. 4.2 and 4.3 the inhomogeneous chemical evolution model is presented and some basic results of our standard model are discussed. Constraints on the SFR in the early Galaxy are gained from the enrichment of the ISM with r- and s-process elements in Sect. 4.4. Finally, the impact of SN II and NSM as r-process sites on Galactic chemical evolution and conclusions are presented in Sects. 4.5 and 4.6, respectively.

4.2. The chemical evolution model

The large scatter seen in element abundances of metal-poor halo stars is generally attributed to local chemical inhomogeneities of the interstellar medium (ISM) during the earliest stages of Galaxy formation and enrichment (e.g. McWilliam et al. 1995a, 1995b; Ryan et al. 1996; Burris et al. 2000; Mishenina & Kovtyukh 2001). Several authors developed chemical evolution models (Ishimaru & Wanajo 1999; Raiteri et al. 1999; Tsujimoto, Shigeyama & Yoshii 1999, 2000; Argast et al. 2000; Travaglio et al. 2001) that investigate the impact of local chemical inhomogeneities on the enrichment of the ISM and the scatter in element abundances. Although the methods employed by these authors differ significantly, the model results are in qualitative agreement. The notion of inhomogeneous chemical evolution therefore seems to be well established.

In the present work we use the stochastic chemical evolution model presented in Argast et al. (2000, hereafter Paper I) to investigate the enrichment of the ISM with r- and s-process elements, namely Europium and Barium. The model was described in detail in Paper I and again in Argast et al. (2002, hereafter Paper II). In the following, we give a short summary of the model and discuss some major changes (mass infall, star formation rate and SN Ia events) that were implemented for this work.

4.2.1. Basic ingredients

We model the chemical enrichment of the halo ISM within a cube $(2.0\ \mathrm{kpc})^3$, down to a resolution of 50 pc. Primordial matter is assumed to be falling into this volume, following an infall law of the form

$$\dot{M}\,(t) = a \cdot t^b \cdot \exp(-t/\tau). \tag{4.1}$$

Instead of specifying parameters a and b directly, we use the fact that with this description the time of maximal infall, t_{max}, is given by

$$t_{max} = b \cdot \tau, \tag{4.2}$$

and that the total mass, M_{tot}, falling into the volume is

$$M_{tot} = \int_0^{t_{end}} a \cdot t^b \cdot \exp(-t/\tau)\, dt, \tag{4.3}$$

where t_{end} is the age of the system. The infall law is therefore fully described by the parameter set $\{M_{tot}, \tau, t_{max}, t_{end}\}$.

A crucial ingredient of chemical evolution models is the treatment of star formation (SF). Unfortunately, it is also one of the least understood. In this work we adopt a simple SF description based on Schmidt's law (Schmidt 1959). The number $n\,(t)$ of stars that are formed per time-step (of duration 10^6 yr) is determined by the product

$$n\,(t) = \frac{\nu}{N_{tot}} \cdot \sum_{i=1}^{N_{tot}} \rho_i^\alpha\,(t)\,, \tag{4.4}$$

where $\rho_i\,(t)$ is the local ISM density at time t in a cell of volume (50 pc)^3 and the sum goes over all cells in the volume (N_{tot}). The parameter ν determines the star formation efficiency, whereas possible values for α range from 1 (SF proportional to gas density) to 2 (SF triggered by cloud-cloud collisions, Larson 1991). The factor N_{tot}^{-1} was introduced to keep the number of newly formed stars independent of the model resolution, so that Eq. 4.4 evaluates to $n\,(t) = \nu\,\langle\rho\,(t)\rangle^\alpha$ if the ISM is homogeneously distributed ($\rho_i\,(t) = \langle\rho\,(t)\rangle$ for all i).

The masses of newly formed stars are chosen randomly, with the condition that the mass distribution of all stars follows a Salpeter initial mass function ($dN/dm \propto m^{-2.35}$) with lower and upper mass limits of $m_{lo} = 0.1\,\mathrm{M}_\odot$ and $m_{up} = 50\,\mathrm{M}_\odot$, respectively. Thus, the average mass $\langle m\rangle$ of a star, integrated over the initial mass function (IMF), is given by

$$\langle m\rangle = \frac{\int_{m_{lo}}^{m_{up}} m \cdot dN}{\int_{m_{lo}}^{m_{up}} dN}. \tag{4.5}$$

The number $n\,(t)$ of star formation events translates into an average star formation rate (SFR) at each time-step by multiplication with the average stellar mass $\langle m\rangle$, i.e.

$$\begin{aligned}\langle SFR\,(t)\rangle &= n\,(t) \cdot \langle m\rangle \\ &= \frac{\nu}{N_{tot}} \cdot \sum_{i=1}^{N_{tot}} \rho_i^\alpha\,(t) \cdot \frac{\int_{m_{lo}}^{m_{up}} m \cdot dN}{\int_{m_{lo}}^{m_{up}} dN}.\end{aligned} \tag{4.6}$$

Due to the stochastic nature of our SF law, small deviations from the average SFR have to be expected at each time-step.

The cells that undergo star formation are also chosen randomly, though the probability for a cell to get selected scales with its density. In this description, patches of denser material, e.g. in the neighbourhood of a supernova remnant, are predominantly chosen for star formation events. Note that a cell is only allowed to form stars, if it contains at least $50\,\mathrm{M}_\odot$ of gas. This restriction has to be imposed, so that the IMF is not biased towards low mass stars, i.e. if a cell forms a star, then it can be of any mass in the range $0.1 - 50\,\mathrm{M}_\odot$. Consequently no SF will occur until enough material has fallen into the volume to exceed this limit. Newly born stars inherit the abundance pattern of the ISM out of which they formed, carrying therefore information about the chemical composition of the ISM at the place and time of their birth.

Low mass stars ($\lesssim 1\,\mathrm{M}_\odot$) do not evolve significantly during the considered time but serve to lock up part of the total mass, affecting therefore the abundances of elements with respect to hydrogen. Stars of intermediate mass ($\sim 1 - 10\,\mathrm{M}_\odot$) return most of their mass after their stellar lifetime, leaving a white dwarf as stellar remnant. Stars in the mass range from $10 - 50\,\mathrm{M}_\odot$ are assumed to explode as SNe II, polluting the neighbouring ISM with their highly enriched ejecta. Stellar lifetimes are taken from the *Geneva Stellar Evolution and Nucleosynthesis Group* (cf. Schaller et al. 1992; Schaerer et al. 1993a; Schaerer et al. 1993b; Charbonnel et al. 1993). Stellar yields for O, Mg, Si, Ca and Fe are taken from Thielemann et al. (1996) and Nomoto et al. (1997) and are scaled according to Samland (1998) to account for the global chemical enrichment of the Galaxy.

SN events pollute the neighbouring ISM with their nucleosynthesis products and sweep up the material in

Table 4.1. Parameter values of the standard model.

Parameter	Description	Value
V	volume	$8\ \mathrm{kpc}^3$
M_{tot}	total system mass	$10^8\ \mathrm{M}_\odot$
τ	infall decline timescale	$5 \cdot 10^9$ yr
t_{max}	time of maximal infall	$2 \cdot 10^9$ yr
t_{end}	age of the system	$14.0 \cdot 10^9$ yr
ν	SF efficiency	15
α	exponent of SF law	1.5
M_{lo}	lower IMF mass limit	$0.1\,\mathrm{M}_\odot$
M_{up}	upper IMF mass limit	$50\,\mathrm{M}_\odot$
P_{SNIa}	SN Ia probability	$6 \cdot 10^{-3}$

a spherical, chemically well mixed shell. Here, it is assumed that each SN pollutes $\approx 5 \times 10^4\ \mathrm{M}_\odot$ of ISM (Ryan et al. 1996; Shigeyama & Tsujimoto 1998). Stars which form out of material enriched by a single SN II inherit its abundance ratios and therefore show an element abundance pattern which is characteristic for this particular progenitor mass. This will lead to a large scatter in element abundances ([el/Fe]), as long as local inhomogeneities caused by SN II events dominate the halo ISM. As time progresses, supernova remnants overlap and the abundance pattern in each cell approaches the IMF average, leading to a decrease in the element abundance scatter at later times.

To determine which intermediate mass stars form Type Ia SN events, we adopt the following simple procedure: With probability P_{SNIa} a newly formed intermediate mass star has a companion in the same mass range and one of these two stars will end its life as SN Ia. The mass of its companion (again in the range $1 - 10\,\mathrm{M}_\odot$ and following a Salpeter IMF) is determined randomly and the SN Ia event occurs after the less massive of the two stars enters the red giant stage. Although this procedure admittedly is rather simple, it has the advantage that the SN Ia frequency is determined by only one free parameter, namely the probability P_{SNIa}. This parameter is chosen in such a way that the slope observed in [α/Fe] abundances at [Fe/H] $\gtrsim -1$ is reproduced. We chose $10\,\mathrm{M}_\odot$ as upper mass limit for SN Ia progenitors to be consistent with the lower mass limit of SN II. Since we use such a simplified description to determine the occurrence of SN Ia, the upper mass limit of SN Ia progenitors is not very relevant: Assuming a Salpeter IMF, more than 99% of the binary systems will consist of stars with masses $\leq 8\,\mathrm{M}_\odot$ each. Finally, the yields of Type Ia SNe are taken from Iwamoto et al. (1999, Model CDD2).

In Table 4.1 we list the parameter values adopted for our standard model.

4.2.2. Treatment of r- and s-process sources in the model

In the following, r-process yields of Eu and Ba are estimated under the assumption of a robust r-process for nuclei more massive than Ba. Matter ejected in an r-process event (independent of its source) is considered to consist of pure r-process nuclei more massive than Ba. First, the mass fractions of Ba and Eu are calculated with the help of Table 5 in Burris et al. (2000) and the standard solar system element abundances of Anders & Grevesse (1989):

$$f_{\mathrm{Ba}} = \frac{N^r_{\mathrm{Ba}} \cdot < m_{\mathrm{Ba}} >}{\sum_i N^r_i \cdot < m_i >} \approx 7.7 \cdot 10^{-2} \tag{4.7}$$

$$f_{\mathrm{Eu}} = \frac{N^r_{\mathrm{Eu}} \cdot < m_{\mathrm{Eu}} >}{\sum_i N^r_i \cdot < m_i >} \approx 1.2 \cdot 10^{-2}, \tag{4.8}$$

where N^r_i is the number fraction of r-process nuclei of a nuclear species i, $< m_i >$ its mean atomic weight and the sum goes over all elements beyond Ba ($Z \geq 56$). Final yields are estimated by multiplying these mass fractions with the mass M_r ejected in an r-process event, i.e.

$$Y_{\mathrm{Ba}} \approx 7.7 \cdot 10^{-2} \cdot M_r \tag{4.9}$$

$$Y_{\mathrm{Eu}} \approx 1.2 \cdot 10^{-2} \cdot M_r. \tag{4.10}$$

The total ejected r-process matter, M_r, is either deduced from observational evidence and/or theoretical considerations or is treated as a free parameter that is adjusted so that the results of the chemical evolution model are consistent with observations.

We now shortly discuss the implementation of s-process nucleosynthesis in $1.5 - 4\,\mathrm{M}_\odot$ stars and the three suspected r-process sites, mentioned in the introduction, in our model. We did not consider a hybrid model, where different r-process sites contribute to the enrichment of the ISM with neutron capture elements. Instead, it is assumed that for each of the three cases the corresponding r-process site is responsible for the whole neutron capture element inventory (with $Z \geq 56$) of the Galaxy, i.e. is the mayor source of r-process elements beyond Ba.

a. s-process yields from stars of mass $1.5 - 4\,\mathrm{M}_\odot$

The main s-process in TP-AGB stars is strongly metallicity dependent, since seed nuclei (such as iron) have to be available to capture the free neutrons (i.e. s-process elements are *secondary*). Recent calculations suggest, that the major contribution to Ba by the main s-process occurs only in low mass stars, e.g. in the mass range $1.5 - 3\,\mathrm{M}_\odot$ (Lambert et al. 1995; Gallino et al. 1998; Busso et al. 1999; Arlandini et al. 1999) or $2 - 4\,\mathrm{M}_\odot$ (Travaglio et al. 1999). We note however the detection of lead in the very metal-poor halo star LP 625-44 by Aoki et al. (2000): The observed lead abundance in LP 625-44 is two orders of magnitudes lower than predicted by models of s-process nucleosynthesis. This suggests that the assumptions underlying present models of s-process nucleosynthesis in very metal-poor stars have to be critically reviewed or that alternative s-process sites in the early Galaxy have to be considered (Aoki et al. 2000).

Raiteri et al. (1999) presented metallicity dependent s-process Ba yields, based on calculations of Gallino et al. (1998) and Busso et al. (1999). For simplicity, we did not (yet) implement the dependence of Ba yields on metallicity, but instead calculated an average Ba yield based on Raiteri et al. (1999) and Travaglio et al. (1999): Stars of $1.5\,\mathrm{M}_\odot$ yield $10^{-7}\,\mathrm{M}_\odot$ of Ba from the s-process, whereas the Ba yield of $3\,\mathrm{M}_\odot$ stars is twice as much and the Ba yield of $4\,\mathrm{M}_\odot$ stars is set to $10^{-8}\,\mathrm{M}_\odot$. For stars between 1.5 and $4\,\mathrm{M}_\odot$, the yields are interpolated linearly.

b. r-process yields from core-collapse SNe in the mass range $8 - 10\,\mathrm{M}_\odot$

Lower mass core-collapse SNe ($8 - 10\,\mathrm{M}_\odot$) are suspected to be major r-process sources without contributing much iron-peak elements to the enrichment of the ISM (Hillebrandt et al. 1984; Wheeler et al. 1998). Recently, Sumiyoshi et al. (2001) presented results of r-process nucleosynthesis occurring during the *prompt* explosion of an $11\,\mathrm{M}_\odot$ star. Approximately $0.025\,\mathrm{M}_\odot$ of r-process matter was ejected in the explosion, which is an unusually large amount compared to the expected r-process yield from SN II of $\approx 10^{-5}\,\mathrm{M}_\odot$. Note, that it is still doubtful if the prompt explosion of a massive star may occur in reality (Liebendörfer et al. 2001; Sumiyoshi et al. 2001). Chemical evolution models including lower mass SNe as r-process source were presented by Ishimaru & Wanajo (1999) and Travaglio et al. (1999).

In the treatment of such lower mass SNe, we proceed similar to Ishimaru & Wanajo (1999): r-process nucleosynthesis is assumed to occur in the mass range $8 - 10\,\mathrm{M}_\odot$ with constant Ba and Eu yields over the whole mass range. The yields then are deduced from the average [Eu/Fe] and [Ba^r/Fe] ratios of metal-poor halo stars: $Y_{\mathrm{Ba}} = 1.1 \cdot 10^{-6}\,\mathrm{M}_\odot$ and $Y_{\mathrm{Eu}} = 1.7 \cdot 10^{-7}\,\mathrm{M}_\odot$, which equals to a total of $\approx 1.4 \cdot 10^{-5}\,\mathrm{M}_\odot$ of ejected r-process matter per event (Eqs. 4.9 and 4.10). Furthermore, we assume that the amount of α- and iron peak elements synthesized in these SN II events are negligible (Hillebrandt et al. 1984).

c. r-process yields from core-collapse SNe more massive than $20\,\mathrm{M}_\odot$

Nucleosynthesis of r-process elements might also occur in neutrino driven winds from nascent neutron-stars during the delayed explosion of high-mass stars with masses $\gtrsim 20\,\mathrm{M}_\odot$ (e.g. Woosley & Hoffman 1992; Woosley et al. 1994; Qian & Woosley 1996; Thompson et al. 2001; Wanajo et al. 2001). Williams (1987) reported the detection of Ba absorption lines in the spectra of SN 1987A (progenitor mass $\approx 20\,\mathrm{M}_\odot$), and Mazzali et al. (1992) noted that Ba was lacking at the very surface of the ejecta. Because of this remarkable feature, Tsujimoto & Shigeyama (2001) identify SN 1987A as r-process site and estimate that $\approx 6 \cdot 10^{-6}\,\mathrm{M}_\odot$ of Ba were synthesized during the SN event. However, the poor knowledge of the far UV radiation field in the envelope of SN 1987A makes it difficult to determine a truly reliable Ba abundance in its ejecta (Utrobin & Chugai 2002).

Complementary to the observation of Ba in SN 1987A, Tsujimoto et al. (2000) deduce Ba and Eu yields from observations of metal-poor halo stars and inhomogeneous chemical evolution models, suggesting that core-collapse SNe in the mass range $20 - 25\,\mathrm{M}_\odot$ dominate the production of r-process elements. They propose a Ba yield of $8.5 \cdot 10^{-6}\,\mathrm{M}_\odot$ and $4.5 \cdot 10^{-8}\,\mathrm{M}_\odot$ and a Eu yield of $1.3 \cdot 10^{-6}\,\mathrm{M}_\odot$ and $7.0 \cdot 10^{-9}\,\mathrm{M}_\odot$ for a 20 and $25\,\mathrm{M}_\odot$ progenitor, respectively. Here, we adopt yields similar to the ones given by Tsujimoto et al. (2000) and assume, that SNe outside the indicated mass range do not contribute significantly to r-process nucleosynthesis. In our model, a $20\,\mathrm{M}_\odot$ star produces $7.1 \cdot 10^{-6}\,\mathrm{M}_\odot$ of Ba and $1.1 \cdot 10^{-6}\,\mathrm{M}_\odot$ of Eu, whereas a $25\,\mathrm{M}_\odot$ star yields $3.7 \cdot 10^{-8}\,\mathrm{M}_\odot$ of Ba and $5.8 \cdot 10^{-9}\,\mathrm{M}_\odot$ of Eu. (The small differences arise because we adopted different iron yields than Tsujimoto et al. 2000.) For stars between 20 and $25\,\mathrm{M}_\odot$, the yields are interpolated linearly. Thus, a SN II in this mass range ejects on average $\approx 5 \cdot 10^{-5}\,\mathrm{M}_\odot$ of r-process matter (Eqs. 4.9 and 4.10).

d. r-process yields from neutron star mergers (NSM)

Another major source of r-process elements might be neutron star mergers (Freiburghaus et al. 1999b; Rosswog et al. 1999; 2000). A scheme similar to the determination of SN Ia events was applied for the determination of their occurrence (c.f. Sect. 4.2.1): With probability P_{NSM} a newly formed high mass star (in the range $10 - 50\,\mathrm{M}_\odot$) has a companion in the same mass range. It is assumed that, subsequent to both SN II events, the remaining neutron stars will eventually merge. The time t_c that is needed for the coalescence of the two neutron stars and the probability P_{NSM} for the occurrence of NSM events are treated as free parameters which can be adjusted within given observational constraints on the coalescence rate of binary compact objects and merger timescales (van den Heuvel & Lorimer 1996; Kalogera & Lorimer 2000; Belczynski et al. 2002). As was the case for SN Ia events, this treatment is very simplified, but has the advantage that all difficulties associated with the determination of formation channels of neutron star binaries (or neutron star / black hole binaries) and the corresponding formation rates (Belczynski et al. 2002) are combined in only one free parameter. Furthermore, the lower mass boundary for neutron star formation (here $10\,\mathrm{M}_\odot$) is of little importance: The decisive term for the enrichment of the ISM with r-process material in this case is the NSM rate. Since a decrease of the lower mass boundary results in an increase of the NSM rate, a simple adjustment of the parameter P_{NSM} is sufficient to retrieve a NSM rate consistent with observations.

Coalescence timescales for neutron star mergers are typically estimated to be of the order $100 - 1000$ Myr (e.g. Portegies Zwart & Yungel'son 1998; Fryer et al. 1999b). Recently, Belczynski et al. (2002) suggested a *dominating* population of short lived neutron star binaries with merger times less than 1 Myr. This population of neutron star mergers might be formed through channels involving mass-transfer episodes from helium stars, leading to tightly bound binary systems with very short orbit decay timescales. However, this result depends on the occurrence of a common envelope (CE) phase of the progenitor He stars, which was treated in a simplified manner by Belczynski et al. (2002). The authors caution, that detailed hydrodynamical calculations of the CE phase still have to confirm these results. In view of these uncertainties, we adopt three different coalescence times t_c, namely 1, 10 and 100 Myr. Coalescence timescales of the order 1 Gyr have not been considered, since they are not consistent with observations of neutron capture elements in ultra metal-poor stars.

Table 4.2. Parameter values adopted for NSM events (see text for details). For each value of P_{NSM}, three models with the indicated coalescence timescales t_c have been calculated.

P_{NSM}	M_r [$\mathrm{M}_\odot$]	f_{NSM} [yr^{-1}]	t_c [Myr]
$6.5 \cdot 10^{-1}$	10^{-5}	$2 \cdot 10^{-2}$	1, 10, 100
$4.1 \cdot 10^{-2}$	10^{-4}	$2 \cdot 10^{-3}$	1, 10, 100
$4.0 \cdot 10^{-3}$	10^{-3}	$2 \cdot 10^{-4}$	1, 10, 100
$4.0 \cdot 10^{-4}$	10^{-2}	$2 \cdot 10^{-5}$	1, 10, 100
$3.9 \cdot 10^{-5}$	10^{-1}	$2 \cdot 10^{-6}$	1, 10, 100

Observational constraints on the Galactic NSM rate are controversial. Van den Heuvel & Lorimer (1996) estimate a rate of approximately $8 \cdot 10^{-6}\,\mathrm{yr}^{-1}$, Kalogera & Lorimer (2000) give an upper limit of $\left(7.5 \cdot 10^{-7} - 1.5 \cdot 10^{-5}\right)\,\mathrm{yr}^{-1}$ whereas Belczynski et al. (2002) get rates in the range $\left(10^{-6} - 3 \cdot 10^{-4}\right)\,\mathrm{yr}^{-1}$ from theoretical considerations. The amount of r-process matter ejected in a NSM event, M_r, is of the order of a few times $10^{-3} - 10^{-2}\,\mathrm{M}_\odot$, depending on the initial configuration of the binary system (Rosswog et al. 1999). Taking general relativistic effects into account, Oechslin et al. (2002) get $5 \cdot 10^{-5} - 2 \cdot 10^{-4}\,\mathrm{M}_\odot$ as lower limit for M_r.

Table 4.2 lists the parameter values adopted for the NSM probability P_{NSM}, the amount of ejected r-process matter M_r, the NSM rate f_{NSM} and coalescence timescales t_c. After a value for P_{NSM} has been chosen, the coalescence timescale is the only free parameter remaining in the model since the NSM rate is determined by the NSM probability and the SF rate (resulting from the parameter values given in Table 4.1). The NSM rate and the amount of ejected r-process matter are tightly correlated, since the total amount of r-process matter in the Galaxy ($\approx 10^4\,\mathrm{M}_\odot$, Wallerstein et al. 1997), has to be reproduced. Thus, higher NSM rates require that less r-process matter is ejected in each event.

Comparing the values in Table 4.2 with observational constraints reveals that the NSM rate of the first row is much too high and that the corresponding low value of $10^{-5}\,\mathrm{M}_\odot$ of ejected r-process matter is comparable to the amount of r-process matter that might be ejected in SN II events (c.f. Sect. 4.2.2.b and 4.2.2.c). Thus, models adopting this NSM rate are also representative for the cases when r-process nucleosynthesis originates in core-collapse SNe. NSM rates indicated in the four lower rows seem to be consistent with observations. However, the ejected r-process matter in the last case is clearly at the upper limit of allowed values.

4.3. Basic model results in comparison to observations

In this section we shortly discuss the basic results of our standard model, namely the enrichment of the ISM with O, Mg, Si, Ca and Fe. Further discussions of model results, e.g. the effect of chemical inhomogeneities in the halo ISM at early times and the importance of the progenitor mass dependence of nucleosynthesis yields, are given in Paper I and Paper II, respectively. The discussion of neutron capture elements is given in Sect. 4.4.

Fig. 4.1 shows an overview of the results of our standard model. In the uppermost panel on the left the SFR (red), mass-return rate (MRR, blue) and mass infall rate (purple) in $\mathrm{M}_\odot/\mathrm{yr}$ per galaxy are plotted. Here, the term "per galaxy" means that the rates are scaled to account for a total baryonic mass of $10^{11}\,\mathrm{M}_\odot$ (instead of $10^8\,\mathrm{M}_\odot$ in the modelled volume) so that they can be (roughly) compared to observations. This procedure was also applied to the ISM mass and SN rates. Note that the small oscillations in the SFR and the MRR are caused be the stochastic SF description of our model.

Unfortunately, observational estimates of the present day mass infall and star formation rate are scarce and not well constrained. From a survey of high velocity clouds, Oort (1970) estimates a present day mass infall rate of $\approx 1\,\mathrm{M}_\odot\,\mathrm{yr}^{-1}$ onto the galactic plane but stresses that only the order of magnitude of this value is certain. According to Scalo (1986), the present day star formation rate in the Galaxy is on average $\approx 3\,\mathrm{M}_\odot\,\mathrm{yr}^{-1}$. For our standard model, the corresponding values are close to the observed ones, namely $\approx 2.3\,\mathrm{M}_\odot\,\mathrm{yr}^{-1}$ and $\approx 4.1\,\mathrm{M}_\odot\,\mathrm{yr}^{-1}$ for mass infall and star formation rate, respectively.

In the uppermost panel on the right the ISM mass $M(t)$ as function of time is plotted. The scale on the left indicates $M(t)$ in absolute numbers, whereas the scale on the right gives the fraction of the ISM mass with respect to the total infalling mass, i.e. $M(t)/M_{\mathrm{tot}}$. Observations estimate the total mass of molecular gas in our galaxy to be $\approx 3-4\cdot 10^9\,\mathrm{M}_\odot$ (Rana 1991; Evans 1999). The present day ISM mass in our model is in good agreement with observations: $\approx 4\cdot 10^9\,\mathrm{M}_\odot$, which corresponds to 4% of the total mass of the system.

SN II + SN Ibc (red) and SN Ia (blue) rates (number of SN events per *year*) are given in the second panel on the left and the SN Ia/(SN Ibc + SN II) ratio is indicated in the second panel on the right. Tamman et al. (1994) estimate the present day total SN rate (SN Ia and SN II/Ibc) in the Galaxy to be $2.5^{+0.8}_{-0.5}$ events per *century*, with SN Ia/(SN Ibc + SN II) ≈ 0.2. The present day SN rate in our model gives a good match to observations: We obtain a SN Ibc + SN II rate of 2.2 and a SN Ia rate of 0.57 events per century, resulting in a total of ≈ 2.8 SN events per century. The present day SN Ia/(SN Ibc + SN II) ≈ 0.25 ratio is slightly larger than the observed one. However, if the lower mass limit for SN II progenitors is decreased to $8\,\mathrm{M}_\odot$, the number of SN II events increases by $\approx 40\%$, whereas the SN Ia rate remains essentially unaffected (decrease $< 1\%$). In this case, the SN II and SN Ia rates evaluate to 3.1 and 0.57 events per century, which is still consistent with observations, and SN Ia/(SN Ibc + SN II) ≈ 0.2. Furthermore, SNe with low-mass progenitors are thought to produce only minute amounts of heavy elements (mostly iron-peak nuclei) due to the dramatic difference in the core structure compared to "common" core-collapse SNe with higher mass progenitors. Their impact on the chemical enrichment of the ISM is therefore expected to be neg-

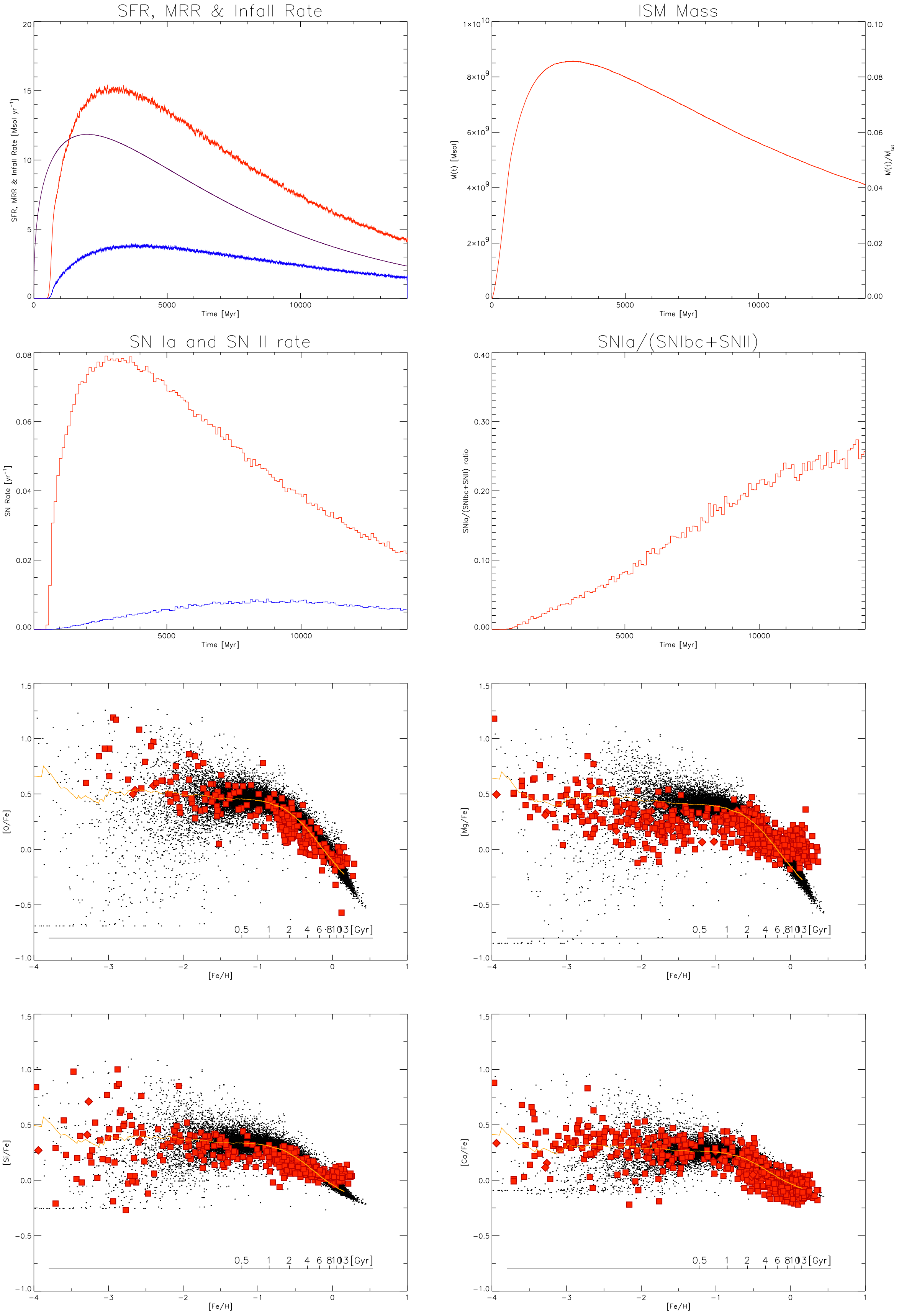

Fig. 4.1. Overview of basic model results (see text for details).

ligible while, on the other hand, they may account for a large fraction of Galactic core-collapse SNe (Hillebrandt et al. 1984). However, SNe with low-mass progenitors might be major contributors to the enrichment of the ISM with r-process nuclei (c.f. Sect. 4.2.2).

The four panels in the lower half of Fig. 4.1 show the evolution of [O/Fe], [Mg/Fe], [Si/Fe] and [Ca/Fe] as function of metallicity [Fe/H]. Model stars are shown as black dots, whereas observations are indicated by filled red squares and diamonds. Observations are taken from Peterson et al. (1990), Bessel et al. (1991), Gratton & Sneden (1991a, 1991b), Ryan et al. (1991), Spite & Spite (1991), Spiesman & Wallerstein (1991), Edvardsson et al. (1993), Norris et al. (1993), Beveridge & Sneden (1994), Nissen et al. (1994), Fuhrmann et al. (1995), McWilliam et al. (1995a), Ryan et al. (1996), Israelian et al. (1998), Boesgaard et al. (1999), Jehin et al. (1999), Carretta et al. (2000), Idiart & Thévenin (2000), Norris et al. (1993), Israelian et al. (2001), Mishenina & Kovtyukh (2001) and Stephens & Boesgaard (2002). Single observations of stars are marked by a square. In the case where multiple observations of a star are present, we plot the most recent one if all observations were published before 2000 (also marked by squares). If several more recent observations are available, the given element abundances are averaged (marked by diamonds). The yellow line shows the average element abundances in the model ISM and can directly be compared to classical chemical evolution models, which assume that the ISM is well mixed at all times (“instantaneous mixing approximation”). At the bottom of each panel, the time since the first SF event needed to reach a given metallicity ([Fe/H]) is shown. Note however, that the first SF event takes place roughly 0.5 Gyr after the start of the simulation (c.f. Sect. 4.2.1).

The impact of chemical inhomogeneities in the early halo ISM is readily seen in the large scatter of the [el/Fe] ratios at [Fe/H] $\lesssim -2$. As the enrichment proceeds, the chemical inhomogeneities disappear, the scatter decreases and the [el/Fe] ratios converge to the value of IMF averaged abundances. At [Fe/H] $\gtrsim -1$, the ISM can be considered well mixed. The mean [el/Fe] ratios of metal-poor halo stars and the turn-off due to increasing iron injection by Type Ia SNe is well reproduced (within the inherent uncertainties of theoretical nucleosynthesis yields and observational errors). A detailed analysis of the enrichment process and an account of uncertainties in present nucleosynthesis calculations is given in Paper I and Paper II.

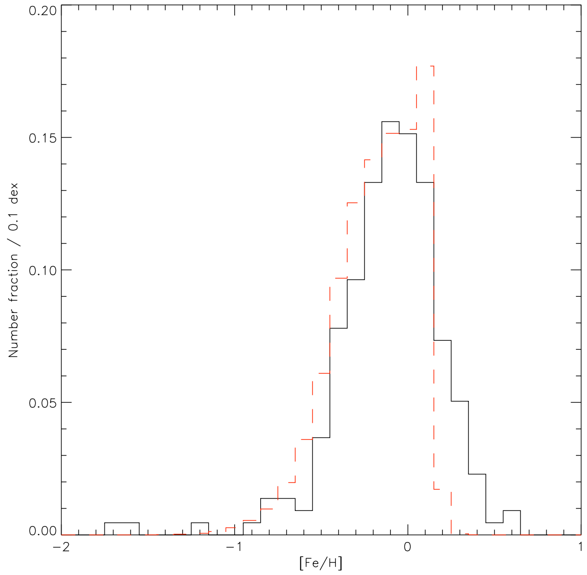

Fig. 4.2. Distribution of G-dwarfs in the solar neighbourhood (Haywood 2001, solid line) and low-mass model stars (red dashed line).

Approximately 800 Myr after the first SF event, the ISM reaches an average metallicity of [Fe/H] $= -1$. After this time, Type Ia SNe start to significantly contribute to (and soon dominate) the enrichment of the ISM with iron peak nuclei. Solar metallicity ([Fe/H] = 0) is reached after approximately 9 Gyr, which is consistent with the age of the solar system. Note that [O/Fe] and [Mg/Fe] abundances at [Fe/H] > 0.0 are too low compared to observations, indicating the that SN II rate in the late evolution of the ISM is slightly too low.

Fig. 4.2 shows the G-dwarf distribution in the solar neighbourhood (Haywood 2001, solid line) and the corresponding distribution of low-mass model stars (in the mass-range $0.8 - 1.05\,M_\odot$, red dashed line). Both distributions agree remarkably well, which is primarily a consequence of the infall of metal-poor gas. In addition, some of the most metal-poor stars already ended their life, since the lifetime of stars also depends on metallicity, i.e. metal-poor stars have shorter lifetimes than their more metal-rich counterparts. The larger fraction of model stars at [Fe/H] = 0.1 also is an indication that the present-day SN II rate in the model is too low. However, we are mainly interested in the early enrichment phases of the Galaxy and on the

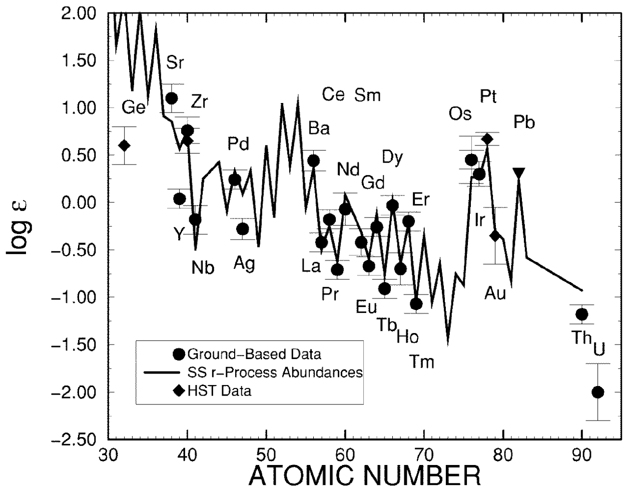

Fig. 4.3. Neutron capture element abundances in BD +17°3248 obtained by ground based and HST observations, compared to a scaled solar system r-process abundance curve. Figure taken from Cowan et al. (2002).

whole the results of our standard model are in good agreement with observational constraints.

4.4. Enrichment of the ISM with neutron capture elements

4.4.1. A robust r-process beyond barium?

Increasing evidence from observations of neutron capture elements in ultra metal-poor halo stars suggests that the synthesis of r-process elements started early in the galactic evolution and that the r-process for elements heavier than Ba ($Z \geq 56$) is robust, i.e. originates from a single astrophysical site or at least occurs under well defined physical conditions. To date, there are four ultra metal-poor halo stars where most neutron-capture element abundances could be determined with high accuracy, namely CS 22892–052 (Sneden et al. 2000a), HD 115444 (Westin et al. 2000), BD +17°3248 (Cowan et al. 2002) and CS 31082-001 (Hill et al. 2002). In these halo stars, the abundance pattern of elements heavier than Ba perfectly matches the scaled solar system r-process abundances. This indicates that these stars have been enriched by an r-process source, which produces neutron capture elements beyond Ba under narrowly constrained physical conditions, and that they presumably do not contain any s-process contribution to their neutron capture elements. (See however Hill et al. 2002 for the case of CS 31082-001, which shows some evidence that actinides might not necessarily be produced together with lighter neutron capture elements in the range $56 \leq Z \leq 72$).

As a representative example, the abundances of neutron capture elements observed in BD +17°3248 are shown in Fig. 4.3 (taken from Cowan et al. 2002). For comparison, the scaled solar system r-process abundance curve is shown. Observed neutron capture elements from barium up to gold ($56 \leq Z \leq 79$) are in perfect agreement with the scaled solar system r-process abundance pattern (within observational errors). For lead, only an upper limit was derived. The ostensible underabundance of thorium and uranium with respect to the scaled solar value is due to radioactive decay of these nuclei and the old age of these halo stars, which opens up an independent way of putting a lower limit to the age of the universe (Sneden et al. 2000a; Westin et al. 2000; Cayrel et al. 2001; Cowan et al. 2002; but see also Hill et al. 2002). Further evidence of a robust r-process is the first detection of isotopic abundances of Eu in stars other than the Sun, namely the three of the four stars mentioned above (CS 22892–052, HD 115444 and BD +17°3248): Even the *isotopic* abundance fractions of ^{151}Eu and ^{153}Eu in these stars are in excellent agreement with their solar system values (Sneden et al. 2002).

On the other hand, the lower mass neutron capture elements ($30 < Z < 56$) show significant deviations from the scaled solar system abundance curve, indicating the possible existence of a second r-process source. This notion is further supported by (^{182}Hf/^{180}Hf) and (^{129}I/^{127}I) ratios in meteorites dating from the formation of the solar system, which are at odds with the assumption of a single source for all r-process elements. Two r-process sources seem to be required, one which operates on a timescale of $\sim 10^7$ years and is responsible for Hf (i.e. $Z \geq 56$) and another one which is responsible for iodine (i.e. $Z < 56$) and operates on a timescale of $\sim 10^8$ years (Wasserburg et al. 1996). These two r-process sites could either be two types (frequent and less common) of SN events (Wasserburg & Qian 2000; Qian 2000; 2001), or a mixture of SNe and NSM (Rosswog et al. 1999; 2000). On the other hand, Cameron (2001) was able to reproduce the abundance distribution of both, light and heavy neutron capture elements, in two different regions of a single source, namely the accretion-disk and jet of a core-collapse SN.

However, the evidence that the r-process beyond Ba (at least in the range $56 \leq Z \leq 72$) is robust is very convincing and we will use this property in the following to gain some insight into the enrichment of the Galaxy with neutron capture elements.

4.4.2. Disentangling the r- and s-process contributions to neutron capture elements

Under the assumption that the r-process abundance pattern for elements heavier than Ba is constant throughout the evolution of the Galaxy (i.e. the r-process for elements beyond Ba is robust), it is possible to disentangle the s- and r-process fractions of a given neutron capture element as long as the abundance of an r-only element beyond Ba is known. A typical r-only element is Europium, for which the solar r-process fraction is estimated to be 97% of its total abundance, and a typical neutron capture element that is dominantly produced in the main s-process is Barium, for which the solar r-process fraction is only 15% (c.f. Table 5 of Burris et al. 2000).

Let $N_{\odot,\star}(\mathrm{el})$ denote the abundance of a given element in the sun (in a star) and $N^{r,s}_{\odot,\star}(\mathrm{el})$ the corresponding r- and s-process fractions in the sun (in a star). For simplicity, we assume that Europium is produced solely in the r-process, i.e. $N^{r}_{\odot,\star}(\mathrm{Eu}) = N_{\odot,\star}(\mathrm{Eu})$. Furthermore, we adopt the r- and s-process fractions given in Burris et al. (2000):

$$N^{r}_{\odot}(\mathrm{Ba}) = 0.15 \cdot N_{\odot}(\mathrm{Ba}) \qquad \text{and} \tag{4.11}$$

$$N^{s}_{\odot}(\mathrm{Ba}) = 0.85 \cdot N_{\odot}(\mathrm{Ba})\,. \tag{4.12}$$

Under the assumption of a robust r-process, the ratio of the r-process fractions of Ba and Eu is constant throughout the evolution of the galaxy, i.e.

$$\frac{N^{r}_{\star}(\mathrm{Ba})}{N_{\star}(\mathrm{Eu})} = \frac{N^{r}_{\odot}(\mathrm{Ba})}{N_{\odot}(\mathrm{Eu})}. \tag{4.13}$$

The abundance of the r-process fraction of Ba with respect to Eu ([Ba^r/Eu]) is therefore simply

$$\begin{aligned}[\mathrm{Ba}^r/\mathrm{Eu}] &= \log\frac{N^{r}_{\star}(\mathrm{Ba})}{N_{\star}(\mathrm{Eu})} - \log\frac{N^{r}_{\odot}(\mathrm{Ba})}{N_{\odot}(\mathrm{Eu})} \\ &= 0.\end{aligned} \tag{4.14}$$

With the help of this relation, the r-process abundance of Ba ([Ba^r/Fe]) in a star with known Eu abundance is determined to be

$$\begin{aligned}[\mathrm{Ba}^r/\mathrm{Fe}] &= [\mathrm{Ba}^r/\mathrm{Eu}] + [\mathrm{Eu}/\mathrm{Fe}] \\ &= [\mathrm{Eu}/\mathrm{Fe}].\end{aligned} \tag{4.15}$$

The contribution of the s-process to the total Ba abundance can now easily be computed. First, let us remark that

$$\log\frac{N_{\star}(\mathrm{Ba})}{N_{\star}(\mathrm{Fe})} = [\mathrm{Ba}/\mathrm{Fe}] + \log\frac{N_{\odot}(\mathrm{Ba})}{N_{\odot}(\mathrm{Fe})} \tag{4.16}$$

and that by applying Eqs. (4.11) and (4.15) we find

$$\begin{aligned}\log\frac{N^{r}_{\star}(\mathrm{Ba})}{N_{\star}(\mathrm{Fe})} &= [\mathrm{Ba}^r/\mathrm{Fe}] + \log\frac{N^{r}_{\odot}(\mathrm{Ba})}{N_{\odot}(\mathrm{Fe})} \\ &= [\mathrm{Eu}/\mathrm{Fe}] + \log\frac{0.15 \cdot N_{\odot}(\mathrm{Ba})}{N_{\odot}(\mathrm{Fe})}.\end{aligned} \tag{4.17}$$

The s-process fraction of Ba is simply the residual after the r-process fraction to Ba is subtracted. With the use of Eqs. (4.16) and (4.17) we find

$$\begin{aligned}\frac{N^{s}_{\star}(\mathrm{Ba})}{N_{\star}(\mathrm{Fe})} &= \frac{N_{\star}(\mathrm{Ba}) - N^{r}_{\star}(\mathrm{Ba})}{N_{\star}(\mathrm{Fe})} \\ &= 10^{[\mathrm{Ba}/\mathrm{Fe}]} \cdot \frac{N_{\odot}(\mathrm{Ba})}{N_{\odot}(\mathrm{Fe})} \\ &\quad - 10^{[\mathrm{Eu}/\mathrm{Fe}]} \cdot \frac{0.15 \cdot N_{\odot}(\mathrm{Ba})}{N_{\odot}(\mathrm{Fe})} \\ &= \left(10^{[\mathrm{Ba}/\mathrm{Fe}]} - 0.15 \cdot 10^{[\mathrm{Eu}/\mathrm{Fe}]}\right) \cdot \frac{N_{\odot}(\mathrm{Ba})}{N_{\odot}(\mathrm{Fe})}\end{aligned} \tag{4.18}$$

Finally, the s-process abundance of Ba is given by

$$\begin{aligned}[\mathrm{Ba}^s/\mathrm{Fe}] &= \log\frac{N^{s}_{\star}(\mathrm{Ba})}{N_{\star}(\mathrm{Fe})} - \log\frac{N^{s}_{\odot}(\mathrm{Ba})}{N_{\odot}(\mathrm{Fe})} \\ &= \log\left(10^{[\mathrm{Ba}/\mathrm{Fe}]} - 0.15 \cdot 10^{[\mathrm{Eu}/\mathrm{Fe}]}\right) \\ &\quad + \log\frac{N_{\odot}(\mathrm{Ba})}{N_{\odot}(\mathrm{Fe})} - \log\frac{N^{s}_{\odot}(\mathrm{Ba})}{N_{\odot}(\mathrm{Fe})},\end{aligned} \tag{4.19}$$

and since $N^{s}_{\odot}(\mathrm{Ba}) = 0.85 \cdot N_{\odot}(\mathrm{Ba})$,

$$\begin{aligned}[\mathrm{Ba}^s/\mathrm{Fe}] &= \log\left(10^{[\mathrm{Ba}/\mathrm{Fe}]} - 0.15 \cdot 10^{[\mathrm{Eu}/\mathrm{Fe}]}\right) \\ &\quad - \log 0.85.\end{aligned} \tag{4.20}$$

For any given star with observed Ba and Eu abundances, we now have the possibility to separate the r- and s-process contributions to the total Ba abundance by virtue of Eqs. (4.15) and (4.20). (An equivalent procedure can be applied to any other neutron capture element beyond Ba.) Note, that a star does not contain any s-process contribution to its Ba abundance, if $10^{[\mathrm{Ba/Fe}]} - 0.15 \cdot 10^{[\mathrm{Eu/Fe}]} \leq 0$ (Eq. 4.20).

Burris et al. (2000) used this technique to calculate the r- and s-process contributions to Ba of a number of metal-poor halo stars. They concluded that the s-process first appears at metallicities as low as [Fe/H] ≈ -2.7, which is much lower than previously thought. For stars with metallicities lower than this boundary no s-process contribution to Ba is expected and their total Ba abundance presumably can be considered to be of pure r-process origin. Thus, their r-process Ba abundance is simply their total [Ba/Fe] abundance, normalized to the solar r-process fraction of Ba i.e. $[\mathrm{Ba}^r/\mathrm{Fe}]' = [\mathrm{Ba/Fe}] - \log 0.15$. This procedure can be used to derive $[\mathrm{Ba}^r/\mathrm{Fe}]$ of ultra metal-poor stars with no observed Eu abundances. Alternatively, if the Eu abundance of an ultra metal-poor star is known, $[\mathrm{Ba}^r/\mathrm{Fe}] = [\mathrm{Eu/Fe}]$ (Eq. 4.15). Since a few stars more metal-poor than [Fe/H] ≤ -2.7 with observed Ba *and* Eu abundances are known, we can check whether these two methods to derive the r-process fraction of Ba at such low metallicities are consistent.

The 15 observations of stars which fulfil the requirements (i.e. [Fe/H] ≤ -2.7, observed Ba and Eu abundances) are listed in Table 4.3, sorted by decreasing metallicity. Four stars in the list have multiple observations. The first column gives the star identification and the reference to the observations. The second through fourth columns list the observed [Fe/H], [Ba/Fe] and [Eu/Fe] abundances, respectively. The fifth column gives $[\mathrm{Ba}^r/\mathrm{Fe}]'$, i.e. the total Ba abundance normalized to the level of the solar r-process fraction of Ba (as describe above). The difference $[\mathrm{Ba}^r/\mathrm{Eu}] = [\mathrm{Ba}^r/\mathrm{Fe}]' - [\mathrm{Eu/Fe}]$, which should be equal to zero according to Eq. (4.14), is listed in column six. The last two columns show the s-process fraction of Ba ($[\mathrm{Ba}^s/\mathrm{Fe}]$), as calculated by Eq. (4.20), and the difference $[\mathrm{Ba}^s/\mathrm{Eu}] = [\mathrm{Ba}^s/\mathrm{Fe}] - [\mathrm{Eu/Fe}]$, respectively. Since no s-process contribution to the Ba abundance is expected for the ultra metal-poor stars in the list, the values in the last column should be much smaller than zero. (This must not be true for the second last column, since very low iron abundances can result in $[\mathrm{Ba}^s/\mathrm{Fe}]$ ratios larger than zero, as is the case for CS $22892 - 052$, the most metal-poor star in the list.)

With the exception of HD 88609, all stars have $[\mathrm{Ba}^r/\mathrm{Eu}] < 0.3$. This overabundance of up to 0.3 dex may be explained by observational uncertainties (see e.g. Sneden et al. 2000a; Westin et al. 2000; and compare also the abundances of stars with multiple observations in Table 4.3). For BD $-18°5550$ and HD 126587 the $[\mathrm{Ba}^r/\mathrm{Eu}]$ ratio is essentially zero. Consequently, these two stars show the lowest $[\mathrm{Ba}^s/\mathrm{Eu}]$ values and can be considered to be free of any s-process pollution. Considering the difficulties to observe element abundances at such low metallicities, the method to disentangle the r- and s-process contribution to neutron-capture elements beyond Ba seems to work well and that the assumption of a robust r-process beyond Ba holds. It remains to be seen, however, if the assumption of no s-process contribution to neutron-capture elements below [Fe/H] ≤ -2.7 is valid.

It is interesting to note in this context, that for essentially all stars $[\mathrm{Ba}^r/\mathrm{Eu}] \geq 0$ and that the $[\mathrm{Ba}^r/\mathrm{Eu}]$ ratios do not scatter around zero, as would be expected if the deviations from zero were caused by random errors. This could indicate that the solar r-process fraction of Ba is underestimated (a value of 0.20 instead of 0.15 would shift the average $< [\mathrm{Ba}^r/\mathrm{Eu}] >$ of this sample to zero). The table in Burris et al. (2000), from which our solar r- and s-process fractions are taken, is an updated version of a similar table in Sneden et al. (1996). In the updated table, the solar r-process fraction of Ba is increased from 0.12 to 0.15 of the total solar Ba abundance. Unfortunately, no error bar for the solar r-process fraction of Ba is given in Burris et al. (2000) which makes it difficult to decide whether the required fraction of 0.2 is feasible. However, recent s-process calculations in thermally pulsing asymptotic giant branch (TP-AGB) stars estimate that approximately 80% of the solar Ba abundance is of s-process origin (Raiteri et al. 1999 and references therein; Arlandini et al. 1999; Travaglio et al. 1999). Thus, we recalculated the $[\mathrm{Ba}^r/\mathrm{Eu}]$ and $[\mathrm{Ba}^s/\mathrm{Eu}]$ ratios with 0.2 as value for the solar r-process fraction of Ba for comparison with Table 4.3. The results are given in Table 4.4. The new values are much more consistent with the assumption that the s-process was not yet active at [Fe/H] ≤ -2.7, since now eight out of fifteen stars do not show any s-process contribution (instead

Table 4.3. Comparison of r- and s-process contributions to Ba in ultra metal-poor halo stars (solar r-process fraction of Ba set to 0.15). The table is sorted by decreasing metallicity. For stars free of any s-process contribution, [Ba^s/Fe] and [Ba^s/Eu] are marked by "–".

Star	[Fe/H]	[Ba/Fe]	[Eu/Fe]	[Ba^r/Fe]$'$	[Ba^r/Eu]	[Ba^s/Fe]	[Ba^s/Eu]
CS 22896 − 154^a	−2.71	0.21	0.97	1.03	0.06	−0.58	−1.55
BD +58°1218^b	−2.72	−0.50	0.21	0.32	0.11	−1.07	−1.28
HD 122563^b	−2.71	−0.92	−0.30	−0.10	0.20	−1.28	−0.98
HD 122563^c	−2.74	−0.93	−0.36	−0.11	0.25	−1.21	−0.85
CS 22953 − 003^a	−2.79	0.00	0.72	0.82	0.10	−0.60	−1.32
HD 126587^a	−2.83	−0.27	0.41	0.55	0.14	−0.75	−1.16
HD 126587^b	−2.85	−0.06	0.75	0.76	0.01	−1.49	−2.24
CS 22873 − 055^a	−2.86	−0.67	−0.12	0.15	0.27	−0.93	−0.81
BD −18°5550^a	−2.89	−1.02	0.17	−0.20	−0.37	–	–
BD −18°5550^b	−2.93	−0.90	−0.07	−0.08	−0.01	–	–
HD 88609^b	−2.93	−0.70	−0.33	0.12	0.45	−0.82	−0.49
HD 115444^b	−2.77	−0.05	0.65	0.77	0.12	−0.58	−1.23
HD 115444^c	−2.99	0.18	0.85	1.00	0.15	−0.27	−1.12
CS 22892 − 052^a	−3.02	0.93	1.48	1.75	0.27	0.67	−0.81
CS 22892 − 052^d	−3.10	0.96	1.67	1.78	0.11	0.39	−1.28

[a] McWilliam et al. (1995a, 1998); [b] Burris et al. (2000); [c] Westin et al. (2000);

[d] Sneden et al. (2000a)

Table 4.4. The same as Table 4.3, but with a solar r-process fraction of Ba of 0.2 instead of 0.15. For stars free of any s-process contribution, [Ba^s/Fe] and [Ba^s/Eu] are marked by "–". The new values are much more consistent with the assumption that the s-process was not yet active at [Fe/H] ≤ -2.7.

Star	[Fe/H]	[Ba/Fe]	[Eu/Fe]	[Ba^r/Fe]$'$	[Ba^r/Eu]	[Ba^s/Fe]	[Ba^s/Eu]
CS 22896 − 154^a	−2.71	0.21	0.97	0.91	−0.06	–	–
BD +58°1218^b	−2.72	−0.50	0.21	0.20	−0.01	–	–
HD 122563^b	−2.71	−0.92	−0.30	−0.22	0.08	−1.60	−1.30
HD 122563^c	−2.74	−0.93	−0.36	−0.23	0.13	−1.42	−1.06
CS 22953 − 003^a	−2.79	0.00	0.72	0.70	−0.02	–	–
HD 126587^a	−2.83	−0.27	0.41	0.43	0.02	−1.54	−1.95
HD 126587^b	−2.85	−0.06	0.75	0.64	−0.11	–	–
CS 22873 − 055^a	−2.86	−0.67	−0.12	0.03	0.15	−1.11	−0.99
BD −18°5550^a	−2.89	−1.02	0.17	−0.32	−0.49	–	–
BD −18°5550^b	−2.93	−0.90	−0.07	−0.20	−0.13	–	–
HD 88609^b	−2.93	−0.70	−0.33	−0.00	0.33	−0.88	−0.55
HD 115444^b	−2.77	−0.05	0.65	0.65	−0.00	–	–
HD 115444^c	−2.99	0.18	0.85	0.88	0.03	−0.91	−1.76
CS 22892 − 052^a	−3.02	0.93	1.48	1.63	0.15	0.49	−0.99
CS 22892 − 052^d	−3.10	0.96	1.67	1.66	−0.01	–	–

[a] McWilliam et al. (1995a, 1998)); [b] Burris et al. (2000); [c] Westin et al. (2000);

[d] Sneden et al. (2000a)

of only one when the lower solar r-process fraction to Ba is used) and for most of the stars $|[\mathrm{Ba}^r/\mathrm{Eu}]| < 0.1$.

On the other hand, if the solar Ba r-process fraction of Burris et al. (2000) is adopted (as is the case for the rest of this work), the systematic trend of $[\mathrm{Ba}^r/\mathrm{Eu}]$ to ratios larger than zero in Table 4.3 suggests that the s-process already contributed to the enrichment of the ISM at metallicities $[\mathrm{Fe/H}] \leq -2.7$. This is strongly supported by Aoki et al. (2000), who reported s-process enhancement in the carbon-rich star LP 625-44 ($[\mathrm{Fe/H}] = -2.7$; e.g. [Ba/Fe] = 2.74) due to mass transfer from a previous AGB companion. However, three stars in the metallicity range $-3.0 < [\mathrm{Fe/H}] \leq -2.6$, namely BD $-18°5550$ (McWilliam et al. 1995a; Burris et al. 2000), HD 126587 (Burris et al. 2000) and HD 184711 (Gratton & Sneden 1991a; Gratton & Sneden 1991b), seem to be free of any s-process contribution to their Ba abundance (see Figure 4.4), which implies that the s-process operated only on local scales at this stage of the chemical enrichment of the Galaxy. This is consistent with the notion of inhomogeneous chemical evolution, since at these metallicities the ISM was not well mixed and dominated by local chemical inhomogeneities (Paper I).

4.4.3. Constraints on the SFR in the early Galaxy

Fig. 4.4 shows the evolution of $[\mathrm{Ba}^s/\mathrm{Eu}]$ (left hand panel) and $[\mathrm{Ba/Eu}]$ (right hand panel) of a sample of stars as function of metallicity [Fe/H]. The s-process contribution to Ba was calculated assuming the solar s-process fraction given by Burris et al. (2000), i.e. $N^s_\odot(\mathrm{Ba}) = 0.85 \cdot N_\odot(\mathrm{Ba})$. The sample consists of observations of neutron-capture elements by Peterson et al. (1990), Gratton & Sneden (1991a; 1991b), Ryan et al. (1991), Edvardsson et al. (1993), François et al. (1993), Beveridge & Sneden (1994), Woolf et al. (1995), Ryan et al. (1996), McWilliam (1995a, 1998), Jehin et al. (1999), Burris et al. (2000), Mashonkina & Gehren (2000; 2001), Sneden et al. (2000a), Mishenina & Kovtyukh (2001), Stephens & Boesgaard (2002) and Koch & Edvardsson (2002). Multiple observations of a star were treated as already discussed in Sect. 4.3. Stars with s-process enhancement due to binary evolution have been omitted from the sample. Black dots show stars from our standard model and the yellow line gives the [Ba^s/Eu] and [Ba/Eu] ratios of the model ISM.

The left hand panel of Fig. 4.4 shows the s-process contribution to Ba abundances in our observational sample. Inverted triangles at the bottom of this panel denote stars which do not contain any s-process contribution to their Ba abundance ($[\mathrm{Ba}^s/\mathrm{Eu}] \ll 0$). HD 126587 might also be considered to be free of s-process pollution ($[\mathrm{Ba}^s/\mathrm{Eu}] = -2.24$). The chemical enrichment of the ISM with s-process elements is clearly visible in the increase of the s-process fraction to Ba with increasing metallicity. Also visible is a sharp decrease in $[\mathrm{Ba}^s/\mathrm{Eu}]$ below $[\mathrm{Fe/H}] \leq -2.5$. This shows, that the enrichment of the ISM with Ba is dominated at later times by the s-process, whereas the neutron capture element enrichment in the early Galaxy was dominated by r-process events. However, it is also evident from Fig. 4.4 that the s-process was already active in the early Galaxy. Only the three stars with [Ba^s/Fe] < -2 in the sample can be considered free of s-process contributions to their Ba abundances (for the adopted s-process fraction to Ba). The remaining stars show clear (though sometimes minute) evidence of s-process enrichment. This can be understood in the context of inhomogeneous chemical evolution, where separated regions of the ISM can show significantly different element abundance patterns (Paper I).

Since the solar s-process fraction to Ba required to disentangle the s- and r-process fractions in a star is somewhat uncertain, we plotted the total [Ba/Eu] abundances in the right hand panel of Fig. 4.4. The horizontal, dotted lines denote the solar r- and s-process mixture ([Ba/Eu] $= 0$) and the pure r-process ([Ba/Eu] $= \log 0.15 = -0.82$) ratios. The conclusions already drawn from the distribution of [Ba^s/Fe] ratios do not change: The neutron capture element enrichment of the early ISM was *dominated* by r-process events, whereas the s-process contributions to Ba becomes dominant at later times. Again, the sometimes considerable deviation of [Ba/Eu] ratios from the pure r-process value below [Fe/H] < -2.5 is indicative of the occurrence of s-process events early on during Galaxy formation.

The model stars plotted in Fig. 4.4 (dots) show the evolution of [Ba^s/Eu] and [Ba/Eu] in the standard model (discussed in Sects. 4.2 and 4.3). In order to keep the r-process enrichment independent of the specific source, NSM occurring at a very high frequency were assumed to be the major r-process sites (first row in Table 4.2). As already discussed in Sect. 4.2.2.d, this case is also representative for the cases where

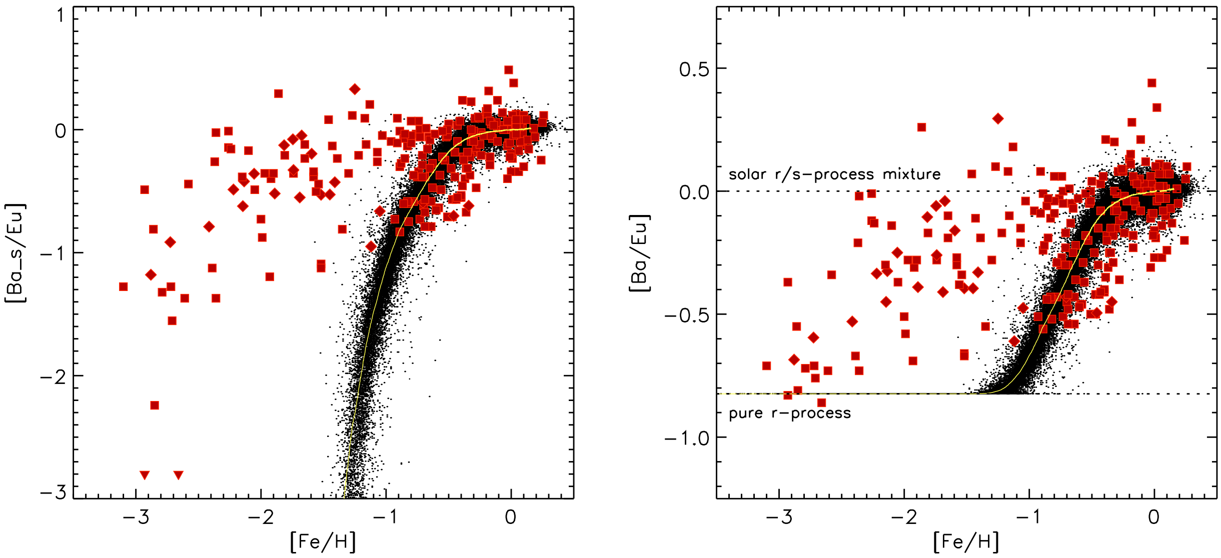

Fig. 4.4. [Ba^s/Eu] and [Ba/Eu] vs. [Fe/H] in stars compared to results of the standard model. Symbols are as in Fig. 4.1. The contribution of s-process material to neutron capture elements at very low metallicities is clearly visible. The standard model, which assumes a short halo-formation timescale, fails to reproduce these observations. Assuming a low star formation rate during halo formation, model results can be reconciled with observations.

SNe II are the dominant contributors of r-process elements (Sect. 4.2.2.b and 4.2.2.c). As can be seen, the location of model stars in Fig. 4.4 reveals a severe shortcoming of the standard model: s-process enrichment starts much too late and observations of Ba abundances in very metal-poor stars ([Fe/H] < -1.5) clearly can not be explained by this model. However, we remark in this context that the results of our standard model are very similar to the ones obtained by Raiteri et al. (1999) and Travaglio et al. (1999).

To simplify the discussion of this shortcoming, we divide the model stars into three metallicity classes and identify these with halo, thick disk and thin disk populations: Model stars with metallicity [Fe/H] $<$ -1 are attributed to the halo, stars in the range $-1 <$ [Fe/H] < -0.5 to the thick disk and stars with metallicity [Fe/H] > -0.5 to the thin disk. This classification is somewhat arbitrary since we have no information about the kinematical behaviour of our model stars. See however Mashonkina & Gehren (2001) for a short summary of the chemical properties of halo, thick disk and thin disk stars.

In the standard model, the "Galactic halo" forms rapidly: $\approx$ 300 Myr after the first SF event, the ISM reaches metallicity [Fe/H] $= -1.5$ and after $\approx$ 800 Myr the iron abundance is [Fe/H] $= -1.0$. The following enrichment of the ISM up to [Fe/H] $= -0.5$ (formation of the "thick disk") takes until $\approx$ 2 Gyr after the first SF event. Nucleosynthesis of Ba by the main s-process is thought to occur primarily in TP-AGB stars in the mass range $1.5 - 4$ $M_\odot$ (Gallino et al. 1998; Busso et al. 1999; Arlandini et al. 1999; Travaglio et al. 1999). Due to the long evolutionary timescale of such low mass stars ($\approx$ 150 Myr and 300 Myr for 4 $M_\odot$ and 3 $M_\odot$ stars, respectively) and the short timescale of halo formation, s-process enrichment starts at the earliest at [Fe/H] ≈ -1.5. The run of [Ba^s/Fe] and [Ba/Fe] ratios of model stars from [Fe/H] ≈ -1.5 on closely follows the apparent branch of observations visible in both panels of Fig. 4.4.

The obstacle to rectify the model results with observations seems to be the incompatibility of two time scales (halo formation time vs. evolution time of low mass stars). Therefore, a natural solution presents itself in the reduction of the SF efficiency during halo formation. To reconcile the model results with observations, the SFR has to be low enough, so that the metallicity of the ISM stays below [Fe/H] $= -2.5$ at least during the first $\approx$ 300 Myr of galactic evolution. This idea is also supported by the work of Abia et al. (2001), which suggests that a low pregalactic star formation efficiency is required so as not to exceed the minimum metallicity of high-redshift systems. Furthermore, the cooling efficiency of primordial gas clouds is much reduced, since the main cooling agents are not present. Thus, cooling has to be provided by molecular hydrogen, rather than dust or heavy molecules (e.g. Sutherland & Dopita 1993; Flower & Pineau des Forêts 2001; Abel et al. 2002, and references therein) and a reduced star formation efficiency can be expected.

The observational clues of a low SF efficiency during halo formation deserve a more detailed analysis, since they imply a long halo formation timescale, in opposition to a fast halo formation scenario (e.g. Mashonkina & Gehren 2001).

First we have to be concerned about the statistical significance of the data. The disentangling of r- and s-process contributions is based on the assumption of a robust r-process beyond Ba. In addition, accurate r- and s-process contributions to solar system Ba and Eu abundances have to be known. For simplicity, it has been assumed that Eu is only produced in the r-process, but calculations by Burris et al. (2000) show it to be $\approx$ 97%. In the case of Ba, the r-process contribution seems to lie somewhere between 15% $-$ 20%. While these uncertainties are not large, they will certainly introduce systematic errors into the calculated [Ba^s/Eu] abundances. Thus, the original [Ba/Eu] abundances are certainly more meaningful. Observational errors in abundances are approximately $0.1 - 0.2$ dex (e.g. Westin et al. 2000), and a change of the solar r-only [Ba/Eu] ratio from 0.15 to 0.20 results in an upward shift of 0.1 dex of the line marked “pure r-process” in Fig. 4.4. Even taking all these uncertainties into account, there are still several observations of metal-poor halo stars at [Fe/H] < -2.5 that show clear evidence of s-process enrichment. Furthermore, a continuous injection of s-process material into the ISM from [Fe/H] $\lesssim -2.5$ to solar metallicity is required to explain the trend in [Ba/Eu] abundances visible in Fig. 4.4.

What kind of objects could be the source of this enrichment? Stars in the mass range $4 - 8\,\mathrm{M}_\odot$ evolve fast enough to be potential sources of s-process elements at very low metallicities. In contrast to lower-mass stars, where the dominant neutron source is the $^{13}\mathrm{C}(\alpha,\mathrm{n})^{16}\mathrm{O}$ reaction, the dominant neutron source in these higher-mass stars is the $^{22}\mathrm{Ne}(\alpha,\mathrm{n})^{25}\mathrm{Mg}$ reaction. But this reaction provides neutron densities which are two orders of magnitude higher than the neutron densities required for the main s-process (Lambert et al. 1995; Wallerstein et al. 1997). Thus, higher-mass stars seem to be ruled out as major s-process sources. However, neutron capture element abundances in the very metal-poor halo star LP 625-44 (Aoki et al. 2000) either cast some doubt on the validity of present s-process models in metal-poor lower-mass stars or require another s-process source active at very low metallicities. If this should be the case, then the alternative s-process source has to operate on short timescales to be consistent with a fast halo formation scenario.

Could metal-free Population III stars be the source of the early s-process enrichment? This scenario has to overcome two obstacles: First, the s-process enrichment of the ISM occurs at a continuous rate (see Fig. 4.4). A one-time pre-enrichment of the ISM by Population III stars would set the [Ba/Eu] ratio to a certain value. Metal-poor halo stars thus would have the same [Ba/Eu] abundances until s-process enrichment by lower-mass TP-AGB stars sets in at [Fe/H] ≈ -1.5. This is clearly not consistent with observations. Second, s-process nucleosynthesis requires that seed nuclei (such as $^{56}\mathrm{Fe}$) are available during the TP-AGB phase, which is not the case in a metal-free environment. For completeness we note that recent stellar models of metal-free intermediate mass stars ($4 - 8\,\mathrm{M}_\odot$) suggest, that the $^{22}\mathrm{Ne}(\alpha,\mathrm{n})^{25}\mathrm{Mg}$ neutron source is active during the final part of the TP-AGB phase of Population III stars, which might activate particular nucleosynthesis channels (Chieffi et al. 2001). Yet, it remains to be seen, if metal-free intermediate mass stars can truly act as s-process sources.

A potential solution to this problem could be the selective loss of iron and europium in SN winds. One may speculate that this mechanism could keep the [Fe/H] abundance at low metallicities during the first few 100 Myr of galactic evolution. It would be very surprising, however, if this mechanism ceased as soon as Ba production by s-process nucleosynthesis started.

Thus, the assumption of a low SF efficiency during halo formation seems to be a natural solution to the problem which does not require a new kind of objects for s-process nucleosynthesis or the occurrence of powerful SN winds.

4.5. Results

4.5.1. A low SF efficiency model

Independent of whether the s-process was already active at metallicities [Fe/H] < -2.7 or started around [Fe/H] ≈ -2.5 (see the discussion in Sect. 4.4.2), the fact that s-process elements are undoubtedly present at very low metallicities suggests a low star formation rate at the beginning of Galaxy formation. In the following, we therefore assume that the SF efficiency during halo formation was indeed very low and that low-mass stars are the dominant contributors to s-process nucleosynthesis. However, observations of Eu abundances in stars with $[\mathrm{Fe/H}] \leq -3.0$ are needed to put a definite lower limit to the occurrence of the first s-process events and yield more stringent constraints on the SFR during halo formation.

In a first attempt to simulate a low SF efficiency during halo formation, we tried to change the parameters of the standard model as little as possible, since its results are in good agreement with observations (Sects. 4.2 and 4.3). Thus, we only set the SF efficiency parameter ν to 1.5 (instead of 15 in the standard model, c.f. Table 4.1) and keep it a this value until the ISM reaches an average metallicity [Fe/H] ≈ -1.3. At this point, close to the end of halo formation, ν is set again to the value of the standard model. None of the other parameters have been changed. Admittedly, this procedure seems rather *ad hoc* and leaves room for a lot of refinement. Especially a gradual increase of the SF efficiency parameter as function of metallicity is desirable. However, the outcome of this low SF efficiency (LE) model is very interesting.

Fig. 4.5 shows an overview of the basic results of the LE model and should be compared with the results of the standard model (Fig. 4.1). The most obvious differences compared to the standard model can be seen in the SFR and SN II rate. The SFR stays below $5\,\mathrm{M}_{\odot}\,\mathrm{yr}^{-1}$ for $\approx$ 1.5 Gyr after the first SF event, whereas the SFR in the standard model peaks at $15\,\mathrm{M}_{\odot}\,\mathrm{yr}^{-1}$ at this time. Consequently, the SN II rate is equally low and the ISM mass reaches $\approx 23\%$ of the total infalling mass (compared to less than $\approx 9\%$ in the standard model). The low iron injection rate by SN II and the build-up of primordial material in the volume lead to the desired slow enrichment of the halo ISM. After the ISM reached an average metallicity of [Fe/H] ≈ -1.3, the SF efficiency is changed by one order of magnitude and a star burst sets in which reaches a peak value of $\approx 50\,\mathrm{M}_{\odot}\,\mathrm{yr}^{-1}$. Obviously, this burst is an artifact of the sudden change in the SF efficiency and would be strongly diminished if the change in the SF efficiency parameter would be continuous. The SN II rate peaks shortly after the SFR and the available gas is rapidly consumed. Approximately 3 Gyr after the first SF event, the ISM mass dropped to 8% of the total infalling mass, which coincides with the value of the standard model at this time. From now on, the evolution proceeds virtually identical to the standard model. This is not surprising, since now the parameters are the same as in the standard case and the SFR (and consequently the SN rate) depends on the available gas mass.

Surprisingly, the enrichment of the ISM with α-elements is not influenced very much by the changes applied to our standard model. The star burst results in a small bump in the mean [α/Fe] ratios (at [Fe/H] ≈ -1.3) of approximately 0.1 dex due to the increased α-element input of Type II SNe. Considering the uncertainties in present day nucleosynthesis models (c.f. Paper II) and observational errors of $\approx$ 0.1 dex (on average), the LE model still is in agreement with observations.

Fig. 4.6 shows a comparison of the mean time-metallicity relation of the standard model (red line) with the detailed time-metallicity relation of the LE model (dots). The scatter in the age-metallicity relation of the LE model is due to local chemical inhomogeneities. This scatter is also present in the standard model but, for the sake of clarity, only its mean relation is shown. Approximately 3 Gyr after the first SF event (equivalent to 3.5 Gyr after the start of the simulation), both age-metallicities relations coincide. The early phase of the low SF efficiency model is characterised by a much slower iron enrichment than in the case of the standard model, followed by a “jump” in the age-metallicity relation due to the ensuing starburst. The apparent discontinuity would also disappear, if a continuously changing SF efficiency had been adopted.

Ages of a few very metal-poor halo stars are also plotted in Fig. 4.6 (with corresponding error-bars), namely CS 2289 − 052 ([Fe/H] = −3.1; age 15.6 ± 4.6 Gyr) and HD 115444 ([Fe/H] = −3.1; age 15.6 ± 4.6 Gyr) by Westin et al. (2000), CD 31082 − 001 ([Fe/H] = −2.9; age 14.0 ± 2.4 Gyr) by Hill et al. (2002), BD +17°3248 ([Fe/H] = −2.1; age 13.8 ± 4.0 Gyr) by

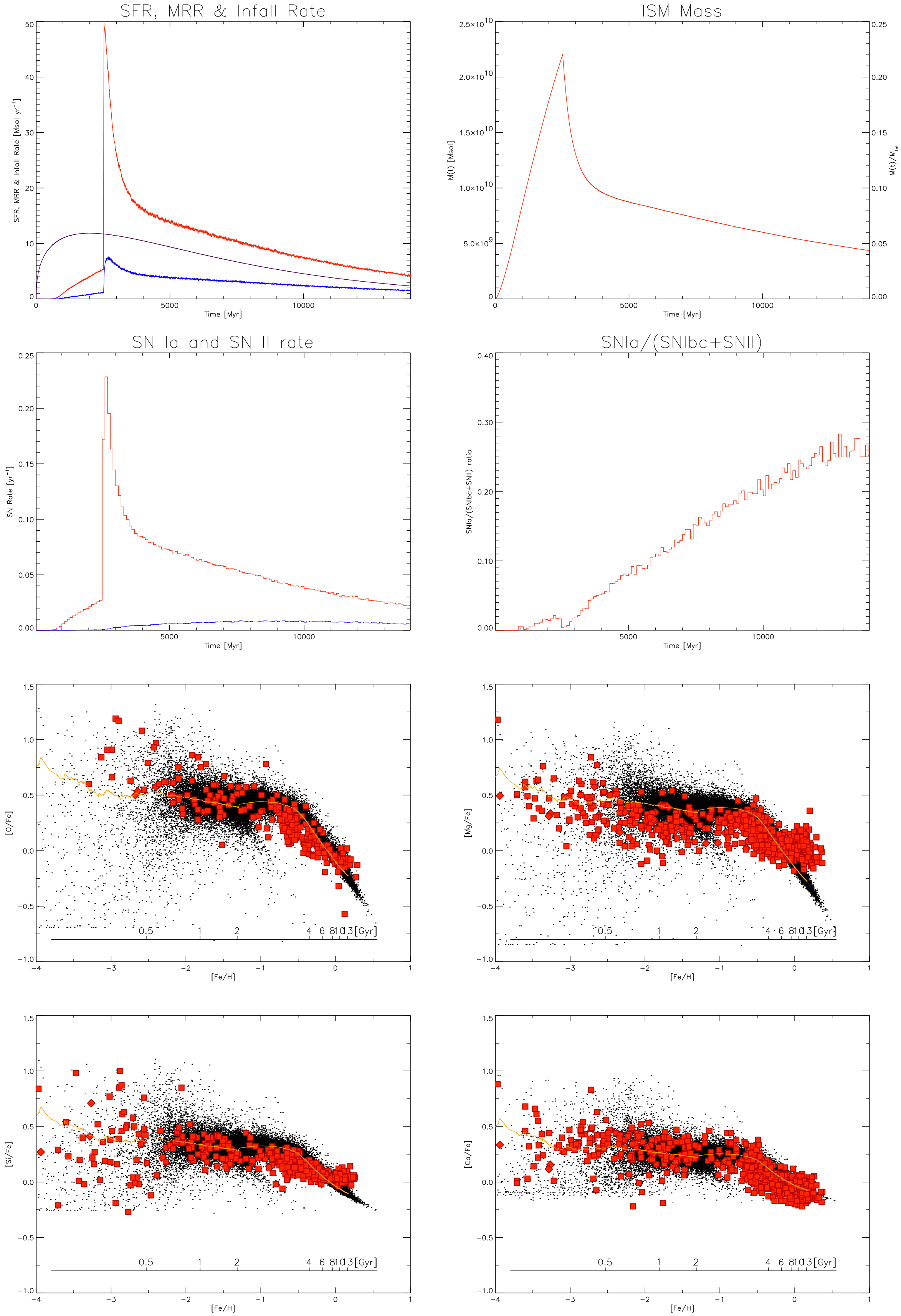

Fig. 4.5. Overview of the low SF efficiency (LE) model (compare to Fig. 4.1).

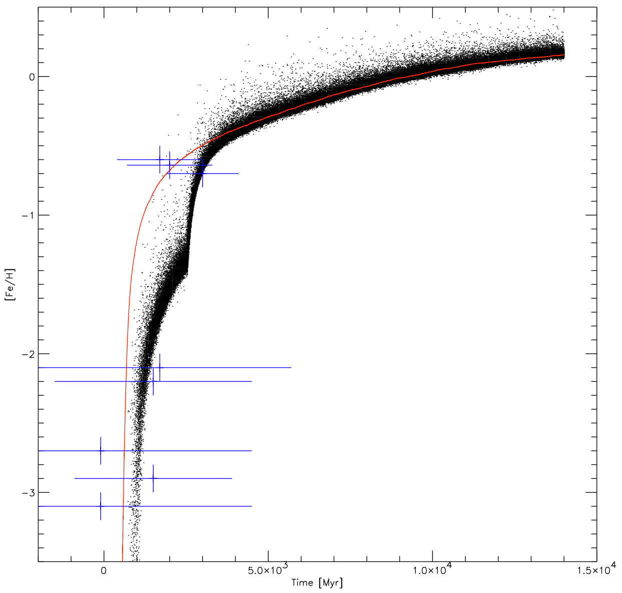

Fig. 4.6. Age-metallicity relations of the standard model (red line) and the low SF efficiency model (dots). The iron enrichment of the low SF efficiency model is much slower at early times compared to the standard model and the "jump" in the relation around 3.5 Gyr is due to the ensuing starburst. Ages of five halo stars and three thick disk stars are plotted, together with error bars. Due to uncertainties in the calibration of model predictions and observations, both models seem to be consistent with observations.

Cowan et al. (2002) and the mean of three stars in the globular cluster M 15 ([Fe/H] $= -2.2$; age 14.0 ± 3.0 Gyr) by Sneden et al. (2000b). Additionally three thick disk stars are plotted (Mashonkina & Gehren 2001): HD 3795 ([Fe/H] $= -0.6$; age 13.8 ± 1.3 Gyr), HD 10519 ([Fe/H] $= -0.6$; age 13.5 ± 1.3 Gyr) and HD 222794 ([Fe/H] $= -0.7$; age 12.5 ± 1.1 Gyr). In principle, the significant difference of both (model) age-metallicity relations at early times would allow us to test the hypothesis of a slow enrichment during halo formation. However, a straightforward comparison of model results and observational data is not possible for the following reasons: First, the error bars in age estimates are huge, especially for the very metal-poor halo stars. Second, ages of the thick disk stars were obtained by a completely different method (stellar evolution calculations vs. radioactive cosmochronometry), which is prone to different systematic errors than the one used for the very metal-poor halo stars. Third, model ages can only be transformed to "real" ages, if a specific cosmology is chosen to define the initial conditions. This is clearly beyond the scope of our simple model. Thus, any zero point adopted for ages of model stars and observed star is highly uncertain. Our model run stops after 14 Gyr, whereas two star are allegedly older than this. Due to the inhomogeneity of the ISM not even the time of solar system formation can be deduced accurately in our model: Stars of solar metallicity are be formed during (at least) 3 Gyr (see Fig. 4.6). For the present plot we chose 15.5 Gyr as zero-point for our age-metallicity relation, corresponding to the ages of CS $2289-052$ and HD 115444, since in this case the average age of the three most metal-poor stars coincides approximately with the first SF event in our model run. We conclude that, adopting this zero-point of the age-metallicity relation, both models seem to be acceptable.

The enrichment of the ISM with r- and s-process elements in the case of the LE model is shown in Fig. 4.7. Symbol are as in Fig. 4.4. Again, r-process elements are assumed to be produced by NSM, occurring at a very high rate (c.f. Sect. 4.2.2.d and 4.4.3). In the context of the LE model, the occurrence of s-process elements early on during Galaxy formation, can be easily explained by the slow enrichment of the halo ISM. Low mass stars now have time enough to reach their TP-AGB phase and to enrich the ISM with their s-process elements even at low metallicities. Note, that due to local chemical inhomogeneities stars with a major s-process contribution coexist with stars that are only enriched with r-process elements at these low metallicities. The ensuing burst then leads to a large increase in SN II events and thus also to a large increase of NSM events (or equivalently, SN II events which synthesize r-process elements). The [Ba^s/Eu] and [Ba/Eu] ratios therefore decrease sharply until, at the end of the burst, Ba enrichment is dominated again by s-process events.

Based on the results of this simple chemical evolution model, we tentatively suggest the following scenario of Galaxy formation: Due to the inefficient cooling ability of primordial gas, the SF efficiency during halo formation was low and the SFR probably did not exceed $\approx 5\,\mathrm{M}_\odot\,\mathrm{yr}^{-1}$. This, together with the infall of primordial material, lead to a slow iron enrichment of the halo ISM, giving low-mass stars time enough to pollute the ISM with s-process elements. Star formation in the halo ceased around [Fe/H] ≈ -1, approximately 2 Gyr after the first SF event, and some of the pre-enriched gas settled in the disk (it does not necessarily have to be the only source for the pre-

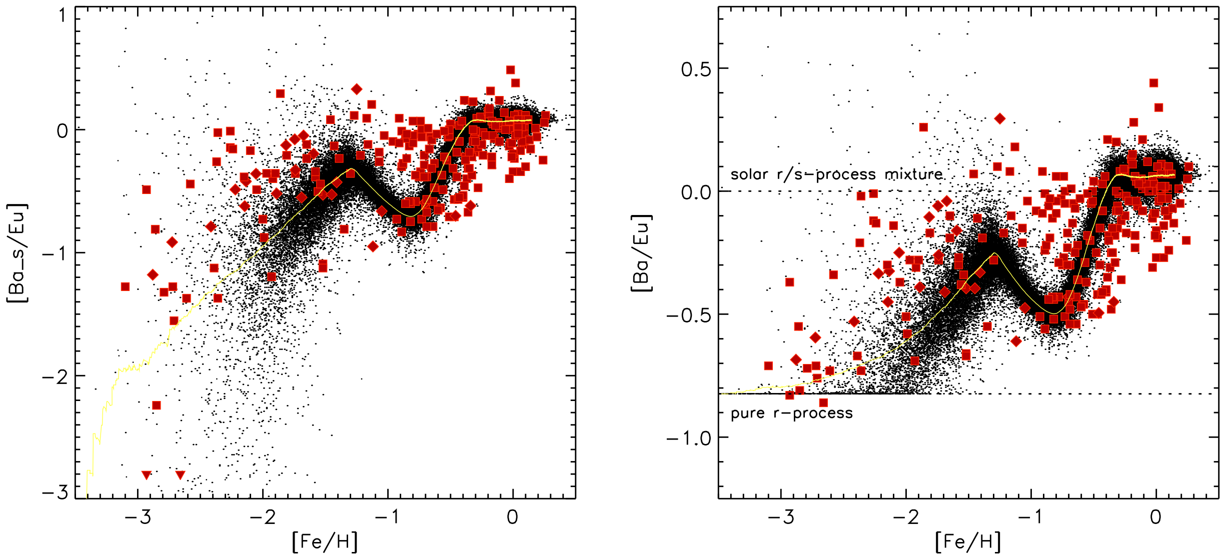

Fig. 4.7. [Ba^s/Eu] and [Ba/Eu] vs. [Fe/H] in stars compared to results of the low SF efficiency model. Symbols are as in Fig. 4.4. The contribution of s-process material to neutron capture elements at very low metallicities can be reproduced under the assumption of a low SF efficiency during halo formation.

enrichment of the disk). Since cooling of enriched gas is much more efficient than cooling of metal-poor gas, the SF efficiency in the forming disk was higher than in the halo. The increased injection rate of r-process elements lead to a decrease in [Ba^s/Eu]. However, local chemical inhomogeneities still permitted considerable scatter in [Ba^s/Eu] values (visible in Fig. 4.7 in the range, $-1 \le$ [Fe/H] ≤ -0.5). Approximately 2.8 Gyr after the first SF event, the disk ISM reached [Fe/H] ≥ -0.5 and Ba enrichment was dominated again by s-process events.

This formation scenario is in qualitative agreement with a chemo-dynamical formation model of a massive disk galaxy (Samland & Gerhard 2003). In their model, the collapse of the initial primordial gas cloud takes up to 3 Gyr, due to the stellar feedback and the initially shallow potential of the dark halo. The phase of low SF efficiency during the collapse (SFR below $5\,\mathrm{M}_\odot\,\mathrm{yr}^{-1}$ for the first 1.5 Gyr) is followed by an extended peak in the SFR (up to $50\,\mathrm{M}_\odot\,\mathrm{yr}^{-1}$). Furthermore, Samland & Gerhard (2003) found a sequential formation of halo, bulge and disk, with a (vertical) disk scale height that decreases with time, corresponding to the formation of the thick and thin disk.

In addition, there is some observational evidence for a slow enrichment of the halo ISM from globular cluster ages, which seem to have formed over an extended period of time (2 Gyr or more) with more metal-rich clusters formed at later times (Chaboyer et al. 1996). Also, Rocha-Pinto et al. (2000) found indeed evidence of an intermittent SF history in the Galaxy, although on smaller scales than the extensive burst encountered in the LE model.

However, we point out two discrepancies of model stars and observations in Fig. 4.7. First, the average [Ba^s/Eu] and [Ba/Eu] at metallicities [Fe/H] ≤ -1 are too low by $\approx$ 0.4 dex. This can most likely be attributed to the adopted s-process yields of Ba, since we did not include its strong metallicity dependence. On the other hand, a slight overestimate of Eu yields might also cause (at least part of) this underabundance. Second, in our model, s-process enrichment starts primarily around [Fe/H] ≈ -2.1 and not around [Fe/H] ≤ -2.5 as observations suggest. A SF efficiency even lower than adopted in our model will shift the start of s-process enrichment to lower metallicities. (Simultaneously, the difference in average [Ba/Eu] ratios of model stars and observations will decrease.) But consequently, halo formation would proceed even slower, which might not be realistic (see e.g. Mashonkina & Gehren 2001 who deduce a halo formation timescale of only $\approx$ 1 Gyr). Furthermore we note, that in our model the main s-process is assumed to occur in stars of up to $4\,\mathrm{M}_\odot$. A decrease of this upper mass limit down to $3\,\mathrm{M}_\odot$ would require an even more dramatic reduction of the early SF efficiency, since evolution time-scales of $3\,\mathrm{M}_\odot$ stars are approximately twice as long as those of $4\,\mathrm{M}_\odot$ stars.

Yet, although our simple model leaves room for improvement, we will use it in the following as basis for the comparison of SNe II and NSM as r-process sites. We emphasize in this context, that such a comparison can only be done if the timescales of halo formation in the model are (roughly) consistent with observations, since the early enrichment of the halo ISM with r- and s-process elements crucially depends on them.

4.5.2. SN II as dominating r-process sites

In this section, the enrichment of the ISM with neutron capture elements is discussed in the context of the LE model, i.e. assuming a low SF efficiency during halo formation followed by a burst as the SF efficiency suddenly increased. Dominating r-process sources are either lower-mass SNe II ($8 - 10\,\mathrm{M}_\odot$), displayed in Fig. 4.8, or higher-mass SNe II ($20 - 25\,\mathrm{M}_\odot$), displayed in Fig. 4.9. In both figures, the evolution of [Eu/Fe], [Ba/Fe], [Ba^r/Fe], [Ba^s/Fe], [Ba^s/Eu] and [Ba/Eu] are shown (from left to right). The last two panels may be compared to Figs. 4.4 and 4.7. Inverted triangles in the panels depicting [Ba^s/Fe] and [Ba^s/Eu] indicate observed stars with no s-process contribution. Note, that in the case of [Ba^s/Eu] only two inverted triangles are shown, since our observational sample does not contain stars more metal-poor than $[\mathrm{Fe/H}] \leq -3$ which have Eu abundances. Inverted triangles in the panel displaying [Ba^s/Fe] ratios belong to stars with $[\mathrm{Fe/H}] \leq -3$, for whom it was *assumed* that their Ba abundance does not contain any s-process contribution (see discussion in Sect. 4.4.2).

Apparently, Fig. 4.8 shows a slope in the abundances of r-process elements [r/Fe] (i.e. [Eu/Fe] and [Ba^r/Fe]) at metallicities below $[\mathrm{Fe/H}] < -3.5$, running just opposite to the one expected if lower-mass SNe II are the dominating r-process site (e.g. Travaglio et al. 1999). This slope is an artifact of the stochastic nature of our inhomogeneous chemical evolution model. Here, the first two SN II events had progenitors in the mass-range $8 - 10\,\mathrm{M}_\odot$, which locally enriched the ISM with r-process elements but did not eject any Fe. Only later on did core-collapse SNe with masses $> 10\,\mathrm{M}_\odot$ contribute iron to the enrichment of the ISM, so that regions with high [r/Fe] ratios existed for some time. Although this is undesired, a more physical SF description (i.e. following the collapse and fragmentation of clouds) clearly goes beyond the scope of our model. However, [r/Fe] ratios soon converge to the average [r/Fe] ratios of metal-poor halo stars and from then on give a good fit to observations.

If higher-mass SNe II are the dominant contributors to r-process nucleosynthesis, then [Eu/Fe] and [Ba^r/Fe] ratios are evenly distributed (as can be seen in Fig. 4.9). The main difference to the case of lower-mass SNe II is the more pronounced scatter in [r/Fe] ratios, so that the slight discontinuity introduced by the star burst at $[\mathrm{Fe/H}] \approx -1.3$ is almost undetectable. Note, that there are also some model stars with very low [Eu/Fe] and [Ba^r/Fe] ratios, which are not observed in reality. This is most likely due to observational constraints, since in this case Eu and Ba lines may be too weak to be detectable (c.f. the observational limits given in Travaglio et al. 2001).

On the other hand, slopes visible in [Ba/Fe], [Ba^s/Fe], [Ba^s/Eu] and [Ba/Eu] (in both Figs. 4.4 and 4.7) are real, since at the time of first s-process injection by TP-AGB stars, the ISM was already pre-enriched with r-process elements due to SN II events. These occur on a timescale approximately ten times faster than the one of s-process events. As already discussed in Sect. 4.5.1, the fit of model stars to [Ba^s/Eu] and [Ba/Eu] is not perfect, but gives a good representation of the trends visible in observations. The dip in [Ba/Fe], [Ba^s/Fe], [Ba^s/Eu] and [Ba/Eu] at $[\mathrm{Fe/H}] \approx -1.3$ is due to the burst of star formation, which leads to a sudden increase in Fe and Eu production (short SN II timescale), whereas the injection of s-process elements was delayed (long low mass star timescale). As soon as the low mass stars reach their TP-AGB phase, Ba synthesized in the s-process is injected into the ISM and Ba abundances rise again. The location of the "dips" and "cusps" in the Ba abundances strongly depends on the SF efficiencies before and after the burst in our model and the time of the burst. A SF efficiency somewhat lower than the one adopted in the present model at early times together with a *gradual* increase at later times (instead of the sudden burst) might improve the fit considerably. Note, that the dips and cusps seen in observed [Ba^s/Fe], and [Ba^s/Eu] (and marginally also in [Ba/Fe] and [Ba/Eu]) are not visible in [Eu/Fe] and [Ba^r/Fe] abundances. It is a

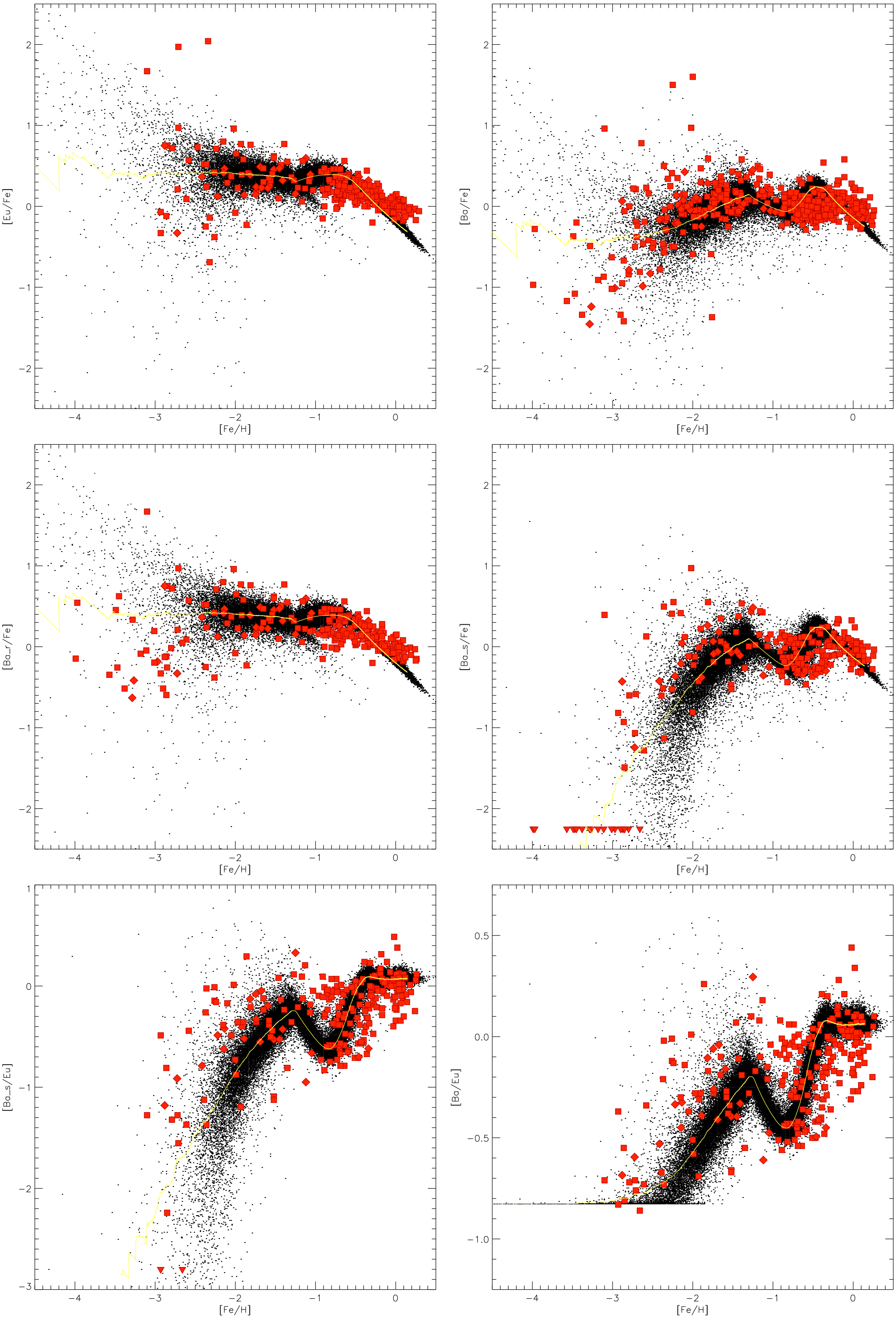

Fig. 4.8. Evolution of neutron capture element abundances as function of metallicity [Fe/H]. Lower-mass SN II ($8 - 10\,\mathrm{M}_\odot$) are assumed to be the dominating r-process sources. Symbols are as in Fig. 4.4.

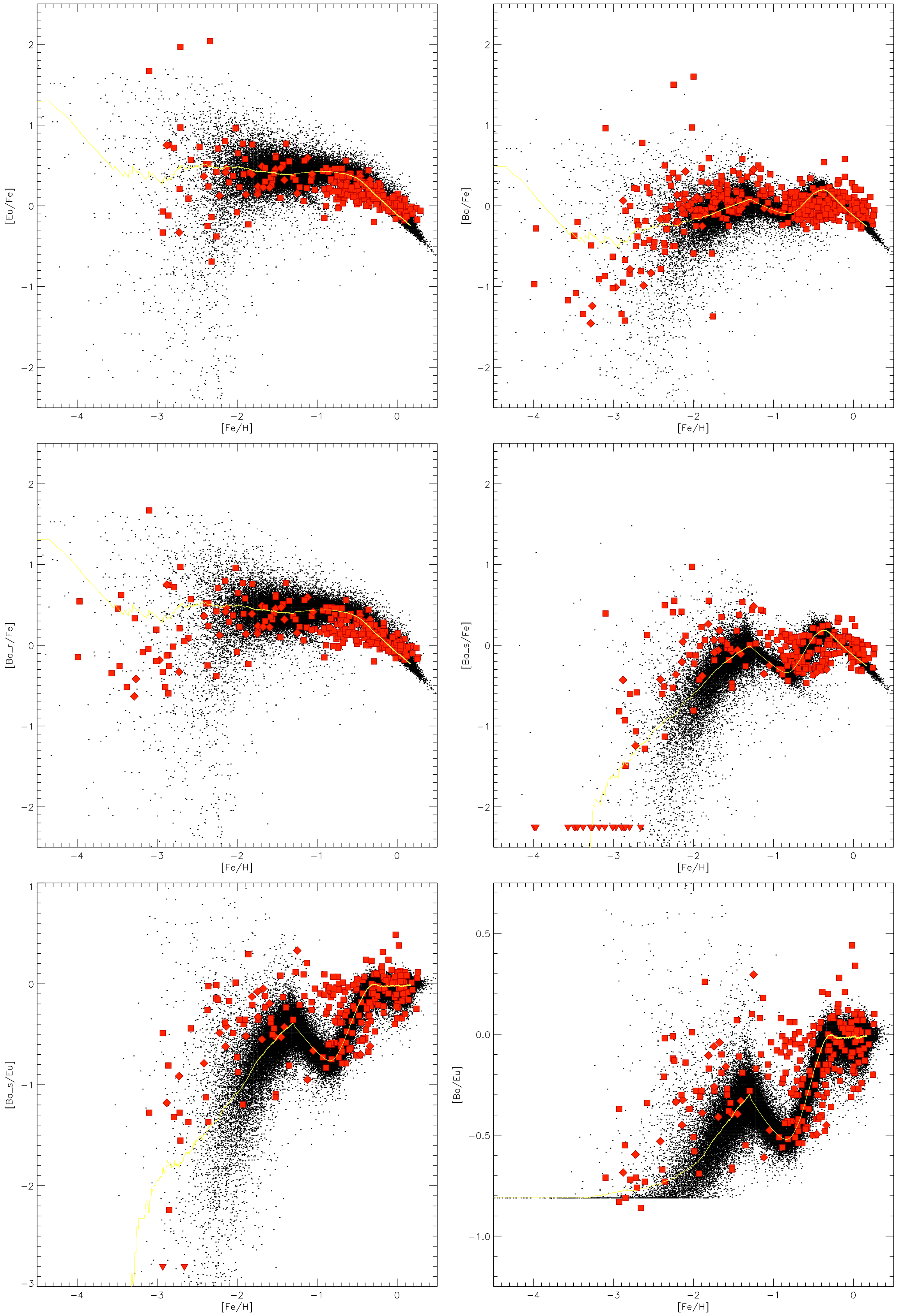

Fig. 4.9. Evolution of neutron capture element abundances as function of metallicity [Fe/H]. Higher-mass SN II (20 − 25 $M_\odot$) are assumed to be the dominating r-process sources. Symbols are as in Fig. 4.4.

unique feature coupled to the different timescales of r- and s-process production.

Since our sample of stars consists of observations made by different authors, different systematic errors may distort the true distributions of neutron capture element abundances as function of metallicity. Furthermore, the determination of r- and s-process contributions to Ba abundances in observed stars introduces another uncertainty. This raises the question if the dips and cusps seen in s-process abundances are statistically significant. Our scenario (i.e. low SF efficiency in the halo, increased SF efficiency in the disk) would be strongly supported, if these features are present in abundances of other elements that are *dominantly* produced in the main s-process. Neutron capture elements with a substantial r-process contribution are not suited for this kind of analysis, since in this case the signature might easily be drowned in the errors introduced by disentangling the r- and s-process fractions. Apart from Ba, only Sr and La have a solar system s-process fraction of more than 80% (Burris et al. 2000). Unfortunately, Sr is suspected to have a prominent contribution from the *weak* s-process (probably occurring in the cores of massive stars) to its abundance (e.g. Mashonkina & Gehren 2001) and to date there are not many observations of La in metal-poor stars. Thus, a large, homogeneously analyzed data set of neutron capture element abundances (preferably ranging from solar to very low metallicities and including observations of Ba, La and Eu) is needed to test the scenario put forth in this work. However, even if the features seen in [Ba^s/Fe] abundances around solar metallicities turn out to not be real, the low SF efficiency during halo formation may still be needed to explain the occurrence of s-process elements at very low metallicities.

In summary, core-collapse SNe seem to be a valid source of r-process elements and the distribution of model stars in Figs. 4.4 and 4.7 are virtually identical. Also note, that the initial scatter in [el/Fe] ratios strongly depends on the yields as function of progenitor mass. We have shown in Paper II, that the progenitor mass dependence of stellar Fe yields are not known to date and that slopes in the distribution of element abundances can easily be introduced by a given choice of Fe yields. Additionally, the progenitor mass dependence of r-process yields in this work is chosen completely *ad hoc*. In view of these uncertainties, we conclude in accordance with Ishimaru & Wanajo (1999) that it is not possible to rule out either lower-mass or higher-mass SNe within the framework of inhomogeneous chemical evolution.

4.5.3. NSM as dominating r-process sites

The enrichment of the ISM with neutron capture elements in the case of NSM acting as major r-process sources is shown in Fig. 4.10. As already mentioned in Sect. 4.2.d, 15 models were done in total, assuming NSM rates ranging from $2 \cdot 10^{-6}\,\mathrm{yr}^{-1}$ to $2 \cdot 10^{-2}\,\mathrm{yr}^{-1}$ and coalescence time-scales ranging from $1 - 100$ Myr (see Table 4.2). The case shown in Fig. 4.10 was calculated with a NSM rate of $2 \cdot 10^{-4}\,\mathrm{yr}^{-1}$, a total of $10^{-3}\,\mathrm{M}_{\odot}$ of ejected r-process matter and a coalescence time-scale of 10 Myr, and is representative for the other models with parameters listed in Table 4.2. A condensed overview of all models is shown in Figs. 4.11, 4.12 and 4.13. Note, that in all cases a low SF efficiency during halo formation was assumed.

The evolution of [Eu/Fe] and [Ba^r/Fe], visible in the first two panels on the left in Fig. 4.10, is qualitatively different to the case in which r-process nucleosynthesis occurs in SNe II (see Figs.4.8 and 4.9):

First, r-process nuclei appear at the earliest around [Fe/H] ≈ -2.5, while r-process elements such as Eu are observed at [Fe/H] $= -3$ and probably even down to [Fe/H] $= -4$ in the case of Ba^r. The reason for this late injection of r-process matter is, that in our model the decisive parameter to obtain a given NSM rate is the probability P_{NSM} which, in this case, is set to $2 \cdot 10^{-3}$ (see Sect. 4.2.d). This means, that on average ≈ 250 SNe II events occur before the first NSM event. Thus, NSM inject their r-process nuclei into an ISM already pre-enriched by SNe II. The lower the NSM rate, i.e. the lower P_{NSM}, the later (in metallicity) the occurrence of r-process elements. Note, that the case discussed here already assumes a NSM rate at the upper limit given by observational constraints: Estimates range from $8 \cdot 10^{-6}\,\mathrm{yr}^{-1}$ (van den Heuvel & Lorimer 1996) to $\left(10^{-6} - 3 \cdot 10^{-4}\right)\,\mathrm{yr}^{-1}$ (Belczynski et al. 2002) and Kalogera & Lorimer (2000) even give an *upper limit* of $\left(7.5 \cdot 10^{-7} - 1.5 \cdot 10^{-5}\right)\,\mathrm{yr}^{-1}$. Furthermore, the coalescence timescale adopted in this model is only 10 Myr, which is considerably lower than the classical estimate of $100 - 1000$ Myr (e.g. Portegies Zwart & Yungel'son 1998; Fryer et al.

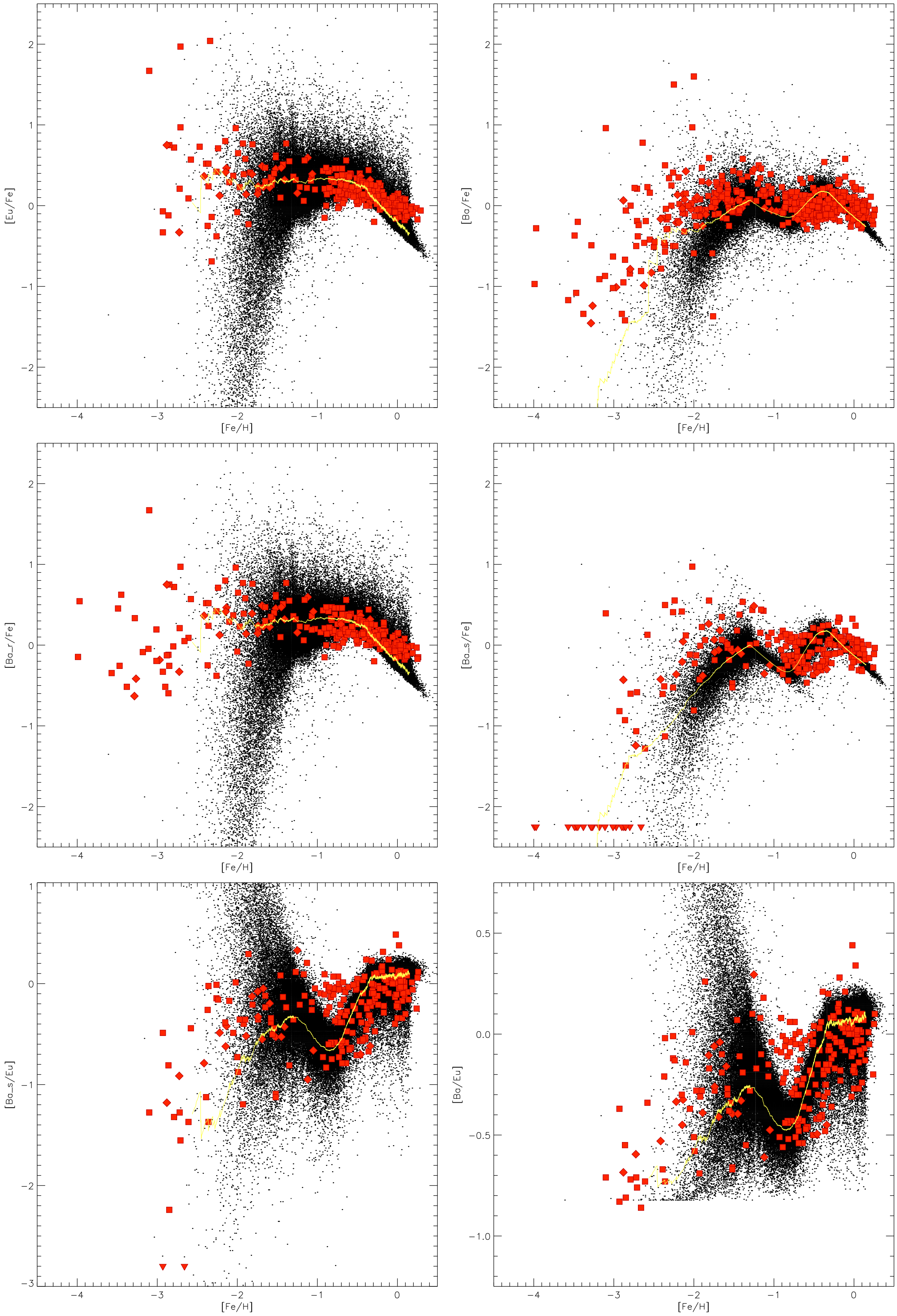

Fig. 4.10. Evolution of neutron capture element abundances as function of metallicity [Fe/H]. NSM occurring at a global rate of $2 \cdot 10^{-4}\ \mathrm{yr}^{-1}$ are assumed to be the dominating r-process sources. Symbols are as in Fig. 4.4.

1999b). To the contrary, Belczynski et al. (2002) suggest the existence of a *dominating* population of short lived neutron star binaries with merger times less than 1 Myr. However, since on average a large number of SNe II events occur before the first NSM event, NSM with coalescence timescales of up to 10 Myr can be considered to occur instantaneous. The late injection of r-process nuclei by NSM is the reason why we did not consider coalescence timescales of the order of 1 Gyr: Even in our low SF efficiency model, the metallicity of the ISM reached [Fe/H] ≈ -1.5 one Gyr after the first SF event, clearly not consistent with observations.

Second, there is a prominent tail of model stars with very low [r/Fe] ratios at [Fe/H] $= -2$. At the same time, the enrichment of the s-process fraction of Ba is slightly more advanced than the enrichment of r-process nuclei, so that a tail with high [Ba^s/Eu] and [Ba/Eu] ratios develops. This tail is seemingly not present in observations, which speaks against NSM as major r-process sites. However, it might be possible that this feature is at present not observable due to intrinsically low Eu abundances (see Travaglio et al. 2001 for detection limits).

Third, even at late times in the enrichment of the ISM (Fe/H] ≥ -1), the scatter in possible [r/Fe] ratios is of the order $1.0 - 1.5$ dex, whereas observations of [Eu/Fe] and [Ba^r/Fe] abundances show a scatter of approximately $0.2 - 0.3$ dex. This important feature does not occur in Figs. 4.8 and 4.9, since the total amount of r-process matter ejected in a single NSM event (here 10^{-3} M$_\odot$) is much larger than the typical r-process yield of SNe II ($\approx 10^{-5}$ M$_\odot$). Thus NSM events may be the cause of significant local chemical inhomogeneities, in spite of the advanced enrichment of the ISM with r-process nuclei.

These aspects strongly argue against NSM as *dominating* r-process source, especially since the parameters used for the model in discussion are at the upper limit set by observational constraints. Lower NSM rates and, consequently, larger ejecta masses, only aggravate the problems mentioned above. This is demonstrated in Figs. 4.11, 4.12 and 4.13, which show [Ba^r/Fe] (left-hand side) and [Ba^s/Eu] (right-hand side) as function of [Fe/H] for the five NSM rates and the coalescence timescales given in Table 4.2. The NSM rates adopted in the models decrease from top to bottom by one order of magnitude for each panel, i.e. from $2 \cdot 10^{-2}\,\mathrm{yr}^{-1}$ for the uppermost panel down to $2 \cdot 10^{-6}\,\mathrm{yr}^{-1}$ for the lowest panel. Figs. 4.11, 4.12 and 4.13 assume coalescence timescales of 1, 10 and 100 Myr, respectively.

The dramatic changes in the distribution of r-process abundances occurring with decreasing NSM rate are clearly visible in the sequence of plots in Figs. 4.11, 4.12 and 4.13. In the uppermost panels (NSM rate $2 \cdot 10^{-2}\,\mathrm{yr}^{-1}$), r-process nuclei first appear around [Fe/H] $= -4$, in contrast to [Fe/H] $= -1$ in the panels at the bottom (NSM rate $2 \cdot 10^{-6}\,\mathrm{yr}^{-1}$). Simultaneously, the scatter in [Ba^r/Fe] and [Ba^s/Eu] at solar metallicity in the top panel, which is of the same order as the one observed, increases to more than 2 dex in the lowest panel, clearly not consistent with observations.

Contrary to expectations, the impact of the coalescence timescale t_c on the distribution of r-process nuclei is rather small. This is surprising, since a large value of t_c results in a delayed injection of r-process matter into the ISM. The largest differences are observed in the uppermost three panels of Figs. 4.11 and 4.13, corresponding to $t_c = 10^6$ yr and $t_c = 10^8$ yr, respectively. Virtually no difference can be seen between the cases $t_c = 10^6$ yr and $t_c = 10^7$ yr (Figs. 4.11 and 4.12). However, this can be understood by recalling that in these models a long halo formation timescale is assumed and that the enrichment of the ISM proceeds very slowly at the beginning of Galaxy formation: It takes ≈ 200 Myr to enrich the ISM from [Fe/H] $= -4$ to [Fe/H] $= -3$, so that coalescence timescales of 1 Myr or 10 Myr hardly make any difference, while a timescale of 100 Myr is of the same order as the halo enrichment timescale, resulting in a slight shift of the first r-process matter injection to higher metallicities. (Note, that, on the basis of these considerations, coalescence timescales of the order 1 Gyr clearly are not consistent with the occurrence of r-process nuclei early on during Galaxy formation.) If, on the other hand, the first injection of r-process matter occurs at very late times due to low NSM rates, the ISM already reached metallicities [Fe/H] ≥ -2. Further enrichment up to [Fe/H] $= -1$ then takes more than 1 Gyr, so that in this case even a coalescence timescale of 100 Myr does not show up as significant shift of first r-process matter injection to higher metallicities.

Thus, we conclude that NSM as dominating r-process contributors have to respect stringent requirements, which most likely are not fulfilled in reality: High NSM rates of the order $10^{-2}\,\mathrm{yr}^{-1}$ are required

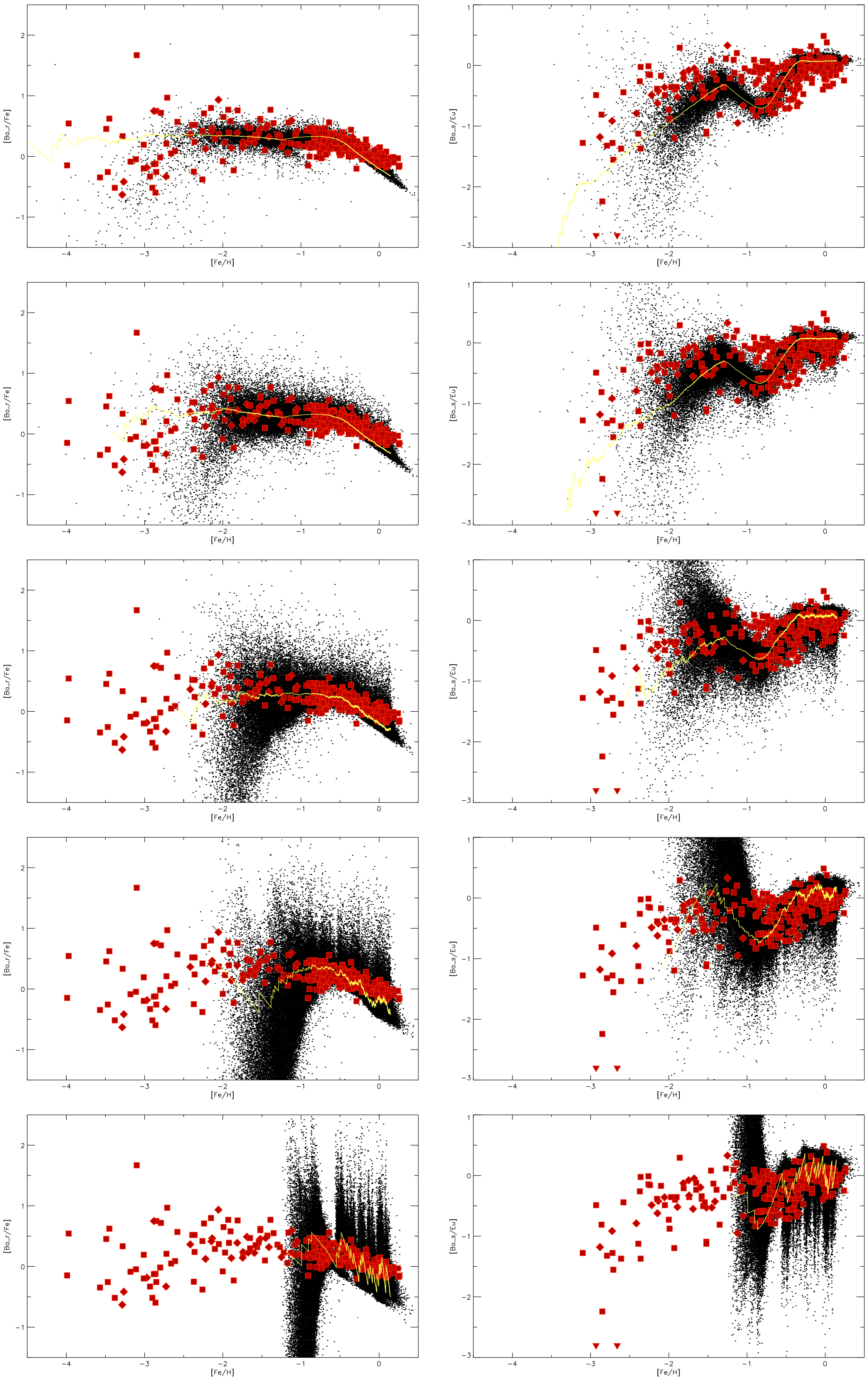

Fig. 4.11. [Ba^r/Fe] and [Ba^s/Eu] vs. [Fe/H] for the NSM rates $2 \cdot 10^{-2}$ yr^{-1}, $2 \cdot 10^{-3}$ yr^{-1}, $2 \cdot 10^{-4}$ yr^{-1}, $2 \cdot 10^{-5}$ yr^{-1} and $2 \cdot 10^{-6}$ yr^{-1} (from top to bottom). The coalescence timescale adopted in these cases is $t_c = 10^6$ yr.

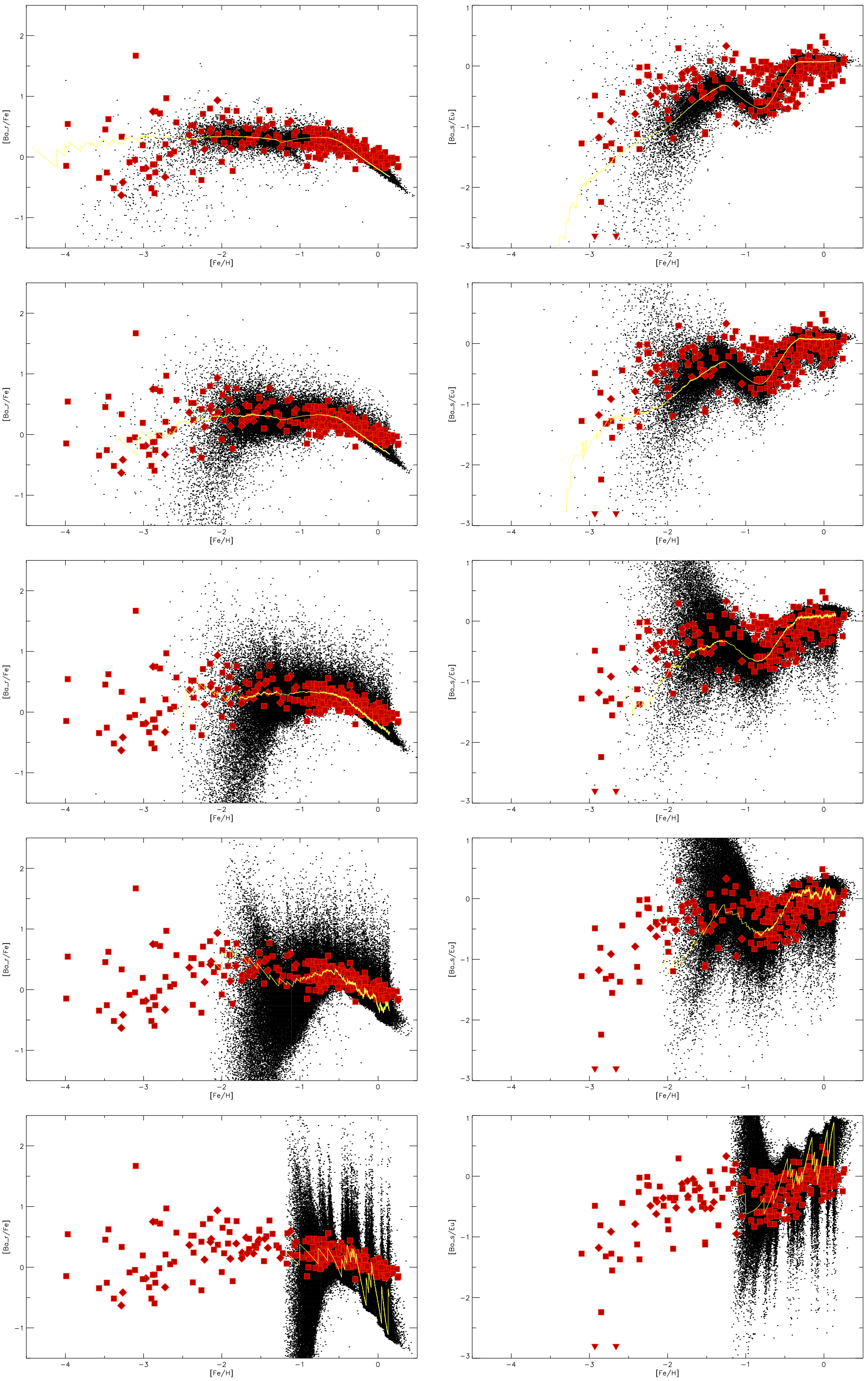

Fig. 4.12. Same as Fig. 4.11 but with $t_c = 10^7$ yr.

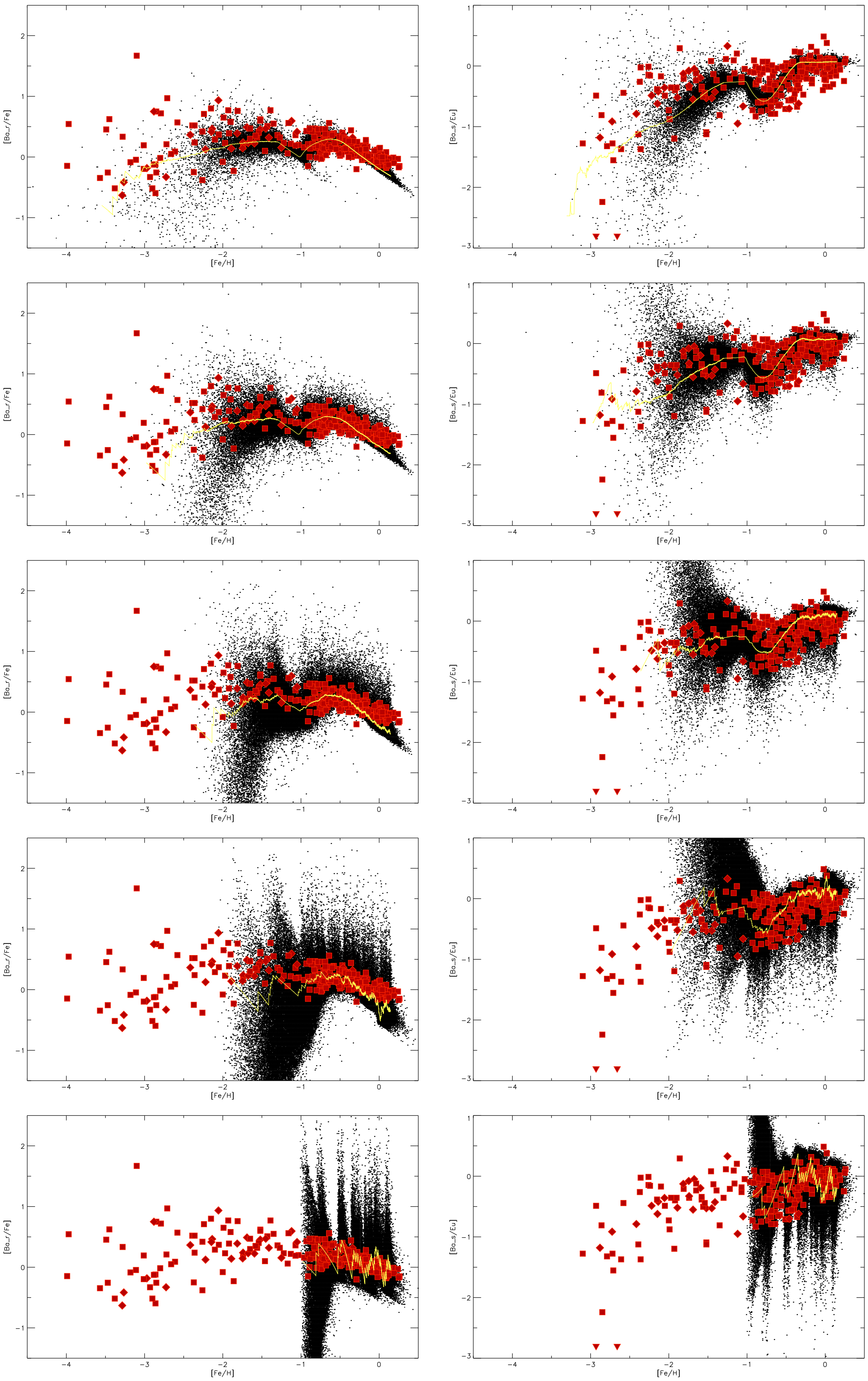

Fig. 4.13. Same as Fig. 4.11 but with $t_c = 10^8$ yr.

to account for the early appearance of r-process nuclei in the ISM, even if a slow halo formation scenario is assumed. Consequently, the amount of r-process matter ejected in a NSM event has to be of the order $10^{-5}\,\mathrm{M}_\odot$, lest the total inventory of r-process nuclei in the Galaxy is exceeded. Additionally, the coalescence timescale of a large fraction of neutron star binaries has to be of the order 1-10 Myr or at the most 100 Myr. If these constraints are indeed respected in reality, then the enrichment of the ISM with r-process matter by NSM is almost indistinguishable from the one caused by core-collapse SNe in the context of inhomogeneous chemical evolution (compare Figs. 4.8 and 4.9 with the uppermost panels of Figs. 4.11, 4.12 and 4.13). Note, that in this case the properties of NSM (i.e. rates and ejected r-process matter) are comparable to the properties of SNe II that (may) give rise to r-process nucleosynthesis.

However, it seems unlikely that NSM fulfill these conditions, which suggests that NSM are ruled out as major r-process source. On the other hand, NSM occurring at low rates and with low ejecta masses of the order $10^{-4} - 10^{-5}\,\mathrm{M}_\odot$ may still contribute to the enrichment of the ISM with r-process nuclei. In this case, the impact of NSM on r-process nuclei enrichment would be almost negligible compared to the fast injection of r-process matter by SNe II.

4.6. Conclusions

In this work, we study the enrichment of the interstellar medium with neutron capture elements in the framework of inhomogeneous chemical evolution and present for the first time a comparison between lower-mass SNe II ($8 - 10\,\mathrm{M}_\odot$), higher-mass SNe II ($\geq 20\,\mathrm{M}_\odot$) and NSM as major r-process sites. In these scenarios, r-process nucleosynthesis occurs on short timescales (on the order of $10-20$ Myr, with the possible exception of NSM), whereas s-process nucleosynthesis occurs in lower mass TP-AGB stars on much longer timescales (on the order of $300 - 400$ Myr). Thus, by comparing abundances of elements formed mainly by the r-process to elements formed mainly by the s-process, important constraints on halo formation timescales and early Galaxy evolution can be gained. Typical elements in this respect are Eu (r-process) and Ba ($\approx 85\%$ s-process, $\approx 15\%$ r-process).

There is strong evidence from the pattern of neutron capture element abundances in metal-poor halo stars, that r-process nucleosynthesis for elements heavier than Ba ($56 \leq Z \leq 72$) is robust, i.e. occurs under well defined conditions. Thus, it is possible to disentangle the r- and s-process contribution to observed Ba abundances, as long as Eu abundances are known. Applying this technique to a sample of stars, we find that s-process elements are present even at very low metallicities ([Fe/H] ≤ -2.5), in accordance to Burris et al. (2000) and Aoki et al. (2000). This finding strongly constraints the star formation efficiency during halo formation. The metallicity of the halo ISM is required to remain below [Fe/H]$= -2.5$ during the first ≈ 300 Myr of early Galaxy evolution to allow lower mass stars ($1 - 4\,\mathrm{M}_\odot$) to reach their TP-AGB phase and s-process nucleosynthesis to start.

Here, we present an inhomogeneous chemical evolution model that takes into account a low SF efficiency during halo formation (SFR stays below $5\,\mathrm{M}_\odot\,\mathrm{yr}^{-1}$), followed by an artificially induced SF burst (up to $50\,\mathrm{M}_\odot\,\mathrm{yr}^{-1}$) approximately 2 Gyr after the first SF event. This model reproduces the early enrichment of the ISM with s-process elements and the cusps and dips seen in the s-process contributions to Ba abundances. We suggest, that these features are signatures of two distinct stellar populations: A population of halo stars forming on a timescale of up to 3 Gyr (in opposition to a fast halo formation scenario, see e.g. Mashonkina & Gehren 2001), and a population of thick/thin disk stars which mainly formed during and since the SF “burst”. Due to the low SFR during halo formation, s-process elements appear at very low metallicities and reach approximately solar [Ba^s/Fe] and [Ba^s/Eu] abundances at the end of halo formation. The enriched ISM settles in the disk, SF in the halo ceases and the SF efficiency in the disk increases (compared to the SF efficiency in the halo). The higher SFR in the disk leads to an increased injection rate of r-process and Fe peak elements and [Ba^s/Fe] and [Ba^s/Eu] abundances decrease again. Later on, these abundance ratios again reach solar values, due to the delayed s-process production in TP-AGB stars. Note that the decisive processes are a low SF efficiency during halo formation and a higher SF efficiency in the disk due to the better cooling ability of enriched gas. The burst itself is an artifact of our simple model and is probably not required to reproduce the abundances of s-process elements.

Yet it is surprising that the low SF efficiency during halo formation and the artificial burst at later times leave signatures in abundances of α-elements, which are barely detectable to date. The sudden increase in [α/Fe] due to the SF burst is of the order 0.1 dex, approximately equal to (random) observational errors at low metallicities. Furthermore, the observational sample used in this work consists of observations of a large number of different authors, introducing unknown systematic errors into the analysis. Another diagnostic of our scenario is the shape of the age-metallicity relation. However, stellar ages are even more uncertain than abundance determinations and models with fast and slow halo formation timescales seem equally probable. The most promising way to test the hypothesis of two distinct stellar populations forming at low (halo) and high (thin/thick disk) efficiencies is to look at other neutron capture elements produced mainly by the main s-process. Our scenario would be strongly supported, if the dips and cusps visible in [Ba^s/Eu] would also be present in abundances of other s-process elements. Lanthanum seems to be the best element for this test, since it is produced by the main s-process and less than 20% of the solar La abundance is of r-process origin. Strontium, on the other hand, is not suited for this kind of analysis, since a large fraction of its abundance is suspected to be synthesized by the *weak* s-process. In addition, it does not belong to the group of neutron capture elements that are also formed in a robust r-process source (i.e. $Z \geq 56$), making a disentangling of r- and s-process contributions difficult. Thus, a homogeneous set of Ba, La and Eu abundance determinations ranging from stars of solar to very low metallicities is needed to reliably test our scenario and to set a lower limit on the occurrence of s-process elements in the ISM. Yet, independent of the later evolution, a low SF efficiency during halo formation seems to be mandatory to account for s-process elements at low metallicities

The model assuming a low SF efficiency during halo formation then is used to investigate the impact of lower-mass SNe II, higher-mass SNe II and NSM as dominating r-process sources on the enrichment of the interstellar medium with r-process elements. Due to the large uncertainties inherent in the progenitor mass dependence of iron yields in SNe II, it is not possible to rule out either lower-mass SNe II or higher-mass SNe II as dominant r-process site from the point of view of inhomogeneous chemical evolution. The distribution of r-process abundances in model stars is virtually indistinguishable in both cases and fit observations well. Additional uncertainties are introduced by the fact, that r-process yields of SNe II are not known. Here, they were determined in such a way that the average [r/Fe] abundances in metal-poor halo stars are reproduced.

On the other hand, NSM seem to be ruled out as major r-process source. Since the NSM rate is much lower than the rate of SNe II acting as r-process source, their r-process yield ($\gtrsim 10^{-3}\,\mathrm{M}_\odot$) is about two orders of magnitudes higher than the r-process yield of typical SNe II ($\approx 10^{-5}\,\mathrm{M}_\odot$). Thus, due to the low NSM rate, the injection of r-process nuclei into the interstellar medium occurs very late during Galaxy formation ([Fe/H] ≈ -2.5), whereas r-process elements are already present at [Fe/H] $= -3$ and probably even at [Fe/H] $= -4$. The late occurrence of r-process elements furthermore leads to prominent “tails” in the distribution of [r/Fe] and [Ba^s/Eu], which are seemingly not consistent with observations. (However, it might be possible that these tails are not observable to date). Additionally, due to the large r-process yield, considerable chemical inhomogeneities are present even at solar metallicity. The scatter in [r/Fe] is predicted to be of the order $1.0 - 1.5$ dex, whereas a scatter of only $0.2 - 0.3$ dex is observed. NSM as major r-process sources are only consistent with observations under the following conditions: First, they occur at rates about two orders of magnitude higher than given by observational estimates. Second, a *dominant* part of the NSM population has coalescence timescales shorter than approximately 10 Myr. Third, the total amount of ejected r-process matter is about two orders of magnitudes lower than present estimates, namely $\approx 10^{-5}\,\mathrm{M}_\odot$. Under these conditions, the enrichment of the ISM with r-process elements is indistinguishable to the enrichment of r-process elements dominated by SNe II. However, it seems highly unlikely that NSM fulfill these conditions, which suggests that NSM are ruled out as major r-process source. Nevertheless, it is still possible that they contribute to the enrichment of the ISM, if they occur on a low rate and the total r-process matter ejected is of the order $10^{-4} - 10^{-5}\,\mathrm{M}_\odot$.

Thus, we conclude, that the *exact* astrophysical nature of r-process sites still remains a mystery, since it is not possible to distinguish between neutron capture element abundance patterns resulting from lower-mass SNe II ($8 - 10\,\mathrm{M}_\odot$) and the ones from higher-mass SNe II ($\geq 20\,\mathrm{M}_\odot$) in the framework of inhomogeneous chemical evolution. However, the present investigation suggests that core-collapse SNe are much more likely to be the *dominant* r-process sites than coalescing neutron star binaries, which at least reduces the list of possible major contributors of r-process nuclei to the enrichment of the interstellar medium.

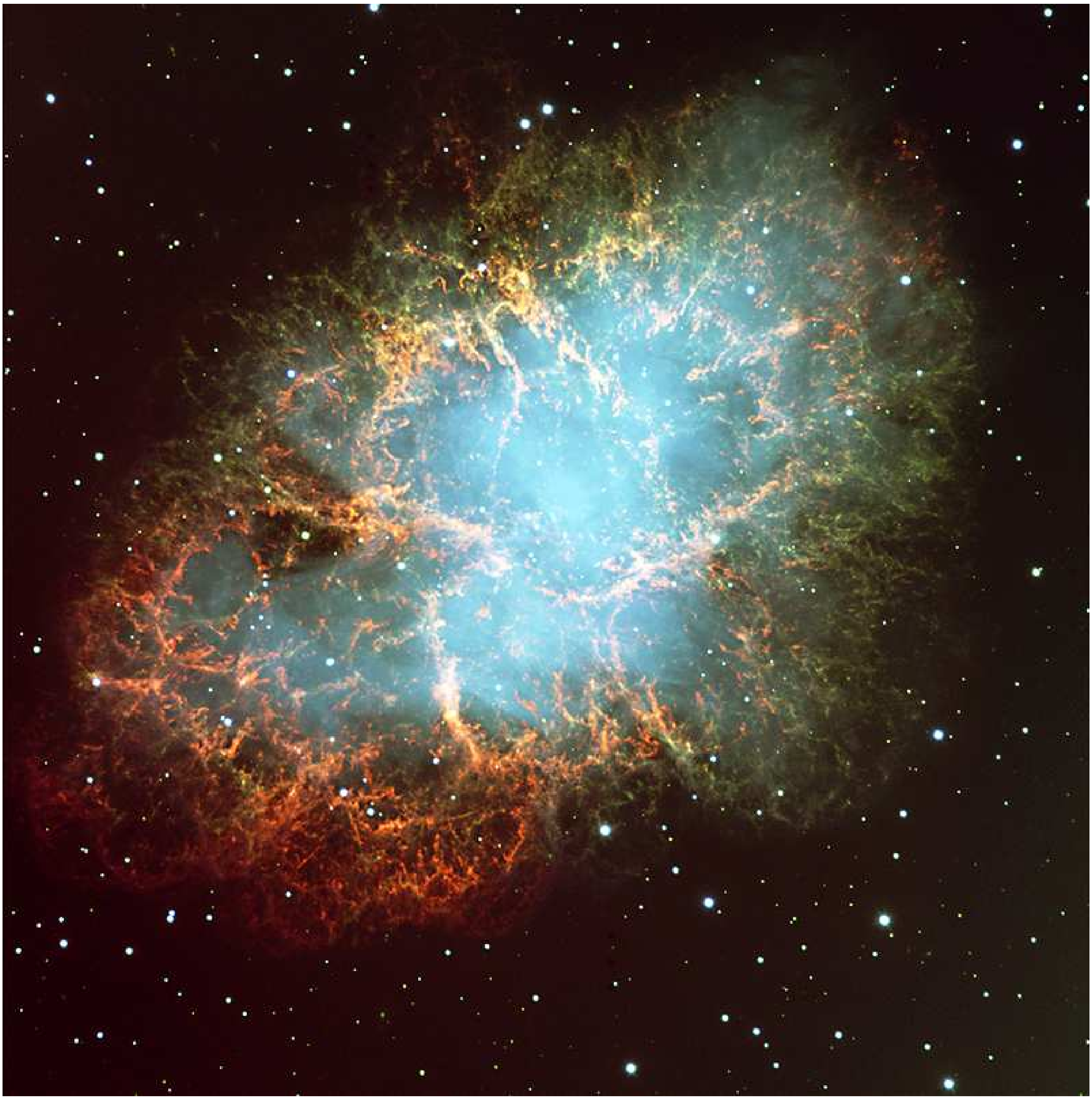

5

Conclusions

Observations of very metal-poor stars suggest that the interstellar medium of the galactic halo was chemically inhomogeneous in the earliest phases of Galaxy formation. This can be seen in the sometimes considerable scatter in element abundances [el/Fe] (e.g. for α- and r-process elements) of very old stars with the same metallicity [Fe/H]. For some elements (such as Si, Mg, Ca, Ba or Eu) the scatter is of the order of 1.0 dex or more, which is much larger than the error of 0.1-0.2 dex generally attributed to abundance determinations. The large scatter in element abundances therefore indicates that there exist intrinsic differences in the chemical compositions of metal-poor halo stars. The decrease in scatter observed at higher metallicities is consistent with local chemical inhomogeneities in the early phases of ISM enrichment, since mixing processes in the ISM tend to average out the element abundances in the course of the further evolution of the Galaxy.

Classic chemical evolution models are not able to simulate the scatter in element abundances of the metal-poor ISM and its decrease with increasing metallicity since they assume that the ISM is well mixed at all times. But the observed scatter has important implications for nucleosynthesis calculations of core-collapse SNe: The most metal-poor stars may have formed out of gas that was enriched by single SNe II originating from stars of Population II or Population III. Thus such stars are fossil records of the stellar yields of single core-collapse SNe with different masses and can be used to directly test nucleosynthesis calculations. A deeper understanding of early halo enrichment therefore requires that the assumption of a well mixed ISM at all times has to be dropped.

To this end I developed a stochastic chemical evolution model which is able to resolve local chemical inhomogeneities in the ISM. The model and its results are described in detail in this work and the main results are summarized in the following.

The evolution of the ISM can be roughly divided into four different stages:

1. At the beginning of Galaxy formation and up to metallicities [Fe/H] ≈ -3, the ISM is unmixed and dominated by local chemical inhomogeneities caused by SNe II. The scatter in element abundances is directly determined by the stellar yields of core-collapse SNe.
2. A transition from the unmixed to the well mixed stage occurs in the metallicity range $-3 \lesssim$ [Fe/H] $\lesssim -2$ and the scatter in element abundances decreases continuously.
3. The ISM can be considered well mixed for metallicities [Fe/H] $\gtrsim -2.0$ and element abundances in stars correspond to the IMF averaged yields of SNe II. The instantaneous mixing approximation of classic chemical evolution is valid.
4. The onset of SN Ia events marks the beginning of a fourth phase in the enrichment of the ISM. The average [α/Fe] ratio decreases from the overabundance of ≈ 0.4 dex observed in metal-poor halo stars to solar values, which is well known from classic chemical evolution models.

These enrichment stages are visible in abundances of most α-elements and r-process elements. A notable exception is oxygen. Recent oxygen abundance determinations from UV-OH lines (e.g. Israelian et al. 1998, 2001; Boesgaard et al. 1999) indicate a small scatter and an increase in [O/Fe] with decreasing metallicity. Abundance determinations from the OI line, on the other hand, show a plateau in [O/Fe] at low metallicities. The reason for this difference is not well known and difficult to assess, but an investigation by Hill (2001) suggests that it might be caused by systematic errors. If the apparent slope in [O/Fe] turns out to be real, it would be hard to explain in chemical evolution models as long as no similar slope is observed in other α-elements (especially in the case of Mg). In Chapter 4, I have shown that a slope can easily be introduced into the distribution of model stars if the iron yields of SNe II are changed in a certain way. But this will also lead to a slope in the abundances of other α-elements. Magnesium is produced alongside with oxygen in hydrostatic carbon and neon burning and does not depend much on the explosion mechanism. A change in oxygen and magnesium yields is therefore not expected, even if iron yields are adjusted (which requires that the details of the explosion mechanism change). Thus, if a slope is present in both oxygen and magnesium abundances, it can be explained by a change in the iron yields which would provide valuable constraints for nucleosynthesis calculations. But if the slope is only present in oxygen abundances and not in magnesium abundances, it will be a challenge to find the reason for this behaviour.

Since the scatter in the early enrichment phases of the ISM is solely determined by the stellar yields, inhomogeneous chemical evolution models can be used to test their accuracy as function of progenitor mass. The scatter seen in observations of metal-poor halo stars can only be reproduced for some elements (e.g. Si and Ca), whereas the scatter predicted for oxygen and magnesium is much too large compared to observations. This indicates that the progenitor mass dependence of stellar yields is not well understood which is hardly surprising, at least in the case of iron-peak nuclei. Since no self-consistent core-collapse SN models are available to date, nucleosynthesis calculations make use of artificially induced explosions. This makes it impossible to accurately determine explosion energies and the placement of the mass cut as function of progenitor mass in a self-consistent way. Yields of iron-peak nuclei are especially sensitive to the placement of the mass cut since they originate from explosive silicon burning close to the forming proto-neutron star. Direct constraints from observations of core-collapse SNe are only available for some progenitor masses and in most cases the placement of the mass cut has to be extrapolated from the scarce information available to date. Hopefully, this will change in the future as more observations of Type Ib/c and Type II SNe become available.

Further constraints on the amount of ejected ^{56}Ni as function of progenitor mass (and thus on the stellar iron yields and the placement of the mass cut) can be gained with the help of inhomogeneous chemical evolution models. Since oxygen and magnesium are mostly unaffected by the explosion itself, stellar iron yields may be artificially changed so that the observed scatter in [O/Fe] and [Mg/Fe] abundances of metal-poor halo stars is reproduced. From the extent of the scatter in [O/Fe] and [Mg/Fe] limiting boundaries for iron yields as function of progenitor mass can be derived. To further narrow the range of probable iron yields, the ejected ^{56}Ni from core-collapse SNe with known progenitor masses have to be used. Unfortunately, the progenitor masses of SN 1997D and SN 1998bw are not well determined since models recovering their light-curves give in each case two significantly different values. Thus, four possible iron yields as function of progenitor mass have been derived in this work which correspond to the four different combinations of probable progenitor masses of SN 1997D and SN 1998bw (details are given in Chapter 3). Since the publication of Argast et al. (2002), new observations of core-collapse supernovae/hypernovae have been obtained which clarify the situation. The late stages of SN 1997D do not show any energy input from an accreting neutron star or pulsar, suggesting a black hole as stellar remnant and thus indicating a progenitor mass of $\approx 26\,\mathrm{M}_\odot$ (Benetti et al. 2001). The Type Ic SN 2002ap has a progenitor mass in the range of $20 - 25\,\mathrm{M}_\odot$ and an ejected ^{56}Ni mass of $\approx 0.07\,\mathrm{M}_\odot$ (Mazzali et al. 2002). A SN event from a lower-mass progenitor is SN 1999em, with a progenitor mass of $\approx 12\,\mathrm{M}_\odot$ and an ejected ^{56}Ni mass of $\approx 0.0022\,\mathrm{M}_\odot$ (Elmhandi & Danziger 2002; Smartt et al. 2002). Finally SN 1999as seems to have a high-mass progenitor $\gtrsim 60\ \mathrm{M}_\odot$ and an equally high ^{56}Ni mass of $\approx 4\ \mathrm{M}_\odot$ (!) that were synthesized in this event (see Nomoto et al. 2002). Thus, the hypernova scenario proposed by Iwamoto et al. (2000) seems to be favoured (compare the new data points to model H1 in Chapter 3 and the corresponding Figs. 3.11 and 3.15). This scenario is characterized by a sudden drop in the iron yields of supernovae/hypernovae with progenitors around $25\,\mathrm{M}_\odot$ due to the formation of a black hole and the strong increase for higher progenitor masses as the hypernova mechanism sets in. Note that this scenario predicts ultra α-element enhanced stars at very low metallicities ([Fe/H] ≤ -2.5), which can be tested by future observations.

In Chapter 4 the enrichment of the ISM with neutron capture elements has been studied. Many astrophysical r-process sites have been suggested, among them lower-mass SNe II ($8 - 10\,\mathrm{M}_\odot$), higher-mass SNe II ($\geq 20\,\mathrm{M}_\odot$) and neutron star mergers (NSM). Nucleosynthesis of s-process elements is thought to occur in thermally pulsing asymptotic giant branch (TP-AGB) stars in the mass range $1.5 - 4\,\mathrm{M}_\odot$. Thus, injection of r-process nuclei into the ISM occurs on timescales of $10 - 20$ Myr if SNe II are the major r-process sites, whereas s-process nucleosynthesis occurs on timescales of $300 - 400$ Myr. An estimate of the r-process injection timescale if NSM are the dominant r-process contributors is uncertain since the NSM rate is not well determined. Since the timescales of r- and s-process nucleosynthesis differ by an order of magnitude, important constraints on halo formation timescales can be gained by comparing abundances of r-process elements (e.g. Eu) to s-process elements (e.g. Ba).

The detection of s-process elements at low metallicities ([Fe/H] ≈ -2.7) suggests a low star formation efficiency during halo formation. The metallicity of the halo ISM is required to remain below [Fe/H]= -2.5 during the first $\approx$ 300 Myr of early Galaxy evolution to allow lower mass stars to reach their TP-AGB phase and s-process nucleosynthesis to start.

Observations of r-process elements at very low metallicities ([Fe/H] ≤ -3) suggest core-collapse SNe as mayor astrophysical r-process site, since NSM occur at a much lower rate and consequently eject more r-process matter than SNe II (to account for the total amount of observed r-process material in the Galaxy). The detailed comparison of SNe II and NSM as r-process sites in the framework of inhomogeneous chemical evolution supports this conclusion: Due to the low NSM rate, the injection of r-process nuclei into the interstellar medium occurs very late during Galaxy formation ([Fe/H] ≈ -2.5), whereas r-process elements are already present at [Fe/H] $= -3$ and probably even at [Fe/H] $= -4$. Additionally, due to the large r-process yield, considerable chemical inhomogeneities are present even at solar metallicity. The scatter in [r/Fe] is predicted to be of the order $1.0 - 1.5$ dex, whereas a scatter of only $0.2 - 0.3$ dex is observed. On the other hand, it is not possible to rule out either lower-mass SNe II or higher-mass SNe II as dominant r-process site from the point of view of inhomogeneous chemical evolution. Both r-process sites lead to r-process abundance distributions which are in agreement with observations.

It has been shown in this work, that inhomogeneous chemical evolution models provide a valuable tool to investigate the early chemical enrichment of the interstellar medium and to derive constraints on the star formation efficiency during halo formation. Furthermore, they can be used to test the progenitor mass dependence of stellar yields and can act as benchmarks for future core-collapse supernova/hypernova models. Thus they complement the classic chemical evolution models which assume that the ISM is well mixed at all times.

Although the inhomogeneous chemical evolution model presented in this work is now quite advanced, there are still many aspects that can be improved in the future. The implementation of metallicity dependent s-process yields and of a metallicity dependent star formation efficiency is of highest priority. In Chapter 4, some unrealistic assumptions had to be made due to this lack of the model. In principle it would also be possible to handle metallicity dependent stellar yields of core-collapse SNe. But it is questionable if it is sensible to implement this dependency since already the stellar yields of progenitors with solar metallicity are uncertain. A revision of yields of core-collapse SNe and their extension to lower metallicity progenitors clearly is needed. The unfortunate situation is, however, that there exists no theoretical foundation to do so for iron-group yields as long as the supernova explosion mechanism is not understood. Still, an emerging generation of nucleosynthesis calculations exhibit many improvements compared to older models. New constraints on the mass cut have been deduced from recently observed core-collapse SNe and effects of rotation on the core structure are now implemented in stellar evolution calculations. Furthermore, nucleosynthesis calculations from hypernovae, i.e. very energetic core-collapse SNe, are now available. Their higher kinetic energy will lead to improved mixing since they are able to pollute a larger ISM mass. This characteristic may help to explain the slope observed in iron-group elements (see Chapter 2). It will also be very interesting to investigate the impact of metal-free Population III stars on the chemical enrichment of the ISM. Population III stars are expected to have an IMF significantly different from the one of “ordinary” stars and to generate a characteristic nucleosynthetic signature.

Finally, no dynamics are implemented in the model to date. Thus, the mixing efficiency in the halo ISM is underestimated by the model. Furthermore, only one gas phase is considered at the moment. In reality, the ejecta of SNe reside in a hot gas phase, whereas star formation occurs only in the cores of cold clouds. Elements present in the hot gas phase thus are excluded from star formation until the gas had time to cool. Consequently a fraction of the newly synthesized elements may be lost in galactic winds. As mentioned in Chapter 4, this might explain the occurrence of s-process elements at low metallicities without assuming a low star formation efficiency during halo formation. The implementation of a hot and a cold gas phase and their interaction, together with a simple algorithm for the dynamics of the gas and stars, will require much work but will result in a major improvement of the model.

References

Abel, T., Bryan, G. L., & Norman, M. L. 2002, Science, 295, 93

Abia, C., Dominguez, I., Straniero, O., et al. 2001, ApJ, 557, 126

Anders, E., & Grevesse, N. 1989, Geochimica et Cosmochimica Acta, 53, 197

Aoki, W., Norris, J. E., Ryan, S. G., et al. 2000, ApJ, 536, L97

Argast, D., Samland, M., Gerhard, O. E., & Thielemann, F.-K. 2000, A&A, 356, 873 (Paper I)

Argast, D., Samland, M., Thielemann, F.-K., & Gerhard, O. E. 2002, A&A, 388, 842 (Paper II)

Arlandini, C., Käppeler, F., Wisshak, K., et al. 1999, 525, 886

Arnett, W. D. 1969, ApJ, 157, 1369

Atkinson, R. d'E. 1931a, ApJ, 73, 250

Atkinson, R. d'E. 1931b, ApJ, 73, 308

Atkinson, R. d'E. 1936, ApJ, 84, 73

Balachandran, S. C., & Carney, B. W. 1996, AJ, 111, 946

Baraffe, I., Heger, A., Woosley, S. E. 2001, ApJ, 550, 890

Bekki, K., & Chiba, M. 2000, ApJ, 534, L89

Belczynski, K., Kalogera, V., & Bulik, T. 2002, ApJ, 572, 407

Benetti, S., Turatto, M., Balberg, S., et al. 2001, MNRAS, 322, 361

Bessel, M. S., Sutherland, R. S., & Ruan, K. 1991, ApJ, 383, L71

Bethe, H. A. 1939, Physical Review, 55, 434

Beveridge, R. C., & Sneden, C. 1994, AJ, 108, 285

Binney, J., & Tremaine, S. 1987, Galactic Dynamics, Princeton University Press, Princeton, New Jersey

Boesgaard, A. M., King, J. R., Deliyannis, C. P., & Vogt, S. S. 1999, AJ, 117, 492

Bouchet, P., Danziger, I. J., & Lucy, L. B. 1991, AJ, 102, 1135

Bouchet, P., Phillips, M. M., Suntzeff, N. B., et al. 1991, A&A, 245, 490

Bouchet, P., & Danziger, I. J. 1993, A&A, 273, 451

Buchmann, L. 1996, ApJ, 468, L127

Buchmann, L. 1997, ApJ, 479, L153

Burbidge, G. R., Burbidge, W. A., Fowler, W. A., & Hoyle, F. 1957, Rev. Mod. Phys., 29, 547 (B^2FH)

Burris, D. L., Pilachowski, C. A., Armandroff, T. E., et al. 2000, ApJ 544, 302

Burrows, A. 1990, Ann. Rev. Nucl. Part. Sci., 40, 181

Burrows, A. 1996, Nucl. Phys., A606, 151

Burrows, A., Hayes, J., & Fryxell B. 1995, ApJ, 450, 830

Burrows, A., & Sawyer, R.F. 1998, Phys. Rev., C58, 554

Busso, M., Gallino, R., & Wasserburg, G. J. 1999, ARA&A, 37, 239

Cameron, A. G. W., & Truran, J. W., 1971, J. R. Astron. Soc. Can., 65, 1

Cameron, A. G. W. ApJ, 2001, 562, 456

Carney, B. W., Laird, J. B., Latham, D. W., & Aguilar, L. A. 1996, AJ, 112, 668

Carretta, E., Gratton, R. G., & Sneden, C. 2000, A&A, 356, 238

Cayrel, R., Hill, V., & Beers, T. C., et al. 2001, Nature, 409, 691

Chaboyer, B., Demarque, P., & Sarajedini, A., 1996, ApJ, 459, 558

Charbonnel, C., Meynet, G., Maeder, A., et al. 1993, A&AS, 101, 415

Chiappini, C., Matteucci, F., Beers, T. C., & Nomoto K. 1999, ApJ, 515, 226

Chiba, M., & Beers, T. C. 2000, AJ, 119, 2843

Chiba M., & Yoshii Y. 1998, AJ, 115, 168

Chieffi, A., Limongi, M., & Straniero, O. 1998, ApJ, 502, 737

Chieffi, A., Dominguez, I., Limongi, M., & Straniero, O. 2001, ApJ, 554, 1159

Chugai, N. N., & Utrobin, V. P. 2000, A&A, 354, 557

Cowan, J. J., Sneden, C., Ivans, I., et al. 1999, BAAS, 194, 67.04

Cowan, J. J., Sneden, C., Burles, S., et al. 2002, ApJ, 572, 861

Edvardsson, B., Andersen, J., Gustafsson, B., et al. 1993, A&A, 275, 101

Elmhandi, A., & Danziger, I. J. 2002, In: Hillebrandt, W., Müller, E. (Eds.) Proceedings of the 11th Workshop on "Nuclear Astrophysics". Max-Planck-Institut für Astrophysik, Garching, p. 148

Eggen, O. J., Lynden-Bell, D., & Sandage, A. R. 1962, ApJ, 136, 748

Evans, N. J. II. 1999, ARA&A, 37, 311

Flower, D. R., & Pineau des Forêts, G. 2001, MNRAS, 323, 672

François, P., Spite, M., & Spite F. 1993, A&A, 274, 821

Freiburghaus, C., Rembges, F., Rauscher, T., et al. 1999a, ApJ, 516, 381

Freiburghaus, C., Rosswog, S., Thielemann, F.-K. 1999b, ApJ 525, L121

Fryer, C. L. 1999, ApJ, 522, 413

Fryer, C. L., Colgate, S. A., & Pinto, P. A. 1999a, ApJ, 511, 885

Fryer, C. L., Woosley, S. E., & Hartmann, D. H. 1999b, ApJ, 526, 152

Fuhrmann, K., Axer, M., & Gehren, T. 1995, A&A, 301, 492

Galama, T. J., Vreeswijk, P. M., van Paradijs, J., et al. 1998, Nature, 395, 670

Gallino, R., Arlandini, C., Busso, M., et al. 1998, ApJ, 497, 388

Gnedin, N. Y. 1996, ApJ, 456, 1

Gratton, R. G. 1989, A&A, 208, 171

Gratton, R. G., & Sneden C. 1991a, A&A, 241, 501

Gratton, R. G., & Sneden C. 1991b, A&A, 287, 927

Harris, W. E., Bell, R. A., Vandenberg, D. A., et al. 1997, AJ, 114, 1030

Haywood, M. 2001, MNRAS, 325, 1365

Heger, A., Langer, N., & Woosley, S. E. 2000, ApJ, 528, 368

Heger, A. & Langer, N. 2000, ApJ, 544, 1016

Heger, A. & Woosley, S. E. 2001, astro-ph/0107037

Henry, R. B. C. 1984, ApJ, 281, 644

Herant, M., Benz, W., Hix, W. R., et al. 1994, ApJ, 435, 339

Hill, V. 2001, Ap&SS, 277, 137

Hill, V., Plez, B., Cayrel, R., et al. 2002, A&A, 387, 560

Hillebrandt, W., Nomoto, K., & Wolff, R. G. 1984, A&A, 133, 175

Hoffman, R. D., Woosley, S. E., Weaver, T. A., et al. 1999, ApJ, 521, 735

Houck, J. C., & Fransson, C. 1996, ApJ, 456, 811

Idiart, T., & Thévenin, F. 2000, ApJ, 541, 207

Imbriani, G., Limongi, M., Gialanella, L., et al. 2001, ApJ, 558, 903

Ishimaru, Y., & Wanajo, S. 1999, ApJ, 511, L33

Israelian, G., Garcia López, R. J., & Rebolo, R. 1998, ApJ, 507, 805

Israelian, G., Rebolo, R., Garcia López, R. J., et al. 2001, ApJ, 551, 833

Iwamoto, K., Nomoto, K., Höflich, P., et al. 1994, ApJ 437, L115

Iwamoto, K., Mazzali, P.A., Nomoto, K., et al. 1998, Nature 395, 672

Iwamoto, K. 1999a, ApJ, 512, L47

Iwamoto, K. 1999b, ApJ, 517, L67

Iwamoto, K., Brachwitz, F., Nomoto, K., et al. 1999, ApJS, 125, 439

Iwamoto, K., Takayoshi, N., Nomoto, K., et al. 2000, ApJ, 534, 660

Janka, H.-T., & Müller, E. 1995, Phys. Rep., 256, 135

Janka, H.-T., & Müller, E. 1996, A&A, 306, 167

Jehin, E., Magain, P., Neuforge, C., et al. 1999, A&A, 341, 241

Kalogera, V., & Lorimer, D. R. 2000, ApJ, 530, 890

Keilk W., & Janka H.-T. 1995, A&A, 296, 145

King, J. R. 1994, ApJ, 436, 331

King, J. R. 2000, AJ, 120, 1056

Kippenhahn, R., & Weigert, A. 1990. In: Appenzeller, I., Harwit, M., Kippenhahn, R. Strittmatter, P. A., Trimble, V. (eds.) Stellar Structure and Evolution, Springer, Berlin

Klypin, A., Kravtsov, A. V., Valenzuela, O., & Prada F. 1999, ApJ, 522, 82

Koch, A. & Edvardsson, B. 2002, A&A, 381, 500

Kozma, C., & Fransson, C. 1998, ApJ, 497, 431

Lambert, D. L., Smith, V. V., Busso, M., et al. 1995, ApJ, 450, 302

Langer, N., & Henkel, C. 1995. In: Busso, M., Gallino, R., Raiteri, C. M. (eds.) Nuclei in the Cosmos III. AIP Press, p. 413

Langer, N., Fliegner, J., Heger, A., & Woosley, S. E. 1997, Nucl. Phys., A621, 457c

Larson, R. B., 1988. In: Pudritz, R. E., Fich M. (eds.) Galactic and Extragalactic Star Formation. NATO ASI Series 232, Kluwer, Dordrecht, p. 5

Larson, R. B., 1991. In: Lambert, D. A. (ed.) Frontiers of stellar evolution. ASP Conf. Ser. 20, 539.

Liebendörfer, M., Mezzacappa, A., Thielemann, F.-K., et al. 2001, Phys. Rev. D, 6310, 3004

MacFadyen, A. I., Woosley, S. E., & Heger, A. 2001, ApJ, 550, 410

Maeder, A. 1992, A&A, 264, 105

Maeder, A. & Meynet, G. 2000, ARA&A, 38, 143

Magain, P. 1989, A&A, 209, 211

Mashonkina, L. & Gehren, T. 2000, A&A, 364, 249

Mashonkina, L. & Gehren, T. 2001, A&A, 376, 232

Mathews, G. J., Bazan, G., & Cowan, J. J. 1992, ApJ, 391, 719

Matteucci, F., Romano, D., & Molaro, P. 1999, A&A, 341, 458

Mazzali, P. A., Lucy, L. B. & Buttler, K. 1992, A&A, 258, 399

Mazzali, P. A., Deng, J., Maeda, K., et al. 2002, ApJ, 572, L61

McWilliam, A., Preston, G. W., Sneden, C., & Searle, L. 1995a, AJ, 109, 2757

McWilliam, A., Preston, G. W., Sneden, C., & Shectman, S. 1995b, AJ, 109, 2736

McWilliam, A. 1997, ARA&A, 35, 503

McWilliam, A. 1998, AJ, 115, 1640

Merill, P. W. 1952, ApJ, 116, 21

Messer, O. E. B., Mezzacappa, A., Bruenn, S. W., & Guidry, M. W. 1998, ApJ, 507, 353

Meyer, B. S., & Brown, J. S. 1997, ApJS, 112, 199

Meynet, G., & Maeder, A. 1997, A&A, 321, 465

Meynet, G. & Maeder, A. 2000, A&A, 361, 101

Mezzacappa, A., Calder, A. C., Bruenn, S. W., et al. 1998, ApJ, 495, 911

Mezzacappa, A., Liebendörfer, M., Messer, O. E. B., et al. 2001, Phys. Rev. Letters, 86, 1935

Mishenina, T. V. & Kovtyukh, V. V. 2001, A&A, 370, 951

Molaro, P., & Bonifacio, P. 1990, A&A, 236, L5

Molaro, P., & Castelli, F. 1990, A&A, 228, 426

Moore, B., Ghigna, S., Governato, F., et al. 1999, ApJ, 524, L19

Nagataki, S., Hashimoto, M., Sato, K., Yamada, S. 1997, ApJ, 486, 1026

Nagataki, S., Hashimoto, M., Sato, K., et al. 1998, ApJ, 492, L45

Nakamura, T., Umeda, H., Nomoto, K., et al. 1999, ApJ, 517, 193

Nakamura, T., Umeda, H., Iwamoto, K., et al. 2001, ApJ, 555, 880

Navarro, J. F., & Steinmetz, M. 2000, ApJ, 538, 477

Nissen, P. E., Gustafsson, B., Edvardsson, B., & Gilmore, G. 1994, A&A, 285, 440

Nomoto, K., & Hashimoto, M., 1988, Phys. Rep., 163, 13h

Nomoto, K., Hashimoto, M., Tsujimoto, T., et al. 1997, Nucl. Phys., A616, 79c13

Nomoto, K., Maeda, K., Umeda, H., et al. 2002. In vna der Huch, K. A., Herrero, A. & Esteban, C. (eds.): A Massive Star Oddyssey, from Main Sequence to Supernova, Proceedings IAU Symposium No. 212

Norris, J. E., Peterson, R. C., & Beers, T. C. 1993, ApJ, 415, 797

Norris, J. E., Beers, T. C., Ryan, S. G. 2000, ApJ 540, 456

Oechslin, R., Rosswog, S., & Thielemann, F. K. 2002, Phys. Rev., D65, 103005

Oort, J. H. 1970, A&A, 7, 381

Öpik, J. 1951, Proc. R. Irish Acad. A., 54, 49

Pearce, F. R., Jenkins, A., Frenk, C. S., et. al. 1999, ApJ, 521, L99

Peterson, R. C., Kurucz, R. L., & Carney, B. W. 1990, ApJ, 350, 173

Pons, J. A., Reddy, S., Prakash, M., et al. 1999, ApJ, 513, 780

Portegies Zwart, S. F., & Yungel'son, L. R. 1998, A&A, 332, 173

Pratchett, T. 1990, In: *Eric – A Discworld Novel*, Victor Gollanz Ltd, ISBN 0 575 60001 2, p. 108

Primas, F., Molaro, P., & Castelli, F., 1994 A&A, 290, 885

Qian, Y.-Z., & Woosley, S. E. 1996, ApJ, 471, 331

Qian, Y.-Z. 2000, ApJ, 534, L67

Qian, Y.-Z. 2001, ApJ, 552, L117

Raiteri, C. M., Villata, M., Gallino, R., et al. 1999, ApJ, 518, L91

Rampp, M., & Janka, H.-T. 2000, ApJ, 539, L33

Rana, N. C. 1991, ARA&A, 29, 129

Rauscher, T., Heger, A., Hoffman, R. D. & Woosley S. E. 2002, astro-ph/0112478

Rebolo, R., et al. 2002, in preparation

Reddy, S., & Prakash, M. 1997, ApJ, 423, 689

Rocha-Pinto, H. J., Scalo, J., Maciel, W. J., & Flynn, C. 2000, ApJ, 531, L115

Rosswog, S., Liebendörfer, M., Thielemann, F.-K., et al. 1999, A&A, 341, 499

Rosswog, S., Davies, M. B., Thielemann, F.-K., & Piran, T. 2000, A&A, 360, 171

Ryan, S. G., & Norris J. E. 1991, AJ, 101, 1865

Ryan, S. G., Norris, J. E., & Bessell, M. S. 1991, AJ, 102, 303

Ryan, S. G., Norris, J. E., & Beers, T. C. 1996, ApJ, 471, 254

Saio, H., & Nomoto, K. 1998, ApJ, 500, 388

Salpeter, E. E. 1952, ApJ, 115, 326

Samland, M. 1998, ApJ, 496, 155

Samland, M. & Gerhard, O. E. 2003, astro-ph/0301499

Schwarzschild, M., & Spitzer, L. 1953, The Observatory, 73, 77

Scalo, J. M. 1986, Fund. Cosmic Phys., 11, 1

Searle, L., & Zinn, R. 1978, ApJ, 225, 357

Schaerer, D., Meynet, G., Maeder, A., & Schaller, G., 1993a, A&AS, 98, 523

Schaerer, D., Charbonnel, C., Meynet, G., et al. 1993b, A&AS, 102, 339

Schaller, G., Schaerer, D., Meynet, G., & Maeder, A., 1992 A&AS, 96, 269

Schmidt, M. 1959, ApJ, 121, 161

Shigeyama, T., & Nomoto, K. 1990, ApJ, 360, 242

Shigeyama, T., Suzuki, T., Kumagai, S., & Nomoto, K. 1994, ApJ, 420, 341

Shigeyama, T., & Tsujimoto, T. 1998, ApJ, 507, L135

Smartt, S. J., Gilmore, G. F., Tout, C. A., & Hodgkin, S. T. 2002, ApJ, 565, 1089

Sneden, C., Preston, G. W., McWilliam, A., & Searle, L. 1994, ApJ, 431, L27

Sneden, C., McWilliam, A., Preston, G. W., et al. 1996, ApJ, 467, 819

Sneden, C., Cowan, J. J., Ivans, I. I., et al. 2000a, ApJ, 533, L139

Sneden, C., Johnson, J., Kraft, P. R., et al. 2000b, ApJ, 536, L85

Sneden, C., Cowan, J. J., Lawler, J. E., et al. 2002, ApJ, 566, L25

Sollerman, J., Leibundgut, B., & Spyromilio, J. 1998, A&A, 337, 207

Sollerman, J., Kozma, C., Fransson, C., et al. 2000, ApJ, 537, L127

Spiesman, W. J., & Wallerstein, G. 1991, AJ, 102, 1790

Spite, M., & Spite, F. 1991, A&A, 252, 689

Spruit, H. C. 1992, A&A, 253, 131

Steinmetz, M., & Müller, E. 1995, MNRAS, 276, 549

Stephens, A., & Boesgaard, A. M. 2002, AJ, 123, 1647

Sumiyoshi, K., Terasawa, M., Mathews, G. J., et al. 2001, ApJ, 562, 880

Suntzeff, N. B., & Bouchet, P. 1990, AJ, 99, 650

Suntzeff, N. B., Phillips, M. M., Elias, J. H., et al. 1992, ApJ, 384, L33

Sutherland, R. S. & Dopita, M. A. 1993, ApJS, 88, 253

Takahashi, K., Witti, J., & Janka, H.-T. 1994, A&A, 286, 857

Talbot, R. J. Jr. & Arnett, W. D. 1973, ApJ, 186, 51

Talon, S., Zahn, J.-P., Maeder, A., & Meynet, G. 1997, A&A, 322, 209

Tammann, G. A., Löffler, W., & Schröder, A. 1994, ApJS, 92, 487

Thielemann, F.-K., Hashimoto, M., & Nomoto, K. 1990, ApJ, 349, 222

Thielemann, F.-K., Nomoto, K., & Hashimoto, M. 1996, ApJ, 460, 408 (TH96)

Thomas, D., Greggio, L. & Bender, R. 1998, MNRAS, 296, 119

Thompson, T. A., Burrows, A., & Bradley, S. M. 2001, ApJ, 562, 887

Tinsley, B. M. 1974, ApJ, 192, 629

Travaglio, C., Galli, D., Gallino, R., et al. 1999, ApJ, 521, 691

Travaglio, C., Galli, D. & Burkert, A. 2001, ApJ, 547, 217

Truran, J. W., & Arnett, W. D. 1970, ApJ, 160, 181

Tsujimoto, T., & Shigeyama, T. 1998, ApJ, 508, L151

Tsujimoto, T., Shigeyama, T., & Yoshii, Y. 1999, ApJ, 519, L63

Tsujimoto, T., Shigeyama, T., & Yoshii, Y. 2000, ApJ, 531, L33

Tsujimoto, T., & Shigeyama, T. 2001, ApJ, 561, L97

Turatto, M., Mazzali, P. A., Young, T. R. et. al. 1998, ApJ 498, L129

Umeda, H., Nomoto, K., & Nakamura, T. 2000, In: Weiss, A., Abel, T., Hill, V. (Eds.) The First Stars. ESO astrophysics symposia proceedings, 1999, Springer

Utrobin, V. P., & Chugai, N. N. 2002, In: Hillebrandt, W., Müller, E. (Eds.) Proceedings of the 11th Workshop on "Nuclear Astrophysics". Max-Planck-Institut für Astrophysik, Garching, p. 136

van den Heuvel, E., & Lorimer, D. 1996, MNRAS, 283, L37

von Weizsäcker, C. F. 1937, Physikalische Zeitschrift, 38, 176

von Weizsäcker, C. F. 1938, Physikalische Zeitschrift, 39, 633

Wallerstein, G., Iben, I., Jr., Parker, P., et al. 1997, Rev. Mod. Phys., 69, 995

Wanajo, S., Toshitaka, K., Mathews, G. J., & Otsuki, K. 2001, ApJ 554, 578

Wasserburg, G. J., Busso, M., & Gallino, R. 1996, ApJ, 466, L109

Wasserburg, G. J., & Qian, Y.-Z. 2000, ApJ, 529, L21

Westera, P., Samland, M., Buser, R., & Gerhard, O. E., 2002, A&A, 389, 761

Westin, J., Sneden, C., Gustafsson, B., & Cowan, J. J. 2000, ApJ, 530, 783

Williams, R. E. 1987, ApJ, 320, L117

Wheeler, J. C., Cowan, J. J., & Hillebrandt, W. 1998, ApJ, 493, L101

Woolf, V. M., Tomkin, J., Lambert, D. L. 1995, ApJ, 453, 660

Woosley, S. E., & Hoffman, R. D. 1992, ApJ, 395, 202

Woosley, S. E., Wilson, J. R., Mathews, G. J., et al. 1994, ApJ, 433, 229

Woosley, S. E., & Weaver, T. A. 1995, ApJS, 101, 181 (WW95)

Yamada, S., Janka, H.-T., & Suzuki, H. 1999, A&A, 344, 533

Zhao, G., & Magain, P. 1990, A&A, 238, 242

Acknowledgements

I thank Ortwin Gerhard for teaching me how to work independently, Friedel Thielemann for his great interest in my work and Markus Samland for his invaluable help and for never despairing when he had to answer again and again the same dumb questions.

Special thanks go to Andreas Immeli, my long time office colleague. He suffered uncomplainingly all the times when I was grumpy in the morning (well, at least when I showed up that early), and it was great fun to discuss with him cutting-edge scientific developments and, not least of all, the happenings at our institute.

I am indebted to U2, Midnight Oil, New Model Army, Manau, Pink Floyd, Simple Minds, The Cranberries, Subzonic, Sonique, Sisters of Mercy, Rage Against the Machine, Nirvana, H-Blockx and Guano Apes for their moral and musical support. This work would never have been completed without it.

Finally, I greatfully acknowledge the financial support of the Swiss National Science Foundation.

Declaration

Ich erkläre, dass ich die Dissertation *Inhomogeneous Chemical Evolution of the Galactic Halo* nur mit der darin angegebenen Hilfe verfasst und bei keiner anderen Fakultät eingereicht habe.

Basel, den 3. September 2002

Dominik Argast

Curriculum Vitae

Name	Dominik Argast
Date of birth	June 28, 1972
Place of birth	Basel
Nationality	Swiss

1979 – 1983	Elementary school in Basel
1983 – 1991	High school in Basel (Mathematisch-Naturwissenschaftliches Gymnasium)
June 1991	Matura
1991 – 1992	Extended stay in Montreal, Canada
1992 – 1998	Studies in mathematics, physics and astronomy at the University of Basel
Summer 1998	Diploma in mathematics
1998 – 2002	PhD thesis at the Astronomical Institute and the Institute for Physics, University of Basel

During my studies, I heard lectures given by: Prof. Dr. C. Bandle, PD Dr. J. Escher, Prof. Dr. H.-C. Im Hof, Prof. Dr. H. Kraft, Prof. Dr. D. Kotschik, Prof. Dr. B. Scarpellini (Mathematics); Prof. Dr. H. Rudin, Prof. Dr. L. Tauscher, Prof. Dr. F.-K. Thielemann, Prof. Dr. D. Trautmann (Physics); PD Dr. B. Binggeli, Prof. Dr. R. Buser, PD Dr. A. Gautschy, Prof. Dr. O. E. Gerhard, Prof. Dr. G. A. Tamman (Astronomy).